Modélisation spatialisée semi-conceptuelle des flux d'eaux surface - souterrain en milieu karstique

Ibrahim Al Khoury

▶ **To cite this version:**

Ibrahim Al Khoury. Modélisation spatialisée semi-conceptuelle des flux d'eaux surface - souterrain en milieu karstique. Hydrologie. Université de Toulouse, 2024. Français. NNT : 2024TLSES131 . tel-04931121

HAL Id: tel-04931121

https://theses.hal.science/tel-04931121v1

Submitted on 5 Feb 2025

HAL is a multi-disciplinary open access archive for the deposit and dissemination of scientific research documents, whether they are published or not. The documents may come from teaching and research institutions in France or abroad, or from public or private research centers.

L'archive ouverte pluridisciplinaire **HAL**, est destinée au dépôt et à la diffusion de documents scientifiques de niveau recherche, publiés ou non, émanant des établissements d'enseignement et de recherche français ou étrangers, des laboratoires publics ou privés.

RÉPUBLIQUE FRANÇAISE
Liberté
Égalité
Fraternité

Université de Toulouse

Doctorat de l'Université de Toulouse

préparé à l'Université Toulouse III - Paul Sabatier

Modélisation spatialisée semi-conceptuelle des flux d'eaux surface - souterrain en milieu karstique

Thèse présentée et soutenue, le 2 octobre 2024 par

Ibrahim AL KHOURY

École doctorale
SDU2E - Sciences de l'Univers, de l'Environnement et de l'Espace

Spécialité
Surfaces et interfaces continentales, Hydrologie

Unité de recherche
GET - Geosciences Environnement Toulouse

Thèse dirigée par
David LABAT et Laurie BOITHIAS

Composition du jury
Mme Hélène CELLE, Rapporteure, Université Franche Comté
M. Nicolas MASSEI, Rapporteur, Université Rouen Normandie
M. Pieter VAN BEEK, Examinateur, Président du jury, Université Toulouse III - Paul Sabatier
M. Stéphane BINET, Examinateur, Agence de l'eau Adour-Garonne
M. Ryan BAILEY, Examinateur, Colorado State University
M. David LABAT, Directeur de thèse, Université Toulouse III - Paul Sabatier
Mme Laurie BOITHIAS, Co-directrice de thèse, Université Toulouse III - Paul Sabatier

Abstract (English Version)

Karst aquifers, which supply freshwater to nearly 25% of the global population, are facing depletion due to climate change and anthropogenic pressure. Hydrological models have been advocated for effective karst water resources planning and management, but studies integrating the recharge-discharge characteristics of karst watersheds and evaluating their response to changes in the flow dominant controls remain limited due to their inherent heterogeneity, anisotropy, flow duality, and non-linearity. This thesis developed the semi-conceptual spatialized numerical model ISPEEKH (Integration of Surface ProcEssEs in Karst Hydrology) by coupling SWAT+, the restructured version of the semi-distributed eco-hydrological model SWAT (Soil and Water Assessment Tool), with the non-linear epikarst-matrix-conduit reservoir module of the rainfall-runoff model KarstMod to simulate the surface-underground water flows in karst watersheds. ISPEEKH was applied to simulate the daily water balance of the Baget catchment (13.25 km^2), located in a poorly gauged region of the French Pyrénées and characterized by conduit-dominated non-linear flow. The model simulated the catchment streamflow satisfactorily (NSE = 0.67, R^2 = 0.68, and PBIAS = 0.7% for the 2008−2013 calibration period, and NSE = 0.65, R^2 = 0.69, and PBIAS = -13.83% for the 2014−2018 validation period), allowing the estimation of the epikarst, matrix, and conduit fluxes, including the bidirectional matrix-conduit exchange flow rate, the contribution of the matrix and conduit outflows to spring flow, and their seasonal variability. The Baget catchment's hydrological response to synthetic land-use change scenarios of afforestation and deforestation was then assessed using ISPEEKH. Results showed that afforestation over the entire catchment did not significantly affect its water balance, while deforestation for wood production increased the mean annual discharge by 6−9%, notably in the low-flow periods, and deforestation for pastureland development reduced the mean annual discharge by 5−7%, mainly in the high-flow period. Various precipitation datasets were then evaluated for the simulation of daily streamflow in the catchment from 2006−2018, including the gauge-based (CPC and E-OBS), reanalysis (SAFRAN, COMEPHORE and ERA5-Land), and satellite-based (PERSIANN-CDR, IMERG-LR, SM2RAIN-ASCAT and CHIRPS) products. ISPEEKH was integrated with a PEST framework for automated calibration, sensitivity analysis, and uncertainty quantification. Results showed that streamflow was significantly underestimated under the ensemble of the precipitation products. The gauge- and satellite-based precipitation products had the worst performance, with a flow underestimation bias ranging from 48 to 74%, while the reanalysis products yielded better streamflow simulation results with a flow underestimation bias of 30−44%. The CPC, E-OBS, ERA5-Land, IMERG-LR, and merged CPC-

IMERG-LR datasets downscaled to 1-km spatial resolution did not improve the model predictive performance compared to the coarse datasets. The downscaled datasets along with COMEPHORE were bias corrected to reduce the water balance discrepancy and re-applied for hydrological modeling. Significant improvement in the streamflow simulation were observed under the corrected COMEPHORE and downscaled E-OBS, CPC, and merged CPC-IMERG-LR precipitation datasets, with COMEPHORE yielding the best model predictive performance (NSE = 0.719, R^2 = 0.736, and PBIAS = 3.2% for the calibration period, and NSE = 0.637, R^2 = 0.732, and PBIAS = -10.65% for the validation period), suggesting that fine-resolution native reanalysis precipitation could be used as a base dataset for the hydrological modeling of remote meso-scale karst catchments.

Abstract (French Version)

Les aquifères karstiques, fournissant de l'eau potable à environ 25% de la population mondiale, sont confrontés à des surexploitations en sus du changement climatique. Des modèles hydrologiques ont été préconisés pour une gestion efficace des ressources en eau karstique. Cette thèse développe le modèle numérique semi-conceptuel spatialisé ISPEEKH en couplant SWAT+, la version restructurée du modèle éco-hydrologique semi-distribué SWAT, avec le module de réservoirs non linéaires épikarst-matrice-conduit du modèle de ruissellement pluvial KarstMod pour simuler les flux d'eau de surface-souterraine dans les bassins versants karstiques. ISPEEKH a été appliqué pour simuler le bilan hydrique quotidien du bassin versant du Baget (13.25 km^2), situé dans les Pyrénées françaises et caractérisé par un écoulement non linéaire dominé par des conduits. Le modèle a simulé le débit du bassin versant de manière satisfaisante (NSE = 0,67, R^2 = 0,68, et PBIAS = 0,7% pour la période de calibration 2008−2013, et NSE = 0,65, R^2 = 0,69, et PBIAS = -13. 83% pour la période de validation 2014−2018), permettant l'estimation des flux des compartiments de l'épikarst, de la matrice et des conduits, y compris le débit d'échange entre la matrice et les conduits, et la contribution de la matrice et des flux de sortie du conduit principal au débit de la source karstique. La réponse hydrologique du bassin versant du Baget à des scénarios synthétiques de changement d'occupation du sol (reforestation et déforestation) a ensuite été évaluée à l'aide du modèle ISPEEKH. Les résultats ont montré que la reforestation sur l'ensemble du bassin versant n'a pas eu d'impact significatif sur son bilan hydrique, Le changement du couvert forestier à un couvert arbustif de transition a augmenté le débit annuel moyen de 6 à 9%, notamment pendant les périodes de faible débit, tandis que le changement du couvert forestier à des pâturages a réduit le débit annuel moyen de 5 à 7%, principalement en périodes de fort débit. En outre, un ensemble de données de précipitation a été évalué pour la simulation du débit journalier dans le bassin versant de 2006 à 2018, y compris les produits basés sur des données pluviométriques (CPC et E-OBS), de réanalyse (SAFRAN, COMEPHORE et ERA5-Land) et satellitaires (PERSIANN-CDR, IMERG-LR, SM2RAIN-ASCAT et CHIRPS). ISPEEKH a été intégré avec PEST pour la calibration automatisée, l'analyse de la sensibilité et la quantification de l'incertitude. Les résultats ont montré que le débit des cours d'eau était significativement sous-estimé sous l'ensemble des produits de précipitations. Les produits basés sur des données pluviométriques et satellitaires sont les moins performantes, avec un biais de sous-estimation du débit allant de 48 à 74%, tandis que les données de réanalyse ont fourni de meilleurs résultats de simulation du débit, avec un biais de sous-estimation du débit allant de 30 à 44%. Les données CPC, E-OBS, ERA5-Land, et IMERG-

LR, ainsi que les données fusionnés CPC-IMERG-LR à une résolution de 1 km n'ont pas amélioré la capacité de prédiction du modèle par rapport aux données brutes. Les données à échelle réduite ainsi que COMEPHORE ont été corrigés pour réduire le biais de l'écart du bilan hydrique et ont été réappliqués pour la modélisation hydrologique. La simulation du débit a été améliorée significativement avec les données de précipitations COMEPHORE, E-OBS, CPC, et CPC-IMERG-LR corrigées. COMEPHORE a fourni la meilleure performance prédictive du modèle, suggérant que les précipitations de réanalyse locale à résolution fine pourraient être utilisées comme ensemble de données de base pour la modélisation hydrologique des bassins versants karstiques de méso-échelle.

Acknowledgements

The thesis's success is attributed to the invaluable support of numerous individuals, to whom I express my sincere gratitude.

First, I would like to extend my deepest gratitude to my thesis supervisors Prof. Dr. David Labat and Dr. Laurie Boithias for their contributions to the completion of this thesis. I am profoundly grateful for their initiative in developing the thesis subject, entrusting me with the process of defending it,

Above all, I wish to thank them for their human qualities—their kindness, compassion, and unwavering encouragement during the past three years. Their support has been a beacon of hope and strength through the challenges I encountered along this journey.

I would like to thank the members of the "comité de suivi de thèse" Prof. Dr. Hélène Roux and Dr. Matthieu Fournier for their valuable discussions during the progression of the thesis, and all the co-authors who contributed with their comments and suggestions to my articles. In particular, I am immensely appreciative to Dr. Ryan Bailey for agreeing to be part of this thesis and providing pivotal knowledge and technical skills necessary for the development of the code used for hydrological modeling in this thesis, and for Dr. Vianney Sivelle for sharing his theoretical knowledge in karst hydrology. I am also grateful to the entire doctoral school, and particularly to Prof. Dr. Geneviève Soucail, Mme Tanya Robinson, and Mr. Adrien Bru, for their assistance with the procedures and the follow-up of our thesis.

Additionally, I extend my gratitude to my friends for the time we spent together to relax, energize, enjoyment our company and surroundings in France, all of which have been indispensable in maintaining my well-being throughout this journey. Finally, I would like to express my deepest gratitude and appreciation to my parents and siblings for their love and support at every stage of my life.

Table of Contents

List of Figures

List of Tables

CHAPTER 1: Scientific background and aims of the thesis

1.1 General Introduction

Karst aquifers are an abundant source of water in many regions across the globe, providing freshwater supply to 20–25% of the world population (Chen et al., 2017) and upwards of 50% of the total drinking water supply in some countries (Biondić et al., 2021). They cover nearly 15.2% of Earth's continental surface (Auler and Stevanović, 2021) and form by chemical dissolution of soluble carbonate rocks (i.e., limestone, dolomite, marble or evaporates) exerted by water enriched with carbon dioxide (CO_2) from the atmosphere or soil zone (Goldscheider et al., 2020). Depending on the degree of karstification, distinctive karst features can develop, including sinkholes and dolines, losing streams, springs, and vast networks of subsurface and hydrologically connected cracks, fissures, conduits, and caves (Zeiger et al. 2021).

A karst system is generally composed of four main water-bearing mediums with distinct geomorphology, hydrodynamic properties, storage, and flow patterns: (1) the soil and non-karstic zone, (2) the epikarst, (3) the transmission zone - the latter three forming the unsaturated zone, and (4) the saturated zone (Dal Soglio et al., 2020b). These contrasting layers, which are interactively connected by water flow and solute transport, form the karstic critical zone (Chen et al., 2018; Wang et al., 2020). **Figure 1** shows a schematic model of a typical karst aquifer, including the surface hydrological processes and flow mechanisms of the underground karst subsystems. Karst aquifers behave as a dual to triple-porosity medium, which consists of intergranular pores (primary porosity) aggregated with fractures and bedding planes (fracture porosity) into a single rock matrix and solution enlarged channels and pipes networks (conduit porosity) that transfer most of the recharge to the karst springs (Geyer et al., 2013; Ghasemizadeh et al., 2012). The epikarst represents a weathered horizon of a few meters above the vadose zone, characterized by high permeability and porosity driven by the large supply of CO_2 that increases dissolution of carbonate rocks near the land surface. Dual recharge mechanisms are generally observed in a karst system: (1) diffuse recharge by slow percolation of infiltrated water from the epikarst to the saturated zone through low permeability small fissures in the vadose zone and (2) concentrated recharge via highly conductive karst features (enlarged fractures, sinkholes), allowing a fast transit of flow through the vadose zone to the saturated zone (Paiva, and Cunha, 2020). The epikarst, together with the soil cover, controls water infiltration, storage, and temporal delay of recharge to the saturated zone by storing percolation water temporarily during the dry and low recharge periods, and releasing the flow quickly via the karst openings at saturation when the infiltration rate exceeds percolation. The epikarst's storage capacity depends on its maturity and the permeability contrast between its bottom part and the underlying transmission zone. At total evolution of the epikarst, surface runoff is reduced and most of the infiltration that passes the epikarst flows through the conduits, while percolation through the matrix and

fissures does not increase Alternatively, the epikarst can be discontinuous, poorly developed, or completely removed by geomorphic processes, reducing its hydrological role (Bauer et al., 2005; Fidelibus et al., 2017; Nannoni and Piccini, 2022; Yan et al., 2022).

The transmission zone connects and transfers recharge water from the epikarst to the saturated zone where the highly permeable karst conduits drain the fissured rock matrix, generating a flow to the groundwater discharge. Karst systems thus exhibit dual storage and subsurface flow fields: (1) prolonged groundwater storage and low-flow velocity (laminar flow) in the matrix, and (2) low groundwater storage with rapid flow velocity/non-linear (turbulent) flow in the conduits. Dual discharge patterns to the aquifer outlet are also observed with (1) slow and continuous flow from the matrix during dry periods and (2) fast flow from the conduits during heavy rainfall events (de Rooji and Graham, 2017; Giese et al., 2018; Hartmann et al., 2021). The conduit and the matrix also exchange flow, which primarily depends on the hydraulic head differences between the two mediums and on the conduit properties (Dal Soglio et al., 2020a), and can contribute substantially to the spring discharge during the dry and low-flow periods (Sivelle et al., 2019). Several studies have established that the nonlinear storage-discharge relationship best represents the epikarst-matrix-conduits flow dynamics (Basu et al., 2022; Chang et al., 2015; Kurtulus and Razack, 2007; Labat et al., 2000; Zhao et al., 2021).

In addition, the recharge boundaries of karst aquifers may not often coincide with the drainage basin boundaries. While direct infiltration from precipitation on the karst outcrops forms autogenic recharge, the infiltration of runoff water from adjacent non-karstic areas constitutes allogenic recharge with an interbasin groundwater flow components that crosses the surface topographic divides through the conduits before emerging at the springs. Allogenic recharge could represent a significant portion of the karst spring discharge, particularly in high-permeability bedrock areas. Therefore, neglecting the discrepancy between the topographic and hydrogeological boundaries of these karst aquifers, known as binary karst systems, and the representation of hydrological processes of their combined karst and non-karst recharge areas, results in unclosed water balance and inaccurate estimates of their water resources. Interbasin groundwater flow is not explicitly measurable, requiring the application of hydrogeochemical approaches based on major dissolved elements, isotopes, electrical conductivity, and water temperature monitoring or hydrogeological studies of groundwater flow paths and physical techniques such as including physical techniques such as the soil–water budget and water level fluctuation, or a combination of these approaches (Belay et al., 2023; Bouaziz et al., 2018; Chen et al., 2018; Hartmann et al., 2021; Le Mesnil et al., 2020; Nguyen et al., 2020; Senent-Aparicio et al., 2020)

Due to their intrinsic properties and complex hydrodynamic behavior, karst aquifers are vulnerable to overexploitation, climate change, and contamination (Goldscheider, 2019; Gutiérrez et al., 2018). Karst groundwater resources continue to face a depletion stress around the globe due to increased water abstraction,

land use change, and climate change (Doummar et al., 2018; Fiorillo and Guadagno, 2012; Hao et al., 2009; Jia et al., 2017; Kovačič et al., 2020; Nerantzaki and Nikolaidis, 2020; Ruiz et al., 2022; Sivelle et al., 2021; Smiatek et al., 2013; Taheri et al., 2016). In well-developed karst systems, natural processes such as absorption, degradation, and filtration are inefficient due to low storage capacity, fast water movement, short residence time, and limited interaction with the material of the aquifer. Thus, contaminants can rapidly reach the groundwater table by concentrated recharge and propagate easily through karst conduits over large distances (Entezari et al., 2016; Iván and Mádl-Szőnyi, 2017).

Therefore, understanding the hydrodynamic functioning of the karst aquifer water bearing components and anticipating the impacts of climate change and anthropogenic pressures on karst water resources are compulsory tasks to safeguard these diminishing water supplies and set effective schemes for their management. Yet, the assessment of karst water resources considering the spatial variability of the surface and underground flow determinants remains a challenge due to the aquifers' heterogeneity, anisotropy, recharge and discharge duality, and flow non-linearity (Hartmann et al., 2014).

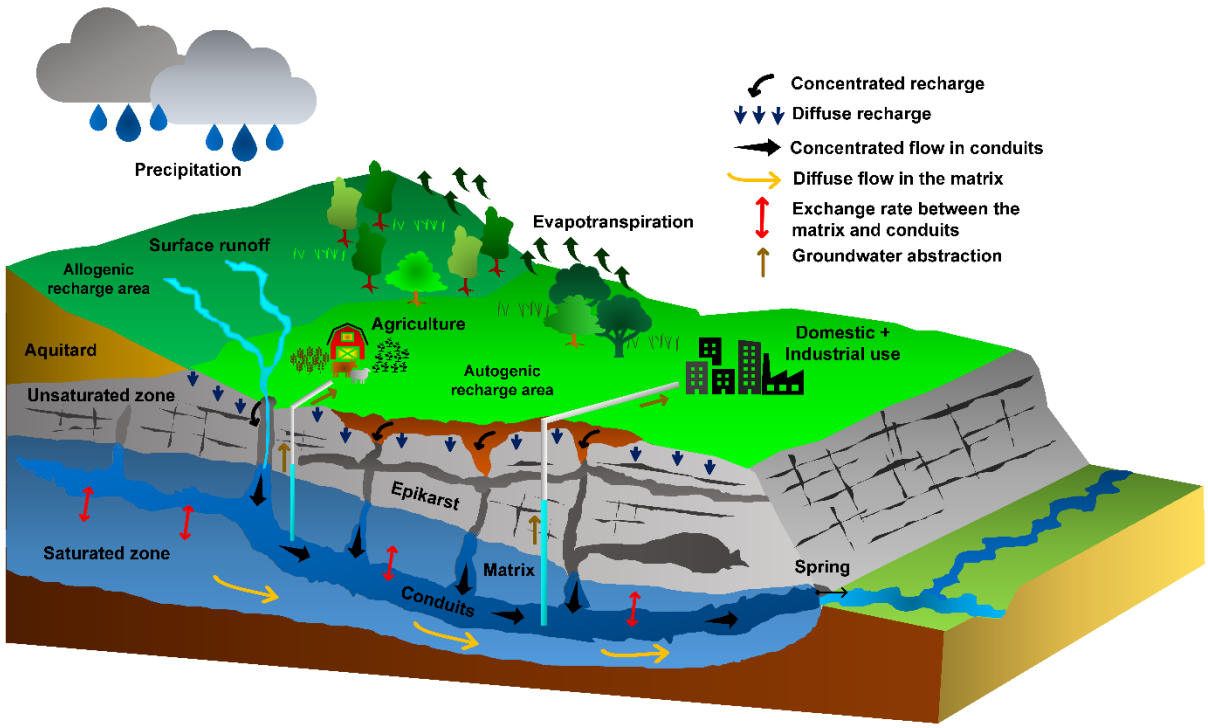

Figure 1. Conceptual schematic of a karst aquifer (modified after Goldscheider (2019) and Hartmann et al. (2014)) illustrating the heterogeneous hydrological behavior of a karst system (epikarst, matrix, and conduits), with dual infiltration and recharge processes, dual subsurface flow fields, and dual discharge characteristics. Karst aquifers are a primary source of freshwater supply for residential, industrial, and agricultural uses and are highly vulnerable to climate change and anthropogenic hazards (Sivelle et al., 2021).

Hydrologists rely on mathematical models, which use spatially lumped to distributed numerical approaches, to simulate the flow processes in karst watersheds, understand their hydrodynamic behavior, and assess their hydrological response to changing climate and anthropogenic pressures (Cardoso de Salis et al., 2019; Mudarra et al., 2019). Lumped models conceptualize the physical processes at the scale of the hydrological system and consider different combinations of the dominant flow components as distinct (linear or non-linear) conceptual buckets with parameters that represent the spatially averaged characteristics of the system (Butscher and Huggenberger, 2008; Dwarakish and Ganasri, 2015; Fleury et al. 2007, 2009; Hartmann et al., 2014; Sivelle et al. 2021; Tritz et al. 2011). In comparison to lumped models, the semi-distributed and distributed models explicitly represent the spatial variability of the watershed land and subsurface characteristics, boundary conditions, flow determinant inputs, and hydrological processes (Dwarakish, and Ganasri, 2015). Semi-distributed models may divide the watershed into hydrological response units (HRUs) and simulate the hydrological processes at the HRU scale, use conceptual reservoirs to model the areal recharge processes that lack spatial resolution, or represent the internal structure of a karst aquifer using pipe networks as conduit domains. Alternatively, fully-distributed models represent processes by discretizing the system in two- or three-dimensional grids, assigning parameters to each grid cell, and simulating a two- or three-dimensional form of the governing groundwater flow equation. In the context of karst hydrogeological modeling, distributed models are generally subdivided into three main categories, namely: (1) the fully equivalent porous media models, which use the average hydraulic properties over the aquifer area without explicitly simulating the diffusive and concentrated fast flows, (2) the double continuum models, which represent the matrix and karst conduits as two interacting continua with their hydraulic attributes, and 3) the combined discrete-continuum models in which the conduits are embedded as discrete elements inside the matrix (Dwarakish and Ganasri, 2015; Gill, et al., 2021). The development and parametrization of distributed models are generally constrained by the need for an adequate knowledge of the geological settings (lithology, fractures, faults), hydraulic and geometric properties of the karst aquifer water bearing components (e.g., porosity, hydraulic conductivity, conduits network geometry), and the dynamic changes in the underground surface permeability structure (Adinehvand et al., 2017; Chang et al., 2019; Fischer et al., 2018; Ghasemizadeh et al., 2012; Gill et al., 2021; Hartmann et al., 2014; Malenica et al., 2018). Consequently, lumped models are more commonly used in data-scare and complex karst regions where distributed models fail to capture the spatial distribution of the aquifer properties (Adinehvand et al., 2017). However, by neglecting the spatial variability of the streamflow dominant controls, lumped models may lack precision in assessing the intricate recharge and discharge within karst aquifers, hindering accurate flow prediction. Several studies have demonstrated the dependence of the predictive capability of hydrological models for streamflow prediction on the meteorological forcing (mainly precipitation) and the significance of incorporating spatial information on the landscape characteristics (i.e., land use, soil, karst landforms) to simulate streamflow for sustainable

water resource management in karst regions (i.e., Bittner et al., 2018; Doummar et al., 2012; Le Mesnil et al., 2021; Mo et al., 2020, 2022; Sarrazin et al., 2018; Yang et al., 2022).

Thus, semi-distributed hydrogeological models are proposed as a hybrid approach to overcome the limitations of the aforementioned two model classes by combining the spatial variability of the surface flow dominant controls (i.e., climatic features, landscape properties) with the underlying karst aquifer dominant flow components.

To date, few attempts have been made to simulate karst watershed hydrology using semi-distributed models that integrate spatially variable recharge, based on the hydrological landscape unit properties (i.e., climate, land use, soil, geology), with lumped reservoir models of the karst aquifer dominant flow components. Hartmann et al. (2013) developed the VarKarst model, which features the soil-epikarst flow processes, diffusive and concentrated recharge components, and spring flow over vertical compartments of unique soil and epikarst characteristics. In this model, the outflow from the epikarst compartment is divided between diffusive and concentrated recharge using a variable separation factor, and spring flow is calculated as the sum of outflows from the matrix and conduit compartments. Sarrazin et al. (2018) then incorporated the Penman-Monteith equation for an improved estimation of evapotranspiration by explicitly including the land cover properties. Bittner et al. (2018) introduced the semi-distributed LuKARS (Land use change modeling in KARSt systems), which lumps the areas of homogeneous land-use and soil properties in a karst watershed into independent spatial units called hydrotopes. These hydrotopes recharge a linear reservoir for the simulation of baseflow (matrix flow) component of the karst spring discharge, while the conduit quick flow component of the spring discharge is modeled as a preferential flow from the hydrotopes to the spring outlet. Moreover, Ollivier et al. (2020) proposed the semi-distributed model KaRaMel (Karst Recharge and discharge Model), which divides the karst aquifer recharge area into grids connected to an upper reservoir that simulates infiltration from the input precipitation and evapotranspiration data linearly to two lower reservoirs reproducing the matrix and conduit flow components of the karst spring discharge. Ollivier et al. (2021) then integrated a remote sensing-driven evapotranspiration model called SimpKcET (Simple Crop coefficient for Evapotranspiration) into KaRaMel in order to estimate evapotranspiration based on the Penman-Monteith approach and derive the fraction of vegetation cover in a karst catchment using the Enhanced Vegetation Index (EVI). Yang et al. (2022) also proposed the grid-based distributed karst Xin'anjiang hydrological model (DK-XAJ) for flood simulation in karst watersheds, by dividing hillslope into strongly-, moderately- and poorly-developed karst terrain cells, and implementing two-parallel linear reservoirs for the routing of the rapid-

conduit and slow-matrix flow components of the discharge in the moderately- or strongly-developed karstic cells.

The Soil and Water Assessment Tool (SWAT) (Arnold et al., 1998) is one of the most extensively used semi-distributed eco-hydrological models internationally, owing to its comprehensive nature, robustness, and flexibility as an interdisciplinary tool (Aloui et al., 2023). The model has been extensively applied in watersheds across the globe to estimate the water budget and yield (Alitane et al., 2022; Ayivi and Jha, 2018; Goyal et al., 2015; Raihan et al., 2020; Saha et al., 2014; Shrestha et al., 2017; Stefanidis et al., 2016), and provide data-driven strategies for the sustainable management of water resources under climate change (e.g., Azari et al., 2015; Hao et al., 2018; Nilawar and Waikar, 2019; Parajuli and Risal, 2021; Rashid et al., 2022; Shrestha et al., 2016; Zabaleta et al., 2014), land-use/cover change (e.g., Chotpantarat and Boonkaewwan, 2018; Muthee et al, 2023; Nakatsugawa, 2021; Rajib et al., 2016; Welde and Gebremariam, 2017) and anthropogenic pressure (e.g., Mittal et al., 2016; Oliver et al., 2014). Despite its wide range of applications (CARD, 2023), few SWAT-based studies have been conducted in karst watersheds (e.g., Afinowicz et al., 2005; Efthimiou, 2018; Jain et al., 2015; Mehdi et al., 2015; Sellami et al., 2016; Sunde et al., 2017, 2018; Zeiger et al., 2021). SWAT simulates diffusive recharge by soil water percolation at the HUR scale to a linear two-reservoir model consisting of a shallow (unconfined) aquifer reservoir with return flow to the stream channels and a deep (confined) aquifer that discharges water outside the watershed (Neitsch et al., 2011). Thus, the groundwater module in SWAT does not represent the recharge, storage and discharge dynamics of the karst aquifer water bearing components, which limit its model's applicability to predict flow and simulate the water balance fluxes in spring-dominated karst watersheds.

Most SWAT studies in karstified watersheds used the standard model source code and fewer modified it to better represent the hydrological processes of the dominant karst features in the study region. These modifications focused on increasing infiltration, simulating the dual slow and concentrated aquifer recharge components, as wells as the fluxes between the karst aquifer water bearing components and the spring. Baffaut and Benson (2009) and Zhou et al. (2022) represented the sinkholes in the James River and the South and North Panjiang River basins as ponds in SWAT and simulated the recharge to the shallow aquifer as the sum of diffusive flow by soil water percolation and concentrated flow by pond drainage. Yactayo (2009) modeled the concentrated recharge through the Opequon Creek watershed sinkholes as direct infiltration of the surface runoff and soil lateral flow generated in the karst areas. Palanisamy and Workman (2015) conceptualized the

sinkholes in the streambed of the Cane Run watershed as orifices that drain streamflow of sinking streams in the karst subbasins feeding the SWAT deep aquifer reservoir, and routed the reservoir discharge as rapid conduit flow to the watershed outlet. Moreover, Eini et al. (2020) proposed increasing aquifer recharge in the karst areas by modifying either the delay time variable of the SWAT recharge function or the SWAT crack flow module so as to model bypass flow in both dry and wet soils. Alternatively, Nikolaidis et al. (2013) interfaced SWAT in the karst areas with a linear matrix-conduit reservoir model fed by the outflow of the deep aquifer reservoir of SWAT with spring flow calculated as the sum of outflows from the matrix and conduit reservoirs, then added spring flow as a point source discharge to calculate the total watershed runoff where the springs are located. Nguyen et al. (2020) incorporated a linear matrix-conduit two-reservoir model into SWAT to simulate spring flow in the karst areas. In this model, the matrix reservoir is fed by diffusive recharge from soil water percolation, while the conduit reservoir is recharged by soil seepage, concentrated water losses (as interbasin groundwater flow) from sinking streams, and diffusive discharge from the matrix reservoir. Spring flow is calculated as the outflow from the conduit reservoir and added to direct runoff to simulate streamflow for a basin with karst springs**.** Furthermore, Wang et al. (2019b) integrated a linear three-reservoir model into SWAT to simulate the fluxes of the epikarst, matrix, and conduits. In this model, the epikarst reservoir is recharged by soil percolation with an attenuation function that depends on the saturation moisture content, the conduit reservoir is fed by discharge from the epikarst reservoir, and direct water infiltration from depressions, and the matrix reservoir is fed by another fraction of the epikarst and conduit reservoirs discharges. Geng et al. (2021) adopted a three-reservoir epikarst-conduit-matrix configuration similar to Wang et al. (2019b) but removed the attenuation function of the epikarst reservoir to simulate quick recharge by soil water percolation and added a direct flow component from the epikarst reservoir to the river channels. In both models, the contribution of spring flow to the watershed runoff is calculated as the sum of the outflows from the matrix and conduit reservoirs. Finally, Wang and Brubaker (2014) applied a non-linear modification to the shallow aquifer reservoir in SWAT to simulate the return flow to the stream channels in the karst areas. These modified SWAT models and along with semi-distributed models applied in karst hydrology (i.e., VarKarst, LuKARS, SimpKcET-KaRaMel, DK-XAJ) did not collectively represent the fluxes of the epikarst, matrix and conduit, which include the matrix-conduit bidirectional exchange flow rate, using non-linear storage-discharge relationships.

Therefore, this thesis aims to develop a semi-distributed karst hydrological model by modification of the SWAT source code, which can simulate the daily surface and subsurface water flows in a karst watershed considering the spatial heterogeneity of the karst surface properties (i.e., land use, soil, lithology) on recharge, and the flow transfers between the epikarst, matrix, and conduit reservoirs using a non-linear approach.

1.2 Introduction Générale

Les aquifères karstiques représentent une source d'eau abondante dans de nombreuses régions du globe, fournissant de l'eau douce à 20–25 % de la population mondiale (Chen et al., 2017) et jusqu'à plus de 50% de l'approvisionnement total en eau potable dans certains pays (Biondić et al., 2021). Ils englobent près de 15.2% de la surface continentale de la Terre (Auler et Stevanović, 2021) et se forment par dissolution chimique des roches carbonatées solubles (i.e., calcaire, dolomite, marbre ou évaporites) exercée par de l'eau enrichie en dioxyde de carbone (CO_2) provenant de l'atmosphère ou de la zone du sol (Goldscheider et al, 2020). En fonction du degré de karstification, des éléments karstiques distinctifs peuvent se développer, notamment des dolines et des gouffres, des ruisseaux souterrains, des sources, et de larges réseaux de fissures, fentes, conduits et grottes souterraines et connectés sur le plan hydrologique (Zeiger et al., 2021).

Un système karstique est généralement composé de quatre principaux éléments hydrogéologiques présentant une géomorphologie, des propriétés hydrodynamiques, un stockage, et des régimes de flux distincts : (1) le sol et la zone non karstique, (2) l'épikarst, (3) la zone de transmission - ces trois derniers formant la zone non saturée, et (4) la zone saturée (Dal Soglio et al., 2020b). Ces zones distinctes, qui sont reliées de manière interactive par l'écoulement de l'eau et le transport de solutés, forment la zone critique karstique (Chen et al., 2018; Wang et al., 2020). La figure 1 présente un modèle schématique d'un aquifère karstique typique, y compris les processus hydrologiques de surface et les mécanismes d'écoulement des sous-systèmes karstiques souterrains. Les aquifères karstiques se comportent comme un milieu à double ou triple porosité, composé de pores intergranulaires (porosité primaire) regroupés avec des fractures (porosité de fracture) dans une matrice rocheuse et des réseaux de canaux et de conduites élargis (porosité de conduit) qui transfèrent la majeure partie de la recharge vers les sources karstiques (Geyer et al., 2013; Ghasemizadeh et al., 2012). L'épikarst représente un horizon altéré de quelques mètres au-dessus de la zone vadose, caractérisé par une perméabilité et une porosité élevée dues à l'apport important de CO_2 qui augmente la dissolution des roches carbonatées près de la surface terrestre. Deux mécanismes de recharge sont généralement observés dans un

système karstique : (1) une recharge diffuse par percolation lente de l'eau infiltrée de l'épikarst vers la zone saturée à travers de petites fissures à faible perméabilité dans la zone vadose et (2) une recharge concentrée via des structures karstiques très conductrices (fractures élargies, dolines), permettant un transit rapide de l'écoulement à travers la zone vadose vers la zone saturée (Paiva, et Cunha, 2020). L'épikarst, avec le sol sus-jacent, contrôle l'infiltration, le stockage et le délai de recharge de la zone saturée en stockant temporairement l'eau de percolation pendant les périodes de sécheresse et de faible recharge, et en libérant rapidement le flux par les canaux karstiques à la saturation lorsque le taux d'infiltration dépasse le taux de percolation. La capacité de stockage de l'épikarst dépend de sa maturité et du contraste de perméabilité entre sa partie inférieure et la zone de transmission sous-jacente. À l'évolution totale de l'épikarst, le ruissellement de surface est réduit et la majeure partie de l'infiltration qui traverse l'épikarst s'écoule dans les conduits, tandis que la percolation à travers la matrice et les fissures n'augmente plus. Par ailleurs, l'épikarst peut être discontinu, peu développé ou complètement dissipé par des processus géomorphologiques, ce qui réduit son rôle hydrologique (Bauer et al., 2005; Fidelibus et al., 2017; Nannoni and Piccini, 2022; Yan et al., 2022). La zone de transmission relie et transfère l'eau de recharge de l'épikarst à la zone saturée où les conduits karstiques à haute perméabilité vident la matrice rocheuse fissurée, générant un flux pour le débit de l'eau souterraine. Les systèmes karstiques présentent donc un double mode de stockage et d'écoulement souterrain : (1) stockage prolongé des eaux souterraines et faible vitesse d'écoulement (écoulement laminaire) dans la matrice, et (2) faible stockage des eaux souterraines avec vitesse d'écoulement rapide/non linéaire (turbulente) dans les conduits. Des décharges doubles vers la sortie de l'aquifère se produisent également avec (1) un écoulement lent et continu à partir de la matrice pendant les périodes sèches et (2) un écoulement rapide à partir des conduits pendant les épisodes de fortes pluies (de Rooji and Graham, 2017; Giese et al., 2018; Hartmann et al., 2021). Le conduit et la matrice échangent également des flux, qui dépendent principalement de la différence de niveaux d'eau entre les deux milieux et des propriétés du conduit (Dal Soglio et al., 2020a), et peuvent contribuer de manière substantielle au débit de la source pendant les périodes sèches et d'étiage (Sivelle et al., 2019). Plusieurs études ont établi que la relation stockage-débit non linéaire représente la dynamique de l'écoulement entre l'épikarst, la matrice et les conduits (Basu et al., 2022; Chang et al., 2015; Kurtulus and Razack, 2007; Labat et al., 2000; Zhao et al., 2021).

En outre, les limites d'alimentation des aquifères karstiques ne coïncident pas toujours avec les limites des bassins versants. Alors que l'infiltration directe des précipitations sur les affleurements karstiques constitue

une recharge autogène, l'infiltration des eaux de ruissellement provenant des zones non karstiques adjacentes constitue une recharge allogène avec une composante d'écoulement souterrain interbassin qui traverse les lignes de partage topographiques de surface à travers les conduits avant d'émerger au niveau des sources. L'alimentation allogène pourrait représenter une part importante du débit des sources karstiques, en particulier dans les régions où la perméabilité du substratum rocheux est élevée. Par conséquent, négliger la différence entre les limites topographiques et hydrogéologiques de ces aquifères karstiques, connus sous le nom de systèmes karstiques binaires, et la représentation des processus hydrologiques de leurs zones de recharge karstiques et non karstiques combinées, aboutit à un bilan hydrique non fermé et à des estimations inexactes des ressources en eau. L'écoulement des eaux souterraines entre les bassins n'est pas explicitement mesurable, ce qui nécessite l'application d'approches hydrogéochimiques basées sur la surveillance des principaux éléments dissous, des isotopes, de la conductivité électrique et de la température de l'eau, ou des études hydrogéologiques des voies d'écoulement des eaux souterraines et des techniques physiques telles que le bilan hydrique du sol et la fluctuation du niveau de l'eau, ou encore une combinaison de ces approches.

En raison de leurs propriétés intrinsèques et de leur comportement hydrodynamique complexe, les aquifères karstiques sont vulnérables à la surexploitation, au changement climatique et à la contamination (Goldscheider, 2019; Gutiérrez et al., 2018). Les ressources en eaux souterraines karstiques continuent d'être confrontées à un stress d'épuisement à l'échelle mondiale en raison de l'augmentation des prélèvements d'eau, de la modification de l'utilisation du sol et du changement climatique (Doummar et al., 2018; Fiorillo and Guadagno, 2012; Hao et al., 2009; Jia et al., 2017; Kovačič et al., 2020; Nerantzaki and Nikolaidis, 2020; Ruiz et al., 2022; Sivelle et al., 2021; Smiatek et al., 2013; Taheri et al., 2016). Dans les systèmes karstiques bien développés, les processus naturels tels que l'absorption, la dégradation et la filtration sont inefficaces en raison de la faible capacité de stockage, du mouvement rapide de l'eau, du temps de séjour court et de l'interaction limitée avec la roche mère en contact avec l’aquifère. Ainsi, les contaminants peuvent rapidement atteindre la nappe phréatique par une recharge concentrée et se propager facilement dans les conduits karstiques sur de grandes distances (Entezari et al., 2016; Iván et Mádl-Szőnyi, 2017).

Par conséquent, la compréhension du fonctionnement hydrodynamique des aquifères karstiques et l'anticipation des impacts du changement climatique et des pressions anthropogéniques sur les ressources en eau karstiques sont impératifs pour sauvegarder ces réserves d'eau en diminution et mettre en place des programmes efficaces pour leur gestion. Cependant, l'évaluation des ressources en eau karstique en tenant

compte de la variabilité spatiale des déterminants des flux de surface et souterrains reste un défi en raison de l'hétérogénéité de ces aquifères, leur anisotropie, la dualité de la recharge et de la décharge, et la non-linéarité des flux (Hartmann et al., 2014).

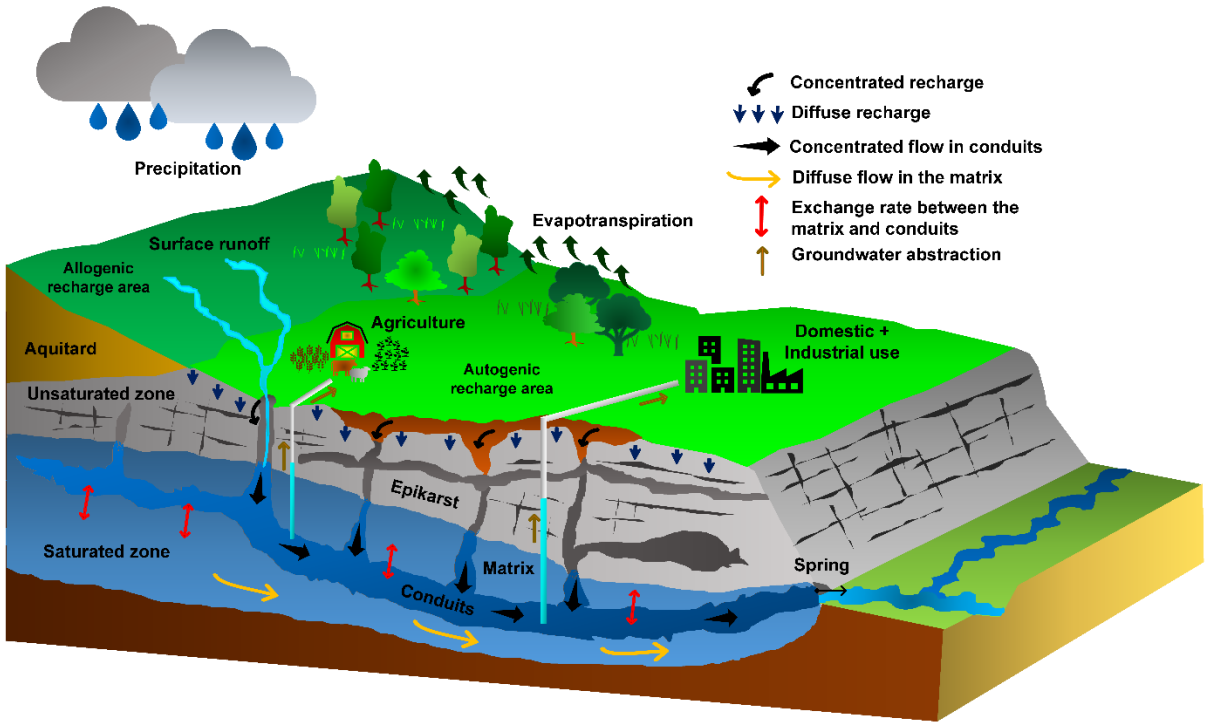

Figure 1. Schéma conceptuel d'un aquifère karstique (modifié d'après Goldscheider (2019) et Hartmann et al. (2014)) illustrant le comportement hydrologique hétérogène d'un système karstique (épikarst, matrice et conduits), avec deux processus d'infiltration et de recharge, deux champs d'écoulement souterrain et deux caractéristiques de décharge. Les aquifères karstiques sont une source primaire en eau douce pour les usages résidentiels, industriels et agricoles et sont très vulnérables au changement climatique et aux dangers anthropogéniques (Sivelle et al., 2021).

Les hydrologues s'appuient sur des modèles mathématiques, qui utilisent des approches numériques spatialement agrégées ou distribuées, pour simuler les processus d'écoulement dans les bassins versants karstiques, comprendre leur comportement hydrodynamique et évaluer leur réponse hydrologique aux changements climatiques et aux pressions anthropiques (Cardoso de Salis et al., 2019 ; Mudarra et al., 2019). Les modèles agrégés conceptualisent les processus physiques à l'échelle du système hydrologique et considèrent différentes combinaisons des composantes dominantes du flux comme des réservoirs conceptuels distincts (linéaires ou non linéaires) avec des paramètres qui représentent les caractéristiques du système moyennées dans l'espace (Butscher and Huggenberger, 2008; Dwarakish and Ganasri, 2015; Fleury et al.

2007, 2009; Hartmann et al., 2014; Sivelle et al. 2021; Tritz et al. 2011). Par rapport aux modèles agrégés, les modèles semi-distribués et distribués représentent explicitement la variabilité spatiale des caractéristiques du bassin versant, les conditions aux limites, les contributions significatives au débit et les processus hydrologiques (Dwarakish et Ganasri, 2015). Les modèles semi-distribués subdivisent le bassin versant en unités de réponse hydrologique (HRU) et peuvent simuler les processus hydrologiques à l'échelle de l'HRU, utiliser des réservoirs conceptuels pour modéliser les processus de recharge de surface de faible résolution spatiale, ou représenter la structure interne d'un aquifère karstique en utilisant des réseaux de conduits. D'autre part, les modèles entièrement distribués représentent les processus en discrétisant le système en grilles à deux ou trois dimensions, en attribuant des paramètres à chaque cellule de la grille et en simulant une forme bidimensionnelle ou tridimensionnelle de l'équation gouvernant l'écoulement des eaux souterraines. Dans le contexte de la modélisation hydrogéologique du karst, les modèles distribués sont généralement subdivisés en trois catégories principales: (1) les modèles de milieux poreux entièrement équivalents, qui utilisent les propriétés hydrauliques moyennes sur la zone de l'aquifère sans simuler explicitement les flux rapides diffusifs et concentrés, (2) les modèles à double continuum qui représentent la matrice et les conduits karstiques comme deux continuums en interaction avec leurs attributs hydrauliques, et (3) les modèles combinés à continuum discret dans lesquels les conduits sont intégrés comme des éléments discrets à l'intérieur de la matrice (Dwarakish and Ganasri, 2015; Gill, et al., 2021). Le développement et la paramétrisation des modèles distribués sont généralement limités par la nécessité d'une connaissance adéquate des conditions géologiques (lithologie, fractures, failles), des propriétés hydrauliques et géométriques des composants de l'aquifère karstique (par exemple, la porosité, la conductivité hydraulique, la géométrie du réseau de conduits) et des changements dynamiques de la structure de perméabilité de la surface souterraine (Adinehvand et al., 2017; Chang et al., 2019; Fischer et al., 2018; Ghasemizadeh et al., 2012; Gill et al., 2021; Hartmann et al., 2014; Malenica et al., 2018). Ainsi, les modèles hydrogéologiques semi-distribués sont proposés comme une approche hybride pour éviter les limitations des deux classes de modèles susmentionnées en combinant la variabilité spatiale des facteurs qui influencent l'écoulement de surface (les caractéristiques climatiques, occupation du sol) avec les composantes dominantes de l'écoulement de l'aquifère karstique sous-jacent.

Peu de tentatives ont été réalisées pour simuler l'hydrologie des bassins versants karstiques à l'aide de modèles semi-distribués qui intègrent la recharge variable spatialement, basée sur les propriétés de l'HRU (le climat, l’occupation du sol, le type du sol, la géologie), avec des modèles de réservoirs globaux des

composants d'écoulement dominants de l'aquifère karstique. Hartmann et al. (2013) ont développé le modèle VarKarst, qui présente les processus d'écoulement sol-épikarst, les composantes de recharge diffusives et concentrées, et l'écoulement de source sur des compartiments verticaux de caractéristiques uniques du sol et de l'épikarst. Dans ce modèle, le débit sortant du compartiment épikarst est divisé entre la recharge diffuse et concentrée à l'aide d'un facteur de séparation variable, et le débit de source est calculé par la somme des débits sortants des compartiments de la matrice et du conduit. Sarrazin et al. (2018) ont ensuite intégré l'équation de Penman-Monteith pour une meilleure estimation de l'évapotranspiration en incluant explicitement les propriétés de la couverture terrestre. Bittner et al. (2018) ont introduit le modèle semi-distribué LuKARS (Land use change modeling in KARSt systems), qui regroupe les zones homogènes d'occupation du sol et les propriétés du sol dans un bassin versant karstique en unités spatiales indépendantes appelées hydrotopes. Ces hydrotopes rechargent un réservoir linéaire pour la simulation du débit de base (débit matriciel) de la décharge de la source karstique, tandis que le débit rapide de la source est modélisé comme un débit préférentiel des hydrotopes vers la sortie de la source. En outre, Ollivier et al. (2020) ont proposé le modèle semi-distribué KaRaMel (Karst Recharge and discharge Model), qui divise la zone de recharge de l'aquifère karstique en grilles connectées à un réservoir supérieur qui simule l'infiltration à partir des données de précipitations et d'évapotranspiration d'entrée de manière linéaire vers deux réservoirs inférieurs reproduisant les composantes d'écoulement matriciel et de conduit de la décharge de la source karstique. Ollivier et al. (2021) ont ensuite intégré le modèle d'évapotranspiration SimpKcET (Simple Crop coefficient for Evapotranspiration) basé sur la télédétection dans KaRaMel afin d'estimer l'évapotranspiration selon l'approche Penman-Monteith et de dériver la fraction de la couverture végétale dans un bassin versant karstique en utilisant l'indice EVI (Enhanced Vegetation Index). Yang et al. (2022) ont également proposé le modèle hydrologique distribué du karst Xin'anjiang (DK-XAJ) pour la simulation des inondations dans les bassins versants karstiques, en divisant la pente des collines en cellules de terrain karstique fortement, modérément et faiblement développées, et en mettant en œuvre deux réservoirs linéaires parallèles pour la simulation des composantes d'écoulement rapide et matriciel du débit dans les cellules karstiques modérément ou fortement développées.

Le Soil and Water Assessment Tool (SWAT) (Arnold et al., 1998) est l'un des modèles éco-hydrologiques semi-distribués les plus utilisés au niveau international, en raison de sa robustesse et de sa flexibilité en tant qu'outil interdisciplinaire (Aloui et al., 2023). Le modèle a été largement appliqué dans des bassins versants pour estimer le bilan hydrique et débit (e.g., Alitane et al., 2022; Ayivi and Jha, 2018; Goyal

et al., 2015; Raihan et al., 2020; Saha et al., 2014; Shrestha et al., 2017; Stefanidis et al., 2016), et fournir des stratégies pour la gestion durable des ressources en eau dans le cadre du changement climatique (e.g., Azari et al., 2015; Hao et al., 2018; Nilawar and Waikar, 2019; Parajuli and Risal, 2021; Rashid et al., 2022; Shrestha et al., 2016; Zabaleta et al., 2014), changement d'occupation du sol (e.g., Chotpantarat and Boonkaewwan, 2018; Muthee et al, 2023; Nakatsugawa, 2021; Rajib et al., 2016; Welde and Gebremariam, 2017) et la pression anthropique (e.g., Mittal et al., 2016; Oliver et al., 2014). Malgré son large éventail d'applications (CARD, 2023), peu d'études basées sur SWAT ont été menées dans les bassins versants karstiques. SWAT simule la recharge diffusive par percolation de l'eau du sol à l'échelle HRU dans un modèle linéaire à deux réservoirs composé d'un réservoir aquifère libre (non confiné) qui se déverse dans les biefs des cours d'eau et un aquifère captif (confiné) qui déverse l'eau en dehors du bassin versant (Neitsch et al., 2011). Ainsi, le module des eaux souterraines de SWAT ne représente pas la dynamique de recharge, de stockage et de décharge des composantes hydriques de l'aquifère karstique, ce qui limite l'applicabilité de son modèle pour estimer le débit et simuler les flux du bilan hydrique dans les bassins versants karstiques dominés par les sources. La majorité des études SWAT sur les bassins versants karstifiés ont utilisé le code source du modèle standard et peu l'ont modifié pour mieux représenter les processus hydrologiques des composantes karstiques dominantes dans la région étudiée. Ces modifications se sont concentrées sur l'augmentation de l'infiltration, la simulation des deux composantes de la recharge lente et concentrée de l'aquifère, ainsi que sur les flux entre les composantes de l'aquifère karstique et la source. Baffaut et Benson (2009) et Zhou et al. (2022) ont représenté les dolines de la rivière James et des bassins des rivières Panjiang Sud et Nord comme des étangs dans SWAT et ont simulé la recharge de l'aquifère libre par la somme du flux diffusif de la percolation de l'eau du sol et du flux concentré provenant du drainage de l'étang. Yactayo (2009) a modélisé la recharge concentrée à travers les dolines du bassin versant d'Opequon Creek comme une infiltration directe du ruissellement de surface et du flux latéral du sol généré dans les zones karstiques. Palanisamy et Workman (2015) ont conceptualisé les dolines dans le lit des cours d'eau du bassin versant de Cane Run comme des orifices qui drainent le débit des cours d'eau dans les sous-bassins karstiques vers le réservoir de l'aquifère profond SWAT, et ont acheminé la décharge du réservoir comme un flux de conduit rapide vers l'exutoire du bassin versant. En outre, Eini et al. (2020) ont proposé d'augmenter la recharge de l'aquifère dans les zones karstiques en modifiant soit la variable de temps de retard de la fonction de recharge de SWAT, soit le module d'écoulement de fissures de SWAT, de manière à modéliser l'écoulement de dérivation dans les sols secs et

humides. Par ailleurs, Nikolaidis et al. (2013) ont couplé SWAT dans les zones karstiques avec un modèle de réservoir linéaire matrice-conduit alimenté par le débit sortant du réservoir aquifère profond de SWAT. Le débit de source a été calculé comme la somme des débits sortants des réservoirs de la matrice et du conduit, puis ajouté en tant que source ponctuelle pour calculer le ruissellement total du bassin versant où les sources karstiques sont situées. Nguyen et al. (2020) ont incorporé un modèle linéaire matrice-conduit à deux réservoirs dans SWAT pour simuler l'écoulement des sources dans les zones karstiques. Dans ce modèle, le réservoir matriciel est alimenté par une recharge diffusive provenant de la percolation de l'eau du sol, tandis que le réservoir du conduit est rechargé par l'infiltration du sol, les pertes d'eau concentrées (en tant que flux d'eau souterraine entre les bassins) provenant des cours d'eau qui se déversent dans l'aquifère, et la décharge diffusive du réservoir matriciel. Le débit de source est calculé à partir le débit sortant du réservoir de conduit et ajouté au ruissellement direct pour simuler le débit d'un bassin avec des sources karstiques. En outre, Wang et al. (2019b) ont intégré un modèle linéaire à trois réservoirs dans SWAT pour simuler les flux de l'épikarst, de la matrice et des conduits. Dans ce modèle, le réservoir epikarst est rechargé par percolation du sol avec une fonction d'atténuation qui dépend de la teneur en eau à saturation, le réservoir conduit est alimenté par la décharge du réservoir epikarst et l'infiltration directe d'eau à partir des dépressions, et le réservoir matrice est alimenté par une autre fraction des décharges des réservoirs epikarst et conduit. Geng et al. (2021) ont adopté une configuration à trois réservoirs épikarst-conduit-matrice similaire à celle de Wang et al. (2019b), mais ont supprimé la fonction d'atténuation du réservoir épikarst pour simuler une recharge rapide par percolation de l'eau du sol et ont ajouté une composante d'écoulement direct du réservoir épikarst vers les biefs. Dans les deux modèles, la contribution du débit de source au ruissellement du bassin versant est calculée comme la somme des débits sortants des réservoirs de la matrice et du conduit. Enfin, Wang et Brubaker (2014) ont appliqué une modification non linéaire au réservoir de l'aquifère peu profond dans SWAT pour simuler le flux de retour vers les canaux des cours d'eau dans les zones karstiques. Ces modèles SWAT modifiés et les modèles semi-distribués appliqués à l'hydrologie karstique (VarKarst, LuKARS, SimpKcET-KaRaMel, DK-XAJ) n'ont pas représenté l'ensemble des flux de l'épikarst, de la matrice et du conduit, qui incluent le débit d'échange bidirectionnel matrice-conduit, par des relations stockage-débit non linéaires.

Par conséquent, cette thèse vise à développer un modèle hydrologique karstique semi-distribué en modifiant le code source de SWAT afin de simuler les flux quotidiens d'eau de surface et souterrains dans un bassin versant karstique, en tenant compte de l'hétérogénéité spatiale des propriétés de surface du karst (i.e.,

l'occupation du sol, les caractéristiques du sol, la lithologie) et son influence sur la recharge, et les transferts de flux entre l'épikarst, la matrice, et les conduits suivant une approche non linéaire.

1.3 Problem statement

Karst aquifers are facing a depletion stress due to increased water abstraction, land use change, and climate change (Kovačič et al., 2020; Nerantzaki and Nikolaidis, 2020; Ruiz et al., 2022; Smiatek et al., 2013; Taheri et al., 2016), which is expected to further exacerbate water scarcity with predicted temperature rises of 1.5−4°C by 2100 (IPCC, 2023). Hydrologists use mathematical models to simulate watersheds and aquifers, understand their hydrodynamic behavior, and assess their response to climate change and anthropogenic pressure for sustainable water resource management (Cardoso de Salis et al., 2019). However, assessing karst water resources using spatially distributed models remains a challenge due to their heterogeneity, anisotropy, recharge and discharge duality, and flow non-linearity (Hartmann et al., 2014). To date, limited attempts have been made to simulate karst watershed hydrology using semi-distributed models that integrate spatially variable recharge based on the meteorological inputs, land use and soil properties. For instance, the VarKarst model (Hartmann et al., 2013) represents the soil-epikarst flow processes, diffusive and concentrated recharge, and spring discharge using vertical compartments of unique soil and epikarst characteristics. LuKARS (Land use change modeling in KARSt systems; Bittner et al., 2018) groups areas of homogeneous land-use and soil properties in a karst watershed as independent spatial units called hydrotopes to simulate the quick flow and baseflow components of the spring discharge. KaRaMel (Ollivier et al., 2020) divides the aquifer recharge area into grids and partitions recharge from an upper reservoir linearly between lower conduit and matrix reservoirs as a function of the soil available water capacity. These models calculate the karst aquifer discharge by combining slow and rapid outflows from the matrix and conduit units to a main spring outlet without considering surface runoff, the recharge and groundwater flow in non-karstic units in partially overlapping surface drainage and groundwater basins of binary karst systems, and the influence of water withdrawals. Additionally, Sivelle et al. (2022) compared the predictive performance of the lumped reservoir-based model KarstMod (Mazzilli et al., 2019) and LuKARS in simulating the spring flow of three small karst catchments (Kerschbaum, Oeillal, and Baget). The study showed mixed results whereby the application of semi-distributed recharge with LuKARS improved the discharge simulation performance for the Kerschbaum (2.5 km^2) and Oeillal (43.2 km^2) catchments but provided no improvement for the Baget catchment (13.25 km^2). Few researchers have also modified the semi-distributed eco-hydrological model SWAT (Soil and Water

Assessment Tool, Arnold et al., 2012) or integrated it with other models to better simulate karst watershed hydrology, but failed to reproduce key flow processes in spring-dominated karst watersheds, including flow non-linearity and the flow components of the epikarst, matrix, and conduits water bearing components. Thus, previous research highlights the need for new numerical approaches that incorporate the recharge and discharge characteristics of karst watersheds and account for the spatial variability of the flow dominant controls for an improved assessment of karst water resources.

1.4 Scientific questions and research objectives

Despite the recent advances in karst hydrological modeling using semi-distributed models, to the best of our knowledge, there exists no semi-distributed hydrological model for karst-dominated conservative watersheds that simulates diffusive and concentrated recharge with flow processes of the epikarst, matrix, and conduits, including the bidirectional matrix-conduit exchange flow rate, using a non-linear storage-discharge relationship. There is also no semi-distributed model that simulates surface and subsurface flows in binary karst systems where the karst aquifer recharge boundaries do not coincide with the surface subbasin boundaries, including autogenic and allogenic recharge in tandem with the epikarst, matrix, and conduits fluxes in karst areas. This raises the question of whether or not we can still improve the simulation of flow processes in karst watersheds by providing a semi-distributed model that incorporates the recharge-discharge characteristics of karst watersheds while accounting for the spatial variability of the watershed surface and subsurface flows.

The general purpose of the thesis is to develop a semi-distributed numerical model to simulate the surface-underground water fluxes in karst watersheds, by coupling the semi-distributed eco-hydrological model SWAT (Soil and Water Assessment Tool) with the karst groundwater module of the lumped rainfall-runoff model KarstMod. The Baget karst catchment, located in piedmont of the French Pyrénées mountains and monitored by the Karst National Observatory Service (SNO Karst) (Jourde et al., 2018), was selected as the study site. The catchment has a recharge contribution zone of 13.25 km^2 on a predominatly karst, mixed lithological terrain (karst landforms: 67%; non-karst rocks: 33%) and is characterized by rapid aquifer recharge and non-linear karst spring flow through conduits.

Specifically, it aims to achieve the following objectives:

Modify the SWAT+ source code by integrating the nonlinear three reservoirs of the epikarst, matrix and conduits adopted in KarstMod, and test the capability of the modified model in simulating the daily water balance and flow dynamics of a spring-dominated conservative karst watershed.

The SWAT+ source code will be modified by adding new subroutines that incorporate fast and diffusive flow recharge equations, the water balance equations that encompass the non-linear flow transfers between the epikarst, matrix, and conduit reservoirs of KarstMod for the simulation of spring flow in conservative karst aquifers, as well as the input parameters associated with new karst modules. The modified source code will be compiled into a new model executable termed ISPEEKH and applied to simulate streamflow in the Baget catchment (13.25 km^2). This step includes verifying the watershed water balance conservation, integrating the model with a Parameter ESTimation Tool (PEST) framework for sensitivity analysis and automated calibration, and assessing the model capability to reproduce the duality of the recharge, storage and discharge in the karst area.

Evaluate the hydrological response of the Baget catchment to land-use change scenarios of afforestation and deforestation to provide insights into the impacts of plausible land management plans on the catchment water resources.

Natural afforestation due to land abandonment, wood production and agro-pastoralism have been identified as drivers of future land-use changes in the French Pyrénées and European mountains. Thus, the first land-use change scenario applied to the Baget catchment will assume afforestation by conversion of pastures, cultivation patterns, moors, heathland, and transitional woodland/shrubland to broad-leaved forests. The remaining scenarios will consider deforestation for wood production (i.e., conversion of forests into transitional woodland/shrub) and pastureland for animal grazing (i.e., transition of forests into pastures). These scenarios will be applied to the karst areas to evaluate their impact on the spring flow component of streamflow, and will be extended to the entire catchment to assess their effects on both spring flow and surface runoff draining non-karst areas. The distribution of land-use classes for each scenario will be determined by modifying the land-use and plant communities in the model input files, and the scenarios will be implemented under the same meteorological data used for the calibrated baseline ISPEEKH model.

To evaluate and compare the reliability of reanalysis, gauge-, and satellite-based precipitation products, at coarse (tens of kilometer) and downscaled (1-km) spatial resolutions, for the daily water

balance and streamflow simulation in a meso-scale and sparsely gauged karst catchment, characterized by a short response time to precipitation.

The ISPEEKH model predictive performance in simulating streamflow of the Baget catchment (13.25 km^2) will be evaluated under various spatially-distributed precipitation datasets of the CPC (0.5° resolution) and E-OBS (10-km resolution) gauge-based products, the SAFRAN (8-km resolution), COMEPHORE (1-km resolution) and ERA5-Land (0.1° resolution) reanalysis products, and the IMERG-LR (0.1° resolution), PERSIANN-CDR (0.25° resolution), CHIRPS (0.05° resolution) and SM2RAIN-ASCAT (10-km resolution) satellite-based products, as well as 1-km resolution downscaled IMERG-LR, ERA5-Land, CPC, E-OBS and merged CPC-IMERG-LR precipitation datasets. ISPEEKH will be integrated with a Parameter ESTimation Tool (PEST) framework for automated calibration, sensitivity analysis, and uncertainty analysis.

1.5 Thesis organization

This thesis is article-based and encompasses six chapters. Following the introduction presented in Chapter 1, Chapter 2 first presents the rainfall-runoff reservoir-based karst model KarstMod and the equations used by this model to simulate various flow processes of the epikarst, conduit, and matrix water bearing components of karst aquifers. It then provides on overview of the semi-distibuted eco-hydrological model SWAT and fundemantal equations adopted in the model to simulate the surface and subsurface water hydrological processes in watersheds with granular type aquifers. Chapter 3 is a review on the applications of standard and modified SWAT models in karst-influenced and dominated watersheds gathered from the SWAT-based peer-reviewed studies published between the years 2000 to 2022. This chapter includes a description of the numerical approaches applied by the modified SWAT models to simulate karst flow processes, and evaluates the general performance of the SWAT models in simulating streamflow in karst watersheds. Chapter 3 has been published in *Water* as a review article titled "*Review of the application of the soil and water assessment tool (SWAT) in karst watersheds*". Chapter 4 provides an overview of the ISPEEKH model development for the hydrological simulation of karst watersheds and presents the groundwater recharge and flow equations adopted from KarstMod in modifying the source code of SWAT+, the latest restructured version of SWAT, into ISPEEKH. The chapter then presents the application of ISPEEKH for the simulation of the daily water balance in the Baget karst catchment (13.25 km^2), located in the southwestern French Pyrénées and characterized by nonlinear conduit-dominated karst spring flow. It analyses the results of the simulated streamflow and fluxes of the epikarst, matrix and conduit fluxes, including the matrix-conduit

bidirectional exchange flow rate and the matrix and conduit flow contributions to the spring. It also evaluates the hydrological response of the Baget catchment to synthetic land-use change scenarios of afforestation (i.e., pasture and transitional woodland/shrub conversion to forests) and deforestation (i.e., forest-to-transitional woodland/shrub conversion and forest-to-pasture land transition), considering the annual and monthly water fluxes, as well as the high and low flows. Chapter 4 has been published in *Journal of Hydrology* under the article titled "*Impact of land-use change on karst spring response by integration of surface processes in karst hydrology: The ISPEEKH model*". Chapter 5 discusses the ISPEEKH model predictive performance in simulating daily streamflow in the mesoscale Baget karst catchment in fucntion of precipitation from gauge-based, reanalysis, and satellite-based products at coarse (tens of kilometer) and 1-km (downscaled) spatial resolution. The chapter features the integration of ISPEEKH with a PEST framework for automated calibration, the analysis of the sensitivity of the ISPEEKH parameters that influence streamflow using the Morris screening method, and parameter estimation using the Gauss–Marquardt–Levenberg algorithm. The model's predictive performance of daily streamflow under raw and corrected precipitation datasets was assessed using metrics commonly applied in karst hydrology, in tandem with an orthogonal wavelet decomposition of the observed and simulated streamflow time series. The work in Chapter 5 has been submitted for publication in *Journal of Hydrology* under the article titled "*Evaluation of Precipitation Products for Small Karst Catchment Hydrological Modeling in Data-scarce Mountainous Region*". Finally, Chapter 6 summarizes the main findings of the research work conducted in the thesis and provides perspectives for future research in spatially-distributed hydrologcal modeling of karst watersheds.

CHAPTER 2: Modeling methodologies

2.1 Lumped parameter rainfall-discharge modeling of karst aquifers: KarstMod Overview

KarstMod (Mazzilli et al., 2019) is a reservoir-based rainfall-runoff modeling tool developed by the French institution INSU-CNRS SNO KARST (Jourde et al., 2018) in the framework of conducting hydrogeological studies in karst aquifers. The platform reproduces the conceptual configuration of most karst models known in the literature and has been successfully applied to several karst regions globally to simulate groundwater discharge at the daily and hourly time steps, analyze the hydrodynamic behavior of complex karst systems (e.g. Baudement et al., 2017; Poulain et al., 2018; Kazakis et al., 2018; Lončar et al., 2018; Sivelle et al., 2019; Arfib et al., 2019; Duran et al., 2020; Frank et al., 2021), and assess the impacts of climate change and anthropogenic pressure by groundwater pumping on karst water resources availability (Sivelle et al., 2021).

KarstMod (**Figure 2**) comprises four conceptual reservoirs arranged in a two-level structure: (1) the high-level reservoir E and (2) the low-level reservoirs L, M, and C. 'Reservoir E' represents the infiltration zone (unsaturated zone) in a karst system and replicates functions of the soil and epikarst. This reservoir is characterized by a minimum water level E_{min} (negative value) for the soil water content available for evapotranspiration. KarstMod allows the user to incorporate evapotranspiration measurements in the input data file or applies the Oudin's formula (Equation (1); Oudin et al., 2005) to estimate potential evapotranspiration at the level of reservoir E using temperature time series in the input file (Mazzilli et al., 2022).

$$PET = \frac{R_e}{\lambda * \rho}\left(\frac{T + K_2}{K_1}\right) \quad if \;\; T + K_2 > 0; \;\; else \; PET = 0 \qquad (1)$$

where R_e is the extraterrestrial radiation ($MJ.L^{-2}.T^{-1}$) based on the latitude and Julian day, λ is the latent heat flux (set to 2.45 $MJ.M^{-1}$), ρ is the water density [$M.L^{-3}$], T is the mean daily air temperature (°C) over the catchment, entered as time series in the user input file, and K_1 (°C) and K_2 (°C) are user-defined correction factors. The recommended value ranges of the adjustment factors are $5-6$ for K_1 and $90-110$ for K_2 in rainfall–runoff modeling. The actual (effective) evapotranspiration is then determined using a lumped approach as a function of the minimum moisture level in the epikarst reservoir (E_{min}), and recharge to the lower reservoirs occurs when the water level in reservoir E exceeds E_{min}.

The hysteretic transfer function proposed by Tritz et al. (2011) can be also implemented in KarstMod to account for the variable connectivity in the soil-epikarst zone and simulate fast flow driven by the saturation of the epikarst and preferential flow paths during heavy rainfall events. Hysteretic discharge is activated when

the water level in reservoir E reaches a minimum threshold $E_{(t)} = E_{hy(t)} + \Delta E_{hy(t)}$, where E_{hy} and ΔE_{hy} are the lower and upper threshold levels for the activation of the discharge, and is applied using a factor ε_{hy} that switches to 1 when water level E surpasses E_{hy}. The hysteretic flux is divided between the conduit reservoir (C) and the spring outlet (S) using a partitioning coefficient $x_{hy} \in [0, 1]$. The hysteretic discharge-water level function from the epikarst reservoir E to the conduit reservoir C and the spring outlet S is defined as follows:

$$Q_{hy(t)} = \varepsilon_{hy} \times k_{hy} \left(\frac{E_{(t)} - E_{hy(t)}}{L_{ref}} \right)^{\alpha_{hy}} \quad (2)$$

$$\left. \begin{array}{c} \varepsilon_{hy} = 0 \\ E_{(t)} = E_{hy(t)} + \Delta E_{hy(t)} \end{array} \right\} \rightarrow \varepsilon_{hy} = 1 \quad (3)$$

$$\left. \begin{array}{c} \varepsilon_{hy} = 1 \\ E_{(t)} = E_{hy(t)} \end{array} \right\} \rightarrow \varepsilon_{hy} = 0 \quad (4)$$

$$Q_{hyEC(t)} = x_{hy} \times Q_{hy(t)} \quad (5)$$

$$Q_{hyES(t)} = (1 - x_{hy}) \times Q_{hy(t)} \quad (6)$$

Losses by surface water drainage from the epikarst catchment recharge area can be integrated in KarstMod using a non-linear discharge function Q_{Loss} applied to reservoir E with a threshold water level for the activation of the loss function, as follows:

$$Q_{loss(t)} = k_{loss}(E_{(t)} - E_{loss})^{\alpha_{loss}} \ \ if\ E_{(t)} > E_{loss}, \quad otherwise \ \ Q_{Loss(t)} = 0 \quad (7)$$

The outflows from reservoir E occur when its storage reaches a positive value. The mass balance equation and discharge functions for the different flow transfers of reservoir E in KarstMod (full configuration) are presented below:

$$\begin{cases} if\ E_{min} < E < 0;\ \dfrac{dE}{dt} = P - ET \\ if\ E_{min} < E < 0; \dfrac{dE}{dt} = P - ET - Q_{EM} - Q_{EC} - Q_{EL} - Q_{ES} - Q_{hyEC} - Q_{hyES} - Q_{loss} \end{cases} \quad (8)$$

With

$$Q_{EM(t)} = k_{EM} \left(\frac{E_{(t)}}{L_{ref}} \right)^{\alpha_{EM}} \ \ if\ E_{(t)} > 0, \quad otherwise \ \ Q_{EM(t)} = 0 \quad (9)$$

$$Q_{EC(t)} = k_{EC} \left(\frac{E_{(t)}}{L_{ref}} \right)^{\alpha_{EC}} \ \ if\ E_{(t)} > 0, \quad otherwise \ \ Q_{EC(t)} = 0 \quad (10)$$

$$Q_{ES(t)} = k_{ES} \left(\frac{E_{(t)}}{L_{ref}} \right)^{\alpha_{ES}} \ \ if\ E_{(t)} > 0, \quad otherwise \ \ Q_{ES(t)} = 0 \quad (11)$$

$$Q_{EL(t)} = k_{EL} \left(\frac{E_{(t)}}{L_{ref}} \right)^{\alpha_{EL}} \ \ if\ E_{(t)} > 0, \quad otherwise \ \ Q_{EL(t)} = 0 \quad (12)$$

where P is precipitation (L.T^{-1}), ET is evapotranspiration (L.T^{-1}), $E_{(t)}$ is the water level in reservoirs E, M, L, and C, respectively, E_{min} is the minimum water level in the epikarst for the activation of discharge into the lower reservoirs (L), Q_{AB} is the internal discharge rate from reservoir A (either E, M, L, or C) to reservoir B (either E, M, L, or C) or to the outlet S (L.T^{-1}), k_{AB} and α_{AB} are respectively the recession coefficient (L.T^{-1}) and emptying (positive) exponents for the flow Q_{AB}, L_{Ref} is a unit length (L), k_{hy} is the specific discharge coefficient (L.T^{-1}), E_{hy} is the threshold water level in reservoir E for the activation of hysteretic discharge, ε_{hy} is a binary indicator of the activation of hysteretic discharge, α_{hy} is the recession coefficient of the hysteretic discharge function, x_{hy} is a partitioning coefficient of the hysteretic discharge, k_{Loss} is the specific discharge coefficient (L.T^{-1}) for the loss function, E_{Loss} is the threshold for the activation of the loss function (L), and α_{Loss} is the recession coefficient of the loss function.

On the other hand, reservoirs L, M, and C reproduce the different sub-systems found primarily at the level of the saturated zone in a karstic aquifer. 'Reservoir M' reproduces to the low permeability matrix unit as well as the small fissures and cracks in the vadose and saturated zones, allowing the simulation of a slow-flow or baseflow component of the aquifer discharge to the spring. 'Reservoir C' represents the highly permeable karst conduits and simulates the fast-flow component of spring flow. The flow exchange between the conduit and surrounding matrix is also modeled using a bidirectional exchange flow rate function that depends on the difference between the water levels of reservoirs M and C. 'Reservoir L' can represent a highly capacitive matrix or a lower-level subsystem of the saturated zone, and is usually traded off with 'reservoir M' for the simulation of diffuse flow in a karst system. The total discharge at the spring that drains the karst aquifer recharge area is computed as the sum of the slow and fast-flow components. All reservoirs can be activated/deactivated depending on the user's knowledge of the karstic system. The discharge-water level function for each reservoir is defined as a function of a specific recession coefficient 'k' and an emptying exponent 'α', both denoted based on the direction of the internal flux between two reservoirs. KarstMod can also account for groundwater abstraction by incorporating water withdrawal functions from either one or all three reservoirs (L, M, and C), and directly from the spring

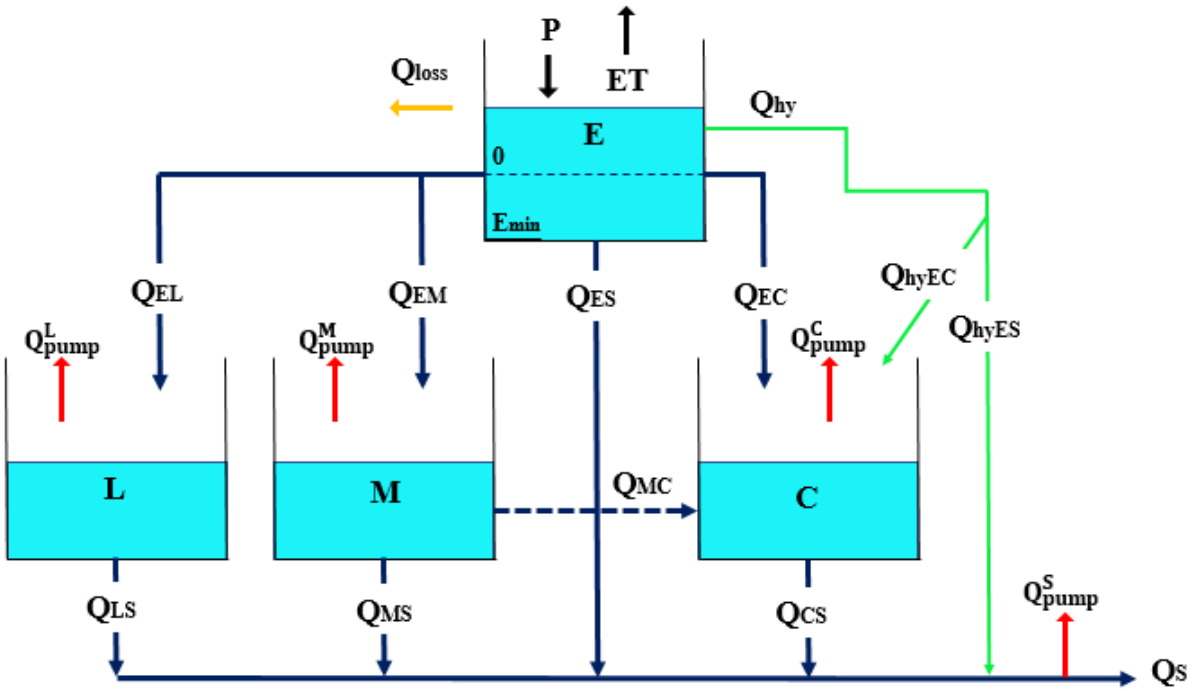

Figure 2. Schematic of KarstMod reservoirs and fluxes, including the hysteretic, losses, and groundwater abstraction functions (modified from Mazzilli et al., 2017)

The mass balance equation and discharge functions for the different flow transfers of reservoirs M, E and L in KarstMod (full configuration) are represented by Equations (13) and (20) below:

Reservoir M

$$\frac{dM}{dt} = Q_{EM} - Q_{MS} - Q_{MC} - Q^{M}_{pump} \tag{13}$$

With

$$Q_{MS(t)} = k_{MS}\left(\frac{M_{(t)}}{L_{ref}}\right)^{\alpha_{MS}} \quad if\ M_{(t)} > 0, \quad otherwise \quad Q_{MS(t)} = 0 \tag{14}$$

$$Q_{MC(t)} = k_{MC} \times sign\left(M_{(t)} - C_{(t)}\right) \times \left|\frac{M_{(t)} - C_{(t)}}{L_{ref}}\right|^{\alpha_{MC}} \tag{15}$$

Reservoir C

$$\frac{dC}{dt} = Q_{EC} - Q_{CS} + Q_{MC} + Q_{hyEC} - Q^{C}_{pump} \tag{16}$$

With

$$Q_{CS(t)} = k_{CS}\left(\frac{C_{(t)}}{L_{ref}}\right)^{\alpha_{CS}} \quad if\ C_{(t)} > 0, \quad otherwise \quad Q_{CS(t)} = \tag{17}$$

Reservoir L

$$\frac{dL}{dt} = Q_{EL} - Q_{LS} - Q_{pump}^{L} \quad (18)$$

With

$$Q_{LS(t)} = k_{LS}\left(\frac{L_{(t)}}{L_{ref}}\right)^{\alpha_{LS}} \quad if\ L_{(t)} > 0, \quad otherwise \quad Q_{LS(t)} = 0 \quad (19)$$

Finally, the discharge at the karst spring outlet is computed as follows:

$$Q_{S(t)} = R_A \times \left(Q_{ES(t)} + Q_{MS(t)} + Q_{CS(t)} + Q_{LS(t)} + Q_{hyES} - Q_{pump}^{S}\right) \quad (20)$$

where $M_{(t)}$, $L_{(t)}$, and $C_{(t)}$ are the water levels (L) in reservoirs M, L, and C, respectively, Q_{AB} is the internal discharge rate from reservoir A (either E, M, L, or C) to reservoir B (either E, M, L, or C) or to the outlet S ($L.T^{-1}$), k_{AB} and α_{AB} are respectively the recession coefficient ($L.T^{-1}$) and emptying (positive) exponents for the flow Q_{AB}, L_{Ref} is a unit length (L), Q_{pump}^{L}, Q_{pump}^{M}, Q_{pump}^{C}, and Q_{pump}^{S} ($L.T^{-1}$) represent the discharge rates per unit surface area of withdrawals from reservoirs L, M, C, and the outlet, respectively, Q_{Spring} ($L^{3}.T^{-1}$) is the discharge at the outlet, and R_A is the total surface of the recharge area (L^2).

Baudement et al. (2017) applied KarstMod to characterize the hydrodynamic behavior of the Dardennes springs (recharge area of ~70 km²), which constitute a major source of freshwater supply for the city of Toulon, in south-eastern France. The conceptual model of the aquifer consisted of the upper soil/epikarst reservoir E, including station-measured evapotranspiration, and the two lower matrix and conduit reservoirs M and C, with diffusive flow from reservoir M and fast flow from the conduit reservoir C to the spring, and no matrix-conduit exchange flow. Hydrograph separation of the karst spring flow revealed that the mean proportion of baseflow was estimated at 36% of the simulated discharge whereas fast flow contribution covered the remaining 64% and exceeded 90% at flood scale due to the presence of a well-connected conduit network in the vadose and saturated zones of the aquifer.

Lončar et al. (2018) applied KarstMod to model the discharge of the Golunbika karst spring (in northern Dalmatia, Croatia) and determine the distribution of groundwater flow between the matrix and fractured components of the aquifer. The numerical model included the epikarst, matrix, and conduit reservoirs, and spring flow was simulated considering linear and non-linear storage-discharge relationships. The non-linear model yielded better discharge simulations and higher correlation with the observed data than

the linear model. Additionally, the matrix (slow flow)/conduits (fast flow) contributions (%) to the spring flow were estimated at 19%/81% and 13%/87% of the flow under the linear and non-linear models, respectively.

Among other studies, KarstMod was used to conceptualize the hydrodynamic regime of the Damasi-Titanos karst aquifer (320 km^2) in eastern central Greece (Kazakis et al., 2018), which provides water supply for a total population of 175,000 in addition to supplying local agricultural and livestock activities. The hydrodynamic characteristics of the aquifer, which include autogenic recharge from precipitation, diffuse allogenic recharge from a river crossing the aquifer recharge area and lateral outflow to adjacent sedimentary aquifers, were represented by reservoirs E and C considering the hysteretic fluxes from the epikarst towards the conduits (Q_{hyEC}) and the spring (Q_{hyES}), and the conduit outflow to the spring (Q_{CS}). Input evapotranspiration to reservoir E was estimated using the Thornthwaite method (Thornthwaite and Mather, 1957) and station-measured data. The measured times series of the river percolation to the karst system were incorporated (as negative values) with the groundwater abstraction and lateral outflow of the karst system to adjacent sedimentary aquifers through the conduit reservoir pumping function.

Poulain et al. (2018) performed percolation monitoring and dye tracing with numerical modeling in KarstMod in order to evaluate groundwater recharge through the karst vadose zone of the Rochefort Cave in Belgium. The vadoze zone behavior was conceptualized with two reservoirs. The first reservoir (E) represents the soil/epikarst receiving effective rainfall and dividing infiltration into a quick flow and a diffuse flow. The diffuse flow, which characterizes flow through matrix and small fissures, joins the epikarst with a lower reservoir representing the vadose zone and leaks to the outlet from the vadose reservoir. The quick flow is a hysteretic discharge that accounts for the variable connectivity in the soil/epikarst zone and represents the fast component of the catchment response to rainfall at the saturation of the epikarst, as described by Tritz et al. (2011). Results showed that diffusive infiltration through the small fissures and matrix contributed to two thirds of the total recharge. while rapid infiltration through open fractures accounted for the remaining one third.

Sivelle et al. (2019) used KarstMod to model the long-term trends of the spring discharge and internal flows between the matrix and conduits, including the bidirectional exchange flow, in the Aliou (11.9 km^2) and Baget (13.25 km^2) catchments at daily and hourly time steps. The KarstMod models of the two catchments were driven solely by precipitation and consisted of the reservoirs E, M, C reservoirs with flow exchange between reservoirs M and C, and only fast flow discharge from reservoir C to the spring outlet. The MASH

(Moving Average over Shifting Horizon) method was then applied over five decades to assess the long-term trends of water levels in the two aquifers, with a primary focus on the matrix water storage and the matrix-conduit flow exchange. The analysis revealed a decrease in the matrix storage during the spring periods, starting in the 1960s, estimated at -13.1% for Aliou and -11.3% for Baget, coupled with a shift in the annual recharge patterns as the matrix water storage started to increase in the month April instead of February since the early 1990s. The flow exchange from the matrix to the conduits, measured as a percentage of the total spring discharge, was also estimated at 2−5% on a yearly basis and around 25% of the spring flow on a monthly basis, depending on the matrix water storage and accumulated precipitation.

Moreover, Duran et al. (2020) applied KarstMod with natural tracer observations, discharge signal analysis, and decomposition methods (Fourier analysis, wavelet multiresolution) in order to interpret the hydrological behavior of the Norville karst aquifer, a sinkhole-spring system draining a small watershed of 10 km^2 in Normandy-France, and identify the contribution of the different aquifer compartments in the signal decomposition between recharge and spring discharge. The KarstMod model included all reservoirs (‘E, C, M, and L‘) with a non-linear discharge from reservoir C to the spring and linear relationships for the internal fluxes of the remaining reservoirs. Results showed that KarstMod successfully reproduced some internal dynamics of the Norville karstic system whereby the trends of the internal fluxes simulated by the conceptual model were consistent with those of the turbidity, conductivity and piezometric measurements at the spring, particularly for the exchange dynamics between the conduits and the surrounding aquifer. The wavelet results obtained from the multiresolution analysis of the spring discharge were also strongly correlated to the internal outflows of reservoirs E and M, highlighting the importance of coupling multiresolution analysis with lumped modelling to understand the functioning of karstic system.

Frank et al. (2021) also applied KarstMod in the framework of investigating the dynamics of the high-alpine karst system of Disnergschroef (6.8 km^2). The model included reservoir E with daily potential evapotranspiration estimates from the “Haude method”, and reservoirs C and M with all spring flow set through reservoir C. The discharge from the epikarst to the matrix and conduit reservoirs was found to be very responsive to rainfall, while the flow from the matrix to the conduits was nearly constant throughout the simulation period with slight increases directly after rainfall. This result highlighted the role of the matrix as a buffer during heavy rainfall events and a storage for water that sustains baseflow during dry periods by continuously releasing flow into the conduits.

Sivelle and Jourde (2020) performed time series analysis of hydrodynamic, physicochemical, and meteorological data, coupled with KarstMod modeling to assess the hydrodynamic functioning and groundwater resources variability in the Oeillal spring catchment (~42.3 km^2) in Southern France. The KarstMod model included reservoir E with inputs of precipitation and potential evapotranspiration estimated using Oudin's formula (Oudin et al., 2005), and reservoir M. The knowledge acquired from the statistical and correlation time series analyses helped optimize the calibration and physical significance of the lumped karst model. The results indicated a slow recession dynamic with a regulating power of 1.8 years, which agreed with the characteristic time scale for the transfer function of reservoir M, estimated at around 200 days. The volume of water stored in the aquifer and the annual transit volume were estimated at 7.5 Mm^3 and 4.2 Mm^3, respectively. The calibration process highlighted the need to combine high-resolution time-series analysis with hydrodynamic simulation of karst aquifers to assess the performance of lumped-parameter rainfall-runoff models.

Sivelle et al. (2021) used KarstMod and LuKARS models to predict the impacts of climate change and anthropogenic pressures on water resources in the Oeillal spring catchment at horizon 2100 by coupling 12 climate model simulations under two emission scenarios (RCP 4.5 and RCP 8.5) with four scenarios of future groundwater extraction for drinking water supply. The results of the simulations revealed that climate change (driven by temperature and potential evapotranspiration increases) had the primary impact on water availability by increasing the spring drying-up periods by up to 30% under RCP 4.5 and 70% under RCP 8.5. Combined with climate change, groundwater abstraction is expected to aggravate the decrease in spring flow and surpass the annual volume of transit at the spring by 2080.

Labat et al. (2022) used KarstMod to simulate the discharge of the Touvre spring resurgence, which represents a binary karst system fed by delayed infiltration of effective rainfall over a karst impluvium (550 km^2) and by direct infiltration of water losses from sinking rivers that drain three adjacent non-karst basins (Tardoire, Bandiat and Bonnieure). The model, which consisted of reservoirs E, M, and C, incorporated the infiltration losses from the river system, inferred from the residence time distribution functions on tracings carried out in the basin, and groundwater withdrawals for domestic and agricultural use into reservoirs M and C as aggregated time series. The calibrated model was then used to quantify the impacts of removing groundwater pumping on the spring discharge and internal water levels of the matrix-conduit reservoir system.

2.2 Semi-distributed hydrological modeling of watersheds: Overview of the Soil and Water Assessment Tool (SWAT)

The “Soil and Water Assessment Tool” (SWAT) is a continuous-time semi-distributed agro-eco-hydrological model developed by the United States Department of Agriculture (USDA) (Arnold et al., 1998) to monitor the impacts of environmental and anthropogenic changes on physical processes in agricultural at small, regional, and subcontinental scales (Kim et al., 2013; Wang et al., 2014; Tan et al., 2015; Mittal et al., 2016; Setegn et al., 2010; De Girolamo et al., 2017; Marhaento et al., 2018; Boufala et al., 2022; Zango et al., 2022; Schilling et al, 2023). SWAT uses meteorological data, i.e., precipitation, air temperature, relative humidity, wind speed, and solar radiation, in addition to topography, soil properties, and land-use data, to simulate the watershed water balance components at different time steps (subdaily to annual). It can also model water quality and soil erosion (Brighenti et al., 2019; Bennour et al., 2022). The watershed is first disaggregated into subbasins connected through a stream channel, and further into HRUs that represent areas of homogenous land use, soil, and slope properties (Yesuf et al., 2015). The definition of HRUs is performed using a geographic information system (GIS), such as the ArcSWAT interface of ArcGIS or the QSWAT plugin of QGIS, coupled to the SWAT model to integrate the topographic, soil, and land-use inputs (Dile t al., 2016). The simulated catchment processes in SWAT include surface runoff, infiltration, evapotranspiration, lateral flow, tile drainage, percolation, water stored in the soil profile, return flow from unconfined aquifers, consumptive water use through pumping (if any), recharge from surface water bodies, and in-stream processes, such as channel routing (main and tributary) and transformation of nutrients and pesticides (Golmohammadi et al., 2014). These hydrological components are represented in each HRU by five storage volumes, namely the canopy interception, snow pack, soil profile, shallow aquifer, and deep aquifer (Mehdi et al., 2015).

SWAT+ (Bieger et al., 2017) is a completely restructured version of SWAT that was developed to improve the spatial representation of the elements and processes within catchments, and facilitate upgrades of the SWAT source code for future applications and development by the general users (Wu et al., 2020). Compared to the previous versions of SWAT, SWAT+ offers a greater flexibility in catchment discretization/configuration and a better simulation of the landscape processes, with improved runoff routing capabilities. In addition, spatial objects in SWAT+ have been constructed as independent modules, each with its own connection file where users can define the routing and the fraction of the flow exchanged between the catchment hydrological entities (Bieger et al., 2019, 2017).

2.2.1 Equations in SWAT for hydrological simulation

Watershed hydrology in SWAT is represented by a land phase and a routing phase, whereby runoff, sediments, and agricultural chemical yields from all subbasin HRUs are aggregated to the main reach of the subbasin and routed rough the channel network to the outlet(s) of the main catchment (Bieger et al., 2015). The fundamental daily water balance equation used in SWAT to represent the land phase of the hydrological cycle is given as follows (Neupane et al., 2014):

$$SW_t - SW_0 = \sum_{i=1}^{t} \left(P_{day} - Q_{surf} - ET_a - W_{seep} - Q_{gw}\right) \qquad (21)$$

where SW_0 and SW_t are the initial and final soil water content of the entire soil profile for the simulation period, respectively, P_{day}, Q_{surf}, ET_a, W_{seep}, and Q_{gw} are precipitation, surface runoff, actual evapotranspiration, percolation and bypass flow exiting the soil bottom to the vadose zone, and return flow, respectively (all variables are expressed in mm $H_2O.day^{-1}$)

SWAT offers different options to simulate scheduled irrigation and auto-irrigation of crops. The auto-irrigation approach is generally used when irrigation scheduling data are lacking. Auto-irrigation is triggered by two stress identifiers: (1) plant water stress, whereby irrigation is applied to meet the plant water demand if the ratio of actual transpiration to potential transpiration falls below a user-specified threshold, and (2) soil water deficit, whereby irrigation is applied if the water content in the soil profile drops below field capacity by more than a user-defined soil water depletion threshold (Uniyal et al., 2019). Sources of irrigation include river reaches, reservoirs, shallow and deep aquifers, or a source from outside the watershed, and irrigation demand is met based on the source water availability (Thomas et al., 2021). When irrigation is applied, the SWAT water balance is adjusted as follows:

$$SW_t - SW_0 = \sum_{i=1}^{t} \left(P_{day} + Irr\right) - \sum_{i=1}^{t} \left(Q_{surf} - ET_a - W_{seep} - Q_{gw}\right) \quad (22)$$

where SW_0 and SW_t are the initial and the final soil water content of the entire soil profile for the simulation period, P_{day}, Irr, Q_{surf}, ET_a, W_{seep}, and Q_{gw} represent the precipitation, irrigation, surface runoff, actual evapotranspiration, percolation and bypass flow exiting the bottom of the soil profile to the vadose zone, and return flow from the shallow aquifer to the stream, respectively (all variables are expressed in mm $H_2O.day^{-1}$).

Water from surface runoff, lateral soil flow, groundwater storage baseflow, and tile flow contributes to the catchment water yield, a crucial parameter in sustainable water resource management (Shao et al., 2019; Ayivi

et al., 2018). Water yield is defined as the net water volume leaving the HRU and entering a reach at the subbasin level into the main channel, as follows:

$$WYLD = Q_{surf} + Q_{lat} + Q_{gw} + Q_{tile} - T_{loss} \quad (23)$$

where $WYLD$ is the water yield, Q_{surf}, Q_{lat} , and Q_{gw} are the surface runoff, soil lateral flow, and return flow from the shallow aquifer to the main channel, respectively, Q_{tile} is the tile flow, and T_{loss} represents the water losses from the tributary via transmission through the riverbed (all variables are expressed in mm $H_2O.day^{-1}$).

A detailed description of the processes and corresponding equations incorporated in SWAT are provided in the SWAT theoretical manual by Neitsch et al. (2011) and the SWAT+ documentation (https://swatplus.gitbook.io/docs/user/io). The following chapter subsection will focus on the flow processes in the critical zone with direct impact on the streamflow simulation in standard SWAT. These processes are grouped under surface water hydrology and subsurface water hydrology. Fundamental equations are provided in each subsection to help readers understand SWAT's methods for simulating surface and groundwater flows.

2.2.1.1 Surface Water Hydrology

2.2.1.1.1 Evapotranspiration

SWAT provides three methods to simulate daily potential evapotranspiration (PET) at the HRU scale, namely the Penman-Monteith (Monteith, 1965), the Priestley-Taylor (Priestley and Taylor, 1972) and the Hargreaves methods (Hargreaves et al. 1985). Between the three approaches, the Penman-Monteith equation is considered the most suited to estimate PET, as it explicitly separates the effects of climate and land cover properties on each of the evapotranspiration components [30,33]. This method is represented with Equation (24), as follows (Neitsch et al., 2011):

$$\lambda E = \frac{\Delta(H_{net} - G) + \rho_{air} \times c_p(e_z^0 - e_z)/r_a}{\Delta + \gamma(1 + r_c/r_a)} \quad (24)$$

where λE is the latent heat flux density ($MJ.m^{-2}.day^{-1}$), λ is the latent heat of vaporization ($MJ.kg^{-1}$), E is the depth rate evaporation ($mm.day^{-1}$), Δ is the slope of the saturation vapor pressure–temperature curve (de/dT) ($kPa.°C^{-1}$), H_{net} is the net radiation ($MJ.m^{-2}.day^{-1}$), G is the heat flux density to the ground ($MJ.m^{-2}.day^{-1}$), ρ_{air} is the air density ($kg.m^{-3}$), c_p is the specific heat at constant pressure ($MJ.kg^{-1}.C^{-1}$), e_z^0 is the saturation vapor pressure of air at height z (kPa), e_z is the water vapor pressure of air at height z (kPa), γ is the psychometric constant ($kPa.°C^{-1}$), r_c is the plant canopy resistance ($s.m^{-1}$), and r_a is the diffusion resistance of the air layer (aerodynamic resistance) ($s.m^{-1}$).

PET in SWAT depends on plant growth, which considers canopy resistance expressed as a function of the minimum effective stomatal resistance for a single leaf and the leaf area index (LAI). The LAI, defined as

one half the total leaf area per unit ground area, reflects the structural characteristics of the plant canopy and defines the (Strauch and Volk, 2013). Evapotranspiration is also related to the canopy height required to determine the aerodynamic resistance parameter (Neitsch et al., 2011).

SWAT uses the LAI in conjunction with a simplified version of the Environmental Policy Integrated Climate (EPIC) plant growth model to simulate the phenological development of plants and estimate evapotranspiration (Ferreira et al., 2021). In addition to the LAI development, the plant growth module of SWAT includes the simulation of daily light interception by plant leaf in function of the incident total solar radiation and LAI, and the conversion of intercepted light into biomass assuming a plant species-specific radiation-use efficiency (Alemayehu et al., 2017). Plant development is primarily dependent on the base temperature for growth, derived from minimum, maximum, and optimum temperature requirements. The plants heat unit requirements are quantified and related to the time of planting and maturity (Ma et al., 2019). The LAI is incremented daily based on the accumulated potential heat units. It first increases to a crop-specific maximum value, remains constant until the senescence stage, then decreases linearly to zero at harvest. Similarly, the canopy height increases until a crop-specific maximum is achieved and stays at this height through the remainder of the growing season (Sinnathamby et al., 2017). The potential crop leaf growth and biomass are first computed under optimal conditions and further adjusted for actual growth under stress factors such as water, temperature, and nutrients (i.e., nitrogen and phosphorus) (Luo et al., 2008). SWAT also uses dormancy in function of day length and latitude to repeat the annual growth cycle for trees and perennials (Strauch and Volk, 2013), and offers management operations to schedule the start and end the growing season based on a calendar date or heat units (Alemayehu et al., 2017).

After estimating potential evapotranspiration, SWAT calculates actual evapotranspiration (ET_a), which includes four components: the canopy evaporation, the plant transpiration, the sublimation and soil surface evaporation, and the groundwater evapotranspiration. The model first evaporates any precipitation intercepted by the plant canopy. Then, actual plant transpiration is estimated as a function of the potential transpiration adjusted for the wet canopy storage, root depth, soil water content, and the leaf area index, which depends on the plant developmental stage. Soil evaporation is modeled as a function of potential evapotranspiration adjusted for canopy evaporation and the rate of shading. If snow is present in the HRUs, sublimation takes place until evaporation from soil could occur after snow melting. Subsequently, SWAT proceeds to adjust the maximum possible soil evaporation for plant water use and partitions the evaporative demand between the different soil layers, in order to estimate the actual evaporation at each layer based on the soil water content (Ferreira et al., 2021; Abiodun et al., 2018; Aouissi et al., 2016).

2.2.1.1.2 Surface Runoff and Infiltration

In SWAT, soil surface runoff and infiltration are estimated from precipitation by one of the following two approaches: (1) the modified Soil Conservation Service Curve Number (SCS-CN) procedure and (2) the

Green and Ampt Mein Larson (GAML) excess rainfall method. The SCS-CN approach simulates cumulative surface runoff based on cumulative precipitation and soil retention properties for daily time step, whereas the GAML approach simulates surface runoff for subdaily time step applications using subdaily precipitation input data (Tan et al., 2020; Campbell et al., 2018; Bacopoulos et al., 2017). Surface runoff is estimated with the SCN-CN procedure as follows (Thomas et al., 2021):

$$Q_{surf} = \frac{(P - I_a)^2}{(P - I_a) + S} \quad when\ P > I_a;\ else\ Q_{surf} = 0 \tag{25}$$

where Q_{surf} is the accumulated runoff (mm H_2O)**,** P is the total precipitation for the day (mm H_2O), S is the soil moisture retention parameter, which varies spatially in function of the soil type, land use, and management practices and temporally with the changes in soil moisture content (mm H_2O), and I_a is the initial water abstraction prior to runoff due to surface storage, interception and infiltration (mm H_2O), generally approximated as $0.2S$, but can vary with the soil type . The retention parameter S is expressed as a function of the daily curve number CN, which corresponds to the Antecedent Moisture Condition-II (AMC-II) for a given land use/land cover hydrological soil group, and 5% slope, as follows (Thomas et al., 2021):

$$S = \frac{25400}{CN} - 254 \tag{26}$$

Where CN is the initial SCS Curve Number for AMC-II (average condition) for a 5% slope.

The SCS approach defines three antecedent moisture conditions, namely AMC-I for dry/wilting point condition, AMC-II for average moisture, and AMC-III for wet/field capacity, represented by curve numbers CN1, CN2 and CN3, respectively. CN1 and CN3 are computed as a function of CN2 as follows:

$$CN1 = CN2 - \frac{20(100 - CN2)}{(100 - CN2 + e^{2.533 - 0.0636(100 - CN2)})} \tag{27}$$

$$CN3 = CN2 \times e^{0.000673(100 - \mathrm{CN2})} \tag{28}$$

Infiltration rate is calculated using the GAML equation as follows (Her et al., 2017a):

$$I(t) = K_e \left(1 + \frac{\psi \times \Delta\theta}{I_{acc}(t)}\right) \tag{29}$$

where $I(t)$ is the infiltration rate (mm H_2O) at the simulation time step t (subdaily), K_e is the effective hydraulic conductivity, which considers soil water content and land-use impact as a function of CN (mm.hour^{-1}), ψ is the wetting front matric potential (mm), $\Delta\theta$ is the change in soil moisture content (mm.mm^{-1}), and $I_{acc}(t)$ is the cumulative infiltration after ponding (mm H_2O.hour^{-1}). The cumulative depth of water infiltration $I_{acc}(t)$ is computed using Equation (30):

$$I_{acc}(t) = I_{acc}(t-1) + K_e \times \Delta t - \psi \times \Delta\theta \times ln\left[\frac{I_{acc}(t) + \psi \times \Delta\theta}{I_{acc}(t-1) + \psi \times \Delta\theta}\right] \quad (30)$$

where $t-1$ is the previous simulation time step. Equation (30) is solved using a successive substitution technique. Subsequently, the infiltration rate is calculated using Equation (29) for each time step. Surface runoff is generated when the rainfall intensity exceeds infiltration rate. Otherwise, the total rainfall volume during the time step infiltrates into the soil.

2.2.1.1.3 Channel Flow and Flow Routing

For stream channel routing, Manning's equation is used to calculate the rate and velocity of flow in the reach of each subbasin when the streamflow is less than the bankfull discharge rate, computed as a function of the bankfull channel width and depth. SWAT incorporates floodplain inundation geometry into the channel routing simulation if the streamflow is greater than bankfull flow (Her et al., 2017b).

The peak runoff rate, reached when all the subbasins are contributing to flow at the outlet, is estimated using the modified rational method, as follows (Malagò et al., 2018):

$$q_{peak} = \frac{\alpha_{tc} \times Q_{surf} \times A}{3.6 \times t_{conc}} \quad (31)$$

where q_{peak} is the peak runoff rate ($m^3.s^{-1}$), α_{tc} is the fraction of daily rainfall that occurs during the time of concentration, Q_{surf} is the surface runoff (mm $H_2O.day^{-1}$), A is the subbasin area (km^2), and t_{conc} is the time of concentration for the subbasin (hours), calculated as the sum of the overland flow time and channel flow time. Water is routed through the channel network using either the Muskingum routing method (based on the continuity and empirical linear storage equations) (Cunge, 1969) or the variable storage routing method (based on the continuity equation) 88] (Wiiliams, 1969; Nguyen et al., 2018a)

Water transmission losses can occur through the side and bottom of the river channels and enter the bank storage or the deep aquifer. Transmission losses are estimated as follows (Holvoet et al., 2008):

$$T_{loss} = K_{ch} \times L_{ch} \times P_{ch} \times TT \quad (32)$$

where T_{loss} represents the channel transmission losses (m^3 H_2O), K_{ch} is the effective hydraulic conductivity of the channel alluvium ($mm.hour^{-1}$), L_{ch} is the channel length (km), P_{ch} is the wetted perimeter in the channel (m), and TT is the flow travel time (hours).

2.2.1.2 Subsurface Water Hydrology

2.2.1.2.1 Soil Water Percolation and Lateral Flow

The water percolation component in SWAT redistributes infiltrated water in the soil profile using a storage routing method combined with an optional crack-flow routine. Percolation is simulated when the water content of a soil layer exceeds its field capacity defined as the sum of the available soil water content and

permanent wilting point. Percolated water moves to the subsequent layer unless it is saturated, frozen, or impervious (Baffaut et al., 2015; Rahbeh et al., 2019; Mapes and Pricope, 2020). Water percolation is estimated as follows:

$$W_{perc,ly} = SW_{ly,excess}\left(1 - e^{\frac{-\Delta t}{TT_{perc,ly}}}\right) \quad (33)$$

where $W_{perc,ly}$ is the water percolating from soil layer (ly) to the underlying soil layer (mm $H_2O.day^{-1}$), $SW_{ly,excess}$ is the drainable volume of water in the soil layer (computed as the difference between the water content of the soil layer and field capacity, in mm $H_2O.day^{-1}$), Δt is the length of the time step (hours), and $TT_{perc,ly}$ is the travel time through the soil layer (hours), calculated as follows:

$$TT_{perc,ly} = \frac{SAT_{ly} - FC_{ly}}{K_{sat,ly}} \quad (34)$$

where $K_{sat,ly}$ (mm.hour^{-1}), SAT_{ly} (mm H_2O), and FC_{ly} (mm H_2O) represent the saturated hydraulic conductivity, saturation water content, and field capacity water content of the soil layer, respectively.

SWAT incorporates a crack flow module that can be used to simulate bypass (crack) or preferential flow in the soil. The use of the crack flow approach to increase infiltration rates from the surface is optional and requires the activation of a crack flow code by the user (Eini et al., 2020). Crack volume for each soil layer is modeled in the dry seasons, which allows infiltrated rainwater to move rapidly through the soil profile along vertical cracks, and disappears in wet conditions (Fu et al., 2014). Bypass flow from the bottom of the soil profile to the saturated zone is computed using Equation (35), and excess water that leaves the bottom of the soil profile through the vadose zone is calculated by combining percolation and bypass flow, as shown in Equation (36) (Neitsch et al., 2011):

$$W_{crk,btm} = 0.5 \times crk\left(\frac{crk_{ly}}{depth_{ly}}\right) \quad (35)$$

$$W_{seep} = W_{perc,ly} + W_{crk,btm} \quad (36)$$

where $W_{crk,btm}$ is the crack flow past the lower boundary of the soil profile (mm $H_2O.day^{-1}$), crk_i is the total crack volume for the soil profile on a given day (mm), crk_{ly} is the crack volume for the deepest soil layer (ly) on a given day (mm), $depth_{ly}$ is the depth of the deepest soil layer (ly) (mm), and W_{seep} is the water drained from the bottom of the soil profile (mm $H_2O.day^{-1}$).

Lateral flow (soil interflow) along a steep hillslope is computed simultaneously with percolation when the soil water content exceeds its field capacity. It is simulated using a kinematic storage routing method (Equation (37) that is based the on slope, slope length, and saturated conductivity of each soil layer (Bieger et al., 2015; Mapes and Pricope, 2020), as follows:

$$Q_{lat} = 0.024\left(\frac{2 * SW_{ly,excess} \times K_{sat} \times slp}{\emptyset_d \times L_{hill}}\right) \quad (37)$$

where Q_{lat} is the daily water flux from the hillslope outlet (mm $H_2O.day^{-1}$), slp is the increase in elevation per unit distance, $\emptyset_d$ is the drainable (residual) porosity of the soil layer (mm/mm), and L_{hill} is the hillslope length (m).

The daily water balance for each soil layer is expressed using Equation (38), as follows (Qi et al., 2018):

$$\Delta SW_{ly} = Q_{p,ly-1} - Q_{p,ly} - Q_{lat,ly} - E_{e,ly} - E_{t,ly} \quad (38)$$

where ΔSW_{ly} is the change of soil water content at soil layer (ly), $Q_{p,ly-1}$ is the percolation received from layer $(ly-1)$, $Q_{p,ly}$ and $Q_{lat,ly}$ are the percolation and lateral flow generated from soil layer (ly), respectively, and $E_{e,ly}$ and $E_{t,ly}$ are the evaporation and transpiration drawn from the soil layer (ly), respectively (all variables are expressed in mm $H_2O.day^{-1}$).

2.2.1.2.2 Groundwater Flow and Baseflow to the Stream

The groundwater module of SWAT comprises a system of two aquifers in each subbasin: (1) a shallow unconfined aquifer that generates baseflow into the stream and (2) a deep confined aquifer contributing to streamflow outside of the watershed (flow lost from the system) (Luo et al., 2012). Recharge from the unsaturated soil profile to the aquifers on a given day is calculated using an exponential decay weighting function that accounts for the time delay of the recharge mechanism, as follows (Shao et al. 2019):

$$W_{rchrg,i} = \left(1 - e^{-\frac{1}{\delta_{gw,sh}}}\right) W_{seep,i} + \left(e^{-\frac{1}{\delta_{gw,sh}}}\right) W_{rchrg,i-1} \quad (39)$$

where $W_{rchrg,i}$ and $W_{rchrg,i-1}$ represent the recharge to the aquifers (shallow and deep) at days i and $i-1$ (mm $H_2O.day^{-1}$), respectively, $W_{seep,i}$ is the water drained from the bottom of the soil profile (mm $H_2O.day^{-1}$), and $\delta_{gw,sh}$ is the delay time required for recharge to reach the aquifers (days).

Recharge components routed to the shallow (unconfined) aquifer and the deep (confined) aquifer are computed using Equations (40) and (41), respectively, as follows:

$$W_{rchrg,sh,i} = (1 - \beta_{dp}) W_{rchrg,i} \quad (40)$$

$$W_{rchrg,dp,i} = \beta_{dp} W_{rchrg,i} \quad (41)$$

where $W_{rchrg,sh,i}$ and $W_{rchrg,dp,i}$ represent the water diverted to the shallow and deep aquifers (mm $H_2O.day^{-1}$), respectively, and β_{dp} is a coefficient of percolation to the deep aquifer.

The shallow aquifer contributes to the streamflow if water stored in the aquifer exceeds a user-specified threshold. Otherwise, return flow is set to zero. The daily groundwater flow to the main river channel is computed using an exponential storage-discharge relationship, which incorporates the recharge from the shallow aquifer and a baseflow recession constant, as follows:

$$Q_{gw,sh,i} = \begin{cases} W_{rchrg,i}\left(1 - e^{-\alpha_{gw,sh}\times\Delta t}\right) + Q_{gw,sh,i-1}\left(e^{-\alpha_{gw,sh}\times\Delta t}\right), & aq_{sh} > aq_{shthr,q} \\ 0, & aq_{sh} \leq aq_{shthr,q} \end{cases} \quad (42)$$

where $Q_{gw,sh,i}$ is the baseflow from the shallow aquifer to the main stream channel (mm $H_2O.day^{-1}$), $\alpha_{gw,sh}$ is the groundwater recession constant of shallow aquifer ($days^{-1}$), aq_{sh} is the amount of water stored in the shallow aquifer (mm $H_2O.day^{-1}$), Δt is the time step (1 day), and $aq_{shthr,q}$ is the threshold water level in the shallow aquifer for return flow to occur (mm H_2O).

The groundwater flow from the deep aquifer is represented by Equation (43), as follows:

$$Q_{gw,dp,i} = W_{rchrg,dp,i}\left(1 - e^{-\alpha_{gw,dp}\times\Delta t}\right) + Q_{gw,dp,i-1}\left(e^{-\alpha_{gw,dp}\times\Delta t}\right) \quad (43)$$

where $Q_{gw,sh,i}$ is the groundwater flow from confined aquifer (mm $H_2O.day^{-1}$), Δt is the time step (1 day), and $\alpha_{gw,sh}$ is the groundwater recession constant of the deep aquifer ($days^{-1}$).

In dry periods, water in the shallow aquifers may be removed by evaporation to the partially saturated overlaying soil through the capillary fringe that separates the saturated and vadose zones. Water can also be directly absorbed by deep rooted plants through transpiration (Uniyal et al, 2019). SWAT accounts for this phenomenon via a process defined as revap, which occurs when water storage in the shallow aquifer exceeds a user-defined threshold. The amount of water that can be potentially consumed by revap is calculated as follows (Xie et al., 2020):

$$ET_{rvp-max} = \beta_{rvp} \times PET \quad (44)$$

where $ET_{rvp,max}$ is the maximum amount of water that can be removed from the shallow aquifer (mm $H_2O.day^{-1}$), β_{rvp} is the groundwater evaporation coefficient, and PET is the potential evapotranspiration (mm $H_2O.day^{-1}$). The actual groundwater evapotranspiration is subsequently calculated based on water availability in the shallow aquifer, considering the following cases (Neitsch et al., 2011):

$$ET_{rvp} = \begin{cases} 0, & aq_{sh} \leq aq_{shthr,rvp} \\ ET_{rvp,max} - aq_{shthr,rvp}, & aq_{shthr,rvp} < aq_{sh} < \left(aq_{shthr,rvp} + ET_{rvp,max}\right) \\ ET_{rvp,max}, & aq_{sh} \geq \left(aq_{shthr,rvp} + ET_{rvp,max}\right) \end{cases} \quad (45)$$

where aq_{sh} is the water stored in the shallow aquifer at the beginning of day i (mm $H_2O.day^{-1}$) and $aq_{shthr,rvp}$ is the threshold water level in the shallow aquifer for groundwater evaporation to occur.

The volumetric water balance for the shallow aquifer is represented as follows (Nguyen and Dietrich, 2018):

$$aq_{sh,i} = aq_{sh,i-1} + W_{rchrg,sh,i} - Q_{gw,sh,i} - ET_{revap,i} - Q_{pump,sh,i} \quad (46)$$

where $aq_{sh,i}$ and $aq_{sh,i-1}$ represent water stored in the shallow aquifer on days i and $i-1$, respectively, $ET_{revap,i}$ is the volume of water that moves upward by capillary rise, and $Q_{pump,sh,i}$ is the water withdrawn by pumping from the shallow aquifer (all variables are expressed in mm $H_2O.day^{-1}$) .

SWAT also simulates other types of water bodies, including wetlands, ponds, and depressions or potholes. These water bodies are modeled within the subbasins of the main stream channel and are fed by runoff originating from the subbasin in which they are located (Phiri et al., 2021). They can also contribute to seepage and groundwater recharge, adding to the recharge from soil water percolation (Rahman et al., 2006).

The downward daily seepage from the pond or wetland V_{seep} (m^3 $H_2O.day^{-1}$) is estimated using Equation (47) (Neitsch et al., 2011):

$$V_{seep} = 240 \times K_{sat} \times A_{wet} \quad (47)$$

where K_{sat} is the saturated hydraulic conductivity of the pond or wetland bottom ($mm.hour^{-1}$) and A_{wet} is the water surface area of the pond or wetland (hectares).

Daily seepage from the pothole/depression is computed as a function of soil water content, as follows (Dash et al., 2020):

$$V_{seep,pot} = \begin{cases} 240K_{sat} \times SA, & SW < 0.5FC \\ 240\left(1 - \dfrac{SW}{FC}\right) \times K_{sat} \times SA, & 0.5FC \leq SW < FC \\ 0, & SW \geq FC \end{cases} \quad (48)$$

where $V_{seep,pot}$ is the seepage from a pothole (m^3 $H_2O.day^{-1}$), K_{sat} is the saturated hydraulic conductivity of the top soil layer ($mm.hour^{-1}$), SA is the pothole surface area (hectares), SW is the daily soil water content of the profile (mm H_2O), and FC is the field capacity moisture content (mm H_2O).

CHAPTER 3: A Review of the Application of the Soil and Water Assessment Tool (SWAT) in Karst Watersheds

Summary

The management and sustainability of karst groundwater resources are challenging due to limited understanding of the critical zone flow processes and the influence of vegetation cover, climate change, and anthropogenic activities on these processes. Jeannin et al. (2021) applied 13 karst numerical models to simulate groundwater recharge and spring flow in a karst watershed. The impact of the spatial distribution of recharge on the discharge simulations was found to be low, with semi- and fully- distributed models having a comparable performance to the lumped reservoir models. On the other hand, other studies (Bittner et al., 2018; Doummar et al., 2012; Sarrazin et al. 2018) have shown a significant impact of the vegetation and soil parameters on evapotranspiration, recharge and discharge simulations.

Over the last two decades, the semi-distributed eco-hydrological model SWAT (Soil and Water Assessment Tool) has been increasingly applied to simulate flow in karst watersheds and predict future karst water resources under climate change and land-use change scenarios. The SWAT groundwater module consists of two aquifer reservoirs: a shallow unconfined reservoir that generates baseflow into the stream and a deep confined reservoir contributing to streamflow outside the watershed. Recharge from the unsaturated soil profile is calculated using an exponential decay weighting function and distributed linearly between the aquifers using a coefficient of percolation. Some studies have directly applied the standard SWAT model to karst basins, while others modified its source code to improve the representation of karst hydrological processes. Thus, Chapter 3 presents a comprehensive review of the SWAT watershed hydrological modeling approach and SWAT applications in karst watersheds, aiming to investigate the different SWAT numerical approaches used to represent the fluxes and non-linear behavior in karst aquifers. The review identified 75 studies on SWAT simulations in karst and partially karstified watersheds between the years 2000-2022. These studies were classified into two main categories: the standard SWAT model applications (50 studies) and the modified SWAT model applications (25 studies). The review also looked into the predictive performance of the models based on the Nash-Sutcliffe Efficiency (NSE), the most commonly used statistical indicator across all the reviewed studies.

Modified SWAT codes, which incorporated diffusive and concentrated recharge functions, and external flows from sinkholes and IGF, have led to semi-distributed karst hydrological models with comparable or better streamflow prediction efficiency compared to standard SWAT (Eini et al., 2020; Geng et al., 2021; Palanisamy and Workman, 2015; Wang and Brubaker, 2014; Wang et al., 2019b; Zhou et al., 2022). However, poor daily and monthly performance statistics were reported after modifications, indicating that modified approaches may not always guarantee successful flow simulation in complex karstic environments (Afinowicz et al., 2005; Baffaut and Benson, 2009, Malagò et al., 2016).

The modified SWAT models reported in the literature can be improved to better represent karst aquifers heterogeneity and non-linearity. For instance, the Karst-SWAT (Nikolaidis et al., 2013) and KSWAT (Malagò et al., 2016) two-reservoir (matrix-conduit) models do not consider the function of the epikarst and do not explicitly include the diffusive and concentrated recharge components of infiltration from karstic soils to the deep aquifer reservoir in SWAT. Both models use the exponential decay weighting function to simulate the recharge to and outflows of the matrix and conduit reservoirs to the spring. The two models also follow the watershed surface delineation in SWAT to determine the recharge area of the spring, which may not always coincide with the groundwater recharge boundaries. The (matrix-conduit) SWAT_IGF (Nguyen et al., 2020) model improves some of the previous modified SWAT modeling constraints by simulating hydrological processes in non-karst and karst regions, as well as IGF, in a single executable file. SWAT_IGF considers the dual recharge and storage functions in karst systems but uses a linear storage-discharge relationship to model outflows of the matrix and conduit reservoirs. The three-reservoir models developed by Wang et al. (2019b) and Geng et al. (2021) represent a complete (epikarst-matrix-conduit) karst system, but their main constraint is that fluxes between the reservoirs are simulated using a linear storage-discharge relationship. Other models, such as SWAT-ML and SWAT-CF (Eini et al., 2020), Topo-SWAT (Amin et al., 2017), and SWAT-WA+ (Delavar et al., 2020, 2022) may be directly applied to basins affected by karst hydrology or other rapid infiltration phenomena but do not represent the underground flow dynamics of karst aquifers.

The findings of this chapter were published as a review paper in Water: *Al Khoury, I., Boithias, L., & Labat, D. (2023). A review of the application of the soil and water assessment tool (SWAT) in karst watersheds. Water, 15(5), 954. https://doi.org/10.3390/w15050954*

Al Khoury's Contributions: Conceptualization, methodology, data curation, writing—original draft preparation, writing—review and editing

water

MDPI

Review

A Review of the Application of the Soil and Water Assessment Tool (SWAT) in Karst Watersheds

Ibrahim Al Khoury *, Laurie Boithias and David Labat

GET, Université de Toulouse, CNRS, IRD, UPS, 31400 Toulouse, France
* Correspondence: ibrahim.al-khoury@get.omp.eu

Abstract: Karst water resources represent a primary source of freshwater supply, accounting for nearly 25% of the global population water needs. Karst aquifers have complex recharge characteristics, storage patterns, and flow dynamics. They also face a looming stress of depletion and quality degradation due to natural and anthropogenic pressures. This prompted hydrogeologists to apply innovative numerical approaches to better understand the functioning of karst watersheds and support karst water resources management. The Soil and Water Assessment Tool (SWAT) is a semi-distributed hydrological model that has been used to simulate flow and water pollutant transport, among other applications, in basins including karst watersheds. Its source code has also been modified by adding distinctive karst features and subsurface hydrology models to more accurately represent the karst aquifer discharge components. This review summarizes and discusses the findings of 75 SWAT-based studies in watersheds that are at least partially characterized by karst geology, with a primary focus on the hydrological assessment in modified SWAT models. Different karst processes were successfully implemented in SWAT, including the recharge in the epikarst, flows of the conduit and matrix systems, interbasin groundwater flow, and allogenic recharge from sinkholes and sinking streams. Nonetheless, additional improvements to the existing SWAT codes are still needed to better reproduce the heterogeneity and non-linearity of karst flow and storage mechanisms in future research.

Keywords: karst hydrology; SWAT model; modified SWAT model; hydrological modeling

check for updates

Citation: Al Khoury, I.; Boithias, L.; Labat, D. A Review of the Application of the Soil and Water Assessment Tool (SWAT) in Karst Watersheds. *Water* **2023**, *15*, 954. https://doi.org/10.3390/w15050954

Academic Editor: Renato Morbidelli

Received: 2 February 2023
Revised: 25 February 2023
Accepted: 27 February 2023
Published: 1 March 2023

Copyright: © 2023 by the authors. Licensee MDPI, Basel, Switzerland. This article is an open access article distributed under the terms and conditions of the Creative Commons Attribution (CC BY) license (https://creativecommons.org/licenses/by/4.0/).

1. Introduction

Karst aquifers are an abundant source of water in many regions across the globe, providing freshwater supply to 20–25% of the world population [1] and upwards of 50% of the total drinking water supply in some countries [2]. They cover nearly 15.2% of Earth's continental surface [3] and form by chemical dissolution of soluble carbonate rocks (i.e., limestone, dolomite, marble or evaporates) exerted by water enriched with carbon dioxide (CO_2) from the atmosphere or soil zone [4]. Depending on the degree of karstification, distinctive karst features can develop, including sinkholes and dolines, losing streams, springs, and vast networks of subsurface and hydrologically connected cracks, fissures, conduits, and caves [5].

1.1. Characteristics of Karst Systems

A karst system is generally composed of four main water-bearing mediums with distinct geomorphology, hydrodynamic properties, storage, and flow patterns: (1) the soil and non-karstic zone, (2) the epikarst, (3) the transmission zone—the latter three forming the unsaturated zone, and (4) the saturated zone [6]. These contrasting layers, which are interactively connected by water flow and solute transport, form the karstic critical zone [7,8].

Figure 1 shows a schematic model of a typical karst aquifer, including the surface hydrological processes and flow mechanisms of the underground karst subsystems. The

3.1 Introduction

The earliest SWAT studies in karst watersheds (a total of 4 articles) have been reported by Gassman et al. (2007) as part of a full range review of research findings and methods for different application categories with SWAT (e.g., discharge, hydrological analyses, sensitivity analyses and calibration techniques, climate change impacts on hydrology, pollutant transport and fate). Their review was based on more than 250 SWAT articles identified in the literature up to the year 2007. Since then, the use of SWAT has seen a tremendous growth globally for a wide range of scales and complex environmental studies, with more than 5000 articles currently published in peer-reviewed journals (CARD, 2022). The number of SWAT review studies has also expanded to cover a variety of applications, such as: SWAT developments in landscape representation, stream routing, and soil phosphorus dynamics (Douglas-Mankin et al., 2010), SWAT improvements in addressing environmental issues (Tuppad et al., 2011), quantification of ecosystem services (Francesconi et al., 2016), runoff simulation, hydrological impacts under changing environment, and non-point source pollution (Wang et al., 2019a) SWAT limitations in simulating subdaily processes (Brighenti et al., 2019), methods used to develop a SWAT model at field-scale (Karki et al., 2022), SWAT simulations of hydro-climatic extremes (Tan et al., 2020), and SWAT applications in coastal watersheds (Aloui et al., 2023) to name a few.

Despite these advancements, the numerical simulation of karst watersheds and their processes in SWAT is still underway. In fact, a recent research study by Eini et al. (2020) cited only 30 articles describing SWAT-based applications in partially karstified and karst dominated watersheds, with just 11 studies featuring a modified SWAT code. To note, Eini et al**.** (2020) did not provide a detailed overview of the karst modeling approaches adopted in articles that they cited but rather an introductory synopsis prior to presenting two modified SWAT codes that they developed and applied in a karst watershed. Therefore, our paper is the first – to our best knowledge – to present an in-depth review of the studies conducted with SWAT in karst watersheds, building on the selected list of publications by Eini et al. (2020) and extending to the full range of studies between the years 2000−2022. The objectives of our present review are to: (1) describe the SWAT subroutines that correspond to the different processes driving the flow of water in the critical zone (i.e., surface runoff, evapotranspiration, infiltration, interflow, recharge, baseflow), (2) summarize and discuss the research methods and findings for the standard and modified SWAT models in karst influenced watersheds, and (3) identify potential constraints of the existing SWAT modeling approaches in representing the heterogeneous and non-linear flow mechanisms in karst aquifers, and (4) propose future research directions in order to enhance the applicability of SWAT in karst watersheds and the reliability assessment of karst water resources for future management and planning.

This review will present the different applications of SWAT (i.e., water quantity and quality, land-use and climate change, erosion processes, ecohydrological assessment, and water resources management) in karst influenced and karst dominated watersheds. However, the primary focus of the discussion will be the

hydrological assessment in the SWAT applications that featured SWAT coupling with other hydrological models or modifications to the SWAT recharge and groundwater flow equations. These studies aimed to improve the representation of karst features, baseflow, and peak flows in SWAT prior to simulating other watershed processes, such sediment or pollutant transport.

3.2 SWAT Studies in Karst Watersheds: Selection and Classification Methods

We used the SWAT Literature Database (CARD) (CARD, 2022) and Google Scholar engine to identify SWAT research studies in karst watersheds, published between the years 2000 (the year that the first SWAT study in a karst watershed was published) and 2022. Searching priority was initially accorded to the 5400+ articles available in CARD and grouped by specific application categories. All SWAT code iterations (standard and modified) were included in the search and selection process of the articles, based on the keywords "hydrologic", "hydrologic and pollutants", and "karst". Consequently, 17 articles were identified in CARD. Then, multiple searches were performed using Google Scholar to identify the studies that have not been included in CARD, considering the above-mentioned criteria terms in combination with the term "SWAT". Only peer-reviewed articles and published thesis reports in Google Scholar were selected for further assessment, whereas technical reports, abstracts/conference papers, and non-English articles were excluded. Combining both literature databases, a total of 75 studies related to SWAT simulations in karstic and partially karstified watersheds were identified. We classified these studies into two main categories: (1) the standard SWAT model applications (category I) and (2) the coupled/modified SWAT model applications (category II). Subsequently, 25 studies reporting an application of a modified SWAT or SWAT coupled with a karstic flow model fell under category II, while the remaining 50 studies fell under the first category I.

In this paper, we grouped the articles under category I by region (North and Latin America, Europe, Asia, and Africa) and study scope (i.e., hydrological or water quality modeling, climate or land-use change impacts) (**Table 1**). For the sake of paper length, we discussed the studies under category I that presented a novel simulation approach or a complex application of the standard SWAT in karst watersheds. Next, we subdivided the articles under category II based upon: (1) the conceptual models/algorithms coupled with SWAT or used to modify the SWAT source code, (2) the studied karst processes/features (e.g., matrix, conduits, springs, sinkholes), and (3) the simulation scope (e.g., hydrological or water quality modeling, climate or land-use change impacts) (**Table 2**). Then, we thoroughly presented the core methodology and major findings of the SWAT studies of category II, which focused primarily on hydrological simulation. Appendices A-K summarize the equations of the karstic models coupled with SWAT and used in the different modified variants of the code. Finally, we identified potential constraints of the modified SWAT models so that they can so that they can be considered in developing future SWAT models adapted to karst hydrology.

The accuracy of the SWAT models' outputs was reported in their respective studies using different statistical indicators, such as the Nash-Sutcliffe Efficiency (NSE), the coefficient of determination (R^2), the percent bias (PBIAS%), the root mean square error observations standard deviation ratio (RSR), and the Kling-Gupta Efficiency (KGE) (Moriasi et al., 2015; Guse et al., 2017). In this review, the overall trends of the hydrological models' performance were examined using NSE, being the most commonly applied statistical indicator across all the reported studies. NSE is a measure of the relative magnitude of the residual variance against the observed data variance. It is used to assess the goodness of fit of the plot of observed versus simulated data, and is computed as follows (Moriasi et al., 2015):

$$NSE = 1 - \frac{\sum_{i=1}^{n}(O_i - S_i)^2}{\sum_{i=1}^{n}\left(O_i - \overline{O}\right)^2} \quad (1)$$

where $O_i$and S_i represent the *ith* value of the observed and simulated data, respectively, $\overline{O}$ is the mean of the observed and simulated data, and n is the total number of observations. NSE values can vary between -∞ and 1. In particular, watershed streamflow simulation at the daily, monthly, and annual scales is judged as satisfactory if 0.5 < NSE ≤ 0.7, good if 0.7 < NSE ≤ 0.8, and very good for NSE ≥ 0.8. Conversely it is unsatisfactory if NSE ≤ 0.5, while negative NSE values indicate an unacceptable model performance (Moriasi et al., 2015).

Table 1. Reference, basin description, and application of the standard SWAT studies in karst watersheds (category I).

Region	Reference	Basin name (country, size in km^2)	Application
North and Latin America	Spruill et al. (2000)	University of KY Research Site (USA; 5.5)	Simulation of streamflow
	Coffey et al. (2004)	(University of KY Research Site (USA; 5.5)	Simulation of streamflow
	Benham et al. (2006)	Shoal Creek (USA; 367)	Simulation of streamflow and bacteria fate and transport
	Amatya et al., 2011	Chapel Branch Creek (USA; 15.55)	Simulation of streamflow in a watershed with a flooded embayment outlet draining to a lake
	Amatya et al., 2013	Chapel Branch Creek (USA; 15.55)	Simulation of streamflow and phosphorus loads and concentrations in karst watershed tributaries and downstream a reservoir-like embayment outlet
	Williams et al. (2014)	Chapel Branch Creek (USA; 15.55)	Simulation of streamflow, nitrogen loads, and phosphorus loads in a karst watershed draining to a lake via a reservoir-like embayment
	Wilson et al. (2014)	South Branch, Root River (USA; 301.8)	Impacts of traditional and alternative conservation management practices on water quality (sediments and phosphorus)
	Jain et al. (2015)	Nueces River Headwaters (USA; 2,126)	Impacts of land-use/cover change on watershed hydrology
	Sunde et al. (2016)	Hinkson Creek (USA; 231)	Impacts of future urban development on watershed hydrology
	Sunde et al. (2017)	Hinkson Creek (USA; 231)	Impacts of climate change on watershed hydrological processes
	Sunde et al. (2018)	Hinkson Creek (USA; 231)	Impacts of future urbanization and climate change on watershed hydrology
	Sarkar et al. (2019)	Conestoga River (USA; 1,230)	Simulation of flow, sediment loads from upland watershed sources, flow routing, and sediment processes using a coupled SWAT-HSPF model
	Merriman et al. (2019)	Upper East River (USA; 375.3)	Impacts of agricultural best management practices on flow, sediment loads, and nutrient loads
	Sullivan et al. (2019)	Edwards aquifer overlain by Cibolo Creek watershed (USA; 707) and Dry Comal Creek watershed (USA; 337)	Simulation of nitrate concentration inputs to MODFLOW CFPv2 and CMT3D models used to assess nitrate transport in an aquifer
	Chen et al. (2020)	Blanco River (N/A)	Multi-model projections of hydrological drought characteristics under climate change
	Zeiger et al. (2021)	James River (USA; 3,770)	Impacts of climate and land use on streamflow, sediment, and nutrient loads, and identification of critical source areas of non-point source pollution
	Al Aamery et al. (2021)	Cane Run-Royal Spring (58)	Simulation of surface runoff, surface routing, and soil water percolation inputs for a fluviokarst-specific combined discrete continuum numerical model

	Karki et al. (2021)	Apalachicola-Chattahoochee-Flint River (USA; 12,000)	Simulation of groundwater areal recharge input for a MODFLOW-NWT aquifer model
Europe	Salerno and Tartari (2009)	Subbasin of the Lake Pusiano watershed (Italy, 52.5)	Simulation of discharge using SWAT supported by wavelet analysis to assess the contribution of external flow component to streamflow
	Vale and Holman (2009)	Bosherston Lakes (UK; N/A)	Quantitative assessment of the hydrological processes controlling water levels and groundwater–surface water interactions in a lake system
	Tzoraki et al. (2013)	Evrotas (Greece; 2,050)	Simulation and analysis of flood events characteristics
	Palazón and Navas (2013)	Linsoles River (Spain; 284)	Simulation of surface runoff and sediment yield
	Palazón and Navas (2014)	The Barasona reservoir catchment (Spain; 1,509)	Simulation of erosion and sediment yield
	Sellami et al. (2014)	Thau catchment (France; 280)	Assessment of SWAT model accuracy in predicting discharge at gauged and ungauged catchments within an uncertainty framework
	Gamvroudis et al. (2015)	Evrotas River (Greece; 1,348)	Simulation of watershed water budget and spatial distribution of runoff and sediment transport
	Malagò et al. (2015)	Scandanavian Peninsula (10^6); Iberian Peninsula (556,000)	Hydrological simulation, sensitivity analysis, multi-variable calibration, and regionalization of the calibrated parameters for the identification of dominant hydrological processes in each region
	Mehdi et al. (2015)	Altmühl River (Germany; 980)	Impacts of climate and land-use changes on streamflow and nutrients loads
	Sellami et al. (2016)	Thau catchment (France; 280)	Impacts of climate change on watershed hydrology
	Palazón and Navas (2016)	The Barasona reservoir catchment (Spain; 1,509)	Simulation of streamflow under different precipitation characterization scenarios
	Vigiak et al. (2017)	Danube River (800,000)	Simulation of sediment fluxes under soil conservation measures and identification of sediment budget knowledge gaps
	Efthimiou (2018)	Kalamas River (Greece; 1,899.25)	Simulation of watershed hydrological budget
	Martínez-Salvador and Conesa-García (2020)	Upper Argos River (Spain; 510)	Simulation of streamflow and sediment load
	Senent-Aparicio et al. (2020)	Castril River (Spain; 120)	Simulation of streamflow using SWAT supported by chloride mass balance to estimate IGF contribution to streamflow
	Busico et al. (2021)	Anthemountas (Greece; 374)	Assessment of groundwater recharge variations and their relationship with other hydrological parameters under climate change
	Sánchez-Gómez et al. (2022)	Henares River (Spain; 4,070)	Optimization of SWAT streamflow simulation by incorporating watershed geological properties in model calibration
Asia	Jiang et al. (2011)	Shibetsu River (Japan; 672)	Simulation of streamflow and external flow contribution to discharge from the water balance equation, using measured data
	Tian et al. (2016)	Shibantang River (China; 2,248)	Assessment of trade-offs and synergic relationships between ecosystem services (water yield, sediment yield, and net primary productivity)
	Bucak et al. (2017)	Lake Beyşehir catchment (Turkey; 4,704)	Impacts of climate and land-use changes on the hydrological balance of a lake catchment and water levels

	Hou and Gao (2019)	Sancha River (China, 4,068)[1]	Simulation of the spatial variability of streamflow, surface runoff, and groundwater runoff, and analysis of their spatial correlation with environmental factors
	Jakada and Chen (2020)	Miaogou subbasin of Gaolan River Basin (China; 45)	Simulation of watershed hydrology using SWAT supported by a geological survey and a tracer test
	Mo et al. (2020)	Xiajia River (China; 799.2)	Simulation of watershed runoff under different precipitation input data
	Hou et al. (2020)	Guizhou Province (China 4,681)	Analysis of the factors affecting streamflow, surface runoff, and groundwater, and their interactions for different geomorphic types
	Gao et al. (2021)	Sancha River (China, 7,061)[1]	Assessment of trade-offs and synergic relationships between ecosystem services (sediment yield and surface/slope runoff, water yield, and slope runoff) and main factors affecting their relationships, for different geomorphic types
	Jiang et al. (2021)	Sancha River (China, 7,061)[1]	Simulation of the spatial distributions of rainfall erosivity and runoff erosivity, and identification of the dominant factors and their interactions affecting the spatial distributions of rainfall/runoff erosivity, for different geomorphic types
	Chang et al. (2022)	Nanpan River (China; 43,200)	Simulation of soil moisture using SWAT and development of a methodology for a comprehensive drought index based on the watershed hydrological processes (precipitation, runoff, and soil moisture)
	Zhang et al. (2022)	Lijiang River (China, 5,444)	Simulation of streamflow and water quality using SWAT and HSPF models driven by different precipitation input data, and impacts of best management practices on non-point-source pollution reduction
	Mo et al. (2022)	Chengbi River (China; 2,087)	Simulation of runoff under different calibration methods and precipitation input data
	Yuan et al. (2022)	Gaoche catchment area of the Dabang River basin (China; 1,877.20)	Assessment of trade-offs and synergic relationships between ecosystem services (surface/underground runoff and surface sediment yield) and driving factors affecting their variation
Africa	Zettam et al. (2017)	Tafna watershed (Algeria; 7,245)	Simulation of watershed hydrological processes and assessment of the impacts of dam construction on water balance and sediment flux
	Zaibak and Meddi (2022)	Cheliff basin (Algeria; 43,750)	Simulation of streamflow at watershed dam-feeding subbasins and outlet

1. There is a variation in the area of the Sancha River basin reported by Hou and Gao (2019) compared to Gao et al. (2021) and Jiang et al. (2021) .

Table 2. Groundwater modeling approach, reference, basin description and application of the modified SWAT codes in karst studies (category II).

Groundwater modeling approach	Reference	Basin name (region; size in km^2)	Application – Modified SWAT name (when applicable)
Conceptual linear one-reservoir groundwater model	Afinowicz et al. (2005)	North Fork, Upper Guadalupe River (Texas-USA; 360)	Simulation of streamflow and water budget, and assessment crop management impacts on water budget
	Baffaut and Benson (2009)[2]	James River (Missouri, USA; 3,600)	Simulation of streamflow and pollutant transport (in-stream phosphorous loads and fecal coliform concentrations) – Adapted SWAT/ SWAT-B&B
	Yactayo (2009)[2]	Opequon Creek (Virginia, USA; 890.2)	Simulation of streamflow and nitrate transport through the sinkholes in a karstic watershed – SWAT-karst
	Palanisamy and Workman, (2015)[2]	Cane Run Creek (Kentucky, USA; 115.6)	Simulation of streamflow through sinkholes in the streambed – KarstSWAT
	Zhou et al. (2022)[2]	South and North Panjiang River (China; 2,762)	Simulation of streamflow through sinkholes in the watershed
Conceptual linear two-reservoir groundwater model	Nikolaidis et al. (2013)	Koiliaris River (Crete, Greece; 132)	Simulation of water budget and in-stream nitrate concentrations, and assessment of climate change impacts on hydrology and water quality – Karst-SWAT
	Nerantzaki et al. (2015)[3]	Koiliaris River (Crete, Greece; 130)	Simulation of suspended sediment transport, and assessment of climate change impacts on flow, soil erosion, and sediment transport
	Tapoglou et al. (2019)[3]	Crete Island (Greece; 8,337)	Assessment of climate change impacts on extreme hydrometeorological events
	Demetropoulou et al. (2019)[3]	Geropotamos (Crete, Greece; 525 km^2)	Methodology for the prioritization of a Program of Measures for water quantity and quality protection
	Nerantzaki et al. (2019)[3]	Crete Island (Greece; 8,265)	Assessment of climate change impacts on hydrology
	Lilli et al. (2020a)[3]	Koiliaris River (Crete, Greece; 132)	Analysis of hydrological and geochemical processes
	Nerantzaki et al. (2020)[3]	Koiliaris River (Crete, Greece; 130)	Uncertainty analysis of flow simulation due to the parameter uncertainty of the SWAT and Karst-SWAT models and internal variability of climate scenarios
	Lilli et al. (2020b) [3]	Koiliaris River (Crete, Greece; 130)	Development of erosion and flood protection nature-based solutions
	Malagò et al. (2016)	Crete Island (Greece; 8,336)	Simulation of hydrological water balance – KSWAT
	Nguyen et al. (2020)	Area in southwest Harz Mountains and southern Harz rim (Lower Saxony; Germany; 384)	Streamflow simulation, including IGF – SWAT_IGF
Conceptual linear three-reservoir groundwater model	Wang et al. (2019b)[2]	Xianghualing River (Hunan, China; 26.8)	Streamflow simulation
	Geng et al. (2021)[2]	Daotian River (Guizhou, China; 99.21)	Simulation of flow (including IGF) and water budget
Conceptual non-linear one-reservoir groundwater model	Wang and Brubaker (2014)[2]	Shenandoah River of the Potomac River Basin (USA; 7,607)	Streamflow simulation
Modified crack flow module; conceptual linear one-reservoir groundwater model	Eini et al. (2020)[2]	Maharlu Lake (Province of Fars, Iran; 4,270)	Simulation of crack/preferential flow, discharge, and water budget – SWAT-ML and SWAT-CF

Variable source area hydrology; conceptual linear one-reservoir groundwater model	Amin et al. (2017)[2]	Spring Creek (Pennsylvania, USA; 370)	Simulation of streamflow, nutrient loads, and sediment loads for different agricultural management practices – Topo-SWAT
	Amin et al. (2018)[4]	Spring Creek (Pennsylvania, USA; 370)	Impact of dairy cropping practices on nutrient and sediment loads
	Amin et al. (2020) [4]	Spring Creek (Pennsylvania, USA; 370)	Impact of agricultural best management practices on nutrient and sediment loads
	Gunn et al. (2021)[4]	Spring Creek (Pennsylvania, USA; 370)	Impact of climate change with increasing atmospheric CO_2 on watershed hydrology – SWAT-VSA_CO2 and SWAT-VSA_CO2+Plant
SWAT + Water Accounting Plus (WA+) framework	Delavar et al. (2020)	Tashk-Bakhtegan (Iran; 27,520)	Assessment of water consumption and supply trends under different water management strategies – SWAT-FARS
	Delavar et al. (2022)	Karkheh River (Iran; 42,267)	Assessment of water supply and demand conditions in wet and dry periods, based on the water resources, consumption, and withdrawal indicators of the WA+ framework– SWAT-Karkheh

2. These studies reported applications of both the standard SWAT model and a modified SWAT model.
3. These studies used the Karst-SWAT version of SWAT developed by Nikolaidis et al. (2013) without making any additional modifications to the model.
4. These studies used the Topo-SWAT version of SWAT developed by Amin et al. (2017)

3.3 Results and Discussions

3.3.1 Applications of Standard SWAT in Karst Watersheds

Different versions of SWAT have been developed over the years to meet the growing need for water resources modeling and management tools, the latest being SWAT+. SWAT+ is a completely restructured version of SWAT that offers an enhanced flexibility in watershed configuration and spatial representation of landscape processes (Bieger et al., 2017, 2019). The identified studies in this review were conducted using the previous SWAT versions, including SWAT v2000, v2005, v2009, and v2012. Noticeably, SWAT+ has not yet been implemented in karst regions.

The standard SWAT model has been applied to a wide range of karst dominated and karst influenced watershed scales to assess the hydrological cycle and simulate streamflow (Spruill et al., 2000; Coffey et al., 2004; Efthimiou, 2018; Spruill et al., 2000; Zettam et al., 2017), flood events (Tzoraki et al., 2013), erosion processes and sediment yield (Martínez-Salvador and Conesa-García, 2020; Palazón and Navas, 2013, 2014), as well as pollutant (nutrients and pathogens) transport (Amatya et al., 2013; Gamvroudis et al., 2015; Williams et al., 2014). The model was also used to compare water quality impacts between scenarios of different crop types and agricultural management practices (Merriman et al., 2019; Wilson et al., 2014).

Several studies evaluated climate change impacts on watershed hydrology based on historical climate patterns and climate projections (Busico et al., 2021; Chen et al., 2020; Sellami et al., 2016; Sunde et al., 2017), as well as the effects of land-use change on the water budget (Jain et al., 2015). Other studies assessed the combined impacts of land-use and climatic changes on watershed hydrology and or water quality (Bucak et al., 2017; Sunde et al., 2017), including the influence of future urbanization and impervious surface growth (Sunde et al., 2018), and other anthropogenic factors, such as wastewater treatment (Zeiger et al., 2021). In other applications, SWAT was used to simulate the spatial and temporal evolution of runoff, groundwater, erosivity, and surface sediment yield in karst watersheds, considering various climatic and land features. These studies identified the driving factors affecting the variation of ecosystem services and analyzed the trade-offs and synergic relationships between them for rocky desertification containment and ecological protection (Gao et al., 2021; Jiang et al., 2021; Hou and Gao, 2019; Hou et al., 2020; Tian et al., 2016; Yuan et al., 2022).

Additionally, SWAT has been coupled with other models to expand the assessment of flow and water quality. For instance, Sarkar et al. (2019) linked SWAT with the Hydrological Simulation Program-FORTRAN (HSPF) to simulate flow and sediment loading from upland agricultural areas in a karstified watershed using SWAT, followed by in-stream sediment processes in HSPF. Sullivan et al. (2019) applied SWAT to model recharge nitrate concentrations from natural and anthropogenic sources in a karst watershed. Then, the recharge output from SWAT was incorporated into the Modular Three-Dimensional Finite-Difference Groundwater Flow Model Conduit Flow Process version 2 (MODFLOW CFPv2) and the Conduit Modular 3-Dimensional Transport (CMT3D) model to predict groundwater flow and nitrate transport and levels in the aquifer. Similarly, Karki et al. (2022) estimated groundwater recharge in a karst watershed using SWAT, then integrated the recharge output from SWAT into a MODFLOW model with Newton-Raphson formulation (MODFLOW-NWT) to evaluate the impacts of irrigation withdrawals on groundwater levels and the stream-aquifer fluxes. Al Aamery et al. (2021) also simulated surface runoff, surface routing, and soil water percolation in SWAT as inputs for a combined discrete-continuum fluviokarst numerical model.

Moreover, the performance of SWAT for karst watersheds hydrological and water quality simulations was evaluated under different precipitation input data (Palazón and Navas, 2016; Mo et al., 2020; Zhang et al., 2022) and with respect to various calibration approaches, such as multi-site calibration (Mo et al., 2022) and zonal calibration that incorporates the basin geological properties (Sánchez-Gómez et al., 2022).

More than 70% of the studies that used NSE to assess the performance of SWAT hydrological models with daily time series calibration scored NSE values greater than 0.5, and over 90% reported NSE values greater than 0.5 for the daily time series validation. In comparison, more than 90% of the studies scored NSE values higher than 0.5 with monthly calibrated models, while upwards of 80% reported NSE values higher than 0.5 with monthly validation (**Figure 3**). These results indicate a satisfactory performance, with numerous applications meeting the criteria of a "good" flow simulation, as proposed by Moriasi et al. (2015). However, some applications conducted in complex karst watersheds scored poor NSE statistics. The studies conducted by Spruill et al. (2000) and Coffey et al. (2004) in the small experimental watershed of Kentucky revealed that SWAT failed to accurately reproduce peak and low flows. The observed and simulated daily hydrographs were asynchronous, with SWAT often underestimating the peak

discharge rates and generating recessions that are faster than the observed data curves. The monthly runoff volumes at the watershed outlet were also underpredicted, which was attributed to the lack of explicit representation of karst geology in SWAT. A similar finding was reached by Benham et al. (2006) who concluded that SWAT inability to reproduce the flows sustained by karst features reduced the prediction efficiency of streamflow in their study watershed. At a larger scale, the studies undertaken in the Scandinavian and Iberian peninsulas of 10^6 km^2 and 556,000 km^2 (Malagò et al., 2015), respectively, and in the Danube River basin of 800,000 km^2 (Vigiak et al., 2017) revealed that the performance of SWAT was lower in karst dominated regions in comparison to non-karst areas, due to the model misrepresentation of baseflow in karst streams. Martinez-Salvador and Conesa-Garcia (2020) also emphasized on the need to improve the representation of extreme hydrological events (e.g., low-flow and peak-flow periods) in SWAT.

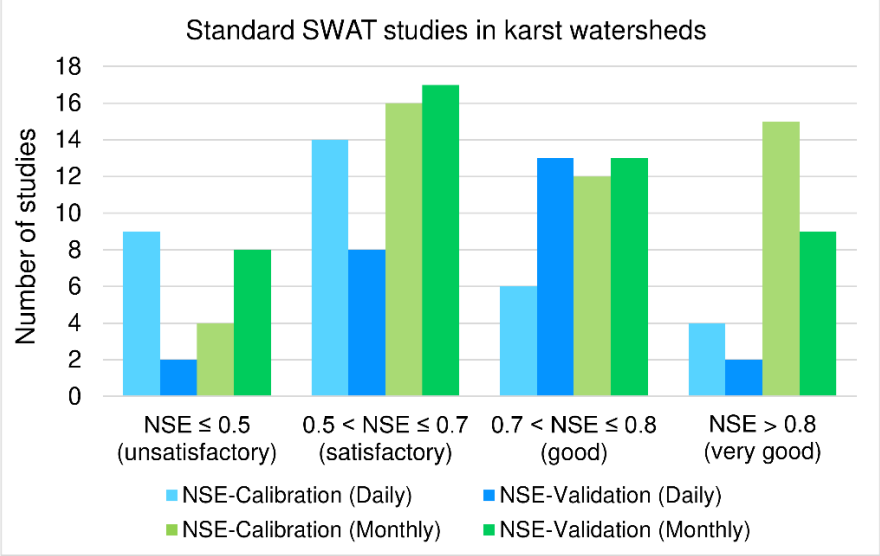

Figure 3. Number of standard SWAT-based studies in karst watersheds under the NSE performance ratings recommended by Moriasi et al. (2015) for daily and monthly discharge simulation.

Furthermore, several studies underlined the need to account for external and interbasin groundwater flows to improve the discharge simulation in SWAT (Gamvroudis et al., 2015; Palazón and Navas, 2013; Jakada and Chen, 2020; Jiang et al., 2011; Salerno and Tartari, 2009; Senent-Aparicio et al., 2020; Spruill et al., 2000). The hydrological simulations performed by Spruill et al. (2000) confirmed the dye tracing results from sinkholes surrounding the study site that an area larger than the watershed topographic boundaries contributes to streamflow. Amatya et al. (2011) underlined the need to couple SWAT with a subsurface hydrology model to accurately

characterize the dynamics of the karst groundwater flow contribution to the surface drainage network. Gamvroudis et al. (2015) estimated that around 33% of the water balance was lost via deep groundwater flow to areas outside their study watershed due to karst formations, while Palazón and Navas (2013) simulated the discharge losses by underground flow through swallow holes in the upper part of the study basin. On the other hand, Jakada and Chen (2020) confirmed the absence of runoff losses by subterranean flow diversion from their study watershed prior to conducting a hydrological simulation in SWAT. Their finding was based on the results of tracer tests conducted through the sinkholes in the watershed and monitoring of the springs within and outside the basin.

In more complex applications, Salerno and Tartari (2009) coupled wavelet analysis with hydrological modeling in SWAT to identify the streamflow components in a non-conservative karst subbasin. After excluding the possibility of an incorrect assessment of the precipitation data, streamflow measurements, and evapotranspiration estimates, a series of continuous wavelet transform, cross wavelet transform, wavelet coherence, and phase difference analyses were applied to precipitation, groundwater levels, observed streamflow, and the time series constructed by the difference between the observed daily discharge and the streamflow simulated by a calibrated SWAT model of the study site. Based on the ensemble of correlations, it was established that the external water contribution to the river discharge was primarily due to groundwater seepage from a hydrogeological catchment that is larger than the surface watershed. The daily time series of the external water contribution was generated by multiplying the SWAT-simulated groundwater inflow by a yearly coefficient. This coefficient was adjusted to match the external contribution time series with the groundwater fluctuations simulated by SWAT and have the annual simulated flows equal to the observed flows. The additional water component improved the prediction efficiency of daily streamflow at the watershed outlet, with NSE increasing from 0.61−0.56 in the calibration and validation periods to 0.66−0.62, and R^2 increasing from 0.71−0.69 to 0.74−0.72. The mean absolute error of streamflow underestimation was also reduced from 47% to 33%.

Jian et al. (2011) simulated discharge in a non-conservative karst watershed with an initial average discrepancy of 47% between the observed and measured water balances. After ruling out the possibility of invalid precipitation, evapotranspiration, and discharge measurements, the external contribution of the underground flow to streamflow was added as a point source discharge in SWAT, adopting the mean value of the difference in the annual water budget. The hydrological

calibration and validation were carried out in a two-stage process. In the first step, the SWAT model and external flow value were calibrated using discharge data, while surface runoff, baseflow, and evapotranspiration were calibrated in the next step using available observational data. As a result, the baseflow component (excluding the external flow contribution) was calibrated in SWAT, and the inclusion of IGF reduced the underestimation bias of streamflow from nearly 50% to less than 3% at the monthly scale and 15% at the daily scale. NSE and R^2 values greater than 0.5 and 0.65, respectively, were also reached both in the calibration and validation periods.

More recently, Senent-Aparicio et al. (2020) applied SWAT with the atmospheric Chloride Mass Balance (CMB) method to simulate streamflow of the Castril River basin (Spain). The study site is steep karst watershed fed by IGF from adjacent aquifers under steady conditions (i.e., no groundwater abstraction, evapotranspiration from shallow aquifers, or underflow to deep aquifers). The net aquifer discharge was equated to the baseflow component of streamflow, and the CMB approach was used to estimate the fraction of net aquifer recharge from the upstream areas as a proxy for the IGF contributing to additional baseflow. The corrected baseflow time series with IGF improved the SWAT model performance, reducing the underestimation bias of the streamflow simulations to less than 20% in both calibration and validation.

3.3.2 Applications of Modified SWAT in Karst Watersheds

A total of 18 modified SWAT models have been developed and applied across 25 studies in watersheds characterized by karst geology (Table 2). Models that were run at daily and monthly time intervals reported a higher prediction efficiency of the flow at the monthly scale than the daily scale, both in calibration and validation periods (Afinowicz et al., 2005; Amin et al., 2017; Nerantzaki et al., 2020; Nikolaidis et al., 2013). Around 80% of the studies that used NSE to evaluate the hydrological model performance at the daily time step reported NSE values greater than 0.5 for the calibration and validation periods. In comparison, more than 80% of the studies that used the monthly time step scored NSE values higher than 0.5 for calibration, and more than 90% reported NSE values greater than 0.5 for validation (**Figure 4**).

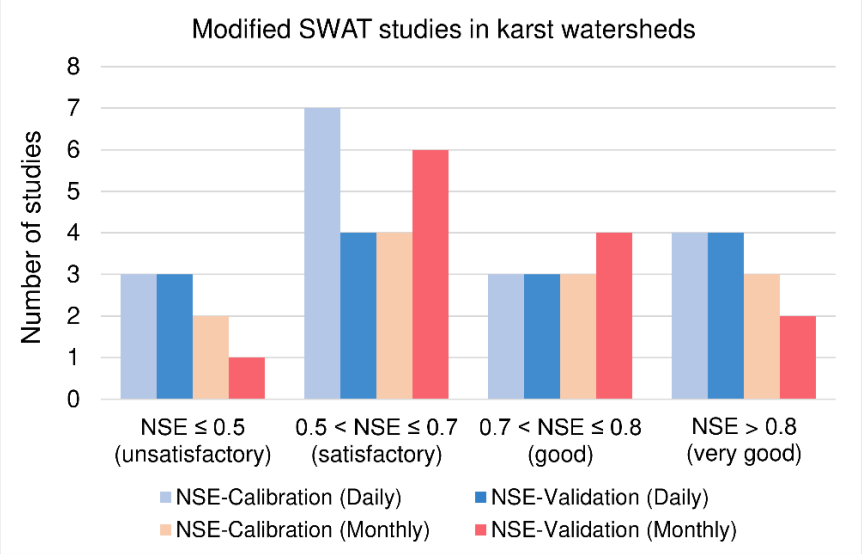

Figure 4. Number of modified SWAT-based studies in karst watersheds under the NSE performance ratings recommended by Moriasi et al. (2015) for daily and monthly discharge simulation.

3.3.2.1 Conceptual Linear One-Reservoir Model

The first application of a modified SWAT code in a karst watershed was performed by Afinowicz et al. (2005) to evaluate the impacts of woody plants management scenarios on the rangeland water cycle of the North Fork of the Upper Guadalupe River, Texas (USA). The watershed has an area of 360 km^2 and is covered by thin soils that overlie fractured limestone formations. The return flow (baseflow) function of the groundwater module of SWAT (v2000) was modified to simulate rapid infiltration in karst areas into the deep aquifer. Therefore, the deep aquifer recharge component was deducted from the baseflow component of streamflow to allow a fraction of infiltrated water to bypass the shallow aquifer and enter the deep aquifer instead of flowing into the channel as baseflow, as shown in Equation (1):

$$Q_{gw,i} = Q_{gw,i-1} \times e^{-\alpha_{gw} \times \Delta t} + \left(w_{rchrg} - w_{deep}\right) \times \left(1 - e^{-\alpha_{gw} \times \Delta t}\right) \quad (1)$$

where $Q_{gw,i}$ and $Q_{gw,i-1}$ are the baseflow values for the current and previous day (mm $H_2O.day^{-1}$), α_{gw} is baseflow recession constant, Δt is the time interval (days), w_{rchrg} is the water percolated past the root zone (mm $H_2O.day^{-1}$), and w_{deep} is the water percolated to the deep aquifer (mm $H_2O.day^{-1}$).

The hydrological model was adjusted using daily streamflow data at the watershed outlet, with a 5-year warm-up period, a 5-year calibration period, and a 7-year validation period. The

model scored monthly NSE values of 0.29 and 0.5 for the calibration and validation periods, respectively. It performed less efficiently at the daily scale, with NSE values of 0.4 and 0.09. It also failed to accurately reproduce all discharge trends at the daily scale, particularly high peak flows. The results of the hydrograph simulations were attributed to the nature of the surface runoff in the watershed, which is characterized by sustained low baseflow and very high flow that brings the soil water capacity to saturation.

Baffaut and Benson (2009) modified the groundwater recharge equation of SWAT (v2005) to model fast infiltration from sinkholes and losing streams to the aquifer and groundwater flow contribution to surface water. The improved SWAT, known as SWAT-B&B/Adapted SWAT model, was applied to the 3,600 km^2 James River basin in southwest Missouri (USA), characterized by losing streams, sinkholes, and springs.

In SWAT-B&B, recharge into the aquifer was partitioned to two components: (1) the infiltration from the soil bottom, representing slow flow to the porous matrix, and (2) the recharge from sinkholes and losing streams, representing fast flow to the conduits. Sinkholes in the study basin were modeled as ponds with a small drainage area and high hydraulic conductivity, while losing streams were represented by tributary channels with high streambed hydraulic conductivity. Thus, the soil and karst infiltration components were simulated using two recharge functions, each with a specific groundwater delay coefficient (Equations (2) and (3)). Return flow was then modeled with the standard SWAT function, based on the groundwater flow of the previous day and the total aquifer recharge of that day (Equation (4)).

$$rchrg_{seep(t)} = \left(1 - e^{\frac{-1}{gw_{delay}}}\right) soil_{seep(t)} + \left(e^{\frac{-1}{gw_{delay}}}\right) rchrg_{seep(t-1)} \qquad (2)$$

$$\begin{cases} rchrg_{karst(t)} = \left(1 - e^{\frac{-1}{karst_{delay}}}\right) karst_{seep(t)} + \left(e^{\frac{-1}{karst_{delay}}}\right) rchrg_{karst(t-1)} \\ karst_{seep(t)} = tloss + twlpnd + twlwet \end{cases} \qquad (3)$$

where $rchrg_{seep(t)}$ and $rchrg_{karst(t)}$ are the slow recharge from the soil layers and fast recharge from the sinkholes and losing streams to the aquifer (mm $H_2O.day^{-1}$), respectively, $soil_{seep(t)}$ and $karst_{seep(t)}$ are the percolation from the soil bottom and losses from the sinkholes and losing streams (mm $H_2O.day^{-1}$), respectively, gw_{delay} and $karst_{delay}$ represent the time delay for the water percolating from the soil bottom and water infiltrating from the sinkholes and riverbeds to

reach the aquifer (days), respectively, $rchrg_{(t-1)}$ is the recharge of the previous day (mm $H_2O.day^{-1}$), $tloss$ is the water lost from a sinking stream (mm $H_2O.day^{-1}$), and $twlpnd$ and $twlwet$ represent the seepage from the ponds and wetlands (mm $H_2O.day^{-1}$), respectively.

$$\begin{cases} Q_{gw,t} = rchrg_{(t)} \times (1 - e^{-\alpha_{gw}}) + Q_{gw,t-1} \times e^{-\alpha_{gw}} \\ rchrg_{(t)} = rchrg_{seep(t)} + rchrg_{karst(t)} \end{cases} \quad (4)$$

where $Q_{gw,t}$ is the daily return flow (mm $H_2O.day^{-1}$), $rchrg_{(t)}$ is the total aquifer recharge calculated as the sum of the slow recharge from the soil layers $(rchrg_{seep(t)})$ and fast recharge from sinkholes and losing streams to the aquifer $(rchrg_{karst(t)})$ (mm $H_2O.day^{-1}$), and α_{gw} is the baseflow recession coefficient (days).

The hydrological model was calibrated for 8 years of daily streamflow records at 5 gauging stations and validated for 7 years. Streamflow biases were all less than 25%, ranging between 4% to 20% during the calibration period and -2% to -21% during validation. The percent bias in surface runoff simulation were all around 10%, indicating a better representation of the baseflow component to streamflow. Moreover, NSE values of around 0.5 were reached for the calibration and validation periods in the main stem of the stream and at the outlet, but lower values close to 0.3 were obtained in the upstream small tributaries. Although a significant improvement in the NSE values could not be spotted by comparing both the standard and modified SWAT models, SWAT-B&B sustained more flows during the dry periods in comparison to SWAT. The model was then used to estimate in-stream phosphorus loads and concentrations, and fecal coliform concentrations. Poor water quality simulation results were obtained in almost all observational river reaches of the basin, both in calibration and validation periods.

Yactayo (2009) further modified the SWAT-B&B code to simulate fast aquifer recharge through sinkholes at the HRU scale by introducing a new parameter called *sink* to the HRU groundwater input file. This sinkhole partitioning coefficient represented the fraction of the runoff drained by a sinkhole to the unconfined aquifer. With this approach, a fraction of the surface runoff and lateral flow in the karst HRU was no longer included in the calculation of total streamflow in the main channel but allocated to the daily seepage from sinking streams and sinkholes. The transmissions losses from the surface runoff entering the sinkholes were also not simulated. Thus, the unconfined aquifer recharge in non-karst regions was calculated using Equation (5), whereas aquifer recharge in karst regions was computed using Equation (6):

$$\begin{cases} rchrg_{seep(t)} = \left(1 - e^{\frac{-1}{gw_{delay}}}\right) seep_{(t)} + \left(e^{\frac{-1}{gw_{delay}}}\right) rchrg_{seep(t-1)} \\ seep_{(t)} = W_{seep} + twlpnd + twlwet \end{cases} \quad (5)$$

where $rchrg_{seep(t)}$ and $rchrg_{seep(t-1)}$ represent the recharge from the water percolating from the soil bottom to the aquifer on a given day and the day before (mm H_2O.day^{-1}), respectively, $seep$ is the recharge from percolating water and seepage from impoundments on a given day (mm H_2O.day^{-1}), W_{seep} is the water drained from the bottom of the soil profile (mm H_2O.day^{-1}), $twlpnd$ is the seepage from the ponds (mm H_2O.day^{-1}), $twlwet$ is the seepage from the wetlands (mm H_2O.day^{-1}), and gw_{delay} is the time delay for the water percolating from the soil bottom to reach the aquifer (days).

$$\begin{cases} rchrg_{karst(t)} = \left(1 - e^{\frac{-1}{[gw_{delay}/10]}}\right) seep_{direct(t)} + \left(e^{\frac{-1}{[gw_{delay}/10]}}\right) rchrg_{karst(t-1)} \\ seep_{direct(t)} = sink \times (surfq + latq) \end{cases} \quad (6)$$

where $rchrg_{karst(t)}$ and $rchrg_{karst(t-1)}$ represent the recharge from sinkholes and losing streams via direct conduits to the aquifer on a given day and the day before (mm H_2O.day^{-1}), respectively, $seep_{direct}$ is the seepage from the sinking streams, ponds, and sinkholes on a given day from the HRU (mm H_2O.day^{-1}), $sink$ is the sinkhole partitioning coefficient (0-1), and $surfq + latq$ is the sum of surface runoff and lateral flow from the HRU (mm H_2O.day^{-1}).

The modified model known as SWAT-karst was applied in the 890.2 km^2 Opequon Creek watershed, located in the Potomac and Shenandoah River basin in Virginia. For SWAT-karst, a new land-use category was added to the land-use map so that sinkholes may be represented by HRUs, based on the area of the sinkhole regions and the land use where the sinkholes are located. Similar to SWAT-B&B, sinking streams were represented by tributary channels with high hydraulic conductivities. SWAT-karst, SWAT-B&B and SWAT were run at the daily time step for a period of 11 years and compared in terms of their performance efficiency in simulating streamflow and other water balance components without any model calibration. All three models overestimated streamflow, and the values of the PBIAS, NSE, and RSR were unsatisfactory at all subbasin outlets and streamflow gages where discharge values were compared. Nonetheless, both SWAT-B&B and SWAT-karst performed better than SWAT in simulating karst discharge, and SWAT-karst had a more significant impact on the distribution of the water balance components,

by simulating less runoff and more baseflow in karst regions with sinkholes. The authors noted that aquifer recharge diverted by sinkholes to regions outside the watershed could be a reason behind SWAT-karst overestimating discharge and failing to meet the acceptable performance criteria. However, they maintained that parameter *sink* values could be modified to control the depth of water that recharges the unconfined and confined aquifers (Equation (7)):

$$deep_{(t)} = W_{seep.dp} + (1 - sink) * (surfq + latq) \quad (7)$$

where $deep$ is the depth of water in the deep aquifer for the day from the HRU (mm $H_2O.day^{-1}$), $W_{seep.dp}$ is the water recharging the deep aquifer from the HRU (mm $H_2O.day^{-1}$), $sink$ is the sinkhole partitioning coefficient (0-1), and $surfq + latq$ is the sum of surface runoff and lateral flow from the HRU (mm $H_2O.day^{-1}$).

Yactayo (2009) also modeled the nitrate loading that recharges the aquifers through the sinkhole as a function of: (1) the volume of surface runoff and lateral flow lost to sinkholes in karst regions, and (2) the nitrate aquifer recharge loading from the soil water percolation. Similar to the flow simulation results, the values of the in-stream nitrate concentrations calculated from aquifer recharge and nitrate in baseflow were unsatisfactory.

Palanisamy and Workman (2015) incorporated an orifice flow transfer function and a successive summation routing algorithm (SSRA) into SWAT in order to simulate groundwater flow from sinkholes located in the streambed to a spring. The modified SWAT code, called KarstSWAT, was applied to the Cane Run watershed of 115.6 km^2 in Kentucky (USA), where numerous sinkholes found along the river streambed divert surface runoff through an underground conduit to the main watershed spring. The karst aquifers to which sinkholes drain the river flow largely overlap the Cane Run surface watershed, and runoff routing into the sinkholes depends on the incoming streamflow volume, the sinkhole size, and the capacity of the underground conduit. To represent this unique hydrological setting, sinkholes were conceptualized as orifices and were modeled as outlets of the karst subbasins during watershed delineation in SWAT. The discharge capacity of the sinkholes was simulated using a head-discharge relationship (Equation (8)) as a function of a diameter range that corresponds to the size of the sinkholes:

$$Q = C_d A \sqrt{2gH} \quad (8)$$

where Q is the capacity of the sinkhole (L^3/T), Cd is a coefficient of discharge, A is the area of the orifice (L^2), g is the acceleration due to gravity (L/T^2), and H is the head (water level) at the orifice mouth, set as the depth of water leaving the reach segment upstream of the sinkhole (L).
The discharge from the sinkholes and infiltration from the soil profile bottom were then added to the deep aquifer reservoir in SWAT, aggregated at HRU level, and transferred to the spring outlet using the SSRA algorithm with a maximum travel time of one day. The number of the subbasin in which the sinkholes are located and the diameter of the sinkholes were specified in an input file called *sink.dat*, while groundwater basins that drain the aquifer water to the spring were defined in a file called *gw_flow.dat*.

KarstSWAT was calibrated for 3 years using daily streamflow measurements at the Cane Run River, and validated for another 3 years using runoff data at the Cane Run River and spring outlet. Compared to the original SWAT model, KarstSWAT showed a better representation of the hydrological cycle in the karst watershed. The average annual surface runoff and recharge to shallow aquifer decreased by 65% and 91%, respectively, while deep aquifer recharge increased many folds as water was partially diverted through the sinkholes rather than the soil. The cumulative observed and simulated streamflow plots, with and without sinkholes, also demonstrated that KarstSWAT reduced channel flow during low flow and high flow periods. The modified model performance was further assessed against the original SWAT model under a multitude of runoff events during which at least 10 mm of peak rainfall was observed. Results showed that KarstSWAT improved the prediction of the peak flows and baseflow, with average the NSE and R^2 values increasing from 0.23 to 0.77 and 0.78 to 0.87, respectively. Moreover, the discrepancy between the observed and simulated spring flow was attributed to the capacity of the orifices to transfer flow, whereby the overestimation of streamflow by KarstSWAT resulted in the underestimation of spring discharge and vice versa. Nonetheless, discharge at the watershed spring was continuously simulated, showing a good agreement with the observed spring hydrographs at different time periods.

Zhou et al. (2022) also modified SWAT (v2012) to simulate fast infiltration through karst sinkholes in the upper course of the South Panjiang River, Southwest China. The basin extends over an area of 2,762 km^2 that is mainly covered by limestone and under the influence of a subtropical humid monsoon climate. Due to the karst effect, sinkholes have formed across the

watershed subbasins as opposed to only in the streambed (the case of the study the Cane Run watershed, Palanisamy and Workman., 2015).

The authors used the pond module of SWAT to represent the sinkhole processes. While infiltration from the bottom of the soil profile in both karst and non-karst areas is modeled using the same delay time variable in the original SWAT, the recharge function was modified to simulate the rapid recharge of groundwater aquifer in sinkholes. Water leaving the ponds to the aquifer was separated from percolation with a delay time variable specific to pond leakage and set to 1/50 of its original value. Hence, recharge was divided into two components: leakage recharge of the soil profile and rapid recharge of the karst sinkholes (Equation (9)).

$$rchrg(j) = \left(1 - e^{-\frac{1}{delay}}\right)\left(sepbtm_{(j)} + gwq_{ru(j)}\right) + \left(1 - e^{-\frac{\frac{1}{delay}}{50}}\right) * rchrg_{karst} + \left(e^{-\frac{\frac{1}{delay}}{50}}\right) rchrg_1 \quad (9)$$

where $rchrg(j)$ is the daily recharge to the shallow aquifer (mm $H_2O.day^{-1}$), $delay$ is the groundwater delay time required for the water to infiltrate from the soil bottom to the aquifer (days), $sepbtm_{(j)}$ is the daily percolation from the bottom of the soil profile (mm $H_2O.day^{-1}$), $gwq_{ru(j)}$ is the daily groundwater contribution to streamflow (mm $H_2O.day^{-1}$), $rchrg_{karst}$ is the amount of water seeping through the ponds (mm $H_2O.day^{-1}$), and $rchrg_1$ is the recharge from the previous day (mm $H_2O.day^{-1}$).

The pond module was added at the subbasin scale, and sinkholes were represented by one pond in each subbasin whereby a fraction of the subbasin area drains the surface flow into the pond. A high hydraulic conductivity value was set at the bottom of the ponds in order to maximize infiltration and groundwater recharge.

The SWAT model was adjusted using monthly streamflow data, with 2 years of warm-up, calibration, and validation each. The modified SWAT model improved the streamflow simulations: the values of the NSE and R^2 indicators increased from 0.35−0.66 (calibration-validation) and 0.7−0.76, respectively, in the original SWAT to 0.61−0.79 and 0.74−0.83 in the modified SWAT, with a higher prediction accuracy of the peak flow and baseflow at the daily time interval. The use of the pond module, with large hydraulic conductivity values and short recharge durations, also reduced the surface runoff and lateral flow in the subbasins with sinkholes and increased baseflow depth by rapidly diverting the surface water to the shallow aquifer.

3.3.2.2 Conceptual Linear Two-Reservoir Model

Nikolaidis et al. (2013) interfaced SWAT with a spreadsheet version of the linear two-reservoir model proposed by Kourgialas et al. (2010) to simulate discharge and nitrate transport in the Koiliaris River basin (132 km^2) in Crete, Greece, under climate change. The modified SWAT model, known as Karst-SWAT, comprises an upper reservoir representative of the fast flow in the conduits and a lower reservoir for the slow flow in the matrix and narrow fractures. The model uses two proportionality coefficients to partition karst recharge between the two compartments and models another flow fraction from the upper to the lower reservoir. The sum of outflows from the matrix and conduit reservoirs forms the total discharge of the karstic area (see Equations (10) to (14)).

$$Q_{in,up} = \alpha_1 \times Q_{in\_deepGW} \quad (10)$$

$$Q_{in,low} = (1 - \alpha_1) \times Q_{in\_deepGW} + \alpha_2 Q_{up} \quad (11)$$

where $Q_{in,up}$ and $Q_{in,low}$ represent the water inflows to the upper and lower reservoirs (mm $H_2O.day^{-1}$), respectively, Q_{in_deepGW} is the deep groundwater flow from SWAT (mm $H_2O.day^{-1}$), α_1 is the fraction of deep groundwater flow entering the upper reservoir, α_2 is the fraction of flow from the upper reservoir to the lower reservoir, and Q_{up} is the outflow of the upper reservoir (mm $H_2O.day^{-1}$).

$$Q_{up} = Q_{up-1} e^{-k_u t} + \left(\alpha_1 Q_{in\_deepGW}\right)(1 - e^{-k_u t}) \quad (12)$$

$$Q_{low} = Q_{low-1} e^{-k_l t} + \left[(1 - \alpha_1) Q_{in\_deepGW} + \alpha_2 Q_{up}\right](1 - e^{-k_l t}) \quad (13)$$

$$Q_T = (1 - \alpha_2) Q_{up} + Q_{low} \quad (14)$$

where Q_T is the total spring discharge (mm $H_2O.day^{-1}$), Q_{up} and Q_{low} represent the outflows of the upper and lower reservoirs (mm $H_2O.day^{-1}$), respectively, Q_{up-1} and $Q_{lower-1}$ are the values of Q_{up} and Q_{low} at the previous time step (mm $H_2O.day^{-1}$), respectively, k_u and k_l are the recession coefficients of the upper and lower reservoirs (day^{-1}), respectively, Q_{in_deepGW} is the deep groundwater flow from SWAT (mm $H_2O.day^{-1}$), α_1 is the fraction of deep groundwater flow entering the upper reservoir, α_2 is the fraction of flow from the upper reservoir to the lower reservoir, and t is the time step (1 day).

In the case of the Koiliaris River basin, the recharge area of the springs contributing to the total watershed flow extends at least 50 km^2 beyond its boundaries. Nikolaidis et al. (2013) first used SWAT to model the surface hydrological processes (precipitation, evapotranspiration, infiltration, runoff) and route the percolated water to the deep groundwater aquifer. The extent of karst areas contributing to the emergence of springs from outside the watershed boundaries was established based on the geologic knowledge of the study site and a mass balance modeling approach. Then, the SWAT-simulated deep groundwater flow in karst areas was assigned to the karstic reservoir model in order to estimate the spring flow contribution to discharge. After calibration of the reservoir model parameters, the resultant karst flow time series were input to SWAT as a point source to simulate the overall watershed runoff.

The parameters of the karst flow reservoir and SWAT models were adjusted using high frequency flow measurements at the watershed outlet, surface runoff measurements at a major tributary of the river, and long-term monthly spring flow records. The overall model prediction efficiency of discharge was satisfactory. At the monthly time step, NSE values of 0.77−0.61, PBIAS of -22.1%; -11.8%, and RSR of 0.62−0.63 were reached during calibration and validation, respectively, whereas NSE of 0.62-0.43, PBIAS of (-22.3%; -11.6%), and RSR of 0.48−0.75 were achieved for the daily runoff simulations.

From the water quality perspective, Nikolaidis et al. (2013) incorporated a nitrate mass balance model to the upper and lower reservoirs of the karst flow model, assuming that nitrate is conservative in karst. A karst factor was added to the nitrate mass balance equation of the lower reservoir to account for the extra dilution of the incoming nitrate loads by the permanent karst flow volume below the spring level. After calculating the nitrogen inputs in the watershed and the extended karst recharge area based on the local land-use practices, the hydrological and water quality modeling parameters were adjusted using nitrates grab sample data at a river tributary and groundwater wells, coupled with high frequency nitrate data, grab samples at the watershed outlet, and flow measurements. The simulated nitrate concentrations were adequate compared to the nitrate grab sample measurements.

The impact of climate change on the water budget of the Koiliaris River basin was also predicted up to the year 2050, using three climate change scenarios for a combination of general and regional circulation climate models. The results of the climatic projections suggested that

precipitation, evapotranspiration, and runoff could decrease by 17%, 8%, and 22%, respectively, for the time horizon 2030−2050 compared to 2010−2029.

Nerantzaki et al. (2015) later adopted the Karst-SWAT flow model by Nikolaidis et al. (2013) to first simulate the hydrology and suspended sediment transport in the Koiliaris River basin then predict the impacts of climate change on discharge, soil erosion, and sediment transport. The concentration of suspended sediments in the karstic watershed was calculated using the same mass balance equations and deep karst factor adopted by Nikolaidis et al. (2013) for nitrates. Four additional years of simulation were added to the validation period of the model previously calibrated by Nikolaidis et al. (2013). Next, climate change scenarios were run up the year 2090 after adjusting the most sensitive flow and water quality parameters. The results of the discharge simulations were adequate, with daily NSE, PBIAS, and RSR of 0.8, 25.3%, and 0.45, respectively, and monthly NSE, PBIAS, and RSR of 0.83, 23.4%, and 0.41, respectively. The suspended sediments calibration results were less adequate, with daily NSE of 0.7, PBIAS of 57%, and RSR of 0.55, suggesting an overestimation bias.

The results of the climate change scenarios showed that surface runoff and spring flow could decrease by nearly 70 to 77% between the time periods of 2010−2049 and 2050−2090. The erosion rate of the watershed main subbasin and surface sediments export were also expected to drop by 48% and 55%, respectively, whereas sediments emerging from the springs were not substantially affected by climate change.

Following an analysis of climate change impacts in the Crete Island using Karst-SWAT, Demetropoulou et al. (2019) proposed a program of measures to improve water governance in the 525 km^2 Geropotamos basin located in central-southern part of the island. Nerantzaki et al. (2019) also used Karst-SWAT to forecast the hydrological response of the Crete region under climate change scenarios up to the year 2098, considering different irrigation sources in SWAT. Moreover, Tapoglou et al. (2019) applied Karst-SWAT to predict the impact of climate change on the hydrological cycle and the frequency of extreme hydrological and meteorological events in Crete. Nerantzaki et al. (2020) further expanded the research work conducted in the Koiliaris River basin with Karst-SWAT by assessing: (1) the uncertainty of the watershed runoff and karstic flow simulations due to the parameter uncertainty in SWAT and Karst-SWAT, and (2) the impact of internal variability (or stochastic uncertainty) of the meteorological input data on the flow simulations for the reference period and under the climate change scenarios. The uncertainty of

the flow models was estimated by combining the Sequential Uncertainty Fitting Version 2 (SUFI-2) in the SWAT Calibration and Uncertainty Program (SWAT-CUP) interface and the @RISK by PALISADE software, while the effect of input internal variability on the flow output was evaluate using Monte Carlo simulations.

Within the framework of studying the hydrological and geochemical processes in the Koiliaris European Critical Zone Observatory, Lilli et al. (2020a) used Karst-SWAT to simulate the hydrological budget of the Koiliaris River basin and gain insight on the hydrological pathways and response of the karst during extreme events. Additionally, Karst-SWAT was applied to simulate surface flow and spring flow in the Koiliaris River basin, which were required to determine the design flows and flood frequency within the framework of developing nature-based solutions for the riparian forest restoration and flood protection project at the Koiliaris Critical Zone Observatory (Lilli et al., 2020b).

Malagò et al. (2016) developed a two-reservoir modeling approach by linking SWAT-B&B (Baffaut and Benson, 2009) and Karst-SWAT (Nikolaidis et al., 2013). The resultant hybrid model, called KSWAT, was used in conjunction with SWAT to simulate the water balance, spring flow, and total discharge in the Island of Crete in Greece. The study area extends over 8,336 km^2 of which 2,730 km^2 is karst.

A SWAT model of the Crete Island was set up and the modified model KSWAT was applied only in the karst subbasins of the region. The daily aquifer recharge from the karst subbasins was simulated using SWAT-B&B. The area of the subbasins contributing to the recharge of a particular spring or group of springs was identified based on the local geological maps and dominant karst soils. Recharge from the soil profile bottom, stream losses, and seepage from other water bodies to the deep aquifer were maximized by: (1) setting the deep aquifer percolation fraction and minimum groundwater delay to 1, (2) adjusting the groundwater coefficient of capillary rise to 0.1 to prevent the upward movement of water to the unsaturated zone, and (3) minimizing the return flow from the shallow and deep aquifers in SWAT. The deep aquifer recharge time series generated by SWAT-B&B were then input to Karst-SWAT in order to simulate and calibrate the discharge of the springs. The parameters of the Karst-SWAT model were adjusted based on daily spring discharge data from 47 gauging stations in Crete.

The hydrologic model in SWAT was adjusted using a step-wise calibration with monthly streamflow data at 15 stream gauging stations. Snow, surface runoff, lateral flow, and baseflow

parameters were first calibrated separately in order to adjust the timing of the runoff signal and the discharge values (peak flow and baseflow). Then, the model was recalibrated based on the streamflow-related parameters combined with the adjusted variables of the other water budget components. The final near optimal parameter set of the calibrated subbasins was transferred to the ungauged subbasins using the hydrological similarity approach with the Partial Least Squares Regression, in order to identify similar subbasins based on the correlation between the watershed and discharge characteristics.

Subsequently, the calibrated spring discharge time series from Karst-SWAT were added to the Crete SWAT model as point sources in order to predict the total monthly runoff across the island, and a final calibration was performed to adjust discharge. The results of the performance indicators showed that only 40% of the calibrated gauging stations scored NSE values greater than 0.5, while 50% had R^2 values higher than 0.5 and 64% reached PBIAS lower than 25%.

Nguyen et al. (2020) added a two-reservoir karstic flow model to the original groundwater module of SWAT. The improved SWAT code, termed SWAT_IFG, consists of two conceptual groundwater models compiled in a single executable file: (1) the standard SWAT one-reservoir model applied to non-karst terrains, and (2) the modified two-reservoir model used in karst areas. The two-reservoir groundwater model of SWAT_IGF represents a variant of the Karst-flow model by Nikolaidis et al. (2013). In SWAT_IGF, the matrix reservoir receives diffuse recharge as a linear function of daily infiltration from the soil bottom, considering the time delay of flow in the unsaturated zone (Equations (15) and (16)):

$$W_{rd,i} = \left[\left(1 - e^{-\frac{1}{\delta_{gw}}}\right) W_{seep,i}\right] \times \boldsymbol{\beta} + \left(e^{-\frac{1}{\delta_{gw}}}\right) W_{rd,i-1} \quad (15)$$

where $W_{rd,i}$ and $W_{rd,i-1}$ (mm $H_2O.day^{-1}$) represent the amount of diffuse recharge to the matrix reservoir on day i and $i - 1$, respectively, δ_{gw} is the delay time for the infiltrated water to reach the matrix storage reservoir (days), β is a recharge separation factor (0-1), $W_{seep,i}$ is the total amount of water exiting the bottom of the soil profile on day i (mm $H_2O.day^{-1}$).

$$Q_{in_{matrix,i}} = \sum_{j=1}^{nhrus} W_{rd,i,j} \times a_j * 10^{-3} \quad (16)$$

Where $Q_{in_{matrix,i}}$ (m^3 $H_2O.day^{-1}$) is the total volume of diffuse recharge to the matrix reservoir on day i, $W_{rd,i,j}$ (mm $H_2O.day^{-1}$) and a_j (m^2) are the diffuse recharge and area of HRU number j,

respectively, 10^{-3} is a unit conversion factor from mm H_2O to m H_2O, and $nhrus$ is the number of HRUs in the recharge area.

The conduit reservoir receives another fraction of the soil water seepage as concentrated recharge with infiltration losses from sinking streams. It is also fed by diffuse discharge from the matrix reservoir, which represents the flow exchange mechanism between the two karst domains (Equations (18) and (19)). Groundwater outflow from the matrix storage reservoir to the conduit is modeled using a linear storage-discharge equation with a matrix recession coefficient (Equation (17)).

$$Q_{matrix,i} = Q_{matrix,i-1}\left(e^{-\alpha_{matrix}\Delta t}\right) + \left(1 - e^{-\alpha_{matrix}\Delta t}\right)\sum_{j=1}^{nhrus} W_{rd,i,j} * a_j * 10^{-3} \quad (17)$$

where $Q_{matrix,i}$ and $Q_{matrix,i-1}$ are the outflows from the matrix storage reservoir on day i and $i-1$ (m^3 $H_2O.day^{-1}$), respectively, α_{matrix} is the recession constant of the matrix storage reservoir (day^{-1}), Δt is the time step (1 day), $W_{rd,i,j}$ (mm $H_2O.day^{-1}$) and a_j (m^2) are the diffuse recharge and area of HRU number j, respectively, 10^{-3} is a unit conversion factor from mm H_2O to m H_2O, and $nhrus$ is the number of HRUs in the recharge area.

$$W_{rc,i} = (1-\beta)W_{seep,i} \quad (18)$$

where $W_{rc,i}$ (mm $H_2O.day^{-1}$) is the concentrated recharge from closed depressions, fractures, and sinkholes to the conduit storage reservoir on day i β is a recharge separation factor (0-1), and $W_{seep,i}$ is the total amount of water exiting the bottom of the soil profile on day i (mm $H_2O.day^{-1}$).

The total volume of concentrated recharge $Q_{in,conduit}$ (m^3 $H_2O.day^{-1}$) to the conduit reservoir on day i is calculated as follows:

$$Q_{in,conduit} = \sum_{j=1}^{nhrus} W_{rc,i,j} * a_j * 10^{-3} + rttlc_i + Q_{matrix,i} \quad (19)$$

where $Q_{in,conduit}$ (m^3 $H_2O.day^{-1}$) is the total volume of concentrated recharge to the conduit reservoir on day i, $Q_{matrix,i}$ is the outflow from the matrix storage reservoir on day i, $rttlc_i$ is the recharge from losing streams on day i (m^3 $H_2O.day^{-1}$), Δt is the time step (1 day), $W_{rc,i,j}$ (mm $H_2O.day^{-1}$) and a_j (m^2) are the concentrated recharge and area of HRU number j, respectively,

10^{-3} is a unit conversion factor from mm H_2O to m H_2O, and $nhrus$ is the number of HRUs in the recharge area.

Outflow from the conduit reservoir to the spring is also modeled via a linear storage-discharge relationship adjusted for the total recharge volume to the conduits and a conduit recession coefficient (Equation (20)). The total discharge of the basin where the spring is located is then simulated as the sum of the direct runoff (surface runoff and lateral flow) and the outflow from the conduit reservoir to the spring (Equation (21)):

$$Q_{conduit,i} = Q_{conduit,i-1}\left(e^{-\alpha_{conduit}\Delta t}\right) + \left[\sum_{j=1}^{nhrus} W_{rc,i,j} \times a_j \times 10^{-3} + rttlc_i + Q_{matrix,i}\right]\left(1 - e^{-\alpha_{conduit}\Delta t}\right) \quad (20)$$

where $Q_{conduit,i}$ and $Q_{conduit,i-1}$ are the outflows from the conduit storage reservoir on day i and i – 1 (m^3 $H_2O.day^{-1}$), respectively, $\alpha_{conduit}$ is the recession constant of the conduit storage reservoir (day^{-1}), $rttlc_i$ is the amount of recharge from losing streams on day i (m^3 $H_2O.day^{-1}$), Δt is the time step (1 day), $W_{rc,i,j}$ (mm $H_2O.day^{-1}$) and a_j (m^2) are the concentrated recharge and area of HRU number j, respectively, 10^{-3} is a unit conversion factor from mm H_2O to m H_2O, and $nhrus$ is the number of HRUs in the recharge area.

The total runoff $Q_{river,i}$ (m^3 $H_2O.day^{-1}$) of the basin at the location of the spring is calculated as follows:

$$Q_{river,i} = Q_{conduit,i} + Q_{direct,i} \quad (21)$$

Where $Q_{river,i}$ (m^3 $H_2O.day^{-1}$) is the total runoff of the basin at the location of the spring $Q_{direct,i}$ is the daily direct runoff calculated as the sum of the surface runoff and lateral flow from the basin where the spring is located (m^3 $H_2O.day^{-1}$), and $Q_{conduit,i}$ is the outflow from the conduit storage reservoir on day i (m^3 $H_2O.day^{-1}$).

SWAT_IGF was applied to simulate discharge in the drainage basin of the karst dominated southern Harz rim and non-karst southwest Harz Mountains in Northern Germany. The watershed covers an area of 384 km^2 and has one river outlet and a main spring outlet (the Rhume spring). The spring is mainly fed by allogenic recharge and river transmission losses from upstream subbasins via a connected network of losing streams in the area, with only 4% of the spring discharge originating from autogenic recharge and nearly 96% from IGF. When applying SWAT_IGF, an aquifer classification map with information about the aquifer types and spring

recharge area in the study site was incorporated into the model to delineate karst and non-karst HRUs. Subsequently, the suitable conceptual reservoir model could be assigned (the two-reservoir model for the karst HRUs and the one-reservoir model for the non-karst HRUs), and recharge from the extended karst area could be routed to the spring outlet.

SWAT_IGF was run for 14 years at the daily time step, with 3 years of warm-up, 6 years of calibration, and 5 years of validation. The model parameters were fitted based on multi-site daily streamflow data and satellite-derived actual evapotranspiration records (the Moderate Resolution Imaging Spectroradiometer MOD16 ETa). A multi-criteria NSE objective function was used to assess the overall performance of the model simulation, with equal weights allocated to the multi-gauge streamflow observations and evapotranspiration data. Results showed that the use of MOD16 ETa data in the calibration did not affect the model performance. The flow simulation at the spring outlet improved with multi-gauge calibration, as the NSE values varied from 0.75−0.48 (calibration-validation) with the single gauge calibration to 0.69−0.62 under the multi-site calibration. The model performance for all remaining streamflow gauging stations also improved with multi-site calibration, and NSE values of 0.54−0.91 and 0.6−0.91 were reached for the calibration and validation periods, respectively. Additionally, the model prediction uncertainty was reduced. The PBIAS values calculated at the different gages fell below 10%, while KGE values ranged between 0.68 and 0.91. Yet, the observed and simulated streamflow hydrographs showed that SWAT_IGF underestimated the high and low flows, which is a property inherited from the original SWAT model. Nonetheless, the model successfully simulated IGF and transmission losses from the rivers contributing to the spring discharge.

3.3.2.3 Conceptual Linear Three-Reservoir Model

Wang et al. (2019b) coupled SWAT (v2012) with a linear three-reservoir model. The modified model consists of: (1) an upper reservoir that reproduces the regulation and storage function of the epikarst and is recharged by percolation from the soil bottom, (2) a middle reservoir that represents the conduits system fed by infiltration from the epikarst, depressions, and avens, and (3) a lower reservoir corresponding to the matrix system recharged by the epikarst and conduit reservoirs. Daily infiltration to the upper reservoir is simulated as a function of the saturation moisture content in the epikarst system, its water-holding content, and saturated hydraulic conductivity (Equations (22) and (23)).

$$TT = \frac{sat - f_c}{k} \quad (22)$$

where TT is the attenuation coefficient, sat is the saturation moisture content in the epikarst system (mm H_2O), f_c is the water holding capacity in the epikarst system (mm H_2O), and k is the saturated hydraulic conductivity (mm.hour^{-1}).

$$Q_i = W_{st}\left(1 - e^{\frac{-t}{TT}}\right) \quad (23)$$

where Q_i is the water infiltrated through the epikarst on a given day (mm H_2O.day^{-1}), W_{st} is the water content in the epikarst which varies in function of the daily percolation from the soil bottom (mm H_2O.day^{-1}), and t is the simulation time step (1 day), and TT is the attenuation coefficient.
To simulate the intercompartment fluxes, a proportionality coefficient (α_1: 0.5-1) is introduced to separate the recharge from the epikarst reservoir between the quick flow and slow flow reservoirs, based on the degree of karstification of the watershed. Another coefficient (α_2: 0.1-0.5) is used to split the discharge from the conduit reservoir between the slow flow reservoir and the basin outlet (Equations (24) and (25)):

$$Q_{in,up} = \alpha_1 Q_i + Q_C \quad (24)$$

$$Q_{in,low} = (1 - \alpha_1)Q_i + \alpha_2 Q_{up} \quad (25)$$

Where $Q_{in,up}$ and $Q_{in,low}$ represent the daily recharge values to the upper and lower reservoirs, respectively, Q_i is the water infiltrated through the epikarst on a given day i, Q_C is the injection volume from the depression and aven (all variables are expressed in mm H_2O.day^{-1}).

The outflows from the conduit and matrix reservoirs are modeled using the standard attenuation functions of SWAT (Equations (26) and (27)).

$$Q_{up} = Q_{up-1}\left(e^{-k_u t}\right) + (\alpha_1 Q_i + Q_C) * \left(1 - e^{-k_u t}\right) \quad (26)$$

$$Q_{low} = Q_{low-1}\left(e^{-k_l t}\right) + \left[(1 - \alpha_1)Q_i + \alpha_2 Q_{up}\right] * \left(1 - e^{-k_l t}\right) \quad (27)$$

where Q_{up} and Q_{low} are the daily discharge values of the upper and lower reservoirs (mm H_2O.day^{-1}), Q_{up-1} and $Q_{low-1}$are the discharge values of the upper and lower reservoirs on the previous day (mm H_2O.day^{-1}), Q_i is the water infiltrated through the epikarst on a given day (mm H_2O.day^{-1}), Q_C is the recharge from the depression and aven (mm H_2O.day^{-1}), α_1 is the coefficient of proportionality for infiltration from the epikarst to the upper reservoir, and α_2 is the coefficient of

proportionality for infiltration from the upper to the lower reservoir, and k_u and k_l are the recession coefficients of the upper and lower reservoirs (day^{-1}), respectively.

Finally, the total karst flow is calculated as the sum of the discharge components of the matrix and conduit reservoirs (Equation (28)), which is then added to the surface runoff to simulate the total discharge at the watershed outlet.

$$Q_T = (1 - \alpha_2)Q_{up} + Q_{low} \quad (28)$$

where Q_T is the total contribution of the reservoirs to streamflow (mm H_2O.day^{-1}), Q_{up} and Q_{low} represent the discharge components from the upper reservoir and lower reservoirs (mm H_2O.day^{-1}), respectively, and α_2 is the coefficient of proportionality for infiltration from the upper to the lower reservoir.

The original and modified SWAT models were applied to predict daily runoff for a fully karstified watershed of 26.76 km^2 located in Hunan Province, China, with a calibration period of 180 days and a validation period of 100 days. The study area is primarily covered by Devonian and Carboniferous limestone and exhibits karst depressions, caves, and underground rivers. The SWAT three-reservoir model yielded a streamflow simulation that was significantly better than that obtained by the standard SWAT model in both calibration and validation, with NSE values increasing from 0.57−0.63 to 0.81−0.83 and R^2 values increasing from 0.58−0.62 to 0.82−0.84.

Geng et al. (2021) later modified the SWAT model proposed by Wang et al. (2019b) in order to improve the simulation of rapid recharge to the epikarst reservoir through direct water percolation from the soil bottom without attenuation. The modelers also added a discharge component from the epikarst reservoir to the river channels. Three coefficients of proportionality were thus introduced to the three-reservoir groundwater model in order to separate the flow from the epikarst reservoir between a surface runoff component and two recharge components to the matrix and conduit reservoirs (Equations (29) to (31)).

$$Q_{kr} = (1 - K_d)twlpnd + K_d Q_{kr0} \quad (29)$$

where Q_{kr} and Q_{kr0} represent the recharge of karst groundwater on a given day and the day before (mm H_2O.day^{-1}), respectively, $twlpnd$ represents pond leakage (mm H_2O.day^{-1}), and K_d is the flow delay coefficient in the karst groundwater recharge from sinkholes (days).

$$\begin{cases} Q_i = Q_{i,0}\left(e^{-\alpha_i \Delta t}\right) + Q_{in,i}\left(1 - e^{-\alpha_i \Delta t}\right) \\ Q_{in,up} = Q_{seep} \\ Q_{in,mid} = Q_{kr} + \beta_1 Q_{up} \\ Q_{in,low} = \beta_2 Q_{up} + \beta_3 Q_{mid} \\ i = up, mid, low \end{cases} \quad (30)$$

where Q_i is the discharge of reservoir i on a given day (mm $H_2O.day^{-1}$), i denotes the reservoir (one of the upper, middle, and lower reservoirs), $Q_{in,i}$ is the daily recharge to reservoir i (mm $H_2O.day^{-1}$), α_i is the recession constant of reservoir i (day^{-1}), Δt is the time step (1 day), $Q_{i,0}$ is the discharge of reservoir i on the previous day (mm $H_2O.day^{-1}$), Q_{kr} is the karst groundwater recharge on a given day (mm $H_2O.day^{-1}$), Q_{seep} the daily infiltration recharge from the soil bottom (mm $H_2O.day^{-1}$), and β_1, β_2, and β_3 are coefficients of proportionality.

$$Q_T = (1 - \beta_1 - \beta_2)Q_{up} + (1 - \beta_3)Q_{mid} + Q_{low} \quad (31)$$

where Q_T is the total discharge of karst groundwater Q_T (mm $H_2O.day^{-1}$), Q_{up}, Q_{mid} and Q_{low} represent the outflows from the upper, middle, and lower reservoirs (mm $H_2O.day^{-1}$), respectively, and β_1, β_2, and β_3 are coefficients of proportionality.

Rapid infiltration through sinkholes, ponors, and fractures was also replaced by pond leakage with concentrated (fast) recharge similar to the computational method proposed by Baffaut and Benson (2009). The remaining intercompartment fluxes were modeled similarly to the model by Wang et al. (2019b).

The modified SWAT model was applied to simulate the hydrological cycle processes in the Daotian River basin, including the contribution of the streamflow and baseflow components to the runoff at the watershed outlet. The study site is situated in the Guizhou Province, China, and has a temperate monsoon climate. It covers a total area of 99.21 km^2 of which ~53% is dolomite, ~38% limestones, and ~9% clastic rocks. The karst landscape is characterized by karst depressions, sinkholes, and well-connected networks of conduits of high hydraulic conductivity, particularly in the limestone area. Due to karst effects, the watershed recharge boundaries extend by 24.75 km^2 beyond its surface drainage area, and the additional water is discharged into the watershed through underground conduits. The areas outside the topographic drainage divides and the flow paths of the karst subterranean rivers that exist in the watershed were determined by conducting a karst survey and an artificial tracer test prior to hydrological modeling. After determining the flow paths of the subterranean river based on the spatial distribution of the

subterranean river inlet, ponors, and sinkholes, the DEM data were modified to convert the subterranean river into a surface river. By adopting this approach, the actual catchment boundaries of the watershed were correctly identified by SWAT for the subbasins delineation.

The modified SWAT model was calibrated using daily streamflow measurements at the watershed outlet for 6 years (1993−1998). Two validation periods were considered under various annual precipitation patterns: the first from 1999 to 2002 (normal, dry, and wet years) and the second from 2003 to 2006 (normal and dry years). The performance of the modified SWAT model was compared to that of a previous model run in SWAT at monthly time scale. Both models had satisfactory simulations of monthly discharge. Yet, the modified SWAT model had a better prediction efficiency than the original SWAT, scoring NSE values of 0.87-0.83/0.85, R^2 of 0.88-0.84/0.86, and PBIAS of 2.5% – (-1.9%/-15%) for the calibration and two validation periods, respectively. The three-reservoir model also improved the simulation of the karst water cycle by increasing the groundwater recharge and return flow components. As a result, the NSE for the baseflow simulation of the modified SWAT model was 0.09 higher than that of the original SWAT model, which underestimated flows below 0.7 $m^3.s^{-1}$ in the dry periods and overestimated runoff during wet periods.

3.3.2.4 Conceptual Non-linear One-reservoir Model

Wang and Brubaker (2014) replaced the linear reservoir model in SWAT with a single non-linear reservoir based on the algorithm of Wittenberg (1994) (Equations (32) and (33)), providing a modified SWAT version called ISWAT. The ISWAT model was tested in the Shenandoah River watershed of the Potomac River basin (USA), which drains a large karstic area of 7,607 km^2. It was calibrated using 13 years of daily discharge records across 14 gauging stations, with 2 years of warm-up, and validated for 4 years. To account for the spatial variability of the geology and soils in the watershed during calibration, the parameters of the non-linear reservoir (i.e., groundwater recession coefficients and exponents) were grouped by soil type.

$$S_{sh} - S_{sh,min} = \frac{1}{\alpha_{gw}} {Q_{gw}}^{\beta_{gw}} \tag{32}$$

$$Q_{gw} = \left(\alpha_{gw}\left(S_{sh} - S_{sh,min}\right)\right)^{1/\beta_{gw}} \tag{33}$$

where S_{sh} is the shallow aquifer storage (L), $S_{sh,min}$ is the minimum storage for groundwater flow to occur (L), α_{gw} is a scale parameter $\left(T^{\beta} L^{3(1-\beta)}\right)$, β_{gw} is a dimensionless coefficient. If β_{gw} = 1, the non-linear model becomes linear.

The ISWAT model performance was assessed against that of the linear SWAT model by comparing the simulated and observed streamflow hydrographs at the different gauging stations, and the recession curves in the low flow periods with the baseflow taken as the lowest 30% of daily discharge. The non-linear ISWAT model reproduced low flow discharge and recession curves better than SWAT, but simulated peak flows with a comparable accuracy to SWAT. The NSE (modified) and R^2 indices improved with the use of the non-linear model at the level of eight and ten observational river reaches, respectively, with values of 0.5 and 0.6. The non-linear model also lowered the overall relative bias of the simulations by 3%, with the majority of the observational river reaches scoring a bias less or equal to 10%.

3.3.2.5 Modified Crack Flow with Conceptual Linear One-Reservoir Model

Eini et al. (2020) modified SWAT (v2012) to increase groundwater recharge in karst areas by: (1) adjusting the groundwater recharge function in SWAT to increase infiltration in karst HRUs (the SWAT-ML model), and (2) expanding the crack flow module in SWAT to retain the formation of cracks independently of soil moisture conditions (the SWAT-CF model). These modifications were based on the premise that preferential flow through the soil sinks and cracks can be representative of rapid recharge in karst landforms. Both SWAT-ML and SWAT-CF were applied in the Maharlu Lake, a large watershed of 4,270 km^2 in Southwest Iran, of which 37% is covered by extensive karst areas (limestone and dolomite). Several karst-fissured aquifers are well developed in these areas due to lithology, climate, and tectonic activity.

In SWAT-ML, infiltration from non-karst areas was calculated using the standard SWAT recharge equation (Equation 34)), while fast infiltration from karst areas was modeled by dividing the delay variable in the original groundwater recharge equation by a new non-dimensional calibration parameter (X) (Equation (35)), which can be increased depending on the volume and numbers of cracks in a karst HRU:

$$rchrg_{(j)} = \left(1 - gw_{delay(j)}\right) * \left(sepbtm_{(j)} + gwq_{ru(j)}\right) + gw_{delay(j)} * rchrg_1 \quad (34)$$

$$rchrg_{karst(j)} = \left(1 - e^{\frac{-1}{\frac{gw_{delay(j)}}{X}}}\right)\left(sepbtm_{(j)} + gwq_{ru(j)}\right) + \left(e^{\frac{-1}{\frac{gw_{delay(j)}}{X}}}\right) rchrg_{karst1} \quad (35)$$

where $rchrg_{(j)}$ and $rchrg_{karst(j)}$ represent the daily recharge values from non-karst and karst HRUs (mm $H_2O.day^{-1}$), respectively, j denotes the HRU number, $gw_{delay(j)}$ is the recharge delay

time (days), $sepbtm_{(j)}$ is the daily percolation from the bottom of the soil profile (mm $H_2O.day^{-1}$), $gwq_{ru(j)}$ represents the seepage from the lakes, wetlands, and riverside branches (mm $H_2O.day^{-1}$), $rchrg_1$ and $rchrg_{karst1}$ represent the recharge values from the previous day (mm $H_2O.day^{-1}$), and X is a non-dimensional calibration parameter (1, +∞) used to adjust infiltration rates in karstic HRUs.

In SWAT-CF, the standard SWAT function that calculates crack volume during the crack flow process was modified by adding a new parameter of the crack volume based on new moisture conditions (Equation (36)) to achieve a year-round crack formation in the soil matrix:

$$volcrk_{(l,j)} = crlag * volcrk_{(l,j)} + (1 - crlag) * volcrknew \quad (36)$$

where $volcrk$ is the crack volume for soil layer (mm), $crlag$ is a daily lag factor for crack development, $volcrknew$ is the crack volume for soil layer based on new moisture conditions (mm), j is the HRU number, and l is the counter.

As a result, SWAT-CF can simulate crack flow in karst HRUs both in dry and wet soil conditions during surface flow events, as opposed to standard SWAT, which only models crack volume on drier days as a function of crop capacity and soil moisture.

SWAT, SWAT-ML and SWAT-CF were applied in the Maharlu Lake, a large watershed of 4,270 km^2 in Southwest Iran, of which 37% is covered by extensive karst areas (limestone and dolomite). Several karst-fissured aquifers are well developed in these areas due to lithology, climate, and tectonic activity. The hydrological models developed with SWAT, SWAT-ML, and SWAT-CF were run using streamflow data recorded at 3 gauging stations, with 3 years of warm-up, 26 years of calibration, and 4 years of validation. Both modified SWAT models outperformed SWAT in simulating monthly streamflow at different stations, with SWAT-ML having the best overall accuracy. The average NSE value increased from 0.64 with SWAT to 0.67 using SWAT-CF and 0.69 using SWAT-ML, while the average R^2 value varied from 0.70 to 0.69 and 0.72 under SWAT-CF and SWAT-ML, respectively. The modified models also increased the prediction accuracy of the baseflow and water budget components.

3.3.2.6 Variable Source Area Hydrology with Conceptual Linear One-Reservoir Model

Other relevant applications of SWAT in karst watersheds include the use of Topo-SWAT (initially termed SWAT-VSA), a modified version of SWAT that was applied to simulate flow, sediments yield, and nutrients loads in a watershed with variable source area (VSA) hydrology

(Amin et al., 2017). Compared to SWAT, Topo-SWAT incorporates a topographic wetness index (TI) that indicates the saturation potential of a landscape unit and the subsequent likelihood of runoff generation. Ten equal-area wetness classes ranging from 1 to 10 (1 being 10% of the watershed with the lowest runoff potential, and 10 being 10% of the watershed with the highest runoff potential) were used to overlay a wetness class layer with the soil map of the study site and generate a single GIS layer and associated lookup tables for the SWAT slope class and soil layers.

Topo-SWAT was tested in the Spring Creek watershed in northeastern USA. Spring Creek has a surface water watershed area of 370 km^2 but is defined by a groundwater recharge boundary of 450 km^2, which is characterized by saturation excess surface runoff from VSAs (e.g., perched and losing streams in the headwater regions of the watershed, low surface runoff in the forested uplands due to quick infiltration through shallow soils, overland flow generated at the base of hillslopes). Some of the adjustments made to the model parameters to accurately represent karst hydrology in the study watershed included reducing the initial curve number, restricting the groundwater delay factor to 1 day, setting the baseflow recession factor to 0.011 day based on observed daily streamflow records, and introducing the contribution of the springs that recharge outside Spring Creek but discharge inside the watershed as point sources.

Topo-SWAT outperformed SWAT in modeling daily streamflow for a 12-year simulation period, with NSE of 0.73−0.79, PBIAS of -2.8 to -3.7%, and R^2 of 0.71-0.77 in the calibration and validation periods. Moreover, Topo-SWAT successfully reproduced the VSA hydrology of the watershed using the wetness class distribution approach and predicted water quality adequately.

The calibrated Topo-SWAT model of the Spring Creek watershed was later used to simulate nutrient and sediment loadings under four dairy cropping scenarios of different land areas, feed production, and nutrient input strategies (Amin et al., 2018). The model was also applied to evaluate the impacts of agricultural best management practices on nutrient water quality in the watershed (Amin et al., 2020). Gunn et al. (2021) further modified SWAT-VSA by integrating a daily dynamic time series of CO_2 into the model and implementing changes to the plant subroutines to additionally include flexible stomatal conductance and LAI parameters. The generated models, namely SWAT-VSA_CO2 and SWAT-VSA_CO2+Plant, were used to predict the impacts of climate change with increasing atmospheric CO_2 on the water balance of the Spring Creek watershed.

3.3.3.7 SWAT + Water Accounting Plus (WA+) Framework

Delavar et al. (2020) coupled SWAT with the Water Accounting Plus (WA+) framework, providing a hybrid tool to analyze water resources and support macro and micro water planning in watersheds, based on past, current and future trends in water demand and supply. WA+ uses four sheets to assess water resources in a basin, including resource base, evapotranspiration, productivity, and withdrawal components. In order to populate these sheets with input data generated by hydrological simulation in SWAT, the SWAT source code was modified to: (1) simulate and report the daily groundwater level changes, and (2) model the interactions and exchanges between the aquifers located in different subbasins by overlaying the subbasin HRUs layer and aquifer boundaries during HRUs definition. The SWAT-WA+ tool was used to evaluate the trends in water supply and consumption in the Tashk-Bakhtegan karst watershed (27,520 km^2) in Iran, where 60% of the irrigation demand is met by groundwater. Delavar et al. (2022) remodified SWAT (v2012) and linked it with WA+, adding the crack flow module proposed by Eini et al. [36] with the other modifications previously implemented by Delavar et al. (2020) to link SWAT and WA+. The model was applied to assess different conditions of water supply and demand under wet and dry periods in the karstified Karkheh River basin (42,267 km^2) in Iran.

The customized SWAT-WA+ frameworks, namely SWAT-FARS for the Tashk-Bakhtegan basin and SWAT-Karkheh for Karkheh River basin, were calibrated for streamflow, groundwater levels, evapotranspiration, and crop yields using a multi-stage calibration process. Both models scored NSE and R^2 values higher than 0.5 for the streamflow and groundwater levels simulations in the calibration and validation periods. The outputs of the modified SWAT models were then used to run the WA+ framework. The results of the WA+ assessments revealed that the Tashk-Bakhtegan basin has suffered a decline in the volume of manageable water by more than 20% while irrigation demand increased by more than 50%, and that the volume of manageable water in the Karkheh River basin has dropped while groundwater abstraction increased by 17% due to climate change.

Several SWAT applications showed that accounting for external flows from sinkholes and IGF, in conjunction with the implementation of reservoir models in SWAT, is needed to achieve an adequate representation of karstic flows (Palanisamy and Workman, 2015; Nikolaidis et al., 2013; Nerantzaki et al., 2015; Nerantzaki et al., 2020; Nguyen et al., 2020; Wang et al., 2019b; Amin et al., 2017; Delavar et al., 2020). Overall, coupling SWAT with karst flow models and adding

external functions that reproduce karst features and processes to the SWAT source code have resulted in semi-distributed karstic flow models that simulated discharge with a comparable or better prediction efficiency than standard SWAT (Eini et al., 2020; Palanisamy and Workman, 2015; Wang et al., 2019b; Zhou et al., 2022; Geng et al., 2021; Wang and Brubaker, 2014) while accounting for the dynamics of the different components in a karst system (when applicable).

However, poor daily and monthly performance statistics were still reported by Afinowicz et al. (2005), Baffaut and Benson (2009), and Malagò et al. (2016) following the modification of the SWAT code. These results which suggest that modified approaches applied to the groundwater recharge and reservoir functions in SWAT may not always guarantee a successful simulation of the flow in complex karstic environments. For instance, Afinowiz et al. (2005) indicated that additional modifications to the SWAT flow modules could be required to adequately simulate the large volumes of surface runoff and return flow during flood events as opposed to baseflow during low flow periods. Additionally, we could not identify published studies in which the modified SWAT models were applied across different watersheds, with the exception of the Karst-SWAT model (Nikolaidis et al., 2013) which has been used in the Koiliaris River Basin and the Island of Crete for a multitude of applications (i.e., hydrological and geochemical analyses, climate change impacts, management practices). Thus, one could infer that these models have not been widely tested in other karst basins or they only worked for watersheds with comparable geomorphological and hydrogeological characteristics to the basins in which they were initially applied.

3.4 Recommendations

The modified SWAT models listed in Table 2 can be further improved to have a better representation of karstic heterogeneity and non-linearity in their structure. Highlighting the constraints of these models would be the initial step to enhance their adaptability to other karst watersheds with more complex surface water-groundwater hydrodynamics. First, the Karst-SWAT (Nikolaidis et al., 2013) and KSWAT (Malagò et al., 2016) two-reservoir models do not consider the function of the epikarst and do not explicitly include the diffuse and concentrated recharge components of infiltration from the karstic soils to the deep aquifer reservoir in SWAT. Both models use the exponential decay weighting function to simulate recharge and outflows of the matrix and conduit reservoirs. However, the non-linear models are generally more suitable than the linear ones in representing the hydraulic behavior of karst systems, particularly during low flow periods and flood events (Chang et al., 2015; Eris and Wittenberg, 2015; Jukic and Denic-

Jukic, 2006). Moreover, the two models follow the watershed surface delineation in SWAT to determine the recharge area of the spring, which may not always coincide with the groundwater recharge boundaries. This requires a tedious assessment of the karst areas recharging the springs outside the watershed in tandem with the introduction of the spring flow time series contributing to the watershed discharge as point sources in SWAT to simulate IGF.

Some of the Karst-SWAT and KSWAT modeling constraints were improved in the two-reservoir SWAT_IGF model (Nguyen et al., 2020), which simulates the hydrological processes in non-karst and karst regions as well as IGF in a single executable file. Although SWAT_IGF considers the dual recharge and storage functions in karst systems, it uses the linear storage-discharge relationship to model the outflows of the matrix and conduit reservoirs and does not account for the function of the epikarst either. In SWAT_IGF, the exchange flow rate between the matrix and conduits is simulated as a diffuse net unidirectional flow from the matrix to the conduit. Yet, flow can be transferred from the conduit to the matrix, and vice versa, based on the change in the water level gradient between the two mediums. Additionally, the spring flow contribution to discharge in karst areas is modeled as a single outflow from the conduit reservoir, whereas both the matrix and conduits can contribute to the karst discharge with different flow regimes (slow matrix discharge during low flow periods and fast conduit discharge during heavy rainfall seasons).

Next, the three-reservoir models developed by Wang et al. (2019b) and Geng et al. (2021) incorporate the epikarst, matrix, and conduit functions, and thus represent a complete underground karst system. Yet, their main constraint is that fluxes between the reservoirs are simulated using a linear storage–discharge relationship.

SWAT-B&B (Baffaut and Benson, 2009), SWAT-karst (Yactayo, 2009), KarstSWAT (Palanisamy and Workman, 2015), and the karst model developed by Zhou et al. (2022) can simulate fast infiltration in karst watersheds dominated by spring flow fed by sinkholes. However, they all apply the linear reservoir of SWAT to model groundwater flow without considering the different storage and recharge functions of the main karst components (epikarst, matrix, and conduits). In comparison with SWAT-B&B, SWAT-karst, and the modified SWAT model of Zhou et al. (2022), which all rely on the pond and wetland modules of SWAT for the simulation of flow through the sinkholes, only KarstSWAT can simulate IGF. With KarstSWAT, groundwater basins that drain the aquifer water to the spring can be identified during watershed delineation and

included in a user defined input file to route the total recharge to the spring. Nonetheless, the model may only be applied in karst watersheds where sinkholes are solely located along the river streambed. Using KarstSWAT, it was also assumed that flow from the losing streams directly recharges the deep aquifer through the sinkholes and emerges at the spring within a day, as the length of the flow path from the aquifer to the spring was unknown. Although this assumption was suitable for a specific study basin, additional data on storage, time of travel, and flow diversion pathways would have been required to simulate discharge in other watersheds. The study by Yactayo (2009) corroborates this finding, as field investigations were needed to improve the model performance by determining whether the sinkholes route the flow within the study watershed or divert it outside of the watershed.

The SWAT-ML and SWAT-CF dedicated to watersheds with crack/preferential flow (Eini et a., 2020), the Topo-SWAT specific to watersheds with variable surface area hydrology (Amin et al., 2017), and the SWAT-WA+ models (Delavar et al., 2020, 2022) may be directly applied to basins affected by karst hydrology or other rapid infiltration phenomena. Nevertheless, they do not represent the underground flow dynamics (epikarst-matrix-conduits) of karst aquifers either.

Finally, the non-linear ISWAT model (Wang and Brubaker, 2014) does not account for the diffuse/slow recharge and concentrated/rapid recharge into karst aquifer systems. In addition, it does not explicitly represent the storage and discharge functions of three main subsystems in karst (epikarst, matrix, and conduits) due to the lumped feature of the reservoir model in SWAT.

On the other hand, climate change effects on karst hydrology and water quality were investigated with the modified SWAT models proposed by Nikolaidis et al. (2013), Nerantzaki et al. (2015), Tapoglou et al. (2019), Nerantzaki et al. (2019), and Gunn et al. (2021). Some studies evaluated water resources in a karst watershed for different trends in water supply and consumption (Delavar et al., 2020) as well as the joint impacts of climate change and groundwater withdrawal on water resources availability (Delavar et al., 2022). Other studies simulated in-stream water quality under different agricultural management practices (Amin et al., 2017, 2018, 2020). However, the use of modified SWAT models for the integrated understanding of the critical zone processes and the quantification of the impacts of evapotranspiration and vegetation cover change on karst water resources are still lacking. Among the studies that applied a modified SWAT code in a karst basin (Table 2), Lilli et al. (2020a) confirmed the conceptualization of the two-reservoir karstic system with Karst-SWAT through geomorphologic and tidal analyses. Then, the authors

used Karst-SWAT to simulate the hydrological budget and pathways in the critical zone and investigate the response of karst during extreme events. Nguyen et al. (2020) investigated the impact of evapotranspiration on the hydrological performance of SWAT_IGF by using satellite-derived ETa (Moderate Resolution Imaging Spectroradiometer MOD16 ETa at 8-day time step and 1 km^2 spatial resolution) in tandem with multi-site streamflow calibration. ET was simulated in SWAT_IGF using the Penman-Monteith approach. Results of the NSE index showed that the use of ETa as an additional variable for the calibration of discharge had little to no effect on the model performance in the study watershed, compared with the case in which multi-gauge streamflow calibration was carried out separately. The authors maintained, nonetheless, that these findings should not be generalized to other remote sensing products and to studies in other karst areas, considering more research on the use of ET_a for the calibration of karst hydrological models and streamflow estimation is needed. Moreover, only Afinowicz et al. (2005) used a modified SWAT code to predict the impact of land-use change on the hydrological cycle of a karst area. In particular, the authors developed scenarios for brush control strategies in function of slope, rangeland cover density, and soil depth, to determine the most favorable areas for increasing the watershed water yield. All scenarios of the brush reduction cover resulted in a decrease in evapotranspiration and increases in surface runoff, baseflow, and deep aquifer recharge, with the greatest effect observed on recharge.

Therefore, future research in the realm of karst hydrological modeling should integrate spatially distributed ET data from remote sensing models that account for the dynamics of the land use (Ollivier et al., 2021) with multi-source precipitation data derived from ground-based observations or satellite products (Mo et al., 2022; Zhang et al., 2022). This approach could improve the spatial distribution of aquifer recharge and the overall rainfall-discharge relationship in karstic watersheds. Other areas of future research could include testing the capabilities of the newly released SWAT+ version in simulating discharge in karst watersheds, particularly extreme flows (peak and low flows), and comparing the performance efficiency of SWAT+ to previous SWAT versions. The performance of SWAT should also be compared to other modeling approaches used in karst hydrological applications (Jeannin et al., 2021) in order to improve its representation of the high and low flows sustained by karst features. Additionally, it is recommended to model the rainfall-discharge relationship in highly dynamic karst aquifers using subdaily time intervals (e.g., hourly time step) in order to reach a better prediction of the flood

peak discharge during high rainfall events. Assessing the discharge at lower time series can improve the mitigation of karst flash floods at the spring outlet and the management of groundwater storage for future water supply (Baudement et al., 2017). Finally, future studies could focus on developing solute transport models that incorporate the different components and flow dynamics in karst hydrosystems.

CHAPTER 4: ISPEEKH Model Development and Application in the Baget Catchment - Impact of land-use change on karst spring response by integration of surface processes in karst hydrology: The ISPEEKH model

Summary

In Chapter 4, the semi-distributed karst hydrogeological model "Integration of Surface Processes in Karst Hydrology (ISPEEKH)" was developed by modifying the uniform recharge and linear reservoir for groundwater and baseflow simulation in SWAT+ into three non-linear reservoirs corresponding to the epikarst (reservoir E), matrix (reservoir M), and conduits (reservoir C) in a karst system. The model uses input digital elevation model, land-use map, and overlapped soil and lithology maps to divide the watershed into subbasins connected through stream channels and hydrological response units (HRUs). It then uses weather input data to simulate daily land surface and soil hydrologic fluxes at the HRU scale, including potential evapotranspiration, actual evapotranspiration, surface runoff, channel flow, soil lateral flow, and soil water percolation. ISPEEKH is suitable for simulating groundwater flow in karst-dominated catchments where surface runoff generation is low and karst spring flow forms the major portion of streamflow. The simulated groundwater fluxes include the fast recharge from the epikarst to conduits, the slow recharge from the epikarst to the matrix, the conduit quick-flow and matrix slow-flow components of the karst spring discharge, and the conduit-matrix bidirectional exchange flow rate.

The ISPEEKH model was applied to the Baget catchment, using a 30-m spatial resolution DEM from the US Geological Survey, a 100-m resolution land use map from the Corine Land Cover database, and a soil map from the Food and Agriculture Organization's Digital Soil Map of the World. The model delineated karst and non-karst HRUs based on catchment lithology. The daily meteorological data included corrected 1-km resolution COMEPHORE precipitation and minimum and maximum air temperature, relative humidity, solar radiation, and wind speed at 8-km resolution from SAFRAN for years 2006-2018.

The model was calibrated using daily streamflow data at the catchment outlet from 2006-2013 (with 2 years of warm-up) and validated from 2014-2018. Parameter sensitivity analysis and calibration were performed using the PEST software, and the model predictive performance was evaluated using various indices applied in hydrological modeling.

The Baget catchment water balance was simulated using ISPEEKH from 2006-2018, with a mean annual precipitation of 1824 mm and evapotranspiration estimated at 601 mm. The model

successfully simulated groundwater storage and spring discharge from recharge to karst reservoirs based on water balance conservation. It adequately reproduced the catchment hydrological response to heavy precipitation events during high-flow periods and provided a reasonably accurate estimation of low-flow magnitude. However, some peaks were underestimated during calibration and validation periods. The model's adequacy in simulating evapotranspiration was also assessed.

ISPEEKH modeled the flow processes of the epikarst, conduit, and matrix in the Baget catchment, revealing a high connectivity between the epikarst and underlying vadose zone through the conduits. The model reproduced the conduit and matrix storages, showing fast rise in water storage during the high-flow periods and attenuated storage in the low recharge periods. The values of the emptying exponents of the epikarst-to-conduit flow and conduit-to-spring flow indicated non-linear flow dynamics. The matrix-to-conduit volumetric flow to total spring flow varied between 5% and 9% during the 2008-2018 study period, with a contribution to monthly discharge varying from 4-7% in the high flow periods to 22% in low-flow periods.

The Baget catchment has experienced significant land abandonment, leading to degeneration of pasture land and increased recolonization of forests. Natural afforestation, wood production, and agro-pastoralism could drive future land-use/land-cover changes. To investigate the impact on hydrology and water resources availability, alternative land-use change scenarios were simulated, including full catchment afforestation, deforestation due to wood production, and conversion to pastureland for animal grazing. The Mann-Whitney U-Test/two-tailed test was used to assess the impact of land-use changes on streamflow variability during the low- and high-flow periods. Results showed that the impact of afforestation on low flow was insignificant. However, low flow increased with deforestation for transitional woodland-shrub, whereas deforestation for pasture development reduced streamflow values ranging between 1 and 2.5 $m^3.s^{-1}$ in the high-flow periods. Peak flows greater than 2.5 $m^3.s^{-1}$ were relatively insensitive to all land-use changes.

The findings of this chapter were published in the Jounral of Hydrology as: *Al Khoury, I., Boithias, L., Bailey, R. T., Ollivier, C., Sivelle, V., & Labat, D. (2023). Impact of land-use change on karst spring response by integration of surface processes in karst hydrology: The ISPEEKH model. Journal of Hydrology, 626, 130300. https://doi.org/10.1016/j.jhydrol.2023.130300*

Al Khoury's Contribution: Conceptualization, Methodology, Software, Formal analysis, Investigation, Data curation, Writing – original draft, Writing – review & editing.

Journal of Hydrology 626 (2023) 130300

Contents lists available at ScienceDirect

Journal of Hydrology

journal homepage: www.elsevier.com/locate/jhydrol

Research papers

Impact of land-use change on karst spring response by integration of surface processes in karst hydrology: The ISPEEKH model

Ibrahim Al Khoury [a,*], Laurie Boithias [a], Ryan T. Bailey [b], Chloé Ollivier [c], Vianney Sivelle [c], David Labat [a]

[a] GET, Université de Toulouse 3, CNRS, IRD, UPS, France
[b] Department of Civil and Environmental Engineering, Colorado State University, 1372 Campus Delivery, Fort Collins, CO, USA
[c] HSM, Univ Montpellier, CNRS, IRD, Montpellier, France

ARTICLE INFO

This manuscript was handled by Corrado Corradini, Editor-in-Chief, with the assistance of Junbing Pu, Associate Editor

Keywords:
Karst hydrological modeling
Distributed modeling
Modified SWAT+
Land-use change
Pyrénées mountain range

ABSTRACT

Karst groundwater represents a source of freshwater for a quarter of the world's population. Modeling the hydrological behavior of karst aquifers while accounting for the spatial variability of the recharge processes and the land-use change impacts on water availability remains a challenge for karst water resources management. Therefore, this study proposes a new semi-distributed hydrological model named Integration of Surface ProcEssEs in Karst Hydrology (ISPEEKH) for simulating the surface-underground water flows in karst-dominated catchments. ISPEEKH couples the restructured version of the Soil and Water Assessment Tool (SWAT+) with a non-linear three-reservoir groundwater model that represents the epikarst and matrix-conduit flow components in a karst aquifer. ISPEEKH was applied to the Baget karst catchment (13.25 km^2) in the Pyrénées mountains of southwest France, characterized by a conduit-dominated spring flow and low surface runoff. The model simulated the catchment daily discharge satisfactorily, with NSE = 0.67 and R^2 = 0.68 for the 2008–2013 calibration period, and NSE = 0.65 and R^2 = 0.69 for the 2014–2018 validation period. The catchment evapotranspiration and discharge amounted to 33 % and 67 % of the average annual precipitation, respectively, and nearly 80 % of the discharge was attributed to spring flow. The matrix-to-conduit flow accounted for 4–7 % of the monthly spring flow during the high-flow period (December to June), and up to 22 % during the low-flow period (July to October). ISPEEKH was then used to assess the hydrological response of the Baget catchment to land-use change scenarios of afforestation and deforestation for wood production and pasture development. Afforestation of the full catchment area did not alter the catchment hydrology significantly. Deforestation for wood production reduced annual evapotranspiration by 12–18 % and increased annual recharge by 7–8 %, resulting in annual discharge rising by 6–9 %. These changes in the water balance components were most noticeable during the low-flow season and would augment freshwater availability. Conversely, deforestation for pasture development raised annual evapotranspiration by 13–17 % while reducing annual recharge by around 7 % and discharge by 5–7 %. These changes in the hydrological components were most remarkable during the high-flow season and affected discharge below 2.5 $m^3.s^{-1}$.

1. Introduction

Karst aquifers cover upwards of 15 % of Earth's continental surface (Goldscheider et al., 2020) and provide freshwater supply for nearly 25 % of the global population (Lukač Reberski et al., 2022). A depletion in karst groundwater levels and an attenuation of karst springs have already been detected in different regions of the world (Fiorillo and Guadagno, 2012; Hao et al., 2009; Jia et al., 2017; Kovačič et al., 2020; Taheri et al., 2016), and are further anticipated due to rising water abstraction and changes in climate and vegetation cover (Doummar et al., 2018; Nerantzaki and Nikolaidis, 2020; Ruiz et al., 2022; Sivelle et al., 2021; Smiatek et al., 2013). The spatiotemporal variability of land use is a main driver of groundwater resources availability through altered critical hydrological components, such as evapotranspiration, surface runoff, infiltration, and aquifer recharge (Bai et al., 2019; Gashaw et al., 2018; Woldesenbet et al., 2017). Afforestation,

* Corresponding author.
E-mail address: ibrahim.al-khoury@get.omp.eu (I. Al Khoury).

https://doi.org/10.1016/j.jhydrol.2023.130300
Received 22 May 2023; Received in revised form 8 September 2023; Accepted 20 September 2023
Available online 12 October 2023
0022-1694/© 2023 Elsevier B.V. All rights reserved.

Abstract

Karst groundwater represents a source of freshwater for a quarter of the world's population. Modeling the hydrological behavior of karst aquifers considering the spatial variability of the recharge processes and land-use change impacts on water availability remains a challenge for karst water resources management. Therefore, this study proposes a new semi-distributed hydrological model named Integration of Surface ProcEssEs in Karst Hydrology (ISPEEKH) for simulating the surface-underground water flows in karst-dominated catchments. ISPEEKH couples the restructured version of the Soil and Water Assessment Tool (SWAT+) with a non-linear three-reservoir groundwater model that represents the epikarst and matrix-conduit flow components in a karst aquifer. ISPEEKH was applied to the Baget karst catchment (13.25 km^2) in the Pyrénées mountains of southwest France, characterized by a conduit-dominated spring flow and low surface runoff. The model simulated the catchment daily discharge satisfactorily, with NSE = 0.67 and R^2 = 0.68 for the 2008−2013 calibration period, and NSE = 0.65 and R^2 = 0.69 for the 2014−2018 validation period. The catchment evapotranspiration and discharge amounted to 33% and 67% of the average annual precipitation, respectively, and nearly 80% of the discharge was attributed to spring flow. The matrix-to-conduit flow accounted for 4−7% of the monthly spring flow during the high-flow period (December to June), and up to 22% during the low-flow period (July to October). ISPEEKH was then used to assess the hydrological response of the Baget catchment to land-use change scenarios of afforestation and deforestation for wood production and pasture development. Afforestation of the full catchment area did not alter the catchment hydrology significantly. Deforestation for wood production reduced annual evapotranspiration by 12−18% and increased annual recharge by 7−8%, resulting in annual discharge rising by 6−9%. These changes in the water balance components were most noticeable during the low-flow season and would augment freshwater availability. Conversely, deforestation for pasture development raised annual evapotranspiration by 13−17% while reducing annual recharge by around 7% and discharge by 5−7%. These changes in the hydrological components were most remarkable during the high-flow season and affected discharge below 2.5 $m^3.s^{-1}$.

4.1 Introduction

Karst aquifers cover upwards of 15% of Earth's continental surface (Goldscheider et al., 2020) and provide freshwater supply for nearly 25% of the global population (Lukač Reberski et al., 2022). A depletion in karst groundwater levels and an attenuation of karst springs have already been detected in different regions of the world (Fiorillo and Guadagno, 2012; Hao et al., 2009; Jia et al., 2017; Kovačič et al., 2020; Taheri et al., 2016), and are further anticipated due to rising water abstraction and changes in climate and vegetation cover (Doummar et al., 2018; Nerantzaki and Nikolaidis, 2020; Ruiz et al., 2022; Sivelle et al., 2021; Smiatek et al., 2013). In particular, the spatiotemporal variability of the land use is a main driver of groundwater resources availability by altering hydrological components, such as evapotranspiration, surface runoff, infiltration and aquifer recharge (Bai et al., 2019; Gashaw et al., 2018; Woldesenbet et al., 2017). Afforestation, deforestation, rapid urbanization, and farmland abandonment are primary examples of land-use changes that have drastically affected catchment water balance and yield around the globe, particularly in the Mediterranean belt and mountainous regions (García-Ruiz et al., 2011; Guo et al., 2023; Palacios-Cabrera et al., 2022). Thus, acquiring accurate data on the spatiotemporal evolution of the surface water and groundwater fluxes by incorporating land-use change impacts on karst catchment hydrology through numerical modeling is fundamental for adequate water resources planning and management (Cardoso de Salis et al., 2019; Messerschmid and Aliewi, 2022; Ruiz et al., 2022). Yet, the assessment of karst groundwater recharge and water resources by integration of climate and geospatial data in distributed karst hydrological models remains a challenge due to the intrinsic heterogeneity, duality, anisotropy, and nonlinearity of karst aquifers (Chang et al., 2021; Hartmann et al., 2014; Jeannin et al., 2021; Messerschmid et al., 2020). To date, studies that have evaluated the hydrological response of karst catchments to changes in vegetation cover and land-use parameters have rarely been conducted (Bittner et al., 2018; Doummar et al., 2012; Ruiz et al., 2022; Sarrazin et al., 2018).

Hydrological models used to simulate the water balance in karst catchments should consider the recharge types and hydrodynamics of the karst aquifer water bearing components. Karst aquifers behave as a dual to triple-porosity medium where diffuse recharge is generated by slow percolation of infiltrated water through the fractures and fissures (matrix porosity), while concentrated recharge develops via enlarged channels and pipe networks (conduit porosity) (Geyer et al., 2013; Goldscheider and Drew, 2007; Paiva and Cunha, 2020). The highly-weathered

uppermost zone of the karst aquifer, known as epikarst, receives surface runoff leakage through fissures and controls the recharge of the saturated zone by storing percolation water temporarily during dry and low recharge periods, and by releasing quick flow via karst openings at saturation during high recharge periods. At total evolution of the epikarst, surface runoff decreases to zero or small values, and most of the infiltration water that passes the epikarst flows through the conduits, while percolation through the matrix and fissures does not increase (Bauer et al., 2005; Fidelibus et al., 2017; Yan et al., 2022). Hartmann et al. (2021) highlighted the need to consider the interplay of partially overlapping surface and subsurface catchments and the influence of non-karstic units on recharge in karst-dominated catchment modeling. Moreover, karst hydrological models must reproduce both the delayed matrix groundwater storage and slow discharge during the dry season and the low conduit storage and fast discharge to springs during the wet period (de Rooij and Graham, 2017; Giese et al., 2018; Hartmann et al., 2021). The matrix-conduit exchange flow rate, generated by the head difference between the two domains (Dal Soglio et al., 2020a), should also be considered in karst groundwater flow modeling as it can represent a substantial portion of the spring discharge during the dry and low-flow conditions (Sivelle et al., 2019). In addition, multiple studies have established that the storage-discharge relationship of the karst flow processes is mostly nonlinear (Basu et al., 2022; Chang et al., 2015; Kurtulus and Razack, 2007; Labat et al., 2000; Tritz et al., 2011; Zhao et al., 2021).

Numerical approaches in karst hydrology are either spatially lumped or spatially distributed. Lumped models are commonly used in data-scarce and complex karst regions. They generally operate by distributing infiltration to several linear or non-linear reservoirs that represent the different karst storage and spring discharge components, and by applying transfer functions that relate the input rainfall signal to the output spring discharge without consideration of the spatial variability of the surface and subsurface flow determinants over the catchment (i.e., meteorological forcing, topography, land use, soil, karst landform). In comparison, fully distributed aquifer models discretize and simulate an orthogonal two- or three-form of the governing groundwater flow equation (e.g., equivalent porous media, dual continuum media, discrete fracture network, coupled discrete conduit network). However, the parametrization of such models in karst aquifers is generally constrained by the need for exhaustive data on the hydrogeological and geometric properties of the karst system, and by the dynamic changes in the hydraulic conditions of the underground surface permeability structure (Adinehvand et al., 2017;

Chang et al., 2019; Fischer et al., 2018; Ghasemizadeh et al., 2012; Hartmann et al., 2014; Malenica et al., 2018; Gill et al., 2021). To overcome the limitations of both methods, conceptually-based distributed karst modeling approaches, which combine lumped conceptual and distributed model features (i.e., spatially distributed recharge coupled with dominant karst flow components as distinct conceptual reservoirs) can provide a transition from traditional lumped to distributed models. This approach maintains the ability to assess the spatial variability of the hydrological factors even with scarce hydrogeological data on the underlying karst structure (Yang et al., 2022).

To date, there have been few attempts to simulate karst hydrology by coupling spatially distributed recharge with conceptually-based groundwater models. Sarrazin et al. (2018) incorporated the Penman-Monteith evapotranspiration equation into the grid-based semi-distributed model VarKarst (Hartmann et al., 2013), which reproduces soil-epikarst flow processes and spring discharge over vertical compartments of unique soil and epikarst characteristics. In VarKarst, the outflow from each epikarst compartment is divided between diffuse and concentrated recharge using a variable separation factor, and spring discharge is calculated as the sum of outflows from the matrix and conduit compartments. Bittner et al. (2018) developed the semi-distributed model Land use change modeling in KARSt systems (LuKARS), which lumps the dominant hydrotopes of homogeneous land-use and soil properties in a karst catchment as independent spatial units. These hydrotopes recharge a shared linear reservoir for baseflow (matrix flow) simulation, while rapid (conduit) discharge is modeled as preferential flow from the hydrotopes to the spring outlet. Ollivier et al. (2021) integrated a remote sensing-driven evapotranspiration model called Simple Crop coefficient for Evapotranspiration (SimpKcET) into the gridded Karst Recharge and discharge Model (KaRaMel). KaRaMel consists of an upper reservoir that recharges lower linear matrix and conduit reservoirs past its storage capacity. It then simulates spring discharge as the sum of the matrix and conduit flow components. Yang et al. (2022) also proposed the distributed karst Xin'anjiang (DK-XAJ) model which classifies hillslopes in a karst catchment as strongly-, moderately- and poorly-developed karst grid cells, and implements a linear two-reservoir model into the moderately- and strongly-developed karstic cells for the simulation of the conduit and matrix flows.

The Soil and Water Assessment Tool (SWAT) (Arnold et al., 1998) is one of the most extensively utilized semi-distributed eco-hydrological models internationally, owing to its

comprehensive nature, robustness, and flexibility as an interdisciplinary tool (Aloui et al., 2023). Despite its wide range of applications (CARD, 2023), SWAT has been used to conduct hydrological studies in only few karstified catchments (e.g., Afinowicz et al., 2005; Efthimiou, 2018; Jain et al., 2015; Mehdi et al., 2015; Sellami et al., 2016; Sunde et al., 2017, 2018; Zeiger et al., 2021). The uniform recharge by soil water percolation to the shallow and deep aquifers and the linear reservoir for groundwater return flow simulation in SWAT (Neitsch et al., 2011) limit its applicability in simulating the water balance of spring-dominated karst catchments and in assessing the impacts of land-use changes on karst water resources. Few authors have modified the SWAT source code to better reproduce recharge to karst aquifers based on the main karst features in the study regions (Baffaut and Benson, 2009; Yactayo, 2009; Nikolaidis et al., 2013; Wang and Brubaker, 2014; Palanisamy and Workman, 2015; Wang et al., 2019b; Nguyen et al., 2020; Geng et al., 2021; Zhou et al., 2022). These modified SWAT models and semi-distributed models (i.e., VarKarst, LuKARS, SimpKcET-KaRaMel, DK-XAJ) applied in karst hydrology did not represent the epikarst, matrix and conduit flow processes, which include the matrix-conduit bidirectional exchange flow rate, using non-linear storage-discharge relationships (Al Khoury et al., 2023b). Therefore, the aim of this study was to develop a semi-distributed model termed as Integration of Surface ProcEssEs in Karst Hydrology (ISPEEKH) that can simulate the daily surface-underground water fluxes in a karst-dominated catchment by accounting for: the spatial heterogeneity of the catchment properties (i.e., weather, land use, soil, lithology), the diffuse and concentrated recharge from karst and non-karst units in the catchment recharge area, the dominant flow processes in the karst aquifer, including the bidirectional flow exchange between the matrix and conduits, and the non-linearity of the karst system. ISPEEKH was developed by implementing a non-linear three-reservoir model of the epikarst, matrix and conduits into SWAT+, the latest restructured version of SWAT (Bieger et al., 2017). It was then applied to the Baget catchment (13.25 km^2) located in the Pyrénées mountains of southwest France and drained primarily by a karst spring with non-linear conduit flow. Thus, the objectives of this research work were to: (1) modify the SWAT+ source code by integrating a karst aquifer reservoir-based model of the epikarst, matrix and conduits with non-linear storage-discharge relationships, (2) test the capability of the new model to simulate the daily water balance and flow dynamics of the karst-dominated Baget catchment, and (3) evaluate the hydrological response of the Baget catchment to land-use

change scenarios of afforestation and deforestation, providing insights into the impacts of plausible land management plans on the catchment water resources.

4.2 Methods and materials

4.2.1 Study site description

The Baget is a karst catchment located in the piedmont of the Pyrénées mountains (station B1 at 42°57'18.06"N; 1°1'52.76"E), in the Ariège Department, southwest of France (**Figure 5a**). It is one of the nine experimental sites monitored by the Karst National Observatory Service (SNO Karst) (Jourde et al., 2018) (https://sokarst.org/en/home-2021/) and part of the French network of Critical Zone Observatories Research and Applications–National Research Infrastructure (OZCAR-RI) (Gaillardet et al., 2018). The groundwater contribution zone of the Baget karst spring is nearly 13.25 km^2 (Mangin, 1975), which extends beyond the catchment topographic boundaries of 8.65 km^2 to the east. The Baget lies on a mixed lithological terrain, consisting of Jurassic and Cretaceous karstified landforms that occupy nearly 67% of the groundwater catchment area and non-karstified rocks that cover the remaining 33% of its surface, primarily at the lower catchment boundary (Debroas, 2009; Mangin, 1975). The large carbonate part of the catchment includes: (1) a crystalline limestone band outcropping between Cretaceous impermeable silicate rocks (black flysch to the south, and breccia-metamorphic layers to the north), and (2) Jurassic dolomites in the northern upper side of the catchment, bounded by silicates (Cretaceous flysch of Arbas, other lithologies, and Paleozoic Lachein schists) (Ulloa-Cedamanos et al., 2021).

The Baget catchment is under an Atlantic oceanic climate with mountainous influence. A mean daily air temperature of 12 ± 6.3°C and a mean annual precipitation of 975.5 mm were recorded at the meteorological station of Saint Girons (43°00'19"N; 01°06'25"E; 414 m a.s.l), located outside the catchment at 8.3 km from its outlet (**Figure 5b**). The catchment snowpack is generally low, and snowmelt does not contibute significantly to discharge (Ulloa-Cedamanos et al., 2020).

The Baget is a highly karstified and dynamic catchment characterized by rapid infiltration, fast transit time between recharge and discharge, and strong non-linear rainfall-runoff relationship, as evidenced by the convolution and spectral analyses of rainfall and discharge rates performed by Labat et al. (1999; 2000). The Baget karst system includes a shallow epikarstic zone with active water storage and drainage to the saturated zone (Ulloa-Cedamanos et al., 2020). The catchment

streamflow is formed predominantly by the discharge of the Las Hountas perennial karst spring through well-developed conduit networks and partially by the Lachein stream, which drains the impermeable terrains in the catchment and usually dries up in the low-flow period (**Figure 5a**). Tracer tests and lumped-parameter modeling of the epikarst-conduit-matrix system of the Baget catchment showed that non-linear conduit flow is the main component of the karst spring discharge, and that the matrix continuously exchanges flow with the conduit networks without direct slow flow contribution to the spring (Sivelle et al., 2019; 2020). The mean annual catchment discharge measured at the outlet gauging station B1, 60 m below the Las Hountas spring (**Figure 5a**), was 0.44 ± 0.67 $m^3.s^{-1}$ (years 1978−2018), with maximum and minimum values of 10.10 and 0.02 $m^3.s^{-1}$ in the high- and low-flow periods, respectively (Ulloa-Cedamanos et al., 2020).

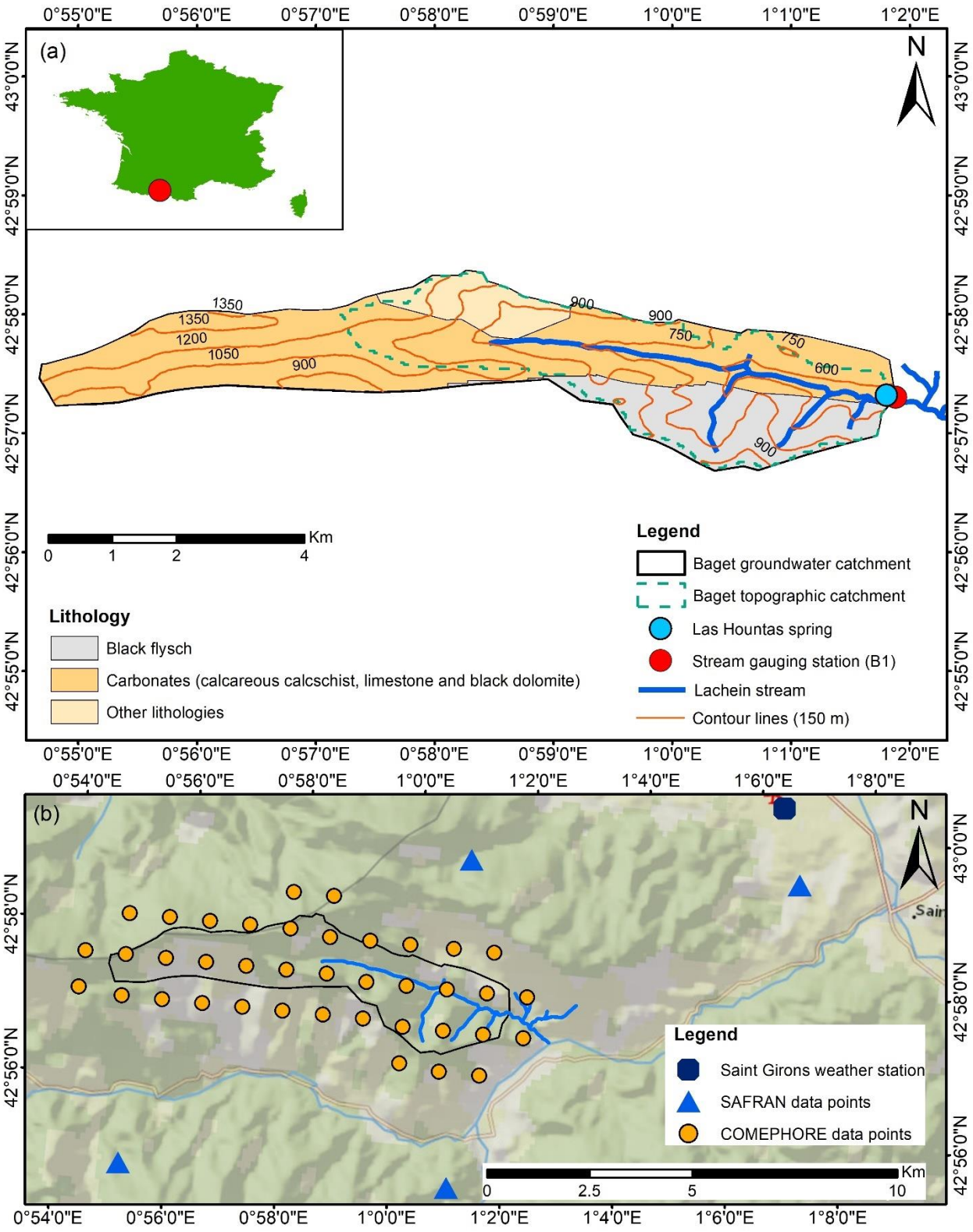
(a)
N
0°55'0"E
0°56'0"E
0°57'0"E
0°58'0"E
0°59'0"E
1°0'0"E
1°1'0"E
1°2'0"E
43°0'0"N
42°59'0"N
42°58'0"N
42°57'0"N
42°56'0"N
42°55'0"N
1350
1200
1050
900
750
600
Km
0 1 2 4
Lithology
Black flysch
Carbonates (calcareous calcschist, limestone and black dolomite)
Other lithologies
Legend
Baget groundwater catchment
Baget topographic catchment
Las Hountas spring
Stream gauging station (B1)
Lachein stream
Contour lines (150 m)
(b)
0°54'0"E
0°56'0"E
0°58'0"E
1°0'0"E
1°2'0"E
1°4'0"E
1°6'0"E
1°8'0"E
Legend
Saint Girons weather station
SAFRAN data points
COMEPHORE data points
Km
0 2.5 5 10

Figure 5. (a) The Baget groundwater catchment, topographic catchment, and lithological composition, the Lachein stream, the Las Hountas karst spring, and the outlet stream gauging station (B1); (b) The meteorological data points within the catchment area.

4.2.2 Overview of SWAT/SWAT+

The Soil and Water Assessment Tool (SWAT) is a time-continuous, semi-distributed, process-based, eco-hydrological model developed by the US Department of Agriculture-Agriculture Research Service (USDA-ARS) to assess the short- and long-term impacts of land management practices on water, erosion and agricultural yields in ungauged basins (Arnold et al., 1998, 2012). It divides catchments into subbasins and further into hydrological response units (HRUs) of homogeneous land-use, slope, and soil characteristics to simulate key processes, such as hydrology, plant growth, and land management. SWAT applies a simplified version of the Environmental Policy Integrated Climate (EPIC) crop growth module (Williams et al., 1989) to simulate the phenological development of plants based on daily heat unit accumulation represented by the sum of the difference between the average daily temperatures and the base temperature. The model uses the intercepted photosynthetically active radiation to compute the daily increase in total plant biomass, which is attenuated by stress factors such as water, temperature, and nutrients (Ferreira et al., 2021; Sinnathamby et al., 2017). The catchment water balance is driven by moisture and energy inputs, such as daily precipitation, minimum and maximum air temperature, solar radiation, wind speed, and relative humidity. The simulated hydrological processes include canopy storage, evapotranspiration, surface runoff, soil water lateral flow and percolation, aquifer recharge, groundwater return flow to the streams, and capillary rise from shallow aquifers into the root zone (Abbaspour et al., 2015). A conceptual representation of the catchment main water balance components simulated by SWAT is shown **in Figure 6.**

Potential evapotranspiration (PET) in SWAT can be estimated using the Penman-Monteith (Monteith, 1965), Priestley-Taylor (Priestley and Taylor, 1972), or Hargreaves (Hargreaves and Samani, 1985) methods, and actual evapotranspiration (ET_a) is simulated as the sum of canopy evaporation, soil evaporation, and plant transpiration (Abiodun et al., 2018). Daily surface runoff is simulated in SWAT by the modified Soil Conservation Service Curve Number method (USDA-SCS, 1972) as a function of the daily precipitation and soil retention properties (Thomas et al., 2021). The peak runoff rate is calculated with the modified rational method (Chow et al., 1988). The simulation of catchment hydrology is split between a land phase and a routing (in-stream)

phase. Flow is modeled for each HRU and area-weighted to subbasin level in the land phase. It is then routed through the streams of the subbasins to the outlets during the routing phase (Romagnoli et al., 2017). The rate and velocity of the channel flow in each subbasin reach are determined using Manning's equation when streamflow is less than the bankfull discharge rate, while floodplain geometry is incorporated into the channel routing simulation when streamflow is greater than the bankfull flow (Her et al., 2017b). Flow is routed through channels using the Muskingum routing method (Overton, 1966) or variable storage coefficient method (Williams, 1969). In this study, the Penman-Monteith approach was adopted for PET estimation as it separates the effects of climate and land cover on each of the evapotranspiration components by explicitly including land cover properties (Sarrazin et al., 2018), and the variable storage coefficient method was used for flow routing.

Water percolation from the bottom of the soil profile is calculated using a layered storage routing model in which downward flow occurs when the soil layer field capacity is exceeded (Rahbeh et al., 2019). Subsurface soil lateral flow is computed simultaneously with soil water percolation using a kinematic storage routing method (Sloan and Moore, 1984) that accounts for the variation in conductivity, slope and, soil water content (Zhou et al., 2013). Water drained from the soil then recharges a shallow (unconfined) aquifer and a deep (confined) aquifer reservoirs, using exponential delay functions and a coefficient to partition the recharge linearly between the two reservoirs. Water losses (Q_{TLOSS}) by transmission through the channels can also be simulated and are assumed to enter the bank storage or the deep aquifer (Holvoet et al., 2008). Baseflow (return flow) to the stream is modeled when the shallow aquifer reservoir storage exceeds a user-defined water level using a linear storage-discharge relationship, whereas discharge from the deep aquifer is considered lost outside the catchment (Pfannerstill et al., 2014). Finally, the watershed streamflow (water yield) is generated by the sum of surface runoff, soil lateral flow, and baseflow from groundwater (Ayivi and Jha, 2018).

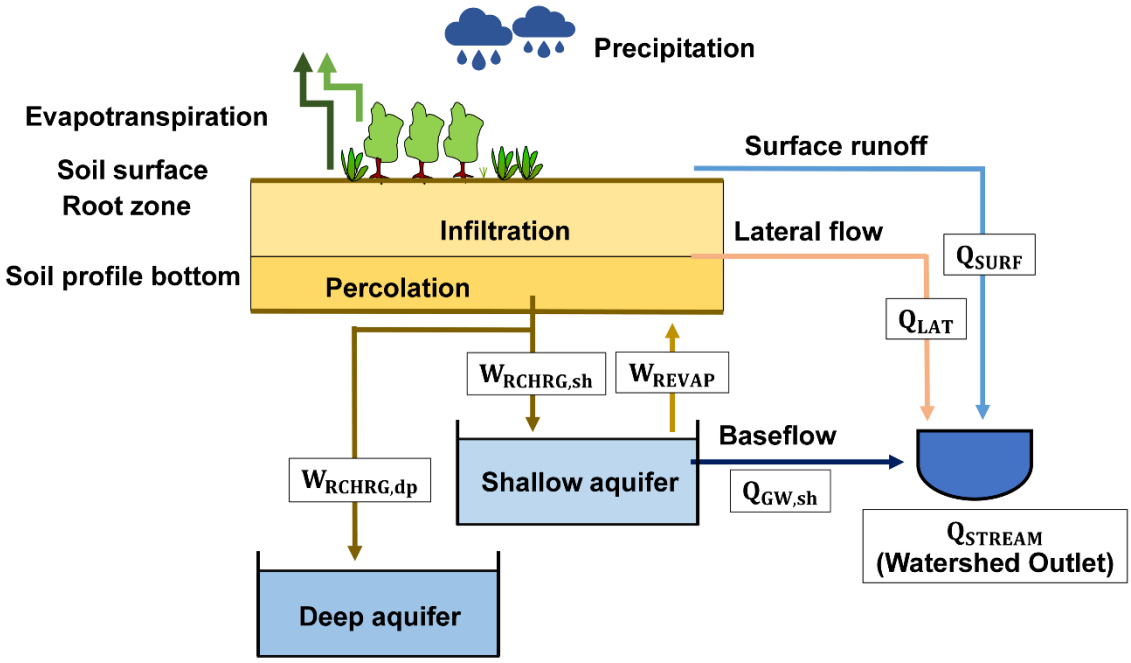

Figure 6. Conceptual representation of the catchment main water balance components simulated by SWAT.

SWAT+ (Bieger et al., 2017) is a restructured version of SWAT that was developed to improve the spatial representation of the elements and processes within catchments, and facilitate upgrades of the SWAT source code for future applications and development by the general users (Wu et al., 2020). Compared to the previous versions of SWAT, SWAT+ offers a greater flexibility in catchment discretization/configuration and a better simulation of the landscape processes, with improved runoff routing capabilities. In addition, spatial objects in SWAT+ have been constructed as independent modules, each with its own connection file where users can define the routing and the fraction of the flow exchanged between the catchment hydrological entities (Bieger et al., 2019, 2017). A detailed description of the processes and corresponding equations incorporated in SWAT are provided in the SWAT theoretical manual by Neitsch et al. (2011) and the SWAT+ documentation (https://swatplus.gitbook.io/docs/user/io), currently under development.

4.2.3 The ISPEEKH model structure and code development

The Integration of Surface ProcEssEs in Karst Hydrology (ISPEEKH) is a semi-distributed model that simulates flow processes of the surface and infiltration zone at the hydrological response unit (HRU) scale, considering the spatial variability of the meteorological inputs,

topography, land use, soil and lithology, and applies three distinct conceptual reservoirs to simulate the dominant flow components of the unsaturated and saturated zones in karst aquifers. We developed ISPEEKH by modifying the linear reservoir module for groundwater and baseflow simulation in SWAT+ revision 60.5.4 into a non-linear three-reservoir model that incorporates functions of the epikarst, matrix and conduits, with recharge from diffuse and concentrated flows to the reservoirs. FORTRAN90 language in Visual Studio 2019 was used to modify the source code of SWAT+.

Figure 7 shows the conceptual structure of the ISPEEKH model, which includes the land surface, recharge zone and karst system water fluxes. The land surface and soil hydrologic fluxes, including precipitation, evapotranspiration, direct (surface) runoff, lateral flow, and percolation are simulated using the original SWAT+ subroutines. The groundwater fluxes, which comprise the recharge from karst and non-karst areas, stream transmission losses, pumping, and spring discharge to the stream channels are simulated using the new karst module added to SWAT+. This karst groundwater flow module incorporates three non-linear reservoirs organized in a two-level structure: (1) the higher-level compartment E, which represents the epikarst, and (2) the lower-level reservoirs M and C corresponding to the matrix and conduit components of karst aquifers, respectively. The structure and storage-discharge functions of the three reservoirs were based on the conceptual configuration of karst aquifers adopted in the rainfall-runoff model KarstMod (Mazzilli et al., 2019), which has been successfully applied in simulating karst springs discharge and analyzing the flow dynamics of complex karst systems globally (Baudement et al., 2017; Duran et al., 2020; Frank et al., 2021; Kazakis et al., 2018; Labat et al., 2022; Lončar et al., 2018; Poulain et al., 2018; Sivelle et al., 2019).

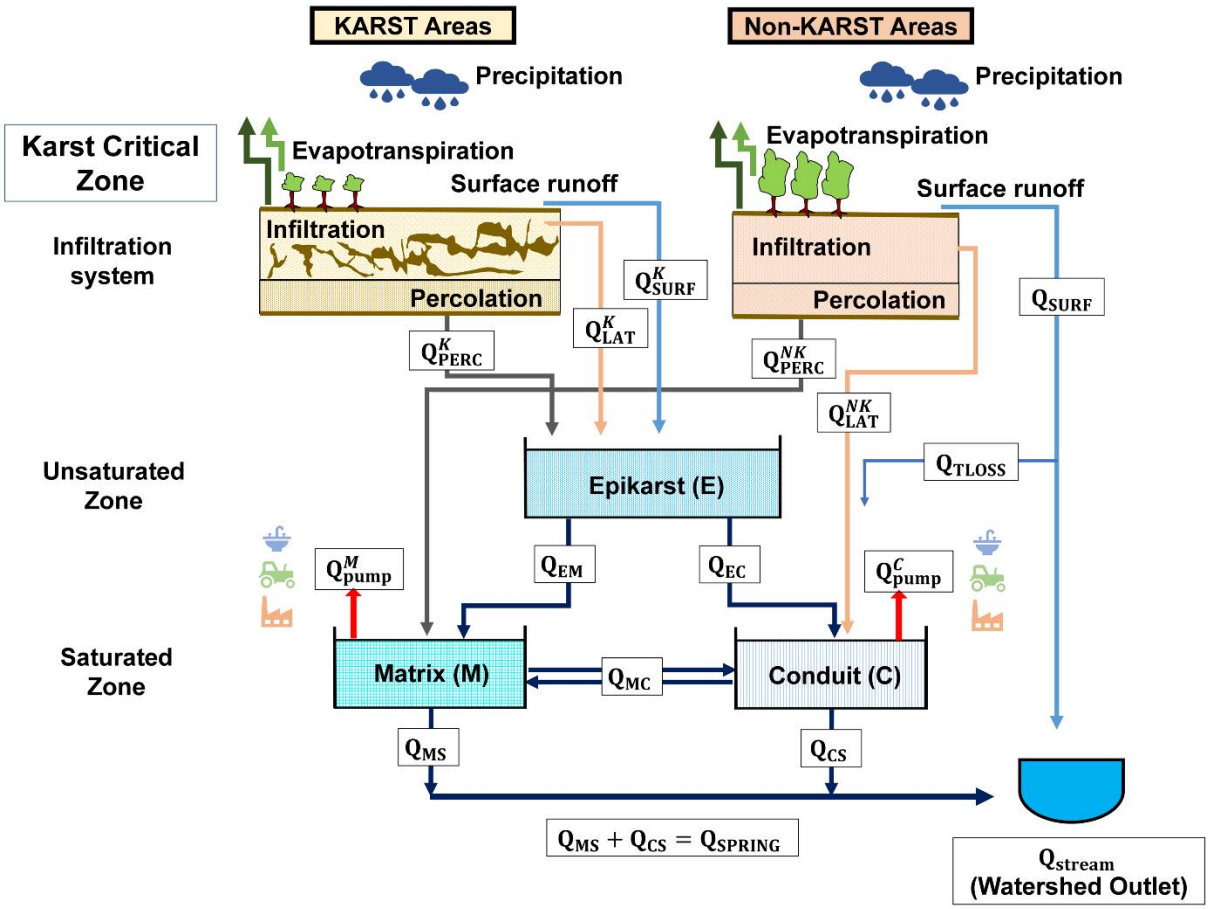

Figure 7. Conceptual representation of the water balance surface and subsurface flows simulated by ISPEEKH for a karst-dominated catchment.

ISPEEKH was developed to simulate the hydrological processes in karst-dominated catchments, wherein surface runoff generation is low and karst spring flow constitutes a significant portion of the stream discharge. The conceptual reservoir of the epikarst considers direct rainfall infiltration without surface runoff generation through surface-exposed and well-developed epikarstic fissures, in addition to infiltrated water that can move laterally down a hillslope through soil layers and water percolation from the bottom of the soil profile where soil overlays the epikarst. Thus depending on the epikarst near-surface development and soil development at the soil–epikarst interface in a study karst catchment, the epikarst reservoir can be recharged by daily surface runoff (Q^K_{SURF}), soil lateral flow (Q^K_{LAT}), and percolation from the bottom of the soil (Q^K_{PERC}) in karst HRUs, considering the delay time in the unsaturated zone, as shown by Equation (1):

$$RECH_{E,i} = RECH_{E,i-1} \times e^{-\frac{1}{\delta_E}} + \left(1 - e^{-\frac{1}{\delta_E}}\right) \times \sum_{j=1}^{nhrus-K} \left(Q^K_{SURF,i,j} + Q^K_{LAT,i,j} + Q^K_{PERC,i,j}\right) \quad (1)$$

where $RECH_{E,i}$ and $RECH_{E,i-1}$ represent the recharge from the land surface and soil to the epikarst reservoir on days i and $i-1$ (mm.day^{-1}), respectively, δ_E is the delay time for infiltrated water to reach the epikarst reservoir (days), $Q^K_{SURF,i,j}$, $Q^K_{LAT,i,j}$ and $Q^K_{PERC,i,j}$ are surface runoff, soil lateral flow and soil percolation on day i from the karst HRU j (mm.day^{-1}), respectively, and $nhrus - K$ is the number of HRUs in the karst recharge area.

The epikarst reservoir then discharges the flows (Q_{EM}) into the matrix reservoir and (Q_{EC}) into the conduit reservoir when its water level exceeds a user-defined threshold. Thus, the water balance of the epikarst reservoir is represented by Equation (2), as follows:

$$\begin{cases} \dfrac{dE(t)}{dt} = RECH_E(t) - Q_{EM}(t) - Q_{EC}(t) \\ \dfrac{dE(t)}{dt} = RECH_E(t) - k_{EM}\left(\dfrac{E(t) - E_{min}}{L_{ref}}\right)^{\alpha_{EM}} - k_{EC}\left(\dfrac{E(t) - E_{min}}{L_{ref}}\right)^{\alpha_{EC}} \end{cases} \quad (2)$$

where $RECH_E$ is the daily recharge from the land surface and soil to the epikarst reservoir (mm.day^{-1}), Q_{EM} and Q_{EC} are the daily outflows from the epikarst reservoir to the matrix and conduit reservoirs (mm.day^{-1}), respectively, E is the daily water level in the epikarst reservoir (mm), E_{min} is the minimum water level for the activation of the epikarst discharge (mm), L_{ref} is a unit length (mm), k_{EM} and k_{EC} are the specific discharge coefficients of the epikarst fluxes to the matrix and conduits reservoirs (mm.day^{-1}), respectively, and α_{EM} and α_{EC} are positive emptying exponents (unitless).

Percolation from the bottom of the soil profile in non-karst HRUs (Q^{NK}_{PERC}) recharges the matrix reservoir, while lateral flow generated in non-karst HRUs (Q^{NK}_{LAT}) seeps directly into the conduit reservoir. The conduit reservoir also receives concentrated recharge from streamflow losses by transmission in the channels (Q_{TLOSS}), as shown by Equations (3) and (4):

$$RECH_{M,i} = RECH_{M,i-1} \times e^{-\frac{1}{\delta_M}} + \left(1 - e^{-\frac{1}{\delta_M}}\right) \times \sum_{j=1}^{nhrus-NK} \left(Q^{NK}_{PERC,i,j}\right) \quad (3)$$

$$RECH_{C,i} = Q_{TLOSS,i} + \sum_{j=1}^{nhrus-NK} \left(Q^{NK}_{LAT,i,j}\right) \quad (4)$$

where $RECH_{M,i}$ and $RECH_{M,i-1}$ represents recharge by soil water percolation from non-karst HRUs to the matrix reservoir on day i and $i-1$ (mm.day^{-1}), respectively, δ_M is the delay time for infiltrated water to reach the matrix reservoir (days), $Q_{PERC,i,j}^{NK}$ is the soil percolation on day i from the non-karst HRU j (mm.day^{-1}), $RECH_{C,i}$ is the recharge to the conduit reservoir on day i (mm.day^{-1}), $Q_{LAT,i,j}^{NK}$ is the soil lateral flow on day i from the non-karst HRU j (mm.day^{-1}), $Q_{TLOSS,i}$ represents water transmission losses on day i (mm.day^{-1}), and $nhrus - NK$ is the number of HRUs in the non-karst recharge area.

The bidirectional exchange flow rate between the matrix and conduit reservoirs (Q_{MC}) is estimated as a function of the difference between the daily water levels of the two reservoirs, with water flowing from the reservoir with the higher water level to the reservoir with the lower water level. Moreover, groundwater pumping from the matrix reservoir (Q_{PUMP}^{M}) and conduit reservoir (Q_{PUMP}^{C}), if any, can be specified by the user to account for domestic, agricultural, and industrial withdrawals. The outflow of the matrix reservoir (Q_{MS}) and the outflow of the conduit reservoir (Q_{CS}) form the spring discharge of the karst system (Q_{SPRING}). Therefore, the water balance of the matrix and conduit reservoirs are represented by Equations (5) and (6), respectively, as follows:

Matrix Reservoir

$$\begin{cases} \dfrac{dM(t)}{dt} = RECH_M(t) + Q_{EM}(t) - Q_{MC}(t) - Q_{MS}(t) - Q_{PUMP}^{M}(t) \\ \dfrac{dM(t)}{dt} = RECH_M(t) + Q_{EM}(t) - k_{MC}\left(\dfrac{C(t)-M(t)}{L_{ref}}\right)^{\alpha_{MC}} - k_{MS}\left(\dfrac{M(t)}{L_{ref}}\right)^{\alpha_{MS}} - Q_{PUMP}^{M}(t) \end{cases} \quad (5)$$

Conduit Reservoir

$$\begin{cases} \dfrac{dC(t)}{dt} = RECH_C(t) + Q_{EC}(t) + Q_{MC}(t) - Q_{CS}(t) - Q_{PUMP}^{C}(t) \\ \dfrac{dC(t)}{dt} = RECH_C(t) + Q_{EC}(t) + k_{MC}\left(\dfrac{C(t)-M(t)}{L_{ref}}\right)^{\alpha_{MC}} - k_{CS}\left(\dfrac{C(t)}{L_{ref}}\right)^{\alpha_{CS}} - Q_{PUMP}^{C}(t) \end{cases} \quad (6)$$

where $RECH_M$ and $RECH_C$ are the recharge components to the matrix and conduit reservoirs (mm.day^{-1}), respectively, Q_{EM} and Q_{EC} are the outflows from the epikarst reservoir to the matrix and conduit reservoirs (mm.day^{-1}), respectively, C and M are the daily water levels in the matrix and conduit reservoirs (mm), respectively, L_{ref} is a unit length (mm), Q_{MC} is the daily bidirectional exchange flow between the matrix and conduit reservoirs (mm.day^{-1}), Q_{MS} and Q_{CS} are the daily

outflows from the matrix and conduit reservoirs to the spring (mm.day^{-1}), respectively, k_{MC}, k_{MS}, and k_{CS} are the specific discharge coefficients of the matrix and conduit fluxes (mm.day^{-1}), α_{MC}, α_{MS}, and α_{CS} are positive exponents (unitless), and Q_{PUMP}^{M} and Q_{PUMP}^{C} are the daily pumping rates from the matrix and conduit reservoirs (mm.day^{-1}), respectively.

Finally, the daily karst spring flow is routed with the surface runoff generated in non-karst HRUs (Q_{SURF}) to the watershed outlet in order to simulate total streamflow (Q_{STREAM}), as follows:

$$Q_{STREAM,i} = Q_{SPRING,i} + Q_{SURF,i} = Q_{CS,i} + Q_{MS,i} + Q_{SURF,i} \quad (7)$$

where $Q_{STREAM,i}$ is the total discharge at the watershed outlet on day i, $Q_{SPRING,i}$ is the daily spring flow contribution to streamflow from karst HRUs (calculated as the sum of conduit outflow $Q_{CS,i}$ and matrix outflow $Q_{MS,i}$), and $Q_{SURF,i}$ is the daily surface runoff in non-karst HRUs (all variables are expressed in mm.day^{-1}). The simulated streamflow hydrograph is given in m^3.s^{-1}.

Three new subroutines for the simulation of the karst flow processes were added to the source code of SWAT+ revision 60.5.4: *karst_module*, *karst_read*, and *karst_control*. The *karst_module* includes an array of the user input parameters of the groundwater model (e.g., initial water levels, infiltration delay time values, discharge coefficients, and emptying exponents of reservoirs E, M, and C) and an array of the output variables for the simulated karst groundwater fluxes. The *karst_module* also contains arrays for the HRU surface runoff, lateral flow, percolation, transmission losses, and HRU properties (e.g., HRU type: karst vs non-karst). The HRU surface runoff, lateral flow, and percolation arrays, defined in the *karst_module* subroutine, are populated in the *hru_control* subroutine, while the channel transmission losses array is defined in the *channel_control* subroutine.

The *karst_read* module is called if one or more karst objects are identified in the model. A karst object is defined as a single epikarst-matrix-conduit reservoir model, and the number of karst objects is specified in the input file "object.cnt". In the case of the Baget catchment, the number of karst object was set to 1 corresponding to one karst apring outlet. The *karst_read* module first searches for the user input file 'karst.data', which contains the values of the input parameters for each karst object, the HRU properties (i.e., karst vs non-karst, HRU pumping source), and the daily pumping rates (if any). Then, it proceeds to read in the data for each karst object and allocates the *karst_module* arrays based on the number of karst objects, as well as the HRU surface runoff,

lateral flow, and percolation arrays based on the number of HRUs in the model. Moreover, the *karst_read* module sets the initial water levels in reservoirs E, M, and C to start the simulation, and prepares the output file "karst_wb_d.txt" that will store the daily simulated values of the water fluxes defined in the *karst_d* array.

The *karst_control* subroutine computes the water flux to/between each karst reservoir and the discharge of the the karst spring to the stream channel (Equations 1 to 7), then stores and writes out the daily karst water fluxes to "karst_wb_d.txt". The spring flow simulated in the *karst_control* module is then routed to one or more channels downstream the watershed outlet(s) by connecting the karst object(s) to the primary outlet channel(s) in the model. For the karst spring flow, this connection is established via the "karst.con" input file, which indicates the number of the channels to which the karst object is connected and the fraction of flow received by each channel.

4.2.4 Data collection

The input data required to develop a hydrological model of the Baget catchment with ISPEEKH included a digital elevation model (DEM), land-use/land-cover map and a soil map, in addition to daily time series of precipitation (mm), minimum and maximum air temperature (°C), relative humidity (fraction), solar radiation ($MJ.m^{-2}.day^{-1}$) and wind speed ($m.s^{-1}$). The complete set of meteorological data was available for the years 2006 to 2018.

4.2.4.1 Topography

The DEM of the Baget catchment was obtained at 30-m spatial resolution from the Shuttle Radar Topography Mission 'SRTM, 2014' files (1 Arc-Second Global) of the US Geological Survey (USGS) (https://earthexplorer.usgs.gov/) (**Figure 8a**). The catchment altitude ranges from 502 to 1404 m m.s.l., and slopes vary mostly between 10 to 30%, becoming steeper (30−40%) in some regions in the lower part of the catchment (**Figure 8b**).

4.2.4.2 Land use and land cover

A land-use/land-cover map of the Baget catchment was extracted at 100-m resolution from Corine Land Cover (CLC) (https://land.copernicus.eu/pan-european/corine-land-cover), considered the reference land-use/land-cover database at the Pan-European level. The CLC nomenclature comprises 44 LULC classes organized in three levels (described in Baudoux et al., 2021). The map is produced in vector format with a minimum mapping unit of 25 hectares and a minimum feature width is 100 meters, and in raster format with a 100×100-m pixel resolution. The

approaches used for CLC mapping vary by country depending on the available technology and access to regional land-cover information (i.e., aerial photographs, local knowledge, and statistics), and range from manual image interpretation via supervised classification of satellite images (i.e. Landsat, SPOT) to bottom-up combination and generalization of existing national datasets. A CLC map has been released for the reference years 1990, 2000, 2006, 2012 and 2018, with a thematic accuracy of 86–98% depending on the country (Aune-Lundberg and Strand, 2021; Baudoux et al., 2021). The land-use trajectory approach was then applied to analyze the land-use dynamics in the catchment area over the hydrological simulation period of 2006−2018. The derived CLC maps of the catchment, available for the years 2006, 2012 and 2018, were integrated in ArcMap 10.8, and the land-use trajectory change was examined pixel by pixel using the overlay method (Nkwasa et al., 2020). Six land-use categories were identified in the catchment, and no interannual changes in the land-use classes and their corresponding area proportion were detected over the study period of 2006−2018. The catchment is mainly covered by broad-leaved and coniferous forests, amounting to 74.6% and 9.9% of its area, respectively, followed by pastures (8.1%), moors and heathland (5%), and sparse transitional woodland-shrub and agricultural lands (around 1% each) (**Figure 8c**). All land-use categories were reclassified into land-use classes that are identifiable in the SWAT land-use database (**Table 4**).

Table 3. Land-use categories of the Baget basin from Corine Land Cover database and the reclassified classes for the ISPEEKH model

Land-use CLC description	CLC Code	Land use (%)	Land-use SWAT description	Land-use SWAT code
Pastures	231	8.3%	Pasture	PAST
Complex cultivation patterns	242	1.2%	Agricultural land-generic	AGRL
Broad-leaved forest	311	74.6%	Forest-Deciduous	FRSD
Coniferous forest	312	9.7%	Forest-Evergreen	FRSE
Moors and heathlands	322	5.0%	Range grasses temperate mountain systems	RNGE_TEMS
Transitional woodland-shrub	324	1.3%	Range brush temperate mountain systems	RNGB_TEMS

4.2.4.3 Soil

A soil map of the Baget catchment was derived from the Food and Agriculture Organization (FAO) Digital Soil Map of the World (with a scale of 1:5,000,000), available at

https://www.fao.org/soils-portal/soil-survey/soil-maps-and-databases/faounesco-soil-map-of-the-world/en/. A single soil class termed ‘Bd77-1-2b-6424’ was identified over the catchment according to the FAO soil map. It corresponds to the soil of sequence number ‘6424’ in the SWAT+ soil database, which has a sandy-loam texture. We overlayed both soil and lithology maps, and named the soil type covering the catchment karst areas ‘Bd77-1-2b-6424-Karst’ instead of ‘Bd77-1-2b-6424’ in the soil map attributes (**Figure 8d**) so as to separate karst and non-karst HRUs based on the catchment lithology and send the surface runoff and unsaturated flows in the soil generated at HRU level to their respective groundwater reservoirs, following the ISPEEKH conceptual representation of the water balance flow processes (**Figure 7**). Accordingly, we updated the SWAT+ “usersoil” database and corresponding look-up table. In addition, local estimations of the hydraulic conductivity of the soil overlaying the epikarstic zone were obtained by measuring infiltration at 30 sampling points with 30s- and 60s-time intervals, which yielded an average hydraulic conductivity value of 29.48 $mm.hr^{-1}$. This value closely matched the average value of the soil hydraulic conductivity (29.62 $mm.hr^{-1}$) inferred from the FAO soil map and SWAT+ soil database.

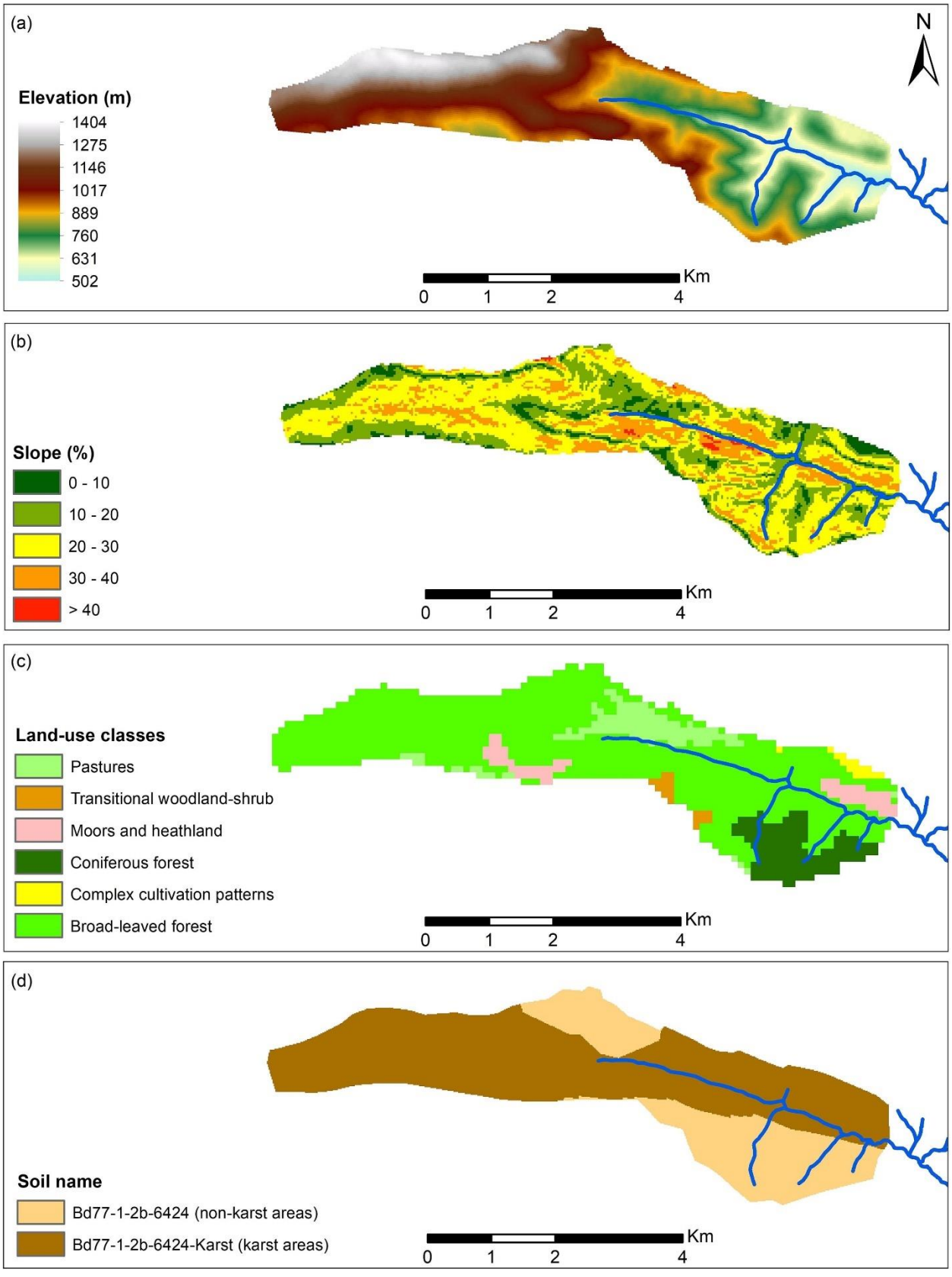
(a)
Elevation (m)
1404
1275
1146
1017
889
760
631
502
N
Km
0 1 2 4
(b)
Slope (%)
0 - 10
10 - 20
20 - 30
30 - 40
> 40
Km
0 1 2 4
(c)
Land-use classes
Pastures
Transitional woodland-shrub
Moors and heathland
Coniferous forest
Complex cultivation patterns
Broad-leaved forest
Km
0 1 2 4
(d)
Soil name
Bd77-1-2b-6424 (non-karst areas)
Bd77-1-2b-6424-Karst (karst areas)
Km
0 1 2 4

Figure 8. The Baget catchment properties in terms of: (a) topography, (b) slope, (c) land use/land cover, and (d) soil.

.

We used QSWAT+ 2.0.3 in QGIS to set up the Baget catchment model based on the input DEM, land-use and soil maps, slope characteristics, and catchment outlet location. All the land-use, soil, and slope classes were maintained in the final HRU definition, resulting in 225 HRUs of which 116 are karst and 109 are non-karst. The HRUs delineation followed the areal distribution of the karst and non-karst regions of the catchment, with karst HRUs accounting for nearly 70% of the catchment area and non-karst HRUs for the remaining 30% (**Figure 9**).

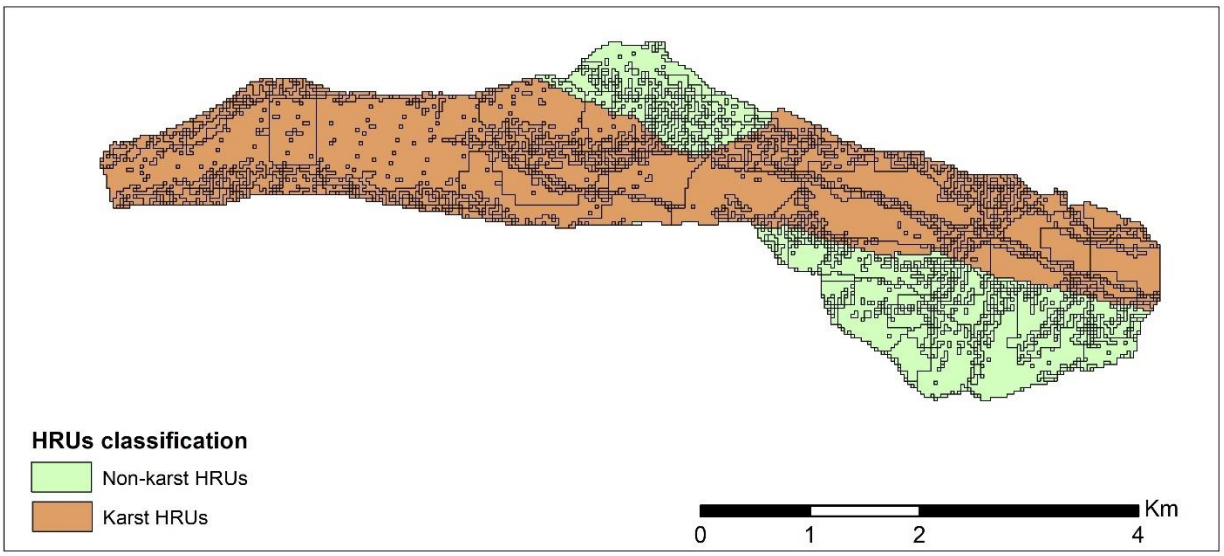

Figure 9. The HRUs of the Baget catchment ISPEEKH model, defined based on the spatial distribution of karst and non-karst areas inferred from the catchment lithology.

4.2.4.4 Hydrometeorological variables

Daily precipitation data in the Baget catchment for the period of 01/01/2006–31/12/2018 were derived at 39 grid points using the COMEPHORE (*COmbinasion en vue de la Meilleure Estimation de la Précipitation HOraiRE*) product of the French weather forecasting agency Météo-France (**Figure 5b**). COMEPHORE is an hourly reanalysis of surface precipitation accumulation over France at a 1-km spatial resolution, which merges data from 24 radars of the French network that provides pseudo-CAPPI (Constant Altitude Plan Position) images every 5 minutes over a 512×512-km area, with observations from nearly 4200 rain gauges, including 1200 gauges at

hourly time step (Fumière et al., 2020; Le Roy et al., 2020). A detailed description of COMEPHORE and its application over France is provided by Tabary (2007) and Tabary et al. (2012). In addition, daily time series of minimum and maximum air temperature, relative humidity, wind speed, and solar radiation for the period of 01/01/2006–31/12/2018 were extracted at four grid points adjacent to the Baget catchment area using the 8-km SAFRAN (*Système d'Analyse Fournissant des Renseignements Adaptés à la Nivologie*) product of Météo-France (**Figure 5b**). The SAFRAN analysis system of atmospheric variables in France is detailed in Durand et al. (1993) and Quintana-Segui et al. (2008). Daily measurements of precipitation, air temperature, relative humidity, wind speed, and solar radiation acquired from the 'Météo-France' weather station of "Saint Girons" (43°00'19"N; 01°06'25"E; altitude: 414 m.s.l., nearly 8.3 km downstream of the Baget catchment outlet) were also used to run ISPEEKH and compare the hydrological simulation results to those obtained from the model driven by the COMEPHORE and SAFRAN meteorological variables.

Streamflow data required for the calibration and validation of the hydrological model were retrieved from the gauging station B1, located 60 m downstream of the Baget catchment spring (**Figure 5a**). At this station, stream water level is measured continuously at 30-min interval by a float-type water-level sensor (OTT Thalimedes; Loveland, CO, USA), and discharge is calculated using the rating curves adopted by Mangin (1975): a linear function for $H < 0.24\ m$ [$Q\ (m^3.s^{-1}) = 2H - 0.45;\ R^2 = 1$] and a polynomial function for $H > 1.3\ m$ [$Q\ (m^3.s^{-1}) = 17.3H3 - 52.6H2 + 65.4H - 24.1;\ R^2 = 1$]. The daily discharge data recorded from 01/01/2006 to 31/12/2018 were used in accordance with the available weather data. Under this period, discharge values ranged between 0.04 to 8.95 $m^3.s^{-1}$, with an average of 0.45 $m^3.s^{-1}$.

4.2.3 Model calibration and validation

The ISPEEKH model was run using the corrected COMEPHORE precipitation data and the temperature, wind speed, solar radiation, and relative humidity datasets of SAFRAN for the period of 2006−2018. The model was then calibrated using the daily streamflow recorded at gauging station B1 from 2006 to 2013 (with 2 years of warm-up), and validated for years 2014−2018. Parameter sensitivity analysis and model calibration were performed with the Parameter Estimation (PEST) software for the automated calibration of the 16 parameters of the ISPEEKH groundwater module and other parameters that affectthe surface and unsaturated zone flows. PEST applies a regulization process and nonlinear techniques (the Gauss-Marquardt-

Levenberg algorithm) to change the values of the calibration parameters and minimize the residual between the simulated and observed datasets (Doherty, 2018). It can also perform a local sensitivity analysis using the paramater derivatives in the Jacobian matrix at each iteration and provide composite sensitivity measures of the model parameters influence on the catchment streamflow (Bailey et al., 2022).

We used the Nash-Sutcliffe Efficiency factor (NSE), coefficient of determination (R^2), and percent of bias (PBIAS) to evaluate the model performance in simulating the catchment daily discharge according to Moriasi et al. (2015), in addition to the Kling-Gupta efficiency coefficient (KGE) (Gupta et al., 2009). KGE is a multi-objective function that has been increasingly applied to evaluate modeling performance in karst hydrology due to its limited bias to high streamflow compared to the commonly used NSE. The KGE function images the Euclidian distance from the ideal point in the scaled space of the three components: the linear correlation coefficient between the observed and simulated discharge, the ratio between the mean observed and mean simulated discharge, and the ratio between the standard deviation of each of the simulated and observed streamflow (Ollivier et al., 2021).

4.2.5 Preliminary catchment water balance assessment

A preliminary hydrological simulation was conducted to evaluate the annual water balance of the Baget catchment for the period of 2006−2018, using the available meteorological input data and the Penman-Monteith approach for evapotranspiration estimation. During this period, the mean annual COMEPHORE precipitation over the catchment was 1235 mm, and the mean annual discharge measured at the gauging station B1 was 1086 mm, compared to mean annual simulated discharge of 590 mm and actual evapotranspiration of 591 mm. Consequently, a negative water balance discrepancy (difference between observed and simulated annual discharge) equivalent to 40% of mean annual precipitation was identified, suggesting either a significant uncertainty in the precipitation records, streamflow measurements and or evapotranspiration estimates, or an additional water contribution from a larger groundwater recharge area or interbasin groundwater flow. The possibility of additional water contribution was first ruled out based on the work of Mangin (1975) who established that the Baget catchment is fed by a groundwater recharge area of 13.25 km^2 and does not gain water from neighboring catchments. The streamflow data of years 2006−2018 were then compared to past measurements at the outlet gauging station B1 between 1969 and 2005. The discharge values had similar order of magnitude at seasonal and annual scales

(e.g., mean annual discharge of 1135 mm for years 1969−1973, 1010 mm for years 2000−2005), showing that the uncertainty due to streamflow magnitude is unlikely to generate the water balance discrepancy. Next, the SAFRAN analysis system was applied to derive daily time series of potential evapotranspiration with the Penman-Monteith approach and actual evapotranspiration over the Baget catchment. The mean annual PET (687 mm) and ET_a (591 mm) simulated with ISPEEKH based on the Penman-Monteith method were comparable to the PET (796 mm) and ET_a (667 mm) values produced from SAFRAN in the period of 2006−2018, indicating that the uncertainty of the evapotranspiration estimation is insufficient to justify the water balance discrepancy.

Thus, the difference in the annual water balance was attributed to inappropriate precipitation data. It appears that the water balance discrepancy has been masked in previous studies (e.g., Sivelle et al., 2019) whereby the Baget catchment streamflow was simulated using the rainfall-runoff model KarstMod driven solely by precipitation input of the Météo-France Saint Girons weather station (43°00'19"N; 01°06'25"E; 414 m m.s.l., 8.3 km from the Baget catchment outlet, **Figure 5b**) without considering the land use and evapotranspiration contribution to the water balance. The mean annual precipitation recorded at this station in the for the 2006−2018 period was 969 mm, which is too low to sustain the observed streamflow at the catchment outlet when other flow determinants (e.g., land use, soil) are incorporated in spatially-distributed hydrological modeling. In addition, the historical precipitation recorded at various observational points of the Météo-France network of weather stations surrounding the study area was also examined. A mean annual precipitation of 1050−1270 mm was determined based on the nearest stations to the catchment (excluding Saint Girons station) at altitudes between 565 and 735 m. However, a mean precipitation of 1750 mm has been previously reported at the Balagué meteorological station (42°58'06.5"N; 01°00'39"E; 658 m m.s.l.) situated 0.5 km from the Baget catchment and monitored in the 1973−1999 period (Johannet et al., 2008). Therefore, it was concluded that the precipitation datasets from the rain gauges in the vicinity of the catchment and COMEPHORE do not represent the precipitation regime of the Baget catchment where the altitude reaches 1000−1400 m m.s.l. in the highlands of the spring groundwater contribution zone. This outcome can be further validated by the findings of Fumière et al. (2020) that COMEPHORE precipitation, derived based on the combination of rain gauges and radar data, is underestimated

in the Pyrénées region compared to the rest of France, due to precipitation under catch and low radar coverage in the mountainous areas.

In order to adjust the COMEPHORE gridded precipitation data over the simulation period of 2006−2018, we calculated an orographic correction multiplicative factor of 1.44 by "Doing Hydrology Backward (DHB) (Kirchner's methodology) (Khan and Koch, 2018) based on the rearranged water balance Equation (8) with the SAFRAN gridded actual evapotranspiration data and discharge at the outlet gauging station B1. Following the approach outlined in Khan and Koch (2018), both the groundwater losses and change of glacier ice volume were considered null for the Baget catchment.

$$OCF_{multiplicative} = \frac{PCP_{true}}{PCP_{obs}} = \frac{Q_{obs} + ET_a + G_w + \Delta g}{P_{obs}} \quad (8)$$

where PCP_{true} is the true (corrected) aerial precipitation, PCP_{obs} is the observed (uncorrected) precipitation, Q_{obs} is the observed discharge of the gauged catchment, ET_a is the actual evapotranspiration, G_w represents groundwater recharge losses, and Δg represents the losses or gains of glacier ice volume.

4.2.6 Land-use change scenarios

Following the calibration and validation of the ISPEEKH model, alternative land-use change scenarios were simulated in order to investigate their potential impact on the Baget catchment hydrology and water resources availability. Land abandonment in the Baget catchment has resulted in substantial degeneration of pasture land and growing recolonization of forests (Ulloa-Cedamanos et al., 2022). Natural afforestation due to the abandonment of pastoral and arable lands has been the main land change trajectory in European mountains, particularly in the Pyrénées, with several scenario-based studies anticipating further expansion of the forest cover in the future. In addition, wood production and agro-pastoralism have been established as drivers of future land-use/land-cover changes in the French Pyrénées (Houet et al., 2017). Therefore, the following land-use change scenarios were developed for the Baget catchment by considering further evolution of the landscape closure by natural afforestation (Scenario 1) and deforestation for local wood production and or pastoral activities as plausible land management practices (Scenarios 2 to 5):

- Scenario 1: supposes full catchment afforestation by converting pastures, cultivation patterns, moors and heathland, and transitional woodland-shrub to broad-leaved forests, that is 15.5% increase in broad-leaved forest area.
- Scenario 2: supposes that only forest areas in the karst regions of the catchment will be replaced by transitional woodland-shrub due to wood production, that is 57.6% increase in transitional woodland-shrub area.
- Scenario 3: supposes that all forest areas in the catchment will be converted to transitional woodland-shrub due to wood production, that is 84.4% increase in transitional woodland-shrub area.
- Scenario 4: supposes that only forest areas in the karst regions of the catchment will be replaced by pastures for animal grazing, that is 57.6% increase pasture area.
- Scenario 5: supposes that all forest areas in the catchment will be converted to pastures for animal grazing, that is 85.8% increase pasture area.

  The land-use change scenarios of deforestation for wood production and pastoral activities were first each applied to the karst areas of the study catchment in order to evaluate their impact on the spring flow component of streamflow, and were then extended to the entire catchment in order to assess their impacts on both streamflow components: the spring flow of the karst aquifer and surface runoff draining the non-karst areas of the catchment.

The distribution of the land-use classes for each of the five scenarios is shown in **Figure 10a-e**. These scenarios were generated by modifying the land-use and plant communities in the model input files to maintain the original spatial set-up of the HRUs, and implemented under the same meteorological data used for calibration of the baseline ISPEEKH model. This approach, called "fixing-changing method" by changing the land use maps and keeping other inputs constant, has been employed extensively in land-use change impact studies to uncover the responses of hydrological components to land-use change scenarios (Cecílio et al., 2019; Gashaw et al., 2018; Rigby et al., 2022).

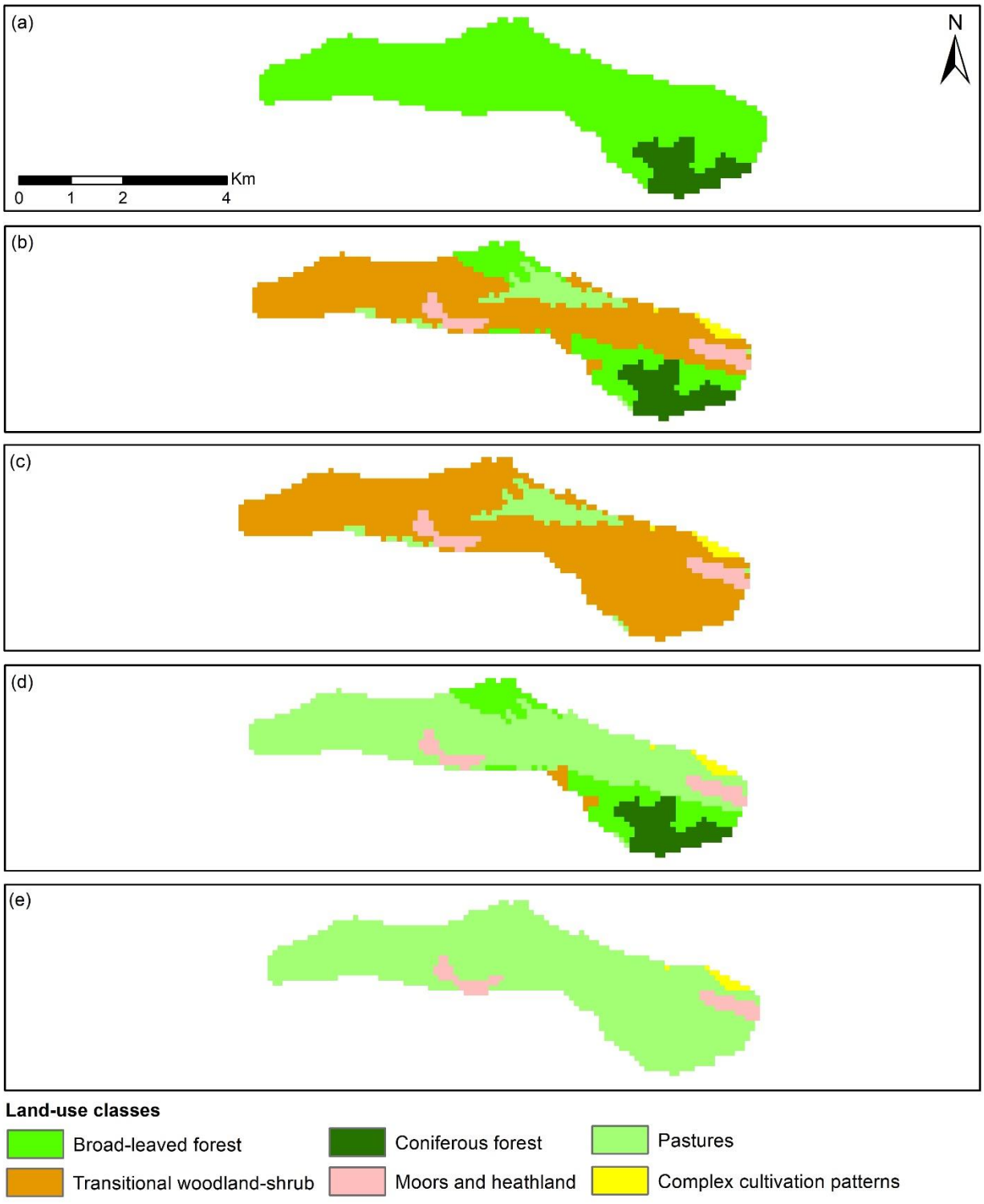

Figure 10. Land-use classes corresponding to land-use change scenarios simulated in the Baget catchment, with: (a) Scenario 1 (afforestation of the full catchment area), (b) Scenario 2 (forest-to-transitional woodland/shrub conversion in the karst areas of the catchment), (c) Scenario 3 (forest-to-transitional

woodland/shrub conversion), (d) Scenario 4 (forest-to-pasture transition in the karst areas of the catchment), and (e) Scenario 5 (forest-to-pasture transition).

4.3 Results and discussion

4.3.1 Annual water balance

The main water balance fluxes of the Baget catchment were simulated using ISPEEKH over the period of 2008−2018 (**Table 4**). The mean annual catchment ET_a was 601 mm, equivalent to 33% of average annual precipitation (1824 mm), which is comparable to the mean annual ET_a estimate (667 mm) from SAFRAN for the catchment. The mean annual catchment Q_{STREAM}, formed by the karst spring flow and surface runoff generated over non-karst terrains, amounted to 1216 mm, which corresponds to 67% of average annual precipitation. The mean annual Q_{SPRING} (972 mm) represented nearly 80% of water yield, whereas SURQ only contributed to the remaining 20%. Additionally, the mean annual RECH (972 mm) was equal to Q_{SPRING}, demonstrating the ability of ISPEEKH to successfully simulate groundwater storage and spring discharge from the recharge to the karst reservoirs based on the water balance conservation. These figures seem to provide a realistic representation of the Baget catchment drainage characteristics, where the Las Hountas perennial spring generates most of the streamflow downstream of the catchment outlet.

Table 4. Annual water fluxes in the Baget catchment (mm.year^{-1}) simulated by ISPEEKH for the period of 2008−2018. PCP: precipitation; ET_a: actual evapotranspiration; $SURQ$: surface runoff; $RECH$: groundwater recharge; Q_{SPRING}: spring flow; Q_{STREAM}: streamflow

Year	PCP	ET_a	SURQ	RECH	Q_{SPRING}	Q_{STREAM}
2008	1558	573	175	789	786	969
2009	1499	645	146	688	693	849
2010	1675	635	155	858	853	1019
2011	1572	624	144	771	762	919
2012	1516	639	141	742	751	906
2013	2672	598	440	1567	1557	2029
2014	2143	567	313	1198	1195	1535
2015	1818	598	268	988	1003	1297
2016	1680	569	176	911	912	1111
2017	1657	580	154	845	824	1001
2018	2271	584	355	1333	1353	1744
Average	1824	601	224	972	972	1216

4.3.2 Streamflow and karst aquifer water fluxes

The fitted values of the calibrated parameters are reported in **Table 5.** The most sensitive parameter was found to be the emptying exponent of the conduit-to-spring flow (α_{cs}), which is consistent with the discharge characteristics of the conduit-dominated Baget catchment. The observed and simulated daily streamflow hydrographs at the Baget catchment outlet for years 2008−2018 are illustrated in **Figure 11**. The calculated values of NSE (0.673 in calibration; 0.653 in validation), R^2 (0.677 in calibration; 0.69 in validation), and PBIAS (0.7% in calibration; -13.83% in validation) indicate a satisfactory model performance for daily streamflow simulation according to Moriasi et al. (2015). Moreover, The KGE values were 0.789 in calibration and 0.782 in validation. Overall, ISPEEKH adequately reproduced the karst hydrological response to heavy precipitation events during the high-flow periods by preserving the rising and recession limbs of the observed hydrograph. It also provided a reasonably accurate estimation of the low-flow magnitude. Yet, several peaks (generally those larger than 3 $m^3.s^{-1}$) were underestimated during the calibration period, whereas the model estimated the peaks more adequately in the validation period. At monthly scale, the model performance was very good (Moriasi et al., 2015) with NSE and R^2 values of 0.924 in calibration and 0.87−0.897 in validation. Monthly KGE was 0.945 in calibration and 0.853 in validation, whereas monthly PBIAS remained comparable to daily PBIAS with 0.726% in calibration and -13.69% in validation (**Figure 12**). In comparison, the KarstMod model of the Baget catchment proposed by Sivelle et al. (2019) yielded daily NSE values of 0.53 and 0.51, and daily KGE values of 0.58 and 0.61, for calibration and validation, respectively.

Moreover, the adequacy of the calibrated ISPEEKH model in simulating evapotranspiration was assessed by comparing the daily simulated evapotranspiration to the SAFRAN-based evapotranspiration in the catchment in years 2008−2018. The NSE, R^2, and PBIAS values were 0.729, 0.799 and 8.94%, respectively, for calibration, and 0.813, 0.86 and 11.1%, respectively, for validation, indicating an adequate model performance (**Figure 13**).

Table 5. Calibration ranges and fitted values of the calibrated parameters for the ISPEEKH model in the Baget catchment

Parameter	Description	Unit	Calibration range	Sensitivity rank	Fitted value
$Esco$	Soil evaporation factor	-	0-1	13	0.95
$Epco$	Plant uptake factor	-	0-1	7	0.99
$Perco$	Soil percolation coefficient	-	0.1-1	2	0.15(1) 0.3(2)
$h_{E,0}$	Initial water level the in epikarst	mm	1-25	15	20
$h_{M,0}$	Initial water level the in matrix	mm	1-25	4	20
$h_{C,0}$	Initial water level the in conduit	mm	1-25	5	20
E_{min}	Minimum water level for epikarst flow activation	mm	0-1	19	0.1
α_{EM}	Emptying exponent of the epikarst-matrix flow	-	0.5-1	16	0.792
α_{EC}	Emptying exponent of the epikarst-conduit flow	-	0.5-2	3	1.968
α_{MC}	Emptying exponent of the matrix-conduit flow	-	0.5-2	6	1.098
α_{MS}	Emptying exponent of the matrix-spring flow	-	0.5-1	12	0.638
α_{CS}	Emptying exponent of the conduit-spring flow	-	0.5-2	1	1.863
k_{EM}	Discharge coefficient of the epikarst-matrix flow	mm.day-1	0.0001-0.01	17	0.001
k_{EC}	Discharge coefficient of the epikarst-conduit flow	mm.day-1	0.0001-0.09	9	0.033
k_{MC}	Discharge coefficient of the matrix-conduit bidirectional flow	mm.day-1	0.0001-0.05	11	0.011
k_{MS}	Discharge coefficient of the matrix-spring flow	mm.day-1	0.0001-0.01	14	0.004
k_{CS}	Discharge coefficient of the conduit-spring flow	mm.day-1	0.0001-0.09	10	0.077
δ_E	Recharge delay from the soil to the epikarst	day	0.5-2	18	1
δ_M	Recharge delay from the soil to the matrix	day	1-3	8	2

(1) this value is set for the karst HRUs; (2) this value is set for the non-karst HRUs

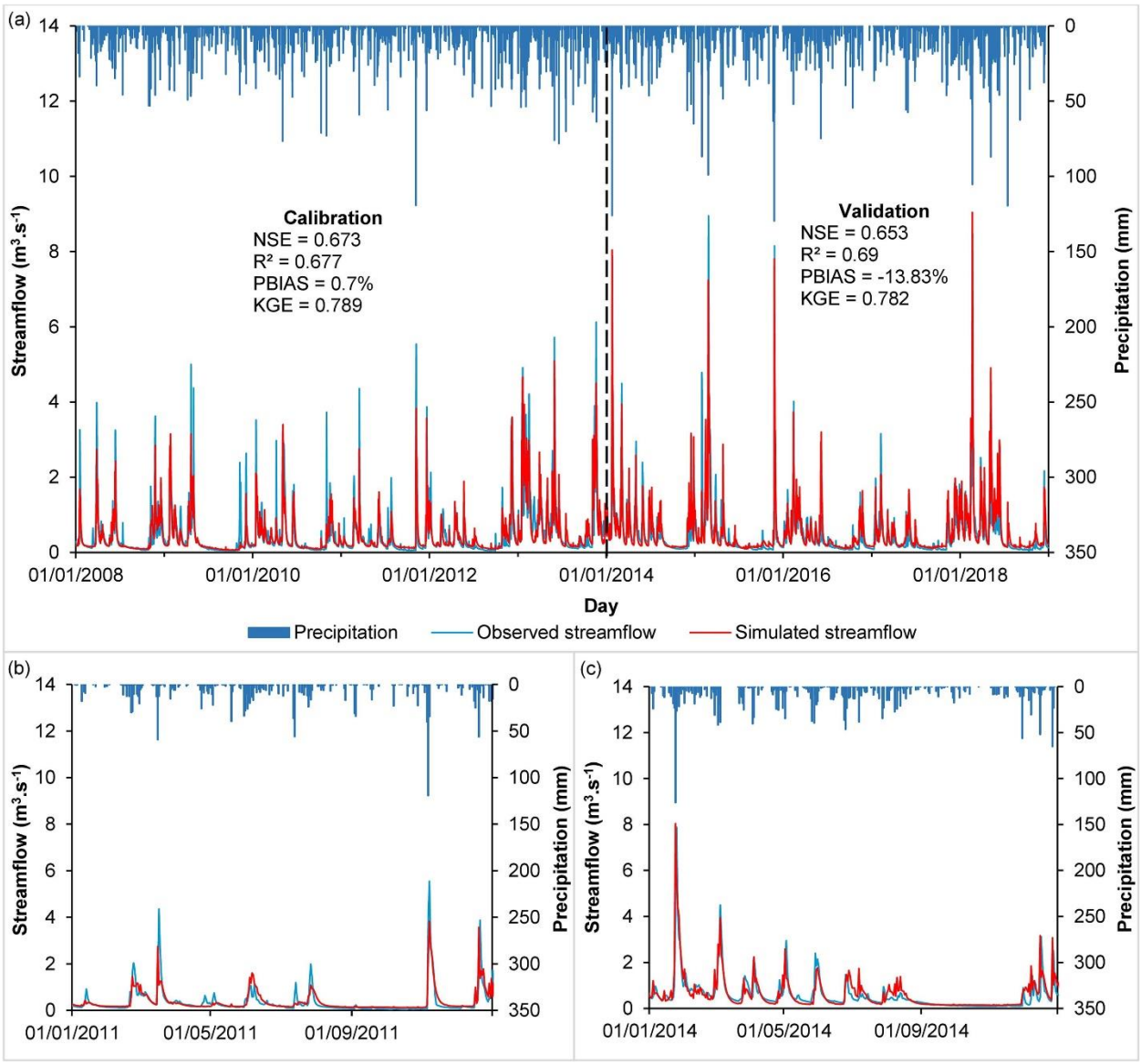

Figure 11. (a) Observed and simulated daily streamflow at the Baget catchment outlet (station B1) for the calibration period (January 2008–December 2013) and validation period (January 2014–December 2018); (b) observed and simulated daily streamflow at station B1 for year 2011; (c) observed and simulated daily streamflow at station B1 for year 2014.

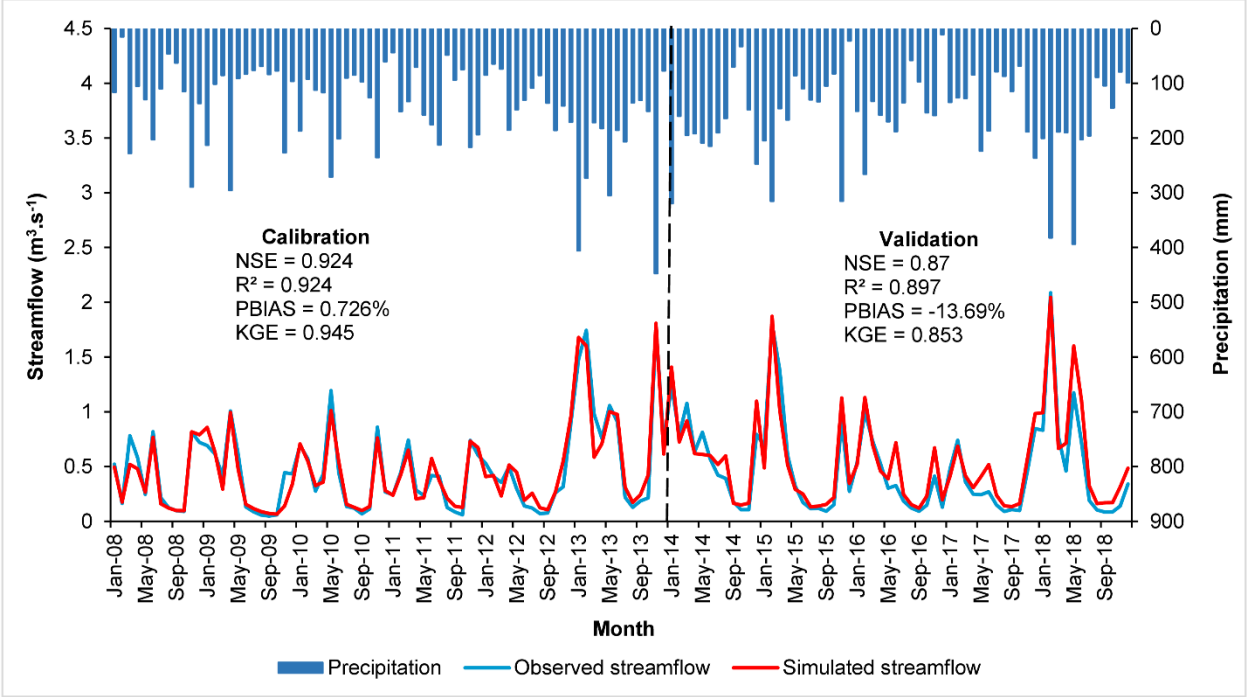

Figure 12. Observed and simulated monthly streamflow at the Baget catchment outlet (station B1) for the calibration period (January 2008–December 2013) and validation period (January 2014–December 2018).

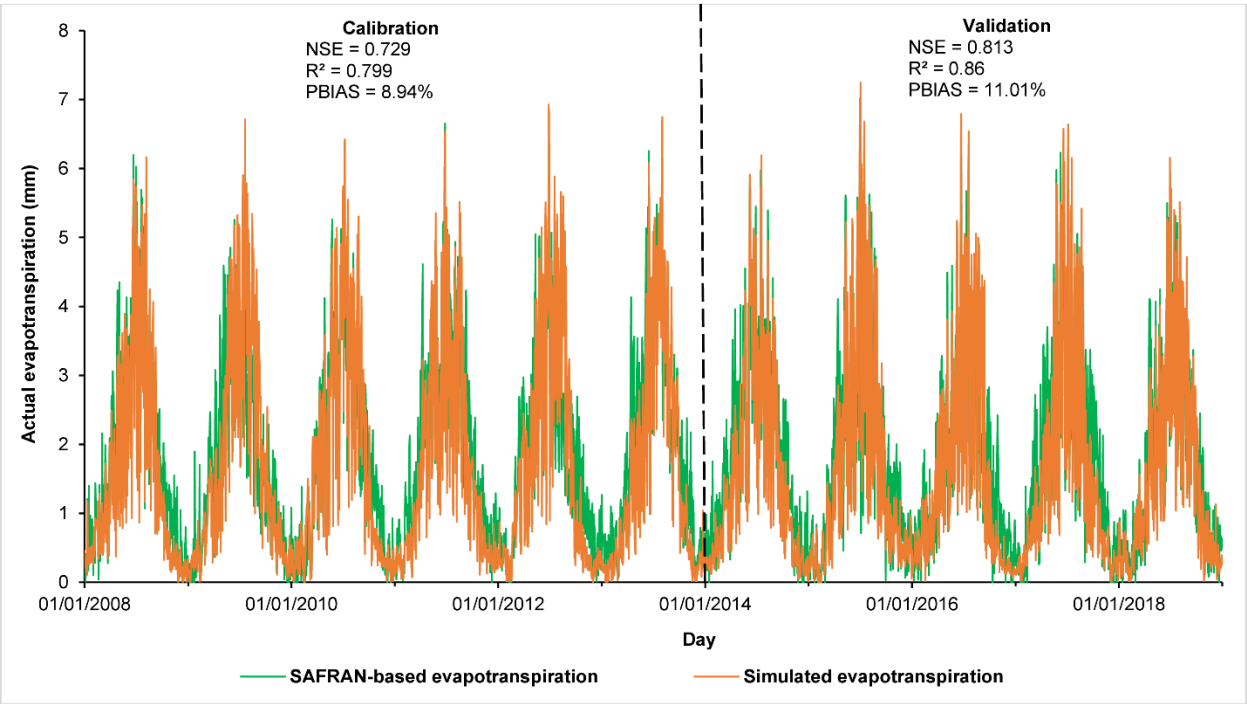

Figure 13. SAFRAN-based and simulated daily evapotranspiration of the Baget catchment for the calibration period (January 2008–December 2013) and validation period (January 2014–December 2018).

ISPEEKH successfully modeled different flow processes of the epikarst, conduit, and matrix. The simulated epikarst recharge and flow to the conduit reservoir reflect a high

connectivity between the epikarst and underlying vadose zone through the conduits, as almost all simulated flow through the epikarst reservoir is transferred to the conduit reservoir with low inflow to the matrix (**Figure 14**). Observations of the daily water storage in the matrix and conduits are not available for the Baget catchment. Nonetheless, the simulated water levels in the matrix and conduit reservoirs revealed that ISPEEKH reproduced the conduit and matrix water storages by following flow patterns that are consistent with the characteristics of a conduit-dominated karst spring. Water level fluctuations in the conduit reservoir showed a fast rise of the water storage followed by a rapid water transfer to the spring during the high-flow period, and an attenuated storage in the low-recharge period (**Figure 15a**). Conversely, **Figure 15b** showed a lower variability of the simulated matrix storage in comparison to the conduit, indicating slow transfer time and low matrix discharge to the spring, with a gradual water storage drop during the low-flow season.

The emptying exponent α_{MC} was found to be nearly linear (**Table 5**), indicating that the exchange flow rate between the conduit and matrix is generally governed by the hydraulic conductivity of the fissured system and the difference between the water levels of the matrix and conduit reservoirs. The simulated exchange flow rate (Q_{MC}) was mostly positive (flow from the matrix to the conduit) as water storage in the matrix reservoir remained less variable and frequently higher than the conduit reservoir water storage, whereas Q_{MC} was negative (flow from the conduit to the matrix) when the water level in the conduit reservoir surpassed the matrix water level during the high-flow period (**Figure 16a-b**). The ratio of the matrix-to-conduit exchange volume to total spring flow varied between 5% and 9% during the 2008–2018 period, with an average value of 8%. Moreover, the matrix contribution to the monthly karst discharge amounted to 4–7% between November and June, and increased to 22% during the July-to-October low-flow period. In addition, the conduit outflow followed a non-linear law and accounted for most of the spring discharge (92–95% of spring flow in the November-to-June period and 75–83% of spring flow in the July-to-October period), while the direct contribution of the matrix to spring flow was negligible (**Figure 16c**). These values generally agree with the study of Sivelle et al. (2019) in which the matrix-conduit flow contribution to spring flow of the Baget catchment was estimated at 2–5% annually and up to 25% in months of low rainfall, based on lumped rainfall-runoff modeling with KarstMod driven by input precipitation of years 1970–2016 from the meteorological station of Saint Girons. The authors adopted a linear law for the matrix-conduit

flow exchange mechanism and set all the spring discharge through the conduit reservoir using a non-linear law.

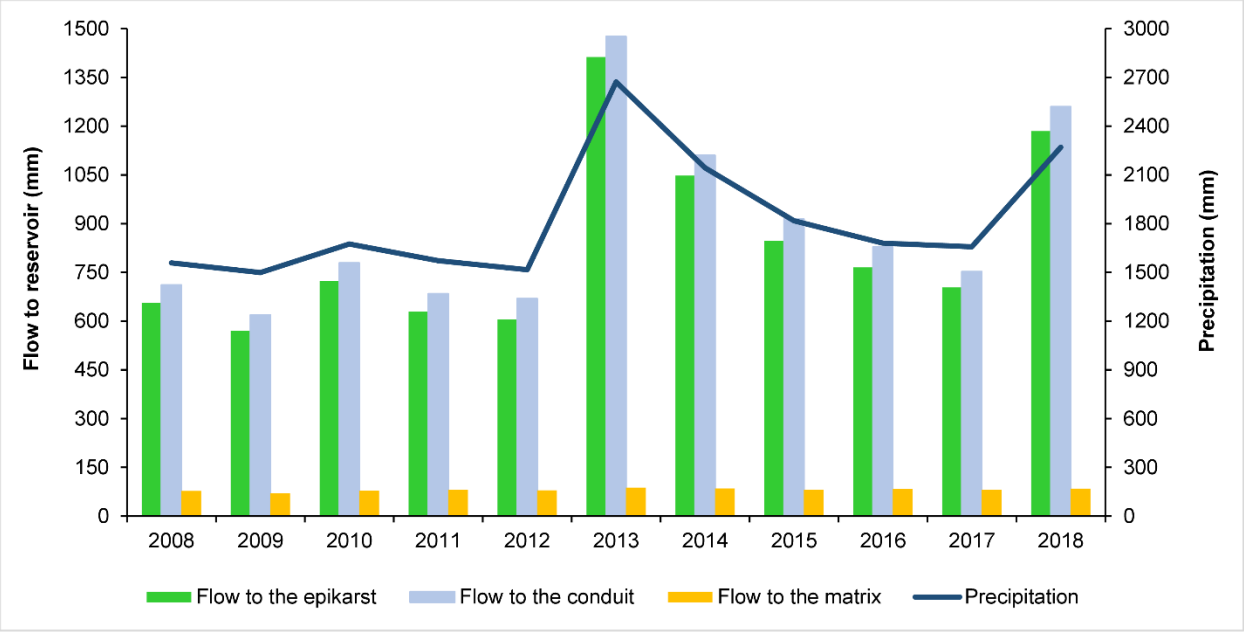

Figure 14. Annual water inflows to the epikarst, conduit, and matrix reservoirs (mm.year^{-1}) simulated by ISPEEKH in the Baget catchment for the period of 2008−2018.

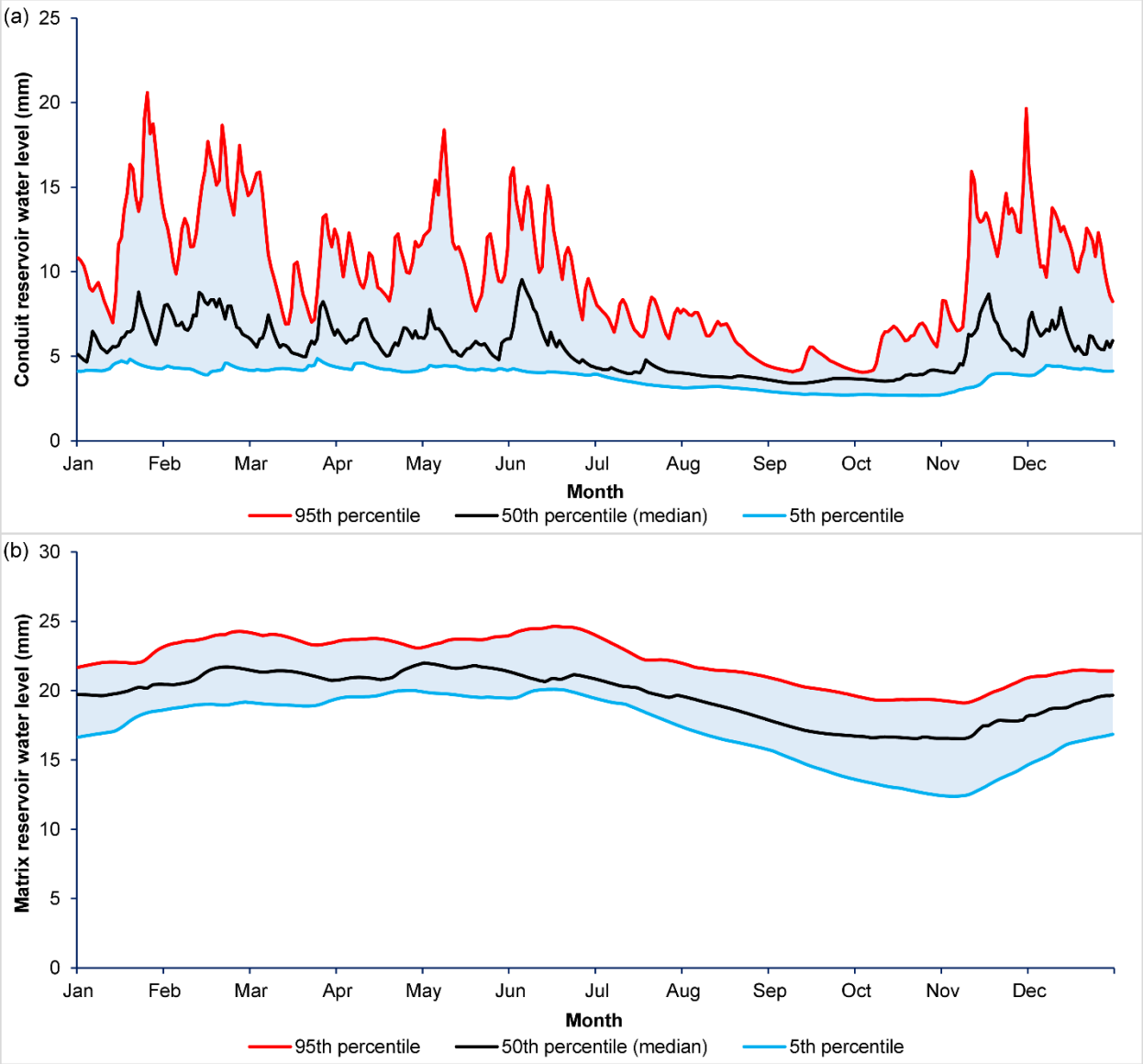

Figure 15. (a) 5th, 50th and 95th percentiles of the water level in the conduit reservoir over the simulation period (2008−2018); (b) 5th, 50th and 95th percentiles of the water level in the matrix reservoir over the simulation period (2008−2018).

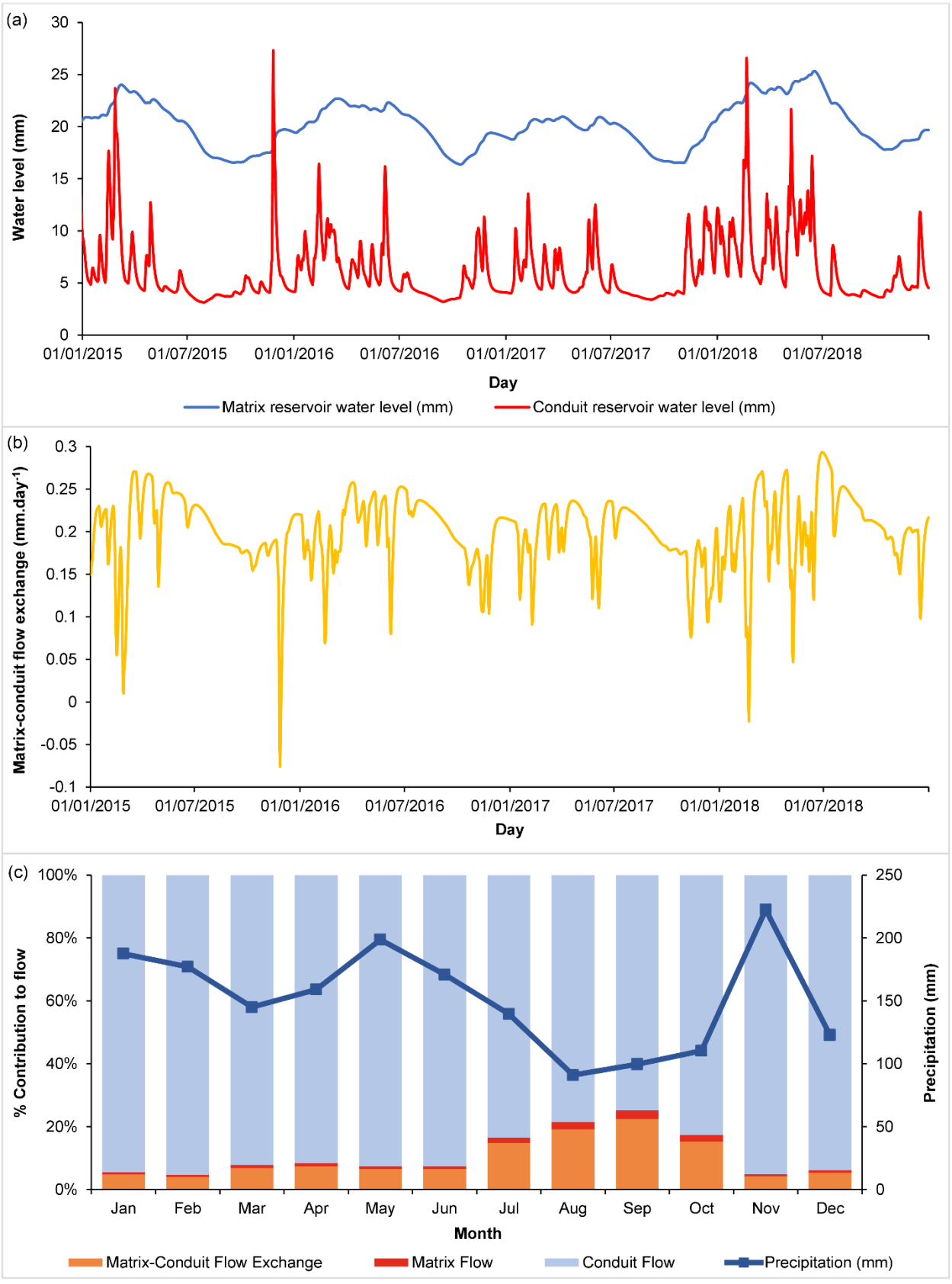
(a)
Water level (mm)
30
25
20
15
10
5
0
01/01/2015
01/07/2015
01/01/2016
01/07/2016
01/01/2017
01/07/2017
01/01/2018
01/07/2018
Day
Matrix reservoir water level (mm)
Conduit reservoir water level (mm)
(b)
Matrix-conduit flow exchange (mm.day-1)
0.3
0.25
0.2
0.15
0.1
0.05
0
-0.05
-0.1
01/01/2015
01/07/2015
01/01/2016
01/07/2016
01/01/2017
01/07/2017
01/01/2018
01/07/2018
Day
(c)
% Contribution to flow
100%
80%
60%
40%
20%
0%
Jan
Feb
Mar
Apr
May
Jun
Jul
Aug
Sep
Oct
Nov
Dec
Month
Precipitation (mm)
250
200
150
100
50
0
Matrix-Conduit Flow Exchange
Matrix Flow
Conduit Flow
Precipitation (mm)

Figure 16. (a) Simulated daily water levels in the matrix and conduit reservoirs in years 2015−2018; (b) daily matrix-conduit exchange flow in years 2015−2018; (c) average monthly contribution of conduit flow, matrix flow, and matrix to conduit flow to spring discharge over the study period (2008−2018).

The modified SWAT models reported in the literature were tested across karstified watersheds with distinct climatic conditions, karst features, and recharge areas ranging from less than 30 km^2 to larger than 8,000 km^2. Moreover, they were calibrated at daily and or monthly scale using different calibration/validation periods (months to years) and single to multi-gauge streamflow calibration. The modified SWAT models that were calibrated at daily scale showed contradictory performances (Moriasi et al., 2015), implying that modified SWAT modeling approaches did not always guarantee an improved simulation of the karst catchment streamflow. More than half of the models had satisfactory (i.e., $0.5 < NSE \leq 0.7$) (Nguyen et al., 2020; Nikolaidis et al., 2013; Palanisamy and Workman, 2015; Wang and Brubaker, 2014) to strong performances (i.e., $NSE > 0.7$) (Geng et al., 2021; Nguyen et al., 2020; Palanisamy and Workman, 2015; Wang et al., 2019b) with respect to daily streamflow simulation, while some studies reported poor performances (i.e. $NSE \leq 0.5$) even at monthly scale (Afinowicz et al., 2005; Baffaut and Benson, 2009; Malagò et al., 2016). In comparison, ISPEEKH showed a satisfactory performance of the daily discharge simulation over 11 years while incorporating additional karst flow processes that allowed an explicit representation of the karst recharge pathways and non-linear dynamics of the epikarst, matrix and conduits. Jeannin et al. (2021) also evaluated the performance of thirteen models commonly used in karst hydrology, including neural networks, reservoir-based, semi-distributed and fully-distributed groundwater models, in simulating the spring discharge of the Milandre karst hydrogeological system (MKHS) located in Northern Switzerland and fed by a recharge area of 13 km^2. The lumped reservoir model Gardenia and semi-distributed model VarKarst were the only two models to score NSE and KGE values of ∼0.8, while the remaining models reported NSE values between -0.24 and 0.65, and KGE values from 0.37 to 0.72 with variations of 0.05 to 0.08 between daily and hourly simulations. It should also be noted that only the KRM_1 semi-distributed model accounted for the land-use spatial variability despite not producing better results than the other models. Thus, the semi-distributed modeling scheme implemented in ISPEEKH could be a promising approach to simulate karst hydrology considering the spatial variability of the flow determinants.

4.3.3 Impact of land-use changes on annual and monthly water fluxes

The calibrated ISPEEKH model was used to simulate the hydrological response of the Baget catchment to five land-use change scenarios of afforestation and deforestation schemes. The average annual values of the catchment main hydrological components were then compared for the baseline land use and the different land-use change scenarios (**Table 6**). Under Scenario 1, which represents afforestation of the full catchment area by 15.5% gain in broad-leaved forest cover, ET_a decreased from 601 to 592 mm.year^{-1} (-1.5%). In particular, afforestation would increase plant transpiration (E_{plant}) from 460 to 470 mm.year^{-1} (+2.17%), while reducing soil evaporation (E_{soil}) from 55 to 39 mm.year^{-1} (-29.1%) and canopy evaporation (E_{canopy}) marginally from 86 to 83 mm.year^{-1} (-3.49%). In addition, SURQ increased marginally to 227 mm.year^{-1} (3 mm increase; +1.33%), and RECH reached 976 mm.year^{-1} (4 mm increase; +0.41%) due to higher surface water infiltration to the epikarst in the catchment karstic areas. These minor changes in evapotranspiration, surface runoff and recharge rates resulted in a slight increase in Q_{STREAM} from 1216 to 1224 mm.year^{-1} (+0.66%).

Under forest-to-woodland/shrub transition in the karst areas of the catchment (Scenario 2), the mean annual ET_a decreased by 71 mm (-11.8%), with 105 mm decrease in E_{plant} (-22.9%), 14 mm increase in E_{canopy} (+16.3%), and 20 mm increase in E_{soil} (+36.4%). The mean annual RECH rose by 67 mm (+6.9%) due to an increase in epikarst recharge from surface runoff and soil water percolation in karst areas, followed by a subsequent 67 mm increase in Q_{STREAM}, which reached a mean annual value of 1284 mm (+5.3%). The changes in the hydrological components were more remarkable with woodland-shrub expansion over the entire catchment (Scenario 3). ET_a further decreased to 494 mm.year^{-1}, with lower E_{plant} (154 mm decrease; -33.5%) and higher E_{canopy} (17 mm increase; +19.3%) and E_{soil} (30 mm increase; +55.1%). RECH then reached 1048 mm.year^{-1} (76 mm increase; +7.6%) due to added recharge by soil lateral flow and percolation to the conduit and matrix, and SURQ contributing directly to discharge further increased to 249 mm.year^{-1}, which is 25 mm up from its value in Scenario 2. Consequently, the average annual Q_{STREAM} rose to 1319 mm.year^{-1} (103 mm increase; +8.5%).

The changes in the water fluxes under forest-to-pasture conversion (Scenario 4 and Scenario 5) were opposite to those simulated under forest-to-woodland/shrub transition (Scenario 2 and Scenario 3). The mean annual ET_a increased to 676 mm.year^{-1} (75 mm increase; +12.5%)

under Scenario 4 of pasture expansion in the catchment karst areas, and further to 705 mm.year^{-1} (104 mm increase; +17.3%) with total deforestation of the catchment for pasture development (Scenario 5). This ET_a intensification was attributed to higher values of all evapotranspiration components, as E_{canopy} increased to 101−106 mm.year^{-1} (15−20 mm increase; +17.4−23.2%), E_{plant} rose to 491−500 mm.year^{-1} (31−40 mm increase; +6.4−8.7%), and E_{soil} increased to 84−99 mm.year^{-1} (29−44 mm increase; +52.7−80%). On the other hand, RECH dropped to 908 mm.year^{-1} (64 mm decrease; -6.6%) under Scenario 4 due to lower recharge to the epikarst, and further to 904 mm.year^{-1} (68 mm decrease; -7%) under Scenario 5 with lower infiltration to the epikarst, matrix and conduit reservoirs. These changes generated a decrease in the mean annual Q_{SPRING} by 64−68 mm (-6.6% to -7%), followed by a fall in Q_{STREAM} to 1153 mm.year^{-1} (63 mm decrease; -5.2%) under Scenario 4 and 1126 mm.year^{-1} (90 mm decrease; -7.4%) under Scenario 5.

Table 6. Changes in the average annual water fluxes in the Baget catchment under different land-use change scenarios. ET_a: actual evapotranspiration defined as the sum of canopy evaporation (E_{canopy}), plant transpiration (E_{plant}) and soil transpiration (E_{soil}); $RECH$: groundwater recharge; $SURQ$: surface runoff; Q_{SPRING}: spring flow; Q_{STREAM}: streamflow

Land-use scenario		**Baseline**	**Scenario 1**	**Scenario 2**	**Scenario 3**	**Scenario 4**	**Scenario 5**
Land-use proportions (%)							
Pastures		8.1	0	8.1	8.1	65.7	93.9
Complex cultivation patterns		1.1	0	1.1	1.1	1.1	1.1
Broad-leaved forest		74.6	90.1	17	0	17	0
Coniferous forest		9.9	9.9	9.9	0	9.9	0
Moors and heathland		5	0	5	5	5	5
Transitional woodland-shrub		1.3	0	58.9	85.7	0	0
Hydrological variable							
ET_a	Value (mm)	601	592	530	494	676	705
	Change (mm)	0	-8	-71	-107	75	104
	Percent change (%)	0	-1.5	-11.8	-17.8	12.5	17.3
E_{canopy}	Value (mm)	86	83	100	103	101	106
	Change (mm)	0	-3	14	17	15	20
	Percent change (%)	0	-3.5	16.3	19.8	17.4	23.3
E_{plant}	Value (mm)	460	470	355	306	491	500
	Change (mm)	0	10	-105	-154	31	40
	Percent change (%)	0	2.2	-22.8	-33.5	6.7	8.7
E_{soil}	Value (mm)	55	39	75	85	84	99
	Change (mm)	0	-16	20	30	29	44
	Percent change (%)	0	-29.1	36.4	54.5	52.7	80
RECH	Value (mm)	972	976	1039	1048	908	904
	Change (mm)	0	4	67	76	-64	-68
	Percent change (%)	0	0.4	6.9	7.8	-6.6	-7
SURQ	Value (mm)	224	227	224	249	224	203
	Change (mm)	0	3	0	25	0	-21
	Percent change (%)	0	1.3	0	11.2	0	-9.4
Q_{SPRING}	Value (mm)	972	976	1039	1048	908	904
	Change (mm)	0	4	67	76	-64	-68
	Percent change (%)	0	0.4	6.9	7.8	-6.6	-7
Q_{STREAM}	Value (mm)	1216	1224	1283	1319	1153	1126
	Change (mm)	0	8	67	103	-63	-90
	Percent change (%)	0	0.7	5.5	8.5	-5.2	-7.4

The changes in the monthly values of the water fluxes were assessed for the five land-use change scenarios with respect to the baseline land use (**Figure 17**). Under full forest cover (Scenario 1), ET_a decreased slightly by 0.3−3.6 mm.month^{-1} between September and May, while

increasing by 0.3−2.1 mm.month^{-1} from June to August (**Figure 17a**). With the transformation of forests to transitional woodland-shrub, a decrease in ET_a occurred throughout the months of May to October. The drop in ET_a was particularly remarkable in the summer season between June and September, amounting to -12.4 to -28 mm.month^{-1} under Scenario 2 and -18 to -40.6 mm.month^{-1} under Scenario 3. As for the remaining months, minor increases in ET_a were generally simulated, with the largest (around 2−5 mm) occurring in March and April (**Figure 17a**). In contrast, deforestation for pasture development raised ET_a in all months. The highest ET_a increases were simulated from March to May and in October, ranging from 10.7 to 16.5 mm.month^{-1} under Scenario 4 and 15.3 to 21 mm.month^{-1} under Scenario 5 (**Figure 17a**).

The impact of land-use changes on SURQ could be explicitly observed under Scenarios 1, 3 and 5 in which the afforestation/deforestation schemes were extended to the karst areas of the catchment. SURQ was relatively stable under afforestation (Scenario 1), increasing by less than 1 mm.month^{-1} from November to May, with no major variation during the summer season (**Figure 17b**). In contrast, SURQ increased by 1−9.3 mm.month^{-1} between May and November following the conversion of forests to woodland/shrub in Scenario 3, and decreased by 1−6.4 mm.month^{-1} from October to June due to pasture land expansion in Scenario 5, with no remarkable changes in the remaining summer months.

Under afforestation in Scenario 1, RECH increased only by 0.2−2 mm.month^{-1} from November to May, while showing a slight decrease of less than 1 mm.month^{-1} between July and October. Forest-to-woodland/shrub transition increased RECH during the summer season by 5.8−13 mm.month^{-1} and 6.2−15.7 mm.month^{-1} under Scenario 2 and Scenario 3, respectively. RECH increased further throughout the months of October and November by upwards of 17.8−20.3 mm.month^{-1} under Scenario 2 and 18.5−22.7 mm.month^{-1} under Scenario 3. On the other hand, deforestation for pasture development did not significantly alter RECH during summer season. Instead, RECH decreased during the rainy season, particularly from March to May and in November, with a decline of 9−13.7 mm.month^{-1} under Scenario 4 and 9.4−14.1 mm.month^{-1} under Scenario 5 (**Figure 17c**).

The seasonal changes in RECH and SURQ directly affected monthly discharge, with Q_{STREAM} increasing by 5−20 mm.month^{-1} between June and December with transitional woodland-shrub expansion in the catchment karst areas (Scenario 2), and upwards of 6.1−29.1 mm.month^{-1} due to the conversion of all forest areas to transitional woodland-shrub (Scenario 3).

The decrease in discharge in Scenarios 4 and 5 was also consistent with the changes in recharge and surface runoff during the rainy season, as Q_{STREAM} dropped by 3−12.6 mm.month^{-1} from October to June under partial forest-to-pasture conversion and further by 4.7−16.7 mm.month^{-1} with complete forest-to-pasture transition. In comparison, the monthly Q_{STREAM} variations due to afforestation in Scenario 1 were considerably lower than those of deforestation: Q_{STREAM} decreased marginally by 0.4−0.8 mm.month^{-1} between July and October, while increasing by 0.2−2.8 mm.month^{-1} from November to June (**Figure 17d**).

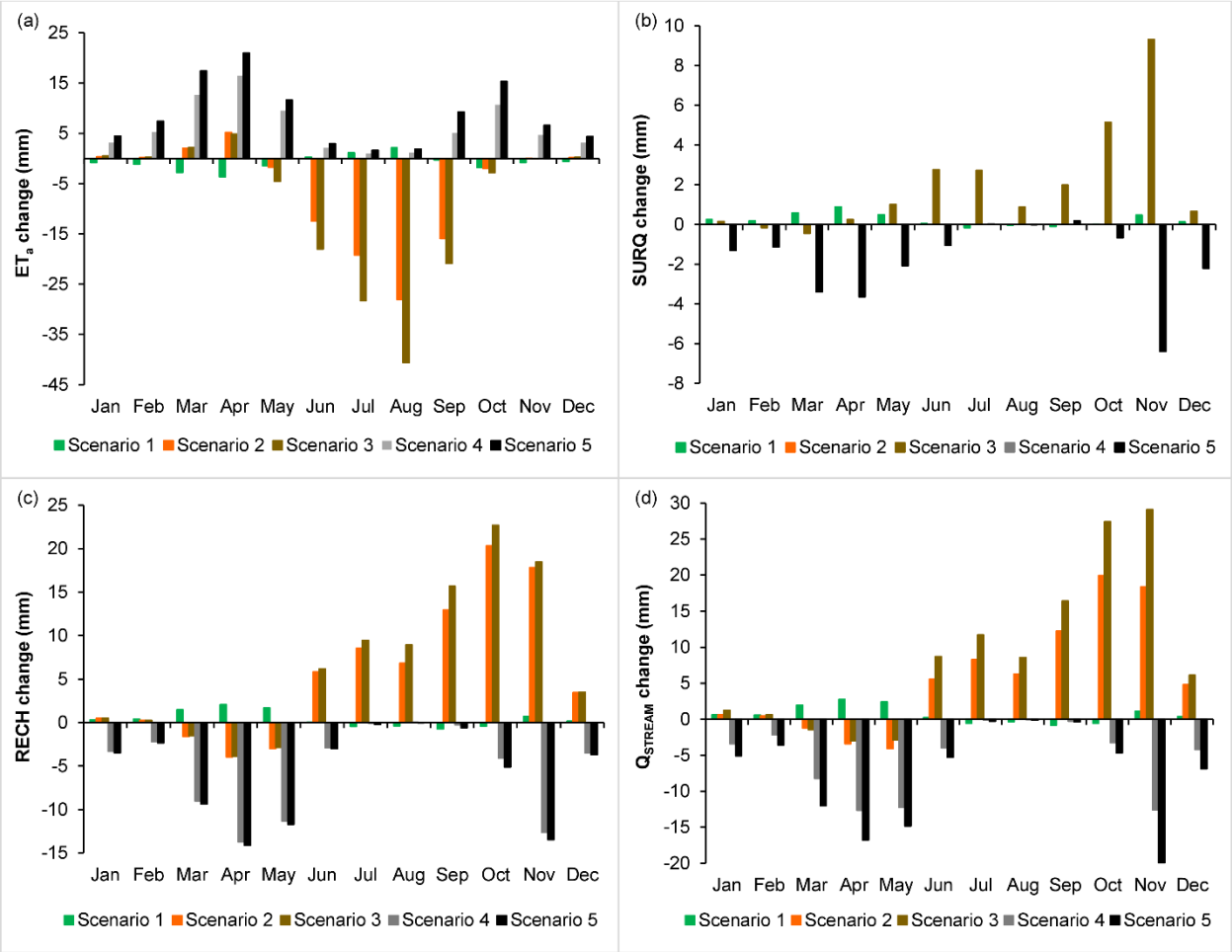

Figure 17. Average monthly changes (mm) in (a) actual evapotranspiration (ET_a), (b) surface runoff (SURQ), (c) groundwater recharge (RECH), and (d) streamflow (Q_{STREAM}) for different land-use change scenarios, with respect to the baseline land use in the Baget catchment.

4.3.4 Impact of land-use changes on high and low flows

The impact of land-use changes on streamflow variability was evaluated with respect to: (1) the low-flow period (July to October) during which the observed discharge values at the

catchment outlet were below 0.35 $m^3.s^{-1}$ 95% of the time, and (2) the high-flow period (November to June), considering the intermediate peak flow values between 1 and 2.5 $m^3.s^{-1}$ and the peaks higher than 2.5 $m^3.s^{-1}$. The Mann-Whitney U-Test/two-tailed test (Mann and Whitney, 1947) was conducted to detect the statistical differences in the low and high flows between Baseline and each of the land-use change scenarios, with a significance threshold at p-value < 0.05.

According to the Mann-Whitney test statistics, no significant difference in the low flow was identified between Baseline and Scenario 1 (p-value = 0.377 > 0.05), suggesting that the impact of full landscape closure by afforestation on the low flow is difficult to identify. This outcome is further validated by the distribution of flow data below 0.35 $m^3.s^{-1}$ (**Figure 18a**), where the median and mean low flow values decreased only from 0.139 and 0.142 $m^3.s^{-1}$ under Baseline to 0.138 and 0.14 $m^3.s^{-1}$, respectively, under Scenario 1.

Conversely, the Mann-Whitney test results were significant for Scenario 2 (p-value < 0.0001) and Scenario 3 (p-value < 0.0001), as low flow showed a tendency to increase with the growing transitional woodland-shrub cover (**Figure 18a**). The interquartile range of the low flow values increased from 0.111−0.163 $m^3.s^{-1}$ (median: 0.139 $m^3.s^{-1}$, mean: 0.142 $m^3.s^{-1}$) under Baseline to 0.136−0.194 $m^3.s^{-1}$ (median: 0.163 $m^3.s^{-1}$, mean: 0.172 $m^3.s^{-1}$) in Scenario 2 that is forest-to-woodland evolution over 57% of the catchment area, and further to 0.145−0.203 $m^3.s^{-1}$ (median: 0.169 $m^3.s^{-1}$, mean: 0.181 $m^3.s^{-1}$) with added degradation of the forest cover in over 84% of the catchment area (Scenario 3).

As regards deforestation for pasture development, the Mann-Whitney test result was insignificant under Scenario 4 (p-value = 0.152 > 0.05), corresponding to forest-to-pasture transition in 57% of the catchment area, whereas it was relatively significant for Scenario 5 (p-value = 0.019 < 0.05) with the transition of all forest areas in over 85% of the catchment to pastures. Accordingly, discharge in Scenario 5 showed a slight downward trend as indicated by the decrease in the interquartile range of the low flow values to 0.109−0.16 $m^3.s^{-1}$ (median: 0.134 $m^3.s^{-1}$, mean: 0.138 $m^3.s^{-1}$) (**Figure 18a**).

Concerning the land-use change impacts on high-flow discharge, the Mann-Whitney test results for Scenario 1 (p-value = 0.757 > 0.05), Scenario 2 (p-value = 0.573 > 0.05), and Scenario 3 (p-value = 0.422 > 0.05) did not reveal any statistically significant differences in the streamflow values between 1 and 2.5 $m^3.s^{-1}$ under afforestation and transition of the forest cover to woodland-shrub. The interquartile flow range only shifted from 1.204−1.75 $m^3.s^{-1}$ (median: 1.424 $m^3.s^{-1}$,

mean: 1.515 $m^3.s^{-1}$) for Baseline to 1.209−1.757 $m^3.s^{-1}$ (median: 1.427 $m^3.s^{-1}$, mean: 1.522 $m^3.s^{-1}$) under Scenario 1, 1.21−1.781 $m^3.s^{-1}$ (median: 1.43 $m^3.s^{-1}$, mean: 1.53 $m^3.s^{-1}$) under Scenario 2, and 1.213−1.8 $m^3.s^{-1}$ (median: 1.437 $m^3.s^{-1}$, mean: 1.538 $m^3.s^{-1}$) under Scenario 3 (**Figure 18b**). However, the changes in the high-flow discharge of 1−2.5 $m^3.s^{-1}$ were more apparent under the deforestation for pasture development scenarios, showing an overall decreasing trend and lower interquartile ranges: 1.155−1.699 $m^3.s^{-1}$ (median: 1.361 $m^3.s^{-1}$, mean: 1.468 $m^3.s^{-1}$) under Scenario 4 (p-value = 0.046 < 0.05), and 1.13−1.678 $m^3.s^{-1}$ (median: 1.344 $m^3.s^{-1}$, mean: 1.448 $m^3.s^{-1}$) under Scenario 5 (p-value = 0.004 < 0.05). As to discharge values greater than 2.5 $m^3.s^{-1}$, the Mann-Whitney test results (Scenario 1 p-value = 0.942 > 0.05; Scenario 2 p-value = 0.873 > 0.05; Scenario 3 p-value = 0.755 > 0.05; Scenario 4 p-value = 0.683 > 0.05; Scenario 5 p-value = 0.544 > 0.05) and associated boxplots (**Figure 18c**) indicated that the high peak flows were relatively insensitive to all applied land-use changes.

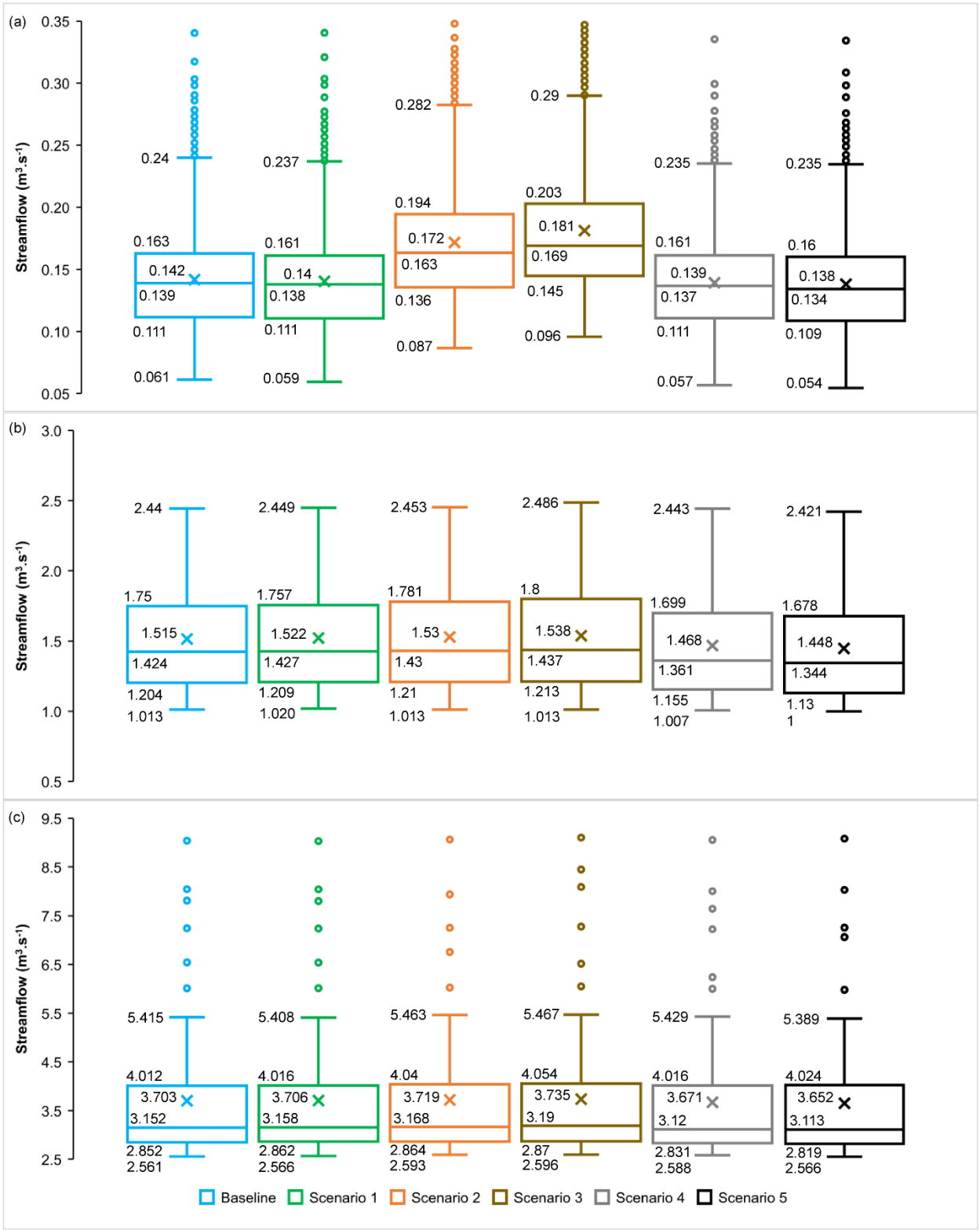

Figure 18. Boxplots comparing the simulated discharge at the Baget catchment outlet for Baseline land use and land-use change scenarios (Scenario 1 to Scenario 5), considering: (a) streamflow ≤ 0.35 $m^3.s^{-1}$ during

the low-flow period (July to October), (b) 1 $m^3.s^{-1}$ ≤ streamflow ≤ 2.5 $m^3.s^{-1}$ during the high-flow period (November to June), and (c) streamflow > 2.5 $m^3.s^{-1}$ during the high-flow period (November to June).

To the best of the authors' knowledge, no spatially-distributed hydrological simulation has been previously conducted on the impacts of forest cover change on karst water resources in the southwestern French Pyrénées. Thus, the results of the land-use change scenario-based analysis were compared to global studies. Filoso et al. (2017) evaluated the impacts of forest cover expansion and restoration on catchment water yield globally, and concluded that annual yield decreased (negative impact) with forest expansion in most of the reviewed case studies, while some studies reported no change, positive, mixed, and unclear effects. At the seasonal scale, the majority of case studies also indicated a decrease in baseflow and peak flows due to forest cover expansion. In our case, the impact of full catchment afforestation on water yield was not statistically significant for a 15.5% gain in forest cover. This outcome agrees with the findings of Brown et al. (2005) stating that forest cover changes of less than 20% in small catchments do not influence water yield. It also corroborates the findings of Zhang et al. (2017) who established, based on a global review of catchment hydrological response to forest cover change, that no significant relationship between annual runoff response and forest cover gain is detectable in small catchments.

In terms of deforestation, the land-use change scenario analysis in this study showed mixed impacts on water resources. Forest cover loss and conversion to transitional woodland-shrub (Scenarios 2 and 3) reduced annual evapotranspiration and increased surface runoff and groundwater recharge in both karst and non-karst areas of the catchment, resulting in a higher annual water yield. These results corroborate the findings of the global review studies by Zhang et al. (2017) and Hou et al. (2023), showing that forest cover loss generally increased annual runoff and decreased evapotranspiration. The increase in discharge mainly occurred in the low-flow season of the Baget catchment, which suggests that supporting local wood production within the catchment could have unintended positive impacts on the seasonal availability of water. In contrast, forest cover loss and transition to pastures (Scenarios 4 and 5) led to higher annual evapotranspiration coupled with lower annual recharge and discharge. These changes in the water balance components were mainly detectable during the high-flow season and reduced flow values as high as 2.5 $m^3.s^{-1}$, suggesting that the conversion of forest areas in the catchment to pastures might be beneficial by reducing flood magnitude (Filoso et al., 2017). Nonetheless, pasture

development might also limit water availability during the low-flow season, particularly in the month of October where the combination of higher evapotranspiration and lower groundwater recharge could become substantial if all forested areas are converted to pastures.

Overall, the hydrological sensitivity of the Baget catchment annual streamflow to forest cover change was 0.045 under forestation and 0.093 under deforestation. These figures are well below the average sensitivities of 1.24% and 0.91% change in annual streamflow established by Hou et al. (2023) for each 1% change in forest cover by forestation and deforestation. Nonetheless, the hydrological response of streamflow to forest cover change varies with climate and catchment characteristics (i.e., tree species, land-use and soil properties, topography, catchment size), and energy-limited catchments such as Baget (dry index < 0.76), where forest growth is more dependent on temperature than water availability, are less responsive to forest cover change than water-limited catchments (Hou et al., 2023; Zhang et al., 2017).

4.3.5 Hydrological modeling uncertainty and recommendations

The results of the ISPEEKH model calibration and land-use change scenarios in the Baget catchment may be biased by uncertainty that stems from: (1) the definition of the baseline hydrological model under the current input data (e.g., weather, topography, land use, soil), model structure and equations used to represent the karst catchment flow processes, (2) the parametrization, (3) the choice of the objective functions and optimization algorithms, and (4) the non-uniqueness of the optimum set of calibrated parameters (Abbaspour et al., 2018).

The input precipitation data used in this study were extracted at 1-km spatial resolution from COMEPHORE, a reanalysis of surface precipitation accumulation over France merging both radar and rain gauge data. The initial hydrological simulation using the COMEPHORE precipitation yielded an underestimation of the Baget catchment water balance due to the low quality of the radar coverage on high altitude and precipitation under catch in the Pyrénées mountainous region. Consequently, the gridded precipitation dataset was adjusted by an orographic correction multiplicative factor of 1.44. Although the correction of precipitation ensured water balance closure, the calibrated ISPEEKH model still underestimated several peaks, particularly in the calibration period, showing that precipitation correction could not accurately capture the daily rainfall amount for all heavy precipitation events over the simulation period. Additionally, watershed modeling and streamflow simulation uncertainty depends on the

uncertainty associated to the 8-km resolution SAFRAN-based meteorological data, as well as the DEM, land use, and soil raster maps resolution and source.

In order to enhance the model's capability to predict the catchment streamflow, mainly peak flow rates during heavy rainfall events, we recommend strategic improvements in monitoring the discharge generation characteristics in the Baget catchment by: (1) installing rain gauges at different observational points that would capture the altitude effect on rainfall within the catchment, and (2) sustaining long-term nested observations of the soil and epikarst properties (e.g., soil water content, soil-epikarst interface infiltration rate), outlet discharge including zero flow, water table and subsurface hydrodynamics. Subsequently, field measurements can be combined with spatial analysis techniques to achieve a better understanding of water movement between the surface and subsurface at different spatial and temporal scales, and detect possible flow processes that might have been ignored or simplified in hydrological modeling of the catchment (Kampf et al., 2020). This approach, coupled with finer resolution DEM, land-use and soil maps, would reduce the hydrological modeling input data and water balance uncertainties, and improve the model structure, the representation of the surface and subsurface flow processes and their interactions, and parametrization (i.e., the choice of parameters for calibration and the regionalization of parameters). Furthermore, future applications of ISPEEKH shall include the simulation of the Baget catchment discharge at subdaily time steps using the Green-Ampt Mein-Larson infiltration module in the SWAT+ source code with subdaily input precipitation data. The use of subdaily time scales could improve the prediction of the peak flow rates measured during event-based floods, which were underestimated by the model run with the Curve Number infiltration method and daily precipitation. Brighenti et al. (2019) reviewed SWAT studies with subdaily flow simulation and compared the hydrological performance of the Green-Ampt Mein-Larson and Curve Number methods. Although the authors did not reach a definitive consensus on which method would generate more robust results, they concluded that the Green-Ampt Mein-Larson approach improved hydrograph peaks, with the one-hour time step being the most suitable time scale for the subdaily model application, while the Curve Number method yielded better performance for medium flows.

On the other hand, a local sensitivity analysis was conducted in this study using PEST, followed by an automated calibration of the selected model parameters. Although the model adequately reproduced the dynamics of the conduit-dominated karst catchment with non-linear

storage-discharge patterns, an uncertainty analysis is recommended to reduce parameter uncertainty and gain more confidence in the numerical modeling results. SWATplus-CUP (https://www.2w2e.com/home/SwatPlusCup) is an interface for the calibration of SWAT+ models, which allows users to perform single and multi-objective calibration, sensitivity analysis (local and global), and uncertainty analysis using several optimization algorithms, namely the Generalized Likelihood Uncertainty Estimation (GLUE) (Beven and Binley, 1992), Parameter Solution (ParaSol) (Van Griensven and Meixner, 2006), and Sequential Uncertainty Fitting (SUFI-2) (Abbaspour et al., 2015). Other open-source tools that have been developed for the calibration of SWAT+ models include the SWAT+toolbox (Chawanda, 2022) and SWATplusR/SWATrunR (Schürz, 2019). These tools currently accommodate the subroutines of the standard SWAT+ source code, requiring further adjustment to integrate the added subroutines of modified SWAT+ codes and implement an uncertainty analysis. Only then, the different optimization algorithms provided by these tools can be tested and evaluated for their performance, using dotty plots to visualize parameter sensitivity, 95% prediction uncertainty (95PPU), and p-factor and r-factor to quantify the uncertainty. This multi-tool calibration and uncertainty analysis would be useful to identify: (a) the optimization approach that captures the most optimal parameters set while yielding the best performance and computational efficiency in terms of the model parameter uncertainty, and (b) possible different parameter ranges with similar discharge results in calibration and validation. Finally, uncertainty arising from parameters non-uniqueness can be reduced by including multiple outlets or other variables such as evapotranspiration (ET) in calibration (Abbaspour et al., 2018; Zhao et al., 2018). In this study, the hydrological model was calibrated using the gauged discharge at the only outlet of the Baget catchment, and the ISPEEKH-simulated ET showed good agreement with the gridded ET available from SAFRAN. In order to further constrain the parameter values by using ET as an additional variable for calibration, we propose applying the remote sensing driven ET model "SimpKcET" (Ollivier et al., 2021), previously tested in the large aquifer of the Fontaine de Vaucluse (1,162 km^2, Southeast of France), to estimate ET of the Baget catchment. SimpKcET simulates ET in karst areas as a function of the fraction of vegetation cover (derived from the Enhanced Vegetation Index) and the fraction of rocks and coarse elements in soils growing on carbonate bedrock.

4.4 Conclusions

In this study, a semi-distributed karst hydrological model termed ISPEEKH was proposed for the simulation of surface and subsurface flow processes in karst-dominated catchments. The model was developed by modifying the recharge functions of the SWAT+ source code and implementing a non-linear three-reservoir karst module that reproduces processes of the epikarst and matrix-conduit system. ISPEEKH was applied to model the water balance of the Baget karst catchment in the southwestern French Pyrénées, for the years 2008−2018. The model simulated the daily discharge at the catchment outlet with good accuracy by reproducing the hydrograph steep rise limbs and recessions with suitable magnitudes of both the high and low flows. It also represented the internal flow dynamics of the conduit-dominated karst catchment adequately. ISPEEKH was then used to predict the impacts of land-use change scenarios of afforestation and deforestation on the Baget catchment hydrology. Results showed that afforestation did not have a significant influence on annual water yield. However, the impacts of deforestation on the catchment hydrology were mixed. The conversion of the forests to transitional woodland/shrub reduced annual evapotranspiration by up to 17.8% and increased annual recharge and discharge by 7.8% and 8.5%, respectively, with a positive impact on water availability during the low-flow period. In comparison, the transition from forests to pastures increased annual evapotranspiration by up to 17.3%, while lowering annual recharge by 7% and discharge by 7.4%. The discharge reduction occurred primarily during the high-flow period, affecting streamflow values below 2.5 $m^3.s^{-1}$. The approach adopted in this study served to improve numerical modeling of karst flow dynamics using semi-distributed models that incorporate the impact of land-use changes on groundwater resources. Future applications of ISPEEKH should include the simulation of the water balance of large karst catchments and the assessment of the impacts of anthropogenic pressures (e.g., groundwater abstractions for domestic, agricultural, and industrial supply) and climate change on karst water availability.

CHAPTER 5: Evaluation of Precipitation Products for Small Karst Catchment Hydrological Modeling in Data-scarce Mountainous Regions

Summary

This study compares the reliability of reanalysis, gauge-, and satellite-based precipitation products for daily water balance and streamflow simulation in the meso-scale Baget karst catchment (13.25 km^2), located in a poorly gauged region in the French Pyrenees mountains. ISPEEKH, integrated with a PEST framework for automated calibration, global sensitivity analysis, and parameter estimation, was applied to simulate the catchment's hydrological response to different precipitation datasets from 2006 to 2018. The daily precipitation datasets used in this study were retrieved from: (1) Saint Girons weather station located 8.3 km from the Baget catchment outlet, (2) CPC (0.5°) and E-OBS (10-km) gauge-based products; (3) SAFRAN (8-km), COMEPHORE (1-km), and ERA5-Land (0.1°) reanalysis products; (4) IMERG-LR (0.1°), PERSIANN-CDR (0.25°), CHIRPS (0.05°), and SM2RAIN-ASCAT (10-km) satellite-based products, and (5) downscaled 1-km resolution CPC, E-OBS, ERA5-Land, IMERG-LR, and merged CPC-IMERG-LR products. The daily minimum and maximum air temperature, relative humidity, wind speed, and solar radiation data were obtained from SAFRAN.

The study used ISPEEKH to simulate Baget catchment daily streamflow from 2006 to 2018, with a 2–year warm-up period, 6–year calibration period, and 5−year validation period. The Morris screening method was used to evaluate the sensitivity of the ISPEEKH parameters governing streamflow. The pestpp-sen software tool, implemented within the PEST++ environment, was used to compute sensitivity indices for the Morris method. The Iterative Ensemble Smoother (iES) method, integrated into the PEST++ environment, was applied to generate prior and posterior estimates of ISPEEKH parameters. The iES uses the Ensemble Kalman Filter (EnKF) for data assimilation, updating state variables by incorporating measured data into the model results. Chen and Oliver (2013) modified the ES to operate iteratively using the Gauss–Levenberg–Marquardt (GLM) algorithm, improving the minimization of the sum-of-squared residuals objective function for non-linear problems.

The model's predictive performance of daily streamflow was evaluated using various metrics such as Nash-Sutcliff efficiency (NSE), coefficient of determination (R^2), percent of bias (PBIAS), and Kling-Gupta efficiency (KGE). A wavelet multiresolution analysis (MRA) was used to project streamflow on an orthogonal basis, allowing for the evaluation of the hydrological model

performance across different temporal scales by calculating the Pearson correlation coefficient on the calibration and validation periods.

The study found that the discharge coefficients and emptying exponents of the conduit-to-spring flow and epikarst-to-conduit flow were the most sensitive parameters, regardless of the precipitation product. This is consistent with the discharge characteristics of the Baget catchment, which has a shallow epikarst with a high connectivity to a network of well-developed conduits. ISPEEKH successfully simulated karst groundwater storage and spring flow from the recharge input, conserving the water balance. However, the Baget catchment water balance for the 2008-2018 period showed a significant streamflow underestimation from 30 to 80%, with a mean annual precipitation varying between 887 mm under the CPC precipitation and 1451 mm under the downscaled ERA5-Land precipitation. The NSE, R^2, PBIAS, and KGE metrics showed unsatisfactory performance for daily streamflow simulation. The reanalysis COMEPHORE, SAFRAN, and ERA5-Land precipitation products outperformed the gauge- and satellite-based precipitation products. The spatial downscaling of the CPC, IMERG-LR, ERA5-Land and E-OBS data, and merging of the CPC and IMERG-LR datasets did not improve the model predictive performance substantially compared to the coarse datasets.

In order to resolve the issue of the water balance discrepancy due to precipitation underestimation and with the lack of reliable precipitation monitoring network, the 1-km resolution COMEPHORE, CPC, E-OBS, ERA5-Land, IMERG-LR, and CPC-IMERG-LR precipitation datasets were corrected using orographic correction multiplicative factors, calculated by "Doing Hydrology Backward" based on the daily measured streamflow at the catchment outlet and actual evapotranspiration estimates from SAFRAN. Following the correction, the calibrated ISPEEKH models for the 2008-2018 period showed comparable water balance components, with mean annual precipitation of 1781-1824 mm, evapotranspiration of 598-623 mm, and streamflow of 1160-1194 mm. The PBIAS values were significantly reduced. The corrected COMEPHORE precipitation improved streamflow simulation with the highest overall NSE, R^2, and KGE values, indicating satisfactory to good performance, whereas the corrected downscaled IMERG-LR precipitation consistently performed poorly, suggesting that that fine-resolution regionally-tailored reanalysis precipitation products, such as COMEPHORE for France, could serve as base data for the hydrological modeling of streamflow in poorly gauged meso-scale karst catchments. Future research should involve installing daily and subdaily operating rain gauges at different altitudes in

the Baget catchment to capture the spatial and temporal distribution characteristics and apply observation-based correction methods to the precipitation products.

The findings of this chapter were were published in the Jounral of Hydrology as:: *Al Khoury, I., Boithias, L., Sivelle, V., Bailey, R.T., Abbas, S.A., Filippucci, P., Massari, C., & Labat, D. (2024). Evaluation of Precipitation Products for Small Karst Catchment Hydrological Modeling in Data-scarce Mountainous Regions. Journal of Hydrology, 132131. https://doi.org/10.1016/j.jhydrol.2024.132131*

Al Khoury's Contribution: Conceptualization, Methodology, Software, Formal analysis, Investigation, Data curation, Writing – original draft, Writing – review & editing.

Abstract

The accuracy of gauge-based, satellite-based and reanalysis precipitation products for streamflow simulation has rarely been investigated in data-scarce and meso-scale karst catchments characterized by infra-daily response time due to the predominance of quick flow processes. This study evaluates and compares the reliability of gauge- and satellite-based precipitation products (CPC, E-OBS, PERSIANN-CDR, IMERG-LR, SM2RAIN-ASCAT, CHIRPS) and reanalysis products (SAFRAN, COMEPHORE, ERA5-Land) in simulating daily flow of the Baget karst catchment (13.25 km^2), located in the Southwestern French Pyrenees. The assessment was conducted over the 2006–2018 period using the semi-distributed karst hydrogeological model ISPEEKH, integrated with a PEST framework for model calibration, global sensitivity analysis using the Morris method, and parameter estimation using an iterative ensemble smoother form of the Gauss-Levenberg-Marquardt algorithm. The discharge coefficients and emptying exponents of the epikarst-to-conduit and conduit-to-spring quick flows were the most sensitive model parameters irrespective of the input precipitation, and ISPEEKH successfully reproduced the non-linear conduit flow dynamics in the catchment. Yet, simulated streamflow was significantly underestimated under the ensemble of precipitation products (up to 32–79% in calibration period and up to 28–70% in validation period), and the reanalysis products outperformed the gauge- and satellite-based products. Downscaling of the CPC, IMERG-LR, ERA5-Land and E-OBS products, and merging of the CPC and IMERG-LR datasets at 1-km spatial resolution did not improve the model predictive performance. Finally, the study showed that watershed-scale precipitation correction can effectively improve the hydrological simulation performance in the catchment, particularly with the French reanalysis precipitation product COMEPHORE. This result emphasizes the need to install representative rain gauge stations at different altitudes in studied karst catchments of similar scale and hydrodynamics characteristics, and apply observation-based correction methods in order to reduce the errors in regional reanalysis precipitation database and optimize the karst discharge simulation.

Keywords: Karst catchment; Pyrenees Mountain range; Satellite precipitation; Reanalysis precipitation; ISPEEKH

5.1 Introduction

Karst landscapes, formed by chemical dissolution of soluble carbonate rocks by acid water enriched with carbon dioxide, cover nearly 15.2% of the Earth's ice-free continental surface (Goldscheider et al., 2020) and supply groundwater to 9–25% of the world's population (Chen et al., 2017; Stevanović, 2019). Compared to granular aquifers, the hydrological behavior of karst aquifers is highly complex, nonlinear, and non-stationary (An et al., 2020; Labat et al., 2000a). Karst aquifers exhibit dual-to-triple porosity with discrete conduit networks embedded in a larger fissured matrix. They are characterized by dual recharge and discharge mechanisms, including diffuse infiltration through the matrix and slow-flow discharge into the spring, primarily in the low-flow periods, and concentrated infiltration into secondary porosity features (i.e., fissures, channels, conduits, fractures and sinkholes), with quick-flow discharge into the spring during the wet periods or after a significant recharge event (Geyer et al., 2013; Paiva and Cunha, 2020). A bidirectional matrix-conduit exchange flow can also occur due to the head difference between the two domains (Dal Soglio et al., 2020a; Zhao et al., 2021). Moreover, karst aquifers often encompass an uppermost weathered zone of carbonate rocks with high porosity and permeability, called epikarst, which stores water and controls the recharge towards the matrix and conduits (Bailly-Comte et al., 2008; Fidelibus et al., 2017). These hydrogeological characteristics render karst aquifers flow behavior very sensitive to changes in precipitation patterns and recharge rates induced by climate change, land use change, and other anthropogenic activities, impacting groundwater storage (Fiorillo and Guadagno, 2012; Klaas et al., 2020; Mo et al., 2023; Nerantzaki and Nikolaidis, 2020; Ruiz et al., 2022; Taheri et al., 2016). Therefore, the adequate management of water resources in karst watersheds requires a sufficient understanding of their recharge and discharge dynamics, coupled with an accurate assessment of their water balance using karst-specific hydrological modeling tools.

Hydrological models aim to approximate the transfer function between meteorological forcing (i.e., precipitation, temperature, potential evapotranspiration) and river streamflow (or spring discharge). One common approach for hydrological modeling consists of considering different combinations of the dominant flow components as distinct conceptual buckets. This approach has been widely developed during the past decades (Azimi et al., 2023; Bittner et al., 2018; Butscher and Huggenberger, 2008; Fleury et al., 2007, 2009; Mazzilli et al., 2019; Sivelle et al., 2023; Tritz et al., 2011), and applied to simulate karst spring discharge and further assess the impact of

groundwater abstraction (Cousquer and Jourde, 2022; Labat et al., 2022) and climate change (Hartmann et al., 2012; Sivelle et al., 2021) on karst water resources. However, by neglecting the spatial variabilities of the meteorological forcing and landscape characteristics (i.e., topography, karst terrains, soil and land use), lumped models may lack precision in assessing the intricate recharge and discharge within karst aquifers, hindering accurate flow prediction and data-driven karst water resources management. On the other hand, fully-distributed models discretize karst watersheds into two- or three-dimensional grid units assigned with specific hydraulic parameters, and simulate flow between these computational units using differential equations. These models, however, require an adequate knowledge of the geological settings (lithology, fractures, faults) and their hydraulic properties (porosity, hydraulic conductivity), which are highly heterogeneous in karst aquifers and can be challenging or impossible to acquire (Fischer et al., 2018; Ghasemizadeh et al., 2012; Gill et al., 2021; Jeannin et al., 2021). Thus, semi-distributed hydrogeological models are proposed as a hybrid approach to overcome the limitations of the aforementioned two model classes by combining the spatial variability of the surface flow dominant controls (i.e., climatic features, landscape properties) with the underlying karst aquifer dominant flow components (Hartmann et al., 2013; Ollivier et al., 2020).

Precipitation is one of the key driving factors in the hydrological modeling of watershed water balance fluxes. Numerous studies have demonstrated the dependence of the predictive capability of hydrological models for streamflow prediction on the input precipitation data (Bárdossy et al., 2022; Camici et al., 2018; Maggioni and Massari, 2018), as well as on the spatial discretization of the precipitation field from lumped to distributed, showing results that vary with the watershed physiographic and climatic properties. By assessing the hydrological response of an ensemble of basins to precipitation variability (i.e., complete precipitation field and sampled precipitation) and rainfall-runoff modeling approaches (i.e., lumped and distributed), Arnaud et al. (2011) concluded that small catchments were mostly sensitive to precipitation input uncertainties produced by sampling of precipitation, while the largest catchments were sensitive to uncertainties generated by discarding the spatial variability of precipitation. Lobligeois et al. (2014) also evaluated streamflow simulation for an ensemble of catchments using lumped and semi-distributed models driven by 1-km high resolution precipitation, and showed that differences in model performance were insignificant between lumped and semi-distributed approaches but highly variable between catchments due to the spatial heterogeneity of the precipitation fields. In addition, Emmanuel et

al. (2017) found that higher spatial resolution of precipitation could improve model performance, while Huang et al. (2019) concluded that streamflow simulations improved marginally with higher precipitation spatial resolution and were more sensitive to the temporal resolution of precipitation. These findings underscore the importance of identifying the most suitable precipitation estimate for hydrological applications.

The sparse distribution of rain gauges in watersheds poses challenges for hydroclimatic analysis, prompting the need for alternative precipitation inputs for streamflow simulation. Apart from gauge-based precipitation, recent developments in Earth observation and atmospheric reanalysis have provided long-term precipitation datasets with comparable or even broader spatial coverage than in-situ station observations. In this regard, there are two main categories of satellite precipitation products: those that infer precipitation from clouds and atmosphere characteristics (Top-Down approach), such as PERSIANN-CDR (0.25° spatial resolution; Ashouri et al., 2015) and IMERG (0.1° resolution, Huffman et al., 2019), and those that infer precipitation from the variation of soil moisture (Bottom-Up approach), such as SM2RAIN-ASCAT (0.1° resolution, Brocca et al., 2019). Moreover, reanalysis data such as ERA5 (0.25° resolution; Hersbach et al., 2020) and COMEPHORE (1-km resolution; Tabary et al., 2012) are commonly used. However, these precipitation products can generate biased streamflow forecasts due to various error sources (Aryal et al., 2023; Bitew et al., 2012; Dos Reis et al., 2017; Peinó et al., 2024; Satgé et al., 2019; Zhang et al., 2020) which hinders their application in assessing the hydrological response of karst watersheds with fast aquifer recharge and conduit flow to changing climate conditions.

Currently, there are very few studies that examine the impact of various precipitation inputs from satellite and reanalysis data products on streamflow simulation in karstified watersheds (Chang et al., 2024; Furl et al., 2018; Gan et al., 2020, 2021; Li et al., 2019; Mo et al., 2020, 2022; Wang et al., 2017). Most of these studies were conducted in China, being one of the largest karst areas in the world, across watersheds ranging from 10^3 to 10^5 km^2. Nonetheless, karst watersheds in Europe are often characterized by smaller recharge areas; for instance, the largest karst spring in Europe, Fontaine de Vaucluse, has a recharge area of around 1,160 km^2 (Ollivier et al., 2019). Of the studies reported in the literature, Mo et al. (2020) evaluated the suitability of coarse and corrected IMERG satellite precipitation for daily and monthly streamflow simulation in the XiaJia River basin (799.2 km^2) using the SWAT model. Results showed that SWAT performance under the original IMERG rainfall dataset was unsatisfactory due to major streamflow underestimation,

while corrected IMERG precipitation significantly improved the simulations. Mo et al. (2022) simulated streamflow of the Chengbi River basin (2,087 km^2) using SWAT driven by gauge-measured precipitation, IMERG precipitation, and 1-km resolution precipitation derived by geographical weighted regression (GWR) fusion of the measured and IMERG data. The station-measured precipitation data performed best, followed by the GWR fusion precipitation dataset, while the IMERG satellite precipitation yielded the worst performance, highlighting the significance of fusion processing to improve streamflow simulation at the daily and monthly scales. Thus, there is a notable research gap associated with assessing the accuracy of gauge-based, satellite-based or reanalysis precipitation products for the hydrological modeling of meso-scale karst basins (approximately $10–10^3$ km^2; Uhlenbrook et al., 2004), using distributed or semi-distributed hydrological models. To the best of our knowledge, this is the first study that aims to evaluate and compare the reliability of reanalysis, gauge-, and satellite-based precipitation products, at coarse (tens of kilometer) and 1-km (downscaled) spatial resolution, for daily water balance and streamflow simulation in a meso-scale karst catchment with short response time to precipitation and sparse precipitation monitoring network. The Baget karst catchment (13.25 km^2) in the piedmont of the Pyrenees mountains, southwest of France, serves as the study area. The semi-distributed karst hydrogeological model ISPEEKH (Al Khoury et al., 2023a), a modified version of SWAT+ (Bieger et al., 2017) for spring flow-dominated karst watersheds, was used to simulate the hydrological response of the Baget catchment to the different precipitation datasets over the years 2006–2018. ISPEEKH was integrated with a Parameter ESTimation Tool (PEST) framework in order to perform automated calibration, identify model parameters that influence streamflow simulation using the Morris method for global sensitivity analysis, and estimate the model parameter values using an iterative ensemble smoother (iES) form of the Gauss-Levenberg-Marquardt algorithm.

5.2 Methods and materials

5.2.1 Study Area

The Baget is a karst catchment in the Pyrenees mountains, southwest of France (station B1 at 42°57'18.06"N; 1°1'52.76"E) (**Figure 19**). It is part of the KARST National Observatory Service (SNO KARST, Jourde et al., 2018) and part of the French network of Critical Zone Observatories Research and Applications–National Research Infrastructure (OZCAR, Gaillardet et al., 2018).

The Baget catchment has a groundwater recharge contribution zone of about 13.25 km^2 and is characterized by rapid infiltration, fast transit time between recharge and discharge, and strong nonlinear rainfall-runoff relationship (Labat et al., 1999, 2000a). The geology within the catchment consists of a mixed lithological terrain: Jurassic and Cretaceous karstified landforms (~67% of the recharge area) and non-karstified rocks (~33% of the recharge area). The large carbonate part of the catchment includes a crystalline limestone band and Jurassic dolomites (Debroas, 2009).

The Baget catchment is exposed to an Atlantic oceanic climate with mountainous influence. The mean daily air temperature is 12 ± 6.3°C and the mean annual precipitation is 975.5 mm, based on the records of the Saint Girons meteorological station (43°00'19"N; 01°06'25"E; 414 m a.s.l). The catchment's snowpack is generally low, and snowmelt does not significantly contribute to discharge (Padilla et al., 1994; Richieri et al., 2024; Ulloa-Cedamanos et al., 2020).

The catchment's streamflow is primarily formed by the perennial karst spring Las Hountas through well-developed conduit networks and partially by the Lachein stream, which drains the impermeable terrains in the catchment. The mean annual catchment discharge measured at the outlet gauging station B1 was 0.44 ± 0.67 $m^3.s^{-1}$. Tracer tests (Sivelle and Labat, 2019) and lumped-parameter hydrological modeling of the Baget karst system (Sivelle et al., 2019; Shirafkan et al., 2023) show that nonlinear conduit flow is the main component of the karst spring discharge.

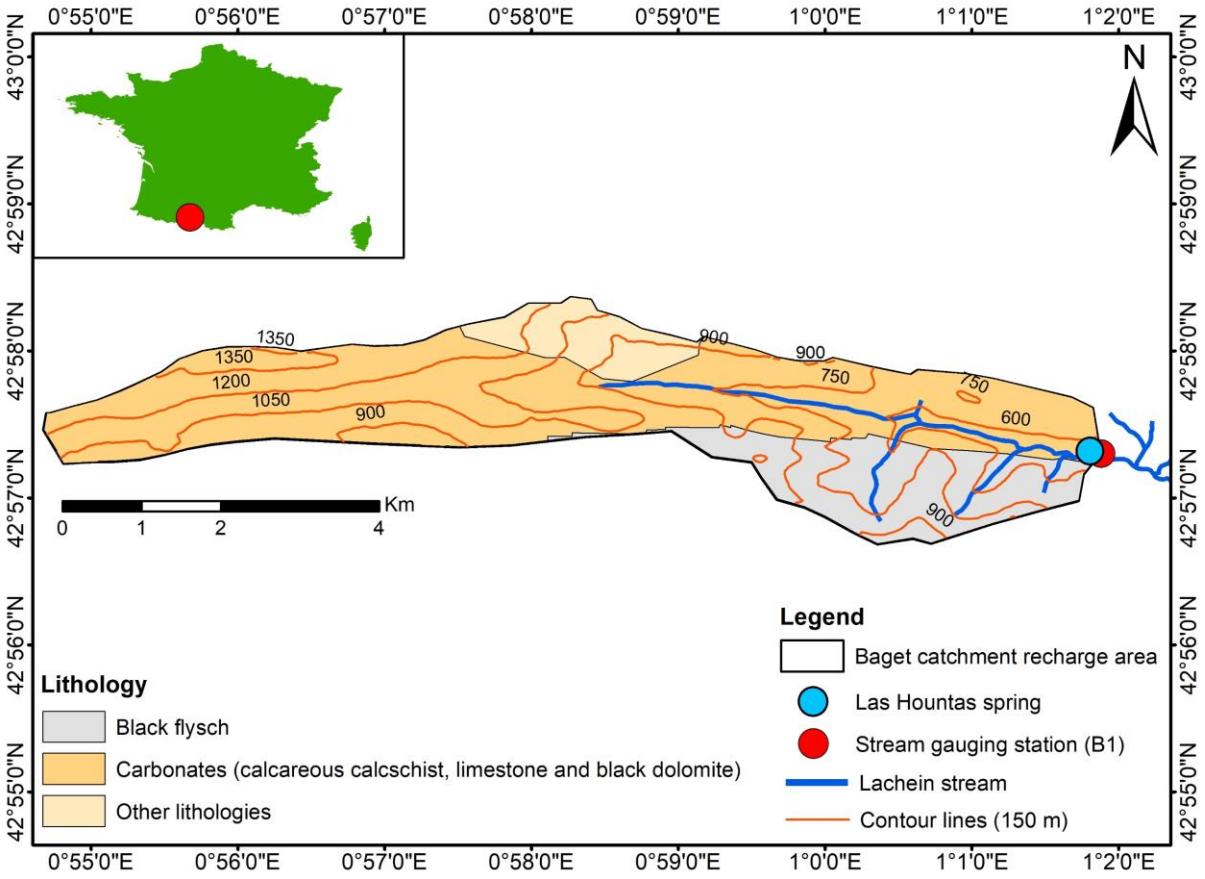

Figure 19. The Baget catchment recharge area and lithological composition, with the Las Hountas karst spring, the Lachein stream, and the stream gauging station (B1) (modified from Al Khoury et al., 2023a)

5.2.2 The ISPEEKH model

The Integration of Surface ProcEssEs in Karst Hydrology (ISPEEKH) is a semi-distributed karst hydrological model (**Figure 20**, Al Khoury et al., 2023a) that was developed by modifying the source code of SWAT+ (revision 60.5.4), the restructured version of the Soil and Water Assessment Tool (SWAT) (Bieger et al., 2017). It was used in the study as other modified SWAT-based models reported in the literature and applied in karst hydrology (e.g., Baffaut and Benson, 2009; Geng et al., 2021; Nerantzaki et al., 2020; Nikolaidis et al., 2013; Nguyen et al., 2020; Palanisamy and Workman, 2015; Wang and Brubaker, 2014; Wang et al., 2019;Yactayo, 2009; Zhou et al., 2022) do not collectively reproduce the flow processes of the epikarst, matrix and conduits, including the matrix-conduit bidirectional exchange flow rate, using non-linear storage-discharge relationships (Al Khoury et al., 2023a).

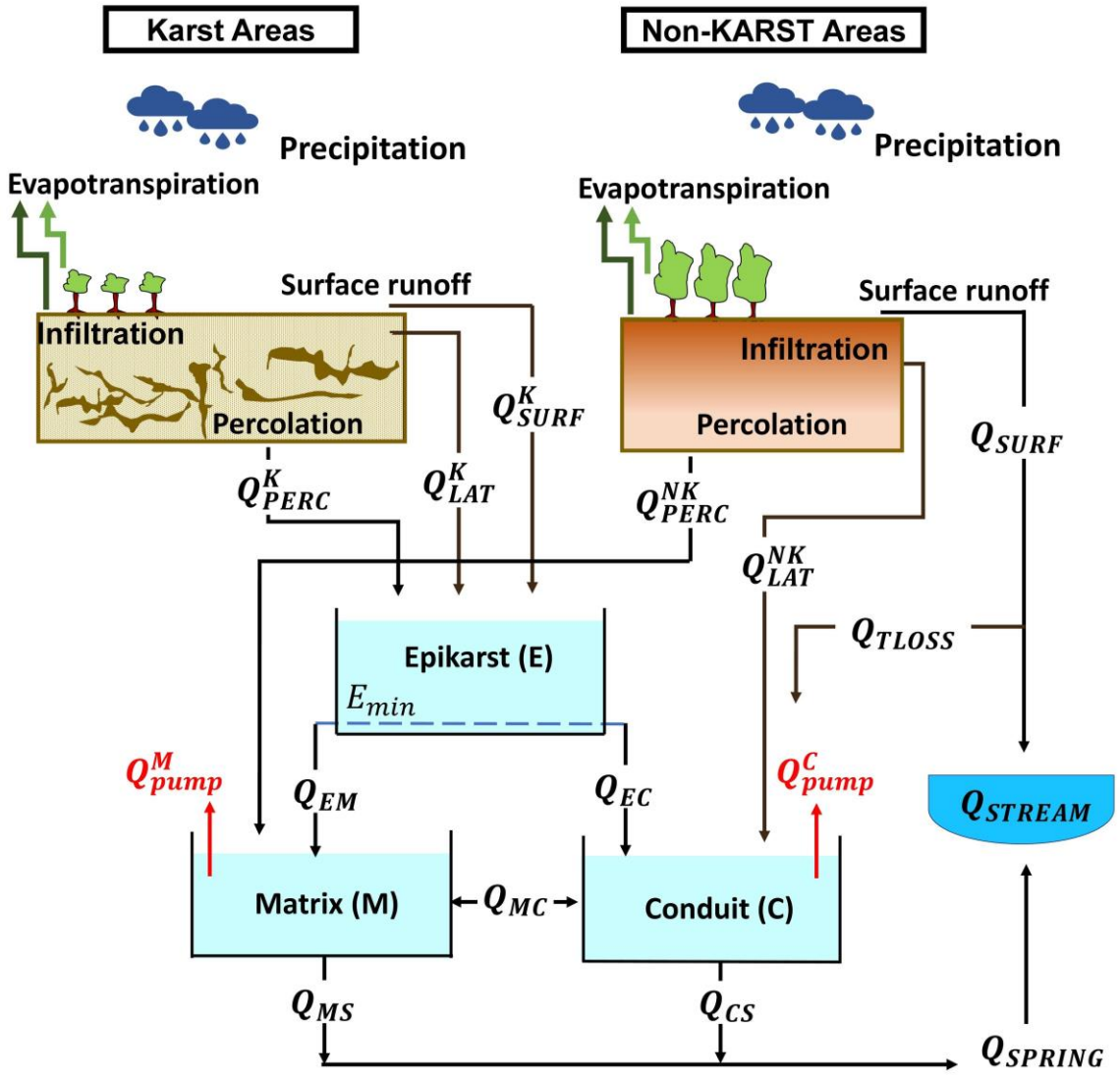

Figure 20. Schematic representation of the hydrological processes simulated by ISPEEKH in a spring flow-dominated karst watershed (modified from Al Khoury et al., 2023a)

ISPEEKH uses input digital elevation model (DEM), land-use map, and overlapped soil and lithology maps to divide the watershed into subbasins connected through stream channels and further into hydrological response units (HRUs) of homogeneous land-use, slope, soil, and karst/non-karst landform properties. It then utilizes spatially-variable weather input data (i.e., precipitation, minimum and maximum air temperature, solar radiation, wind speed, and relative humidity) to simulate the daily vadose zone water balance fluxes at the HRU scale. The land surface and soil hydrologic fluxes, including potential evapotranspiration (Monteith, 1965), actual

evapotranspiration (sum of canopy evaporation, soil evaporation, and plant transpiration), direct (surface) runoff method (USDA-SCS, 1972), lateral flow (Sloan and Moore, 1984), and percolation (Neitsch et al., 2011) are simulated in ISPEEKH using the original SWAT+ subroutines. SWAT differentiates between solid and liquid precipitation based on near-surface air temperature. If the snowfall temperature parameter is lower than the mean daily air temperature, precipitation is classified as snow. When precipitation is considered solid, it accumulates at the ground surface until snowmelt, which is influenced by air and snowpack temperature, daylight hours, and snow areal coverage. A detailed description of the vadose zone water balance fluxes and corresponding equations applied in standard SWAT+ is provided in the SWAT theoretical manual (Neitsch et al., 2011).

To represent the flow in the saturated zone, the diffusive recharge equations and linear reservoir model for baseflow simulation in granular-type aquifers in SWAT+ were modified in ISPEEKH into diffuse and concentrated recharge equations and a nonlinear three-reservoir model of the epikarst, matrix and conduits water bearing components of karst aquifers. Thus, ISPEEKH applies three nonlinear reservoirs organized in a two-level structure: the upper reservoir (E) representing the epikarst zone, and the lower reservoirs (M) and (C) that represent the low-permeability matrix and highly permeable conduits, respectively. For karst-dominated catchments characterized by low surface runoff generation and significant spring flow contribution to the overall discharge, ISPEEKH considers direct rainfall infiltration without surface runoff generation over the surface-exposed and well-developed epikarstic zone, with lateral flow down hillslopes and soil water percolation in areas where the soil covers the epikarst (Equation (1)). Water percolation from the soil profile in non-karst HRUs recharges the matrix reservoir diffusely (Equation (2)), while soil lateral flow generated in non-karst areas and water losses from sinking channels seep directly into the conduit reservoir (Equation (3)). The simulated groundwater fluxes include: fast recharge from the epikarst to conduits (Q_{EC}) and slow recharge from the epikarst to the matrix (Q_{EM}), which are activated when the water level of reservoir E exceeds a lower storage threshold (E_{min}), the conduit quick-flow (Q_{CS}) and matrix slow-flow (Q_{MS}) components of the karst spring discharge, and the conduit-matrix bidirectional exchange flow rate (Q_{MC}) as a function of the difference between the water levels of the two reservoirs M and C. The water balance of the reservoirs E, M and C are represented by Equations (4), (5) and (6), respectively. The model can also account for user input daily groundwater abstraction (pumping) data from the matrix and / or

conduits. Spring flow from the karst aquifer (Q_{SPRING}) is finally added to surface runoff generated over the non-karst areas (Q_{SURF}) to form the total catchment discharge downstream the karst spring outlet(s) (Equation (7)).

$$RECH_{E,i} = RECH_{E,i-1} \times e^{-\frac{1}{\delta_E}} + \left(1 - e^{-\frac{1}{\delta_E}}\right) \times \sum_{j=1}^{nhrus-K} \left(Q^K_{SURF,i,j} + Q^K_{LAT,i,j} + Q^K_{PERC,i,j}\right) \quad (1)$$

$$RECH_{M,i} = RECH_{M,i-1} \times e^{-\frac{1}{\delta_M}} + \left(1 - e^{-\frac{1}{\delta_M}}\right) \times \sum_{j=1}^{nhrus-NK} Q^{NK}_{PERC,i,j} \quad (2)$$

$$RECH_{C,i} = Q_{TLOSS,i} + \sum_{j=1}^{nhrus-NK} Q^{NK}_{LAT,i,j} \quad (3)$$

Where $RECH_{E,i}$ and $RECH_{E,i-1}$ represent the recharge to the epikarst reservoir on days i and $i-1$ (mm.day^{-1}), respectively, δ_E is the delay time for infiltrated water to reach the epikarst (days), $Q^K_{SURF,i,j}$, $Q^K_{LAT,i,j}$ and $Q^K_{PERC,i,j}$ are surface runoff, soil lateral flow, and soil percolation on day i from the karst HRU j (mm.day^{-1}), respectively, $RECH_{M,i}$ and $RECH_{M,i-1}$ represent recharge by soil water percolation from non-karst HRUs to the matrix reservoir on days i and $i-1$ (mm.day^{-1}), respectively, δ_M is the delay time for infiltrated soil water to reach the matrix (days), $nhrus - K$ is the number of karst HRUs in the recharge area, $Q^{NK}_{PERC,i,j}$ is the soil water percolation on day i from the non-karst HRU j (mm.day^{-1}), $RECH_{C,i}$ is the recharge by soil lateral flow in non-karst HRUs and water losses from channels to the conduit reservoir on day i (mm.day^{-1}), $Q^{NK}_{LAT,i,j}$ is the soil lateral flow on day i from non-karst HRU j (mm.day^{-1}), $Q_{TLOSS,i}$ represents water losses from channels on day i (mm.day^{-1}), and $nhrus - NK$ is the number of non-karst HRUs in the recharge area.

Epikarst Reservoir

$$\begin{cases} \dfrac{dE(t)}{dt} = RECH_E(t) - Q_{EM}(t) - Q_{EC}(t) \\ \dfrac{dE(t)}{dt} = RECH_E(t) - k_{EM}\left(\dfrac{E(t) - E_{min}}{L_{ref}}\right)^{\alpha_{EM}} - k_{EC}\left(\dfrac{E(t) - E_{min}}{L_{ref}}\right)^{\alpha_{EC}} \end{cases} \quad (4)$$

Matrix Reservoir

$$\begin{cases} \dfrac{dM(t)}{dt} = RECH_M(t) + Q_{EM}(t) - Q_{MC}(t) - Q_{MS}(t) - Q^M_{PUMP}(t) \\ \dfrac{dM(t)}{dt} = RECH_M(t) + Q_{EM}(t) - k_{MC}\left(\dfrac{C(t) - M(t)}{L_{ref}}\right)^{\alpha_{MC}} - k_{MS}\left(\dfrac{M(t)}{L_{ref}}\right)^{\alpha_{MS}} - Q^M_{PUMP}(t) \end{cases} \quad (5)$$

Conduit Reservoir

$$\begin{cases} \dfrac{dC(t)}{dt} = RECH_C(t) + Q_{EC}(t) + Q_{MC}(t) - Q_{CS}(t) - Q_{PUMP}^{C}(t) \\ \dfrac{dC(t)}{dt} = RECH_C(t) + Q_{EC}(t) + k_{MC}\left(\dfrac{C(t) - M(t)}{L_{ref}}\right)^{\alpha_{MC}} - k_{CS}\left(\dfrac{C(t)}{L_{ref}}\right)^{\alpha_{CS}} - Q_{PUMP}^{C}(t) \end{cases} \quad (6)$$

Where E, M and C are the daily water levels of the epikarst, matrix and conduit reservoirs (mm), respectively, Q_{EM} and Q_{EC} are the discharge components from reservoir E to reservoir M and reservoir C (mm.day^{-1}), respectively, E_{min} is the minimum water level for the activation of the epikarst discharge function (mm), L_{ref} is a reference length for normalization of the water level of the reservoirs, Q_{MC} is the matrix-conduits bidirectional exchange flow (mm.day^{-1}), Q_{MS} and Q_{CS} are the matrix and conduits discharge components into the spring (mm.day^{-1}), respectively, k_{EM}, k_{EC}, k_{MC}, k_{MS}, and k_{CS} are the specific discharge coefficients of the epikarst, matrix and conduit reservoirs fluxes (mm.day^{-1}), α_{EM}, α_{EC}, α_{MC}, α_{MS}, and α_{CS} are positive exponents (unitless), and Q_{PUMP}^{M} and Q_{PUMP}^{C} are the pumping rates from the matrix and conduit reservoirs (mm.day^{-1}), respectively.

$$Q_{STREAM,i} = Q_{SPRING,i} + Q_{SURF,i} = Q_{MS,i} + Q_{CS,i} + Q_{SURF,i} \quad (7)$$

Where $Q_{STREAM,i}$ is the total discharge downstream the Las Hountas karst spring, $Q_{SPRING,i}$ is the spring flow contribution of the karst aquifer to streamflow (sum of the matrix outflow $Q_{MS,i}$ and conduit outflow $Q_{CS,i}$),, and $Q_{SURF,i}$ is the contribution of surface runoff generated in non-karst areas of the catchment to streamflow on day i (all variables are expressed in mm.day^{-1}). The simulated streamflow hydrograph is given in m^3.s^{-1}.

5.2.3 The ISPEEKH model input data

5.2.3.1 Topography, land use, soil and lithology

The DEM of the Baget catchment was obtained from the US Geological Survey's Shuttle Radar Topography Mission files at 30−m spatial resolution (https://earthexplorer.usgs.gov/). The catchment altitude ranges from 502 to 1404 m a.m.s.l., and slopes vary between 10 to 30%. A land-use/cover map of the catchment was extracted at 100−m resolution from Corine Land Cover (CLC) database (https://land.copernicus.eu/pan-european/corine-land-cover), available at the Pan-European level for years 1990, 2000, 2006, 2012 and 2018. The land-use trajectory approach was applied to examine land-use change in the catchment over the hydrological simulation period of 2006−2018. Six land-use categories were identified, with no interannual changes detected. The

catchment is mainly covered by broad-leaved and coniferous forests (~85%), followed by pastures (~8%), moors and heathland (~5%), sparse transitional woodland-shrub (~1%) and agricultural lands (~1%). A soil map of the catchment was derived from the Food and Agriculture Organization (FAO) Digital Soil Map of the World at 1:5,000,000 scale (https://www.fao.org/soils-portal/soil-survey/soil-maps-and-databases/faounesco-soil-map-of-the-world/en/), and overlaid with a lithology map, to delineate karst and non-karst HRUs based on the catchment lithology, and to simulate the recharge from the karst and non-karst landforms to the E, M and C reservoirs following the karst groundwater module of ISPEEKH. The Baget catchment model was created using QSWAT+ 2.0.3 in QGIS based on the input DEM, land-use and soil maps, slope characteristics, and outlet location. A total of 19 subbasins and 225 HRUs were defined, with 116 HRUs being karst and 109 non-karst. The total area of the karst HRUs represented 70% of the catchment area while the non-karst HRUs accounted for 30%, and the HRUs delineation followed the areal distribution of the karst and non-karst regions in the catchment.

5.2.3.2 Meteorological variables

The meteorological variables required to conduct the hydrological simulations with ISPEEKH, using the Penman Monteith approach for evapotranspiration estimation, are daily precipitation, minimum and maximum air temperature, relative humidity, wind speed, and solar radiation. The precipitation datasets used in this study were retrieved from: (1) Saint Girons weather station (43°00'19"N; 01°06'25"E; 414 m a.m.s.l.), located 8.3 km from the Baget catchment outlet, (2) CPC and E-OBS gauge-based products; (3) SAFRAN, COMEPHORE, and ERA5-Land reanalysis products; (4) IMERG-LR, PERSIANN-CDR, CHIRPS, and SM2RAIN-ASCAT satellite-based products. Additionally, the daily minimum and maximum air temperature, relative humidity, wind speed, and solar radiation data were obtained from SAFRAN. The data points of the different products used in this study are shown in **Figure 21**.

The CPC precipitation dataset (Chen et al., 2008) is part of the products suite of the CPC Unified Precipitation Project, underway at the United States National Oceanic and Atmospheric Administration (NOAA) Climate Prediction Center (CPC). The dataset is constructed by interpolating the daily records from more than 30,000 gauge stations using the optimal interpolation (OI) objective analysis technique (Jiang et al., 2023), with a spatial coverage of 0.5° global land and a daily temporal resolution from 1979 to the present (Xie et al., 2007). The CPC data are available for download at https://psl.noaa.gov/data/gridded/data.cpc.globalprecip.html.

E-OBS (European Daily High-Resolution Observational Gridded Dataset; Haylock et al., 2008) is a land-only gridded daily observational dataset for precipitation and other atmospheric variables over Europe. This dataset is based on observations from the meteorological stations (22,600 stations, September 2022) provided by the National Meteorological and Hydrological Services (NMHSs) and other data holding institutes across Europe (Cornes et al., 2018). The E-OBS dataset is delivered on regular latitude-longitude grids with spatial resolutions of 0.1° and 0.25° from 1950 to near present (June 2023), and is accessible through the European Climate Assessment & Dataset (ECA&D, https://www.ecad.eu/download/ensembles/download.php). E-OBS version 25.0e - 10 km spatial resolution was adopted in this study.

COMEPHORE (COmbinasion en vue de la Meilleure Estimation de la Précipitation HOraiRE; Tabary, 2007; Tabary et al., 2012) is an hourly reanalysis of surface precipitation accumulation over metropolitan France at 1-km spatial resolution, provided by the French weather forecasting agency Météo-France for years 1997−2022. The COMEPHORE precipitation estimates are obtained using the data from the French network of 24 radars and hourly and daily precipitation rain gauges (approximately 4200 rain gauges with a daily time step including approximately 1200 rain gauges with an hourly time step) (Fumière et al., 2020; Le Roy et al., 2020).

SAFRAN (Système d'Analyse Fournissant des Renseignements Adaptés à la Nivologie; Quintana-Seguí et al., 2008) is an hourly analysis system of atmospheric variables (precipitation, 2-meter air temperature and humidity, 10-meter wind speed, downward solar and infrared radiation, and cloudiness), from 1958 to present, provided by Météo-France for metropolitan France and Corsica at 8-km spatial resolution. Estimates of the surface variables are derived over homogeneous climatic areas, determined based on topography, and refined with respect to nearby gauge-based observations using the optimal interpolation method. The analyses of temperature, humidity, wind speed, and cloud cover are carried out every 6 hours based on a first guess from the weather prediction model ARPEGE (Déqué et al., 1994) or the ECMWF archives. Precipitation is analyzed at daily time step with an initial guess inferred from climatological fields (Vidal et al., 2010). The analyzed variables are then interpolated at the hourly time step, where hourly precipitation distribution is inferred using the diurnal specific humidity cycle and separated between rainfall and snow using the 0.5 ºC isotherm (Moucha et al., 2021). Solar and infrared radiation are estimated from the vertical profiles of temperature, humidity, and cloudiness, using

a radiative transfer model (Ritter and Geleyn, 1992) due to the lack of observations for these two variables. Finally, all atmospheric variables are projected to an 8-km regular grid at the elevation of the grid cells in each homogeneous climatic zone, using the vertical profiles for each zone.

ERA5-Land (fifth generation European Centre for Medium-Range Weather Forecasts ECMW Reanalysis on global land surface; Hersbach et al., 2020; Muñoz-Sabater et al., 2021) is a spatially enhanced global dataset for the land component of the ERA5 reanalysis product, which is developed by ECMWF at 0.25° spatial resolution and hourly temporal resolution from 1950 onwards. The ERA5-Land dataset is obtained by forcing the HTESSEL land surface component (version Cy45r1 of the Integrated Forecasting System ISF) with low atmospheric meteorological fields from ERA5. Precipitation data in ERA5-Land are generated from ERA5 through a linear interpolation method based on a triangular mesh (Wu et al., 2023), reducing the spatial resolution to 0.10° (Muñoz-Sabater et al., 2021). The dataset is available from the Copernicus Climate data store (https://cds.climate.copernicus.eu/cdsapp#!/dataset/reanalysis-era5-land?tab=overview). In this study, the ERA5-Land hourly dataset was aggregated to obtain daily values.

IMERG (Integrated Multi-satellitE Retrievals for the Global Precipitation Measurement (GPM) mission; Huffman et al., 2019) is a precipitation product with 30-min temporal resolution, 0.1° spatial resolution, and 60° N–60° S full coverage. The product combines microwave precipitation estimates and microwave precipitation-calibrated infrared fields, including monthly surface precipitation gauge analyses to create research-level products. The Late-run version of the dataset (IMERG-LR), characterized by 14 h latency, was adopted in the study, and the product was accumulated to daily time scale (https://gpm.nasa.gov/data/directory).

PERSIANN-CDR (Precipitation Estimation from Remotely Sensed Information using Artificial Neural Networks- Climate Data Record; Ashouri et al., 2015) is a multi-satellite precipitation dataset that provides near-global precipitation information (60°N-60°S latitude and 0°–360° longitude) at 0.25° spatial resolution and daily temporal resolution, from 1983 to near present. The PERSIANN-CDR precipitation estimate is generated by processing the Gridded Satellite (GridSat-B1) infrared data using the PERSIANN algorithm, and by artificial neural network training using the National Center for Environmental Prediction (NCEP) Stage IV hourly precipitation data (Nguyen et al., 2018; Salmani-Dehaghi and Samani, 2021). The PERSIANN-CDR data are publicly available through the U.S. NOAA National Centers for Environmental Information (NCEI) at https://www.ncdc.noaa.gov/cdr/atmospheric/precipitation-persiann-cdr

and the Centre for Hydrometeorology and Remote Sensing (CHRS) Data Portal at http://chrsdata.eng.uci.edu .

CHIRPS (Climate Hazards center InfraRed Precipitation with Station data) is a quasi-global precipitation dataset covering 50°S-50°N (and all longitudes). The dataset incorporates 0.05° resolution satellite imagery with in-situ station data in order to create a gridded daily rainfall time series spanning from 1981 to near present (Funk et al., 2015). The daily/0.05° CHIRPS V2.0 dataset was used in this study (https://data.chc.ucsb.edu/products/CHIRPS-2.0/global_daily/netcdf/).

SM2RAIN-ASCAT (Soil Moisture to Rain—Advanced SCATterometer V1.5) is a global scale daily rainfall product of 10-km spatial resolution, obtained by application of the SM2RAIN algorithm (Brocca et al., 2014, 2019) to the Advanced SCATterometer (ASCAT) satellite soil moisture data (Wagner et al., 2013). In fact, SM2RAIN algorithm allows to invert the soil water equation to infer rainfall from the variation of soil moisture The SM2RAIN-ASCAT used in this study spans the period of 2007–2022, available at (http://hydrology.irpi.cnr.it/download-area/sm2rain-data-sets/).

The CPC, E-OBS, ERA5-Land and IMERG-LR coarse precipitation datasets were downscaled to 1-km resolution by leveraging the statistical information from CHELSA (Climatologies at high resolution for the earth's land surface areas; Karger et al., 2017), a high-resolution (30 arc sec, ~1-km) global downscaled climate product hosted by the Swiss Federal Institute for Forest, Snow and Landscape Research WSL. It is based on a mechanistical statistical downscaling of global reanalysis data or global circulation model output, and includes climate layers for various time periods and variables. A triple collocation technique was then applied to merge the downscaled CPC and IMERG-LR datasets (Filippucci et al., 2024). The resulting high-resolution precipitation products were applied in the hydrological modeling of the Baget catchment (**Figure 21**). Precipitation data that have been downscaled are indicated with '-ds' appended to each product name throughout the manuscript.

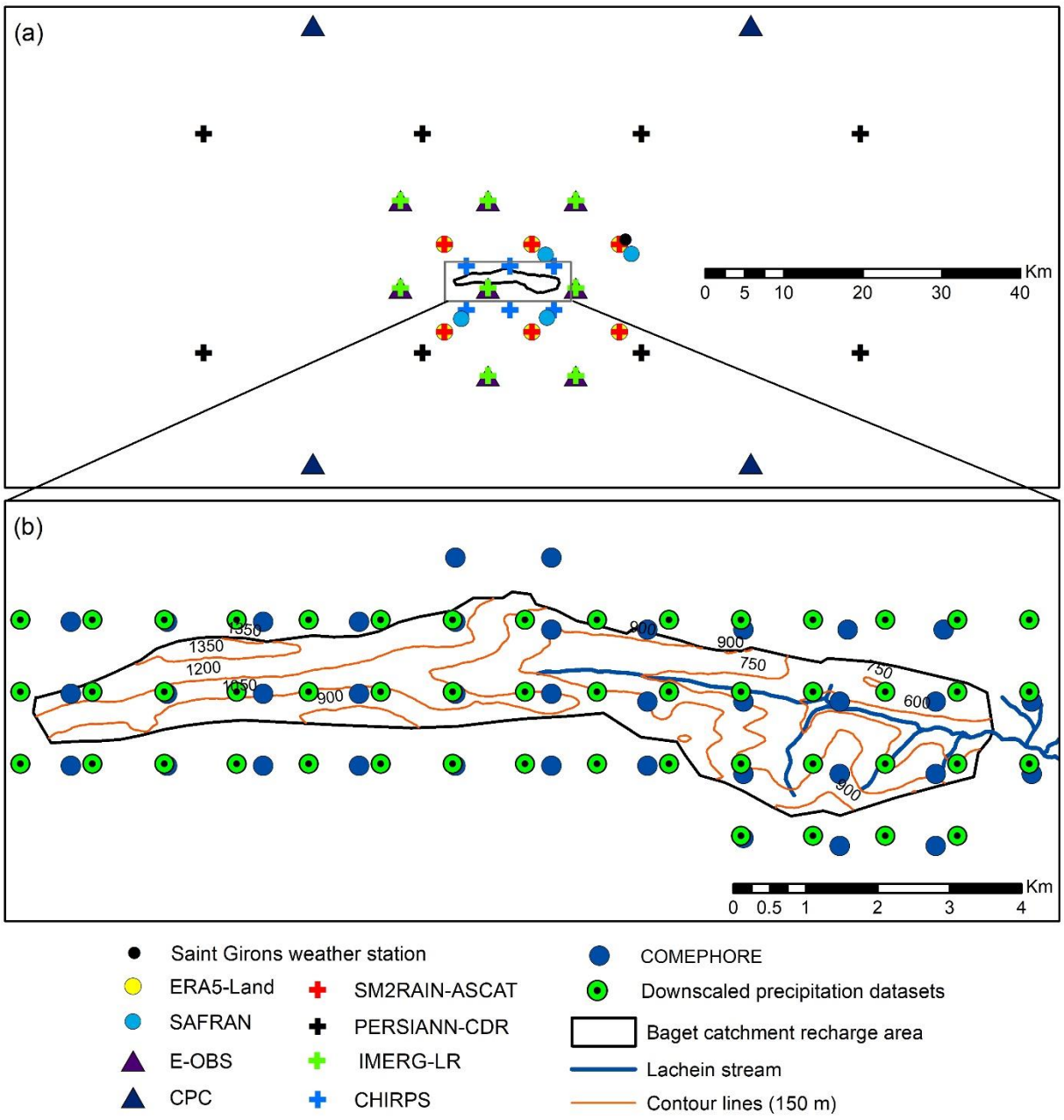

Figure 21. Figure showing the locations of the (a) Saint Girons weather station, data points of the E-OBS and CPC gauge-based products, ERA5-Land and SAFRAN reanalysis products, SM2RAIN-ASCAT, PERSIANN-CDR, IMERG-LR and CHIRPS satellite-based products, and (b) data points of the 1-km resolution COMEPHORE reanalysis product and downscaled E-OBS, CPC, ERA5-Land, IMERG-LR, and CPC-IMERG-LR products with respect to the Baget catchment recharge area.

5.2.3.3 Streamflow data

Streamflow at gauging station B1 (**Figure 19**), located 60 m downstream of the Las Hountas spring, is calculated from the stream water level measured at 30 min-interval by a float-type water-level sensor, and calibrated using rating curves that yield a coefficient of determination (R^2) of 1 annually. The daily streamflow data from 01/01/2006 to 31/12/2018 at station B1 were used to calibrate and validate ISPEEKH for each precipitation dataset. During this period, streamflow was measured continuously, and the daily discharge varied from 0.04 to 8.95 $m^3.s^{-1}$, with an average value of 0.45 $m^3.s^{-1}$.

5.2.4 Sensitivity analysis, parameter estimation, and uncertainty quantification methods for the ISPEEKH model

5.2.4.1 Parameter ESTimation Tool (PEST) followed by sensitivity analysis

For each precipitation dataset, ISPEEKH was set up to simulate the Baget catchment daily streamflow from 2006 to 2018, with a 2–year warm-up period (2006–2007), a 6–year calibration period (2008–2013), and a 5−year validation period (2014–2018). The models were calibrated with respect to daily streamflow measured at the gauging station B1. A preliminary manual calibration was first performed to determine the appropriate range values of the emptying exponents and discharge coefficients that not only optimize the simulated streamflow but also accurately represent the simulated water levels of the epikarst, matrix, and conduit reservoirs. This calibration process is required as the ISPEEKH model's ability to reproduce the dynamic behavior of water storage in these reservoirs is contingent upon these parameters. In particular, the model must capture the flow patterns of the conduit and matrix water storage. For the conduit storage, this includes a rapid rise in water levels followed by a swift water transfer to the spring during the high-flow periods, and an attenuated response with a gradual depletion during the low-recharge periods. In contrast, matrix water storage should exhibit lower variability with slower water transfer and reduced discharge to the spring. This manual calibration helps avoid unrealistic scenarios where certain parameter combinations lead to continuously increasing water levels in one or more reservoir even when the streamflow simulation appears satisfactory. Under this application, it was found that the value of the emptying exponents of the epikarst-to-conduit flow (α_{EC}) and conduit-to-spring flow (α_{CS}) must not exceed 2.5. The models were then calibrated automatically using the nonlinear, model-independent parameter estimator PEST (Doherty, 2018). PEST implements a local optimization technique that is based on the Gauss–Marquardt–Levenberg

algorithm to minimize the objective function of the squared sum of weighted residuals between the simulated and observed data.

The Morris screening method (elementary-effects test) for qualitative global sensitivity analysis (GSA) (Morris, 1991) was applied to assess the sensitivity of the ISPEEKH parameters governing streamflow. The selected parameters, which include those related to evapotranspiration, surface runoff, soil water fluxes, and karst groundwater fluxes, are listed in **Table 7** with their respective value ranges for sensitivity analysis. The Morris method evaluates the relative sensitivity of the model parameters by calculating the change in the model output when a specific model parameter is altered (i.e., elementary effect), while keeping all other parameters constant. A single elementary effect for the ith parameter is computed as follows:

$$EE_i = \frac{f(x_1, \dots, x_i + \Delta_i, \dots, x_p) - f(x)}{\Delta_i} \tag{8}$$

where EE_i is the elementary-effect value of the ith model parameter, f represents the model; $x_1, \dots, x_i$ is the model parameter value, and Δ_i is the change in ith model parameter.

With this method, the mean and standard deviation of all elementary effects for a given model parameter are used to assess parameter sensitivity and are calculated as follows:

$$\mu_i^* = \frac{1}{n}\sum_{j=1}^{n} |EE_i(j)| \tag{9}$$

$$\sigma_i = \sqrt{\frac{1}{n-1}\sum_{j=1}^{n}\left[EE_i(j) - \frac{1}{n}\sum_{j=1}^{n} EE_i(j)\right]} \tag{10}$$

where μ_i^* and σ_i represent the mean and standard deviation of all EE_i for a given parameter i, and n is the number of EE_i computations.

The pestpp-sen software tool (White et al., 2020) within the PEST++ environment was implemented to generate parameter values, update ISPEEKH files, run the model simulations and compute sensitivity indices for the Morris method.

SWAT+ allows for the calibration of various parameters by applying a single value within a given parameter range, adding an increment to an existing value, or applying a relative change of spatial parameters. For the calibration of ISPEEKH with PEST, template files were created from the model input files by replacing the original values of the targeted calibration parameters in their

respective input files with placeholders. Using these template files, the updated values of the calibration parameters are written to the model input files at each iteration of a PEST run. The parameters associated with the epikarst, matrix, and conduits reservoirs in the "karst.data" input file (i.e., the initial reservoir water levels, threshold water level for flow activation, emptying exponents and discharge coefficients) correspond to the karst aquifer properties and independent of the spatial variability of the surface HRUs. The curve numbers, evapotranspiration parameters, and soil parameters are calibrated at HRU level using template files of the "cntable.lum", "hydrology.hyd" and "soil.sol" input files, respectively.

5.2.4.2 Iterative ensemble smoother (iES) for parameter estimation and uncertainty quantification

The Iterative Ensemble Smoother (iES) method (Chen and Oliver, 2013), integrated in the pestpp-ies tool (White, 2018) within the PEST++ environment (Welter et al., 2015), was implemented in this study to generate prior (uncalibrated results) and posterior uncertainty estimates of ISPEEKH parameters. The iES method uses the Ensemble Kalman Filter (EnKF), an algorithm for data assimilation that updates state variables by incorporating measured data into the model results, based on correlations between the state variables and measured data (Evensen, 1994). The EnKF was initially implemented in the ensemble smoother scheme (ES)(Van Leeuwen and Evensen, 1996). ES was then modified by Chen and Oliver (2013) to operate iteratively using the Gauss–Levenberg–Marquardt (GLM) algorithm (the iES method) with a Jacobian matrix filled with finite-difference approximated derivatives, and improve minimization of the sum-of-squared residuals objective function for nonlinear problems. Chen and Oliver (2013) later reformulated the GLM algorithm to derive an approximate Jacobian matrix empirically from an ensemble of random parameter values, whereby the model needs to be run once for each member of the ensemble (i.e. realization) rather than once for each parameter. This reformulation reduced the computational burden of populating a full rank Jacobian matrix for models with a large number of parameters while maintaining the ability to be parallelized and model independent (non-intrusive).

The iES method starts with a prior ensemble of parameter values. A Jacobian matrix of parameter sensitivities is derived from the relationships between the model parameters and output, using a range of parameter values from the prior ensemble. The Jacobian matrix is applied to update each parameter ensemble iteratively by minimizing model residuals through the GLM algorithm, resulting in a posterior ensemble of optimized model parameters. The propagation of the ensemble of parameter realizations until a satisfactory fit with the observed data yields an

estimate of the posterior parameter distribution, which can be used to quantify the uncertainty in the forecasts of interest.

Table 7. Selected parameters, parameters description, and ranges for sensitivity analysis and calibration of the ISPEEKH model

Parameter	Parameter description	Parameter range	Hydrological process
cn_pastg_f **(*cn_a*; *cn_b*; *cn_c*; *cn_d*)**	SCS runoff curve numbers for pastures	-20% to +15% (relative)	Surface runoff
cn_wood_f **(*cn_a*; *cn_b*; *cn_c*; *cn_d*)**	SCS runoff curve numbers for broad-leaved and coniferous forests	-20% to +15% (relative)	
esco	Soil evaporation compensation factor	0.9–1	Evapotranspiration
epco	Plant uptake compensation factor	0.9–1	
perco	Percolation coefficient	0–0.5	Soil water fluxes
awc	Available water capacity (mm $H_2O.mm^{-1}$ soil) of the i^{th} soil layer	-60% to +80% (relative)	
bd	Moist bulk density ($g.cm^{-3}$ or $Mg.m^{-3}$) of the i^{th} soil layer	-20% to +20% (relative)	
sol_k	Saturated hydraulic conductivity ($mm.h^{-1}$) of the i^{th} soil layer	-20% to +20% (relative)	
$h_{E,0}$(***he_init***)	Initial water level in the epikarst (mm)	1–25	Epikarst-matrix-conduit fluxes
E_{min}(***e_min***)	Minimum water level for epikarst flow activation	0.01–1	
δ_E(***gwdelay_e***)	Recharge delay to the epikarst (days)	0.5–2	
α_{EC}(***a_ec***)	Emptying exponent of the epikarst-conduit flow	0.5–2.5	
k_{EC}(***k_ec***)	Discharge coefficient of the epikarst-conduit flow ($mm.day^{-1}$)	0.0001–0.095	
α_{EM}(***a_em***)	Emptying exponent of the epikarst-matrix flow	0.5–1.5	
k_{EM}(***k_em***)	Discharge coefficient of the epikarst-matrix flow	0.0001–0.01	
$h_{M,0}$(***hm_init***)	Initial water level in the matrix (mm)	1–25	
δ_M(***gwdelay_m***)	Recharge delay from the soil to the matrix (days)	1–3	
α_{MC}(***a_mc***)	Emptying exponent of the matrix-conduit flow	0.5–1.3	
k_{MC}(***k_mc***)	Discharge coefficient of the matrix-conduit flow ($mm.day^{-1}$)	0.0001–0.05	
α_{MS}(***a_ms***)	Emptying exponent of the matrix-spring flow	0.5–1.5	
k_{MS}(***k_ms***)	Discharge coefficient of the matrix-spring flow ($mm.day^{-1}$)	0.0001–0.01	
$h_{C,0}$ (***hc_init***)	Initial water level in the conduit (mm)	1–25	

α_{CS} (a_cs)	Emptying exponent of the conduit-spring flow	0.5–2.5
k_{CS} (k_cs)	Discharge coefficient of the conduit-spring flow (mm.day^{-1})	0.0001–0.095

5.2.5 Model predictive performance evaluation

The capacity of the model to predict streamflow under the different precipitation datasets was evaluated with performance metrics commonly used in karst hydrology: the Nash-Sutcliff efficiency NSE (Nash and Sutcliffe, 1970), the coefficient of determination R^2, the percent of bias PBIAS (Gupta et al., 1999) (positive values indicate model underestimation bias, while negative values indicate model overestimation bias), and the Kling-Gupta efficiency KGE (Gupta et al., 2009), adopting the performance quality classes by Moriasi et al. (2015) and Jeannin et al. (2021). The non-parametric Kling-Gupta efficiency KGENP (Pool et al., 2018) and the correlation coefficients of Pearson Rp and Spearman Rs evaluation metrics were also computed so as to account for additional aspects of the model performance.

A wavelet multiresolution analysis (MRA), which is commonly used to decompose a signal into a progression of successive approximations and details in increasing order of resolution, was conducted to project streamflow on an orthogonal basis of wavelet generated from a filter band following a dyadic scale. For an orthogonal decomposition, the sum of all components (details and residue or smooth) returns the initial signal. The usual performance criteria consider the mean errors and do not capture how the model errors can be structured in time and frequency (Labat et al., 2000b; Sivelle et al., 2022). Thus, the application of MRA on both observed and simulated streamflow times series under the uncorrected and corrected precipitation datasets allows the evaluation of the hydrological model performance across different temporal scales by calculating the Pearson correlation coefficient (Rp) on the calibration and validation periods according to the dyadic scale.

5.2.6 Correction of precipitation datasets

The preliminary assessment of the Baget catchment water balance conducted by Al Khoury et al. (2023a) suggests that precipitation is generally underestimated in the study area, which results in the underestimation of the simulated streamflow. Several approaches are reported in the literature to correct the bias of precipitation products based on observed precipitation data from representative meteorological stations, including the ratio bias and dual-core smoothing correction methods, and the cokriging, probability matching, Bayesian correction, and optimal interpolation–

probability matching methods, among others (Ye et al., 2023). In the case of the Baget catchment, the only available observed precipitation dataset is from the meteorological station of Saint Girons (414 m m.a.s.l), which is located outside the catchment at 8.3 km from its outlet. Therefore, in the absence of a precipitation monitoring network that captures the altitude effect within the catchment, the 1-km resolution COMEPHORE, CPC-ds, E-OBS-ds, ERA5-Land-ds, IMERG-LR-ds and merged CPC-IMERG-LR-ds gridded precipitation datasets were corrected in order to resolve the water balance discrepancy prior to model calibration by "Doing Hydrology Backward (DHB) (Kirchner's methodology). Accordingly, an orographic correction multiplicative factor (OCF_m) was computed for each dataset based on a rearranged water balance equation (Khan and Koch, 2018):

$$OCF_{m,i} = \frac{PCP_{true,i}}{PCP_{obs,i}} = \frac{Q_{obs} + ET_a - \Delta g}{P_{obs,i}} \quad (11)$$

Where $OCF_{m,i}$ is the calculated orographic correction multiplicative factor for the gridded precipitation dataset i, Q_{obs} is the mean annual catchment discharge, ET_a is the catchment mean annual actual-evapotranspiration, Δg represents the catchment mean annual change in glacier storage, $P_{obs,i}$ is the observed (uncorrected) precipitation dataset i, and $PCP_{corrected,i}$ is the true (corrected) precipitation dataset i. The measured streamflow data at the gauging station B1 and the grid-based actual evapotranspiration estimates from SAFRAN over the 2006−2018 simulation period were used for the calculation of the OCF_m for each precipitation dataset (**Table 8**), and the change of glacier ice volume is null for the catchment.

Table 8. The orographic correction multiplicative factors (OCF_m) calculated for the 1-km resolution COMEPHORE, CPC-ds, E-OBS-ds, ERA5-Land-ds, IMERG-LR-ds and merged CPC-IMERG-LR-ds gridded precipitation datasets.

Precipitation dataset	OCF_m value
CPC-ds	2.03
E-OBS-ds	1.85
COMEPHORE	1.42
ERA5-Land-ds	1.23
IMERG-LR-ds	1.48
CPC-IMERG-LR-ds	1.89

5.3 Results and Discussion

5.3.1 ISPEEKH parameters sensitivities under the precipitation products

The sensitivities of the selected parameters were computed under all precipitation datasets using the Morris screening method for minimizing streamflow errors. The sensitivity measures (i.e., the mean (μ^*) and the standard deviation (σ)) are based on the elementary effect absolute values of the model parameters and are not related to the scale and magnitude of the input or outputs. Thus, they show relative relation between parameters (Abbas et al., 2024). The order of magnitude of (μ^*) and (σ) for all parameters and parameter sensitivity ranks remained consistent across all precipitation datasets, and the average values of (μ^*) and (σ) obtained from the sensitivity analysis run under each precipitation dataset are illustrated in **Figure 22**. The discharge coefficient and emptying exponent of the conduit-to-spring flow (k_{CS}; α_{CS}) and the discharge coefficient and emptying exponent of the epikarst-to-conduit flow (k_{EC}; α_{EC}) ranked consistently as the top four most sensitive parameters irrespective of the input precipitation data, while the emptying exponents of the epikarst-to-matrix, matrix-to-spring, and bidirectional matrix-to-conduit fluxes (α_{EM}; α_{MS}; α_{MC}) were noticeably less sensitive than their counterparts α_{EC} and α_{CS}. This outcome is compatible with the discharge characteristics of the Baget catchment which includes a shallow epikarst with high connectivity to network of well-developed conduits in the saturated zone, resulting in most infiltration water passing from the epikarst to the conduits and then emerging at the spring outlet through the conduits, with low contribution from the matrix to the overall discharge. The discharge coefficients of the epikarst-to-matrix flow, matrix-to-conduit bidirectional flow, and matrix-to-spring flow (k_{EM}; k_{MC}; k_{MS}) also ranked among the most sensitive parameters along with soil parameters (i.e., percolation coefficient $perco$, available water capacity awc, and moist bulk density bd). Overall, the parameters governing karst groundwater flow and infiltration were the most sensitive while all surface runoff and evapotranspiration parameters ranked among the least sensitive. These results are also consistent with the recharge-discharge characteristics of the Baget catchment, where direct infiltration of most rainfall over the surface-exposed and well-developed epikarst zone of the Baget catchment feeds the karst aquifer and spring flow, with low surface runoff generation and contribution to the catchment streamflow.

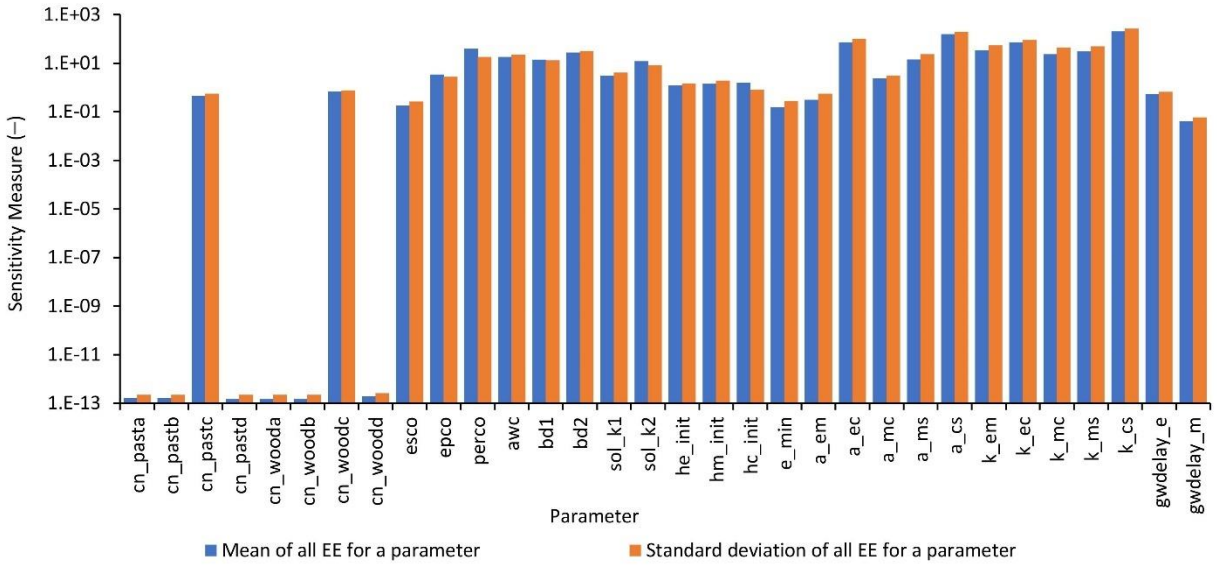

Figure 22. Average values of the elementary effects (EE) mean (μ^*) and standard deviation (σ), calculated with the Morris global sensitivity analysis for the selected parameters of ISPEEKH with different precipitation datasets.

5.3.2 Performance of coarse and downscaled precipitation datasets for catchment water balance and streamflow simulation

The assessment of the Baget catchment water balance for the 2008–2018 period revealed that water balance is in deficit under all the precipitation data series (**Table 9**). The mean annual precipitation (PCP) varied between 887 mm under coarse CPC and 1451 mm under ERA5-Land-ds. The mean annual simulated streamflow (Q_{STREAM}) values ranged from 262 to 802 mm compared to a mean annual observed streamflow of 1145 mm in years 2008–2018. The simulated mean annual recharge ($RECH$) to the karst aquifer reservoirs was consistently equal to the simulated spring flow (Q_{SPRING}), showing that ISPEEKH modeled karst groundwater storage and spring flow from the recharge input successfully by conserving the water balance. The Baget is a conservative catchment with a groundwater recharge zone of 13.25 km^2 (Mangin, 1975), ruling out the possibility of additional water contribution to the spring discharge from a larger recharge area or interbasin groundwater flow. The Q_{SPRING} contribution to Q_{STREAM} varied between 80−92%, while direct surface runoff (Q_{SURF}) accounted for the remaining 18−20%, which is consistent with the Baget catchment discharge characteristics where the perennial Las Hountas karst spring is the primary source of discharge. The simulated mean actual evapotranspiration (ET_a) values (582–721 mm.year^{-1}) were comparable to the SAFRAN-based mean annual ET_a (667

mm), indicating that the uncertainty due to ET estimation is unlikely to generate the water balance discrepancy. Moreover, historical records also show that streamflow magnitude has been in the order of 1000 mm.year^{-1} over the 1969–2005 period, indicating that the streamflow measurement uncertainty does not justify the water balance discrepancy. Thus, precipitation recorded at low altitude at Saint Girons station (414 m. a.m.s.l.), 8.3 km from the catchment outlet, cannot sustain the observed streamflow, while field observations in the 1973−1999 period report a mean annual precipitation of 1750 mm 0.5 km from the catchment (658 m a.m.s.l.) (Johannet et al., 2008).

Subsequently, the values of the NSE, R^2, and PBIAS metrics (**Table 10**) showed unsatisfactory performance for daily streamflow simulation (NSE $\leq$ 0.5, $R^2 \leq$ 0.6, PBIAS $\geq \pm$ 15% in both calibration and validation periods (Moriasi et al., 2015). The SAFRAN and COMEPHORE reanalysis products, with mean annual PCP of 1274 and 1287 mm, respectively, scored higher NSE and R^2 values than all remaining precipitation products, particularly during validation where NSE and R^2 were satisfactory ($0.50 <$ NSE ≤ 0.70; $0.60 < R^2 \leq 0.75$) despite a PBIAS of 40%. The coarse and downscaled ERA5-Land datasets yielded the lowest PBIAS values (28 to 35%) among all precipitation products. In contrast, the performance from the gauge-based and satellite-based precipitation products was unacceptable, with NSE and KGE values close to or below 0, low R^2, and high PBIAS of 50 to 80%. The reanalysis COMEPHORE, SAFRAN, and ERA5-Land precipitation products outperformed the gauge- and satellite-based precipitation products. Moreover, the spatial downscaling of the CPC, IMERG-LR, and E-OBS data to 1-km resolution and merging of the downscaled IMERG-LR and CPC data did not improve the predictive performance compared with the coarse datasets, while downscaling of ERA5-Land only improved the water balance estimation marginally by reducing the underestimation bias by 3−4% across both the calibration and validation periods. The observed and simulated hydrographs under the ensemble of precipitation products are provided in **Figures 23 to 27**. Overall, considerable discrepancies in the average annual precipitation estimates, exceeding 500 mm.year^{-1},were revealed between the products. Hence, the reanalysis, gauge- and satellite-based precipitation products considered in this study do not represent the precipitation regime of the Baget catchment. Precipitation is generally underestimated in the Pyrenees region due to precipitation under catch by the rain gauges and the low-quality radar coverage in the mountainous regions, which corroborates the poor model predictive performance with the gauge- and satellite-based precipitation products. Yet, the French kilometric dataset COMEPHORE benefits from rain gauge

data collected by the French electricity company, which maintains various hydroelectric power plants to increase the quality of the dataset in several regions, such as Normandy and central France. The combination of radar and rainfall data in COMEPHORE provides a dataset on the Pyrenees that is of lower quality than the data on the rest of France but that remains of higher quality than other observational precipitation databases currently available for this mountainous region (Fumière et al., 2020). This could justify the higher streamflow simulation performance obtained under COMEPHORE precipitation compared to the gauge- and satellite-based precipitation products. The results of our study could not be compared to those of previous studies in karst catchments, particularly those conducted by Mo et al. (2020, 2022) in the XiaJia (799.2 km^2) and Chengbi (2,087 km^2) karst river basins in China, due to the discrepancy in the basins' sizes relative to the Baget catchment (13.25 km^2) as well as the differences in the climatic features, landscape properties (i.e., topography, karst terrains, land use, and soil), and karst recharge and groundwater flow dynamics. Nonetheless, both studies reported an underestimation of flow under the raw IMERG satellite precipitation and underlined the need to apply correction and fusion methods based on gauge-measured precipitation to improve the model predictive performance.

Table 9. Mean annual water balance in the Baget catchment ($mm.year^{-1}$) for years 2008−2018, simulated using ISPEEKH with Saint Girons gauge precipitation, gauge-based precipitation products (CPC, E-OBS), reanalysis products (SAFRAN, COMEPHORE and ERA5-Land), and satellite precipitation products (PERSIANN-CRD, IMERG-LR, CHIRPS, SM2RAIN-ASCAT). PCP: precipitation; PET: potential evapotranspiration, ET_a: actual evapotranspiration; $SURQ$: surface runoff; $RECH$: groundwater recharge; Q_{SPRING}: spring flow; Q_{STREAM}: streamflow.

Precipitation dataset	PCP	PET	ET_a	Q_{SURF}	$RECH$	Q_{SPRING}	Q_{STREAM}
Saint Girons	996.36	851.20	720.63	25.53	233.01	232.65	261.73
CPC	886.67	690.64	581.44	19.89	271.36	271.04	293.93
CPC-ds	892.17	686.97	581.87	26.47	265.76	265.43	295.25
E-OBS	949.78	681.60	574.54	44.54	311.30	311.17	360.01
E-OBS-ds	964.98	687.11	584.63	46.03	313.91	313.81	364.42
SAFRAN	1274.09	690.13	599.31	97.14	540.02	540.16	645.29
COMEPHORE	1287.34	686.84	591.07	132.54	517.80	517.49	660
ERA5-Land	1414.97	689.23	620.93	127.48	624.50	624.34	762.96
ERA5-Land-ds	1450.54	685.20	619.58	138.76	651.18	650.99	802.34
PERSIANN-CDR	982.77	692.03	598.29	30.75	341.02	340.66	375.64
IMERG-LR	1202.27	683.79	601.09	75.36	503.45	502.66	585.60

IMERG-LR-ds	1214.14	688.95	607.15	75.39	507.47	506.47	589.30
CPC-IMERG-LR-ds	950.85	687.30	596.73	37.34	296.66	296.36	337.57
CHIRPS	1098.07	695.29	597.00	53.94	441.35	441.45	502.13
SM2RAIN-ASCAT	1180.72	693.38	620.11	66.06	453.84	453.82	526.35

Table 10. Daily streamflow statistical performance for the ISPEEKH model simulations driven by different precipitation datasets.

	Calibration				**Validation**			
Precipitation dataset	**NSE**	**R^2**	**PBIAS**	**KGE**	**NSE**	**R^2**	**PBIAS**	**KGE**
Saint Girons	-0.162	0.202	81.54%	-0.226	0.171	0.46	72.17%	0.016
CPC	-0.149	0.217	79.46%	-0.223	0.106	0.469	68.53%	-0.044
CPC-ds	-0.103	0.266	78.2%	-0.179	0.101	0.474	69.7%	-0.057
E-OBS	0.021	0.345	72.91%	-0.064	0.278	0.537	63.67%	0.109
E-OBS-ds	0.049	0.351	71.36%	-0.034	0.268	0.525	64.62%	0.101
SAFRAN	0.478	0.606	44.15%	0.366	0.557	0.732	43.25%	0.356
COMEPHORE	0.496	0.63	47.76%	0.374	0.625	0.682	36.35%	0.547
ERA5-Land	0.434	0.556	35.09%	0.338	0.452	0.585	31.6%	0.334
ERA5-Land-ds	0.459	0.555	32.06%	0.379	0.477	0.577	27.72%	0.379
PERSIANN-CDR	-0.127	0.113	67.87%	-0.221	-0.102	0.098	66.52%	-0.25
IMERG-LR	-0.018	0.114	51.36%	-0.051	0.111	0.201	46.15%	0.083
IMERG-LR-ds	-0.015	0.126	53.25%	-0.062	0.094	0.174	43.29%	0.088
CPC-IMERG-LR-ds	-0.047	0.296	74.8%	-0.127	0.176	0.481	65.7%	0.021
CHIRPS	0.058	0.201	53.53%	0.03	-0.089	0.064	59.50%	-0.177
SM2RAIN-ASCAT	0.024	0.255	59.08%	-0.065	0.001	0.168	48.39%	-0.105

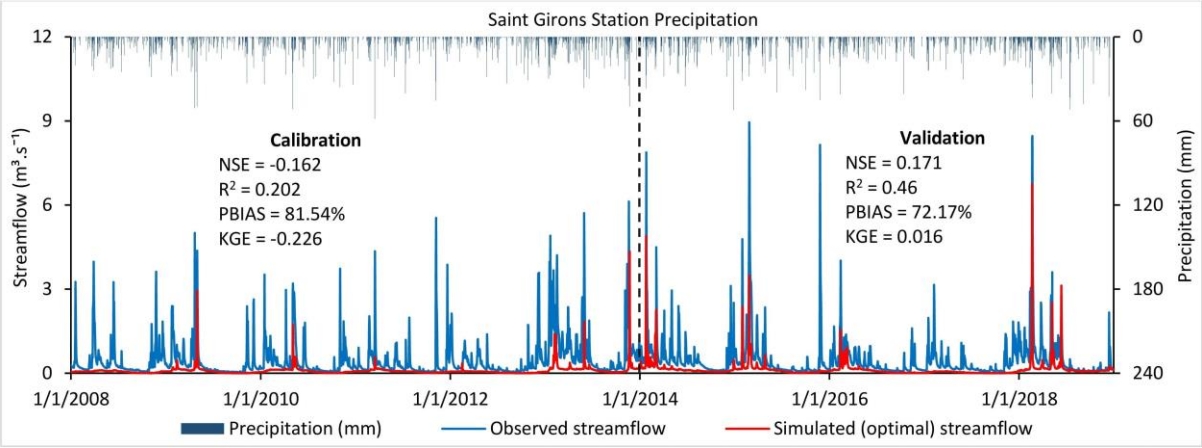

Figure 23. Daily observed and simulated streamflow of the Baget catchment in years 2008–2018, using the ISPEEKH model driven by precipitation of Saint Girons weather station.

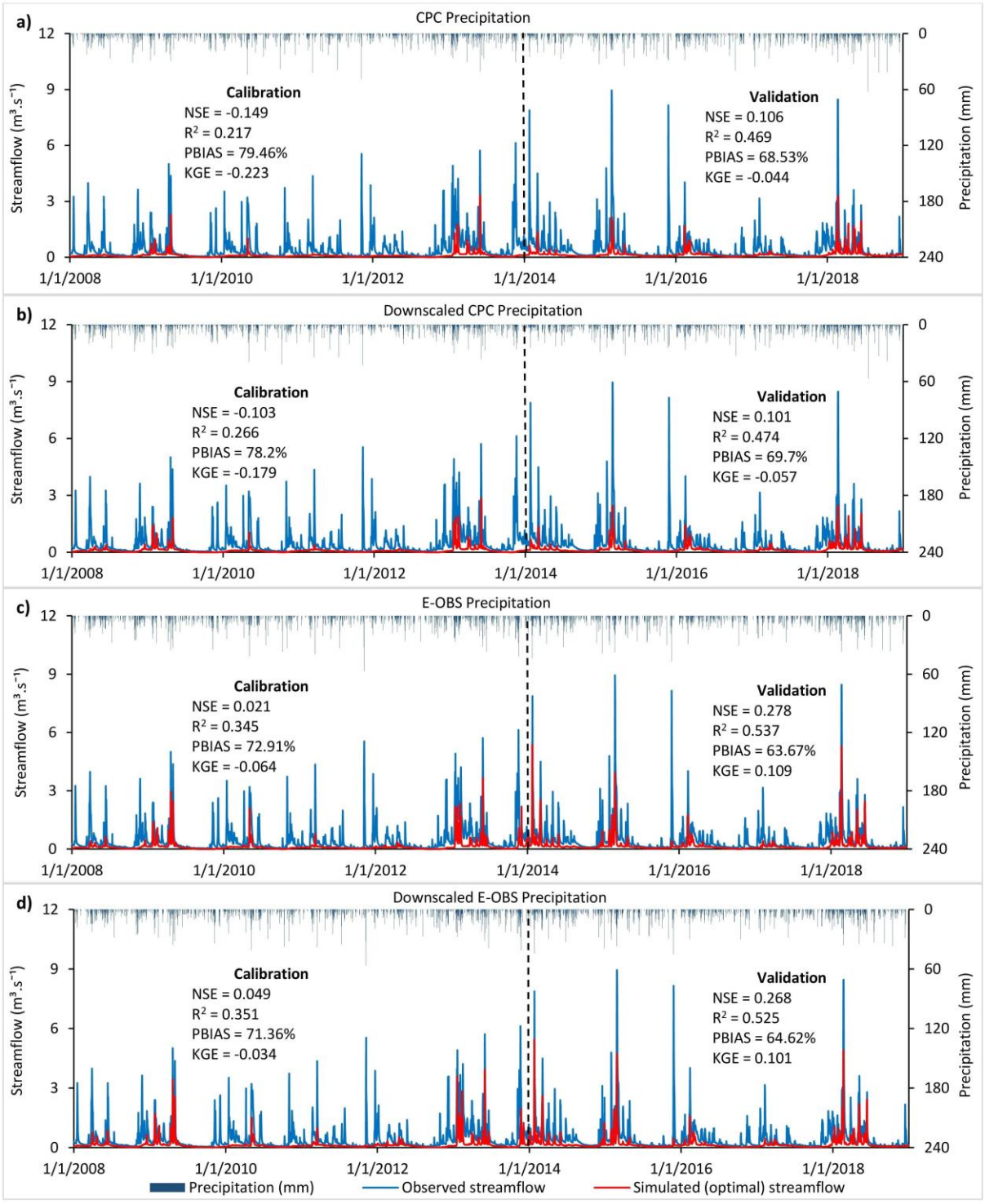

Figure 24. Daily observed and simulated streamflow of the Baget catchment in years 2008–2018, using the ISPEEKH model driven by precipitation of the (a) CPC, (b) downscaled CPC, (c) E-OBS, and (d) downscaled E-OBS gauge-based products.

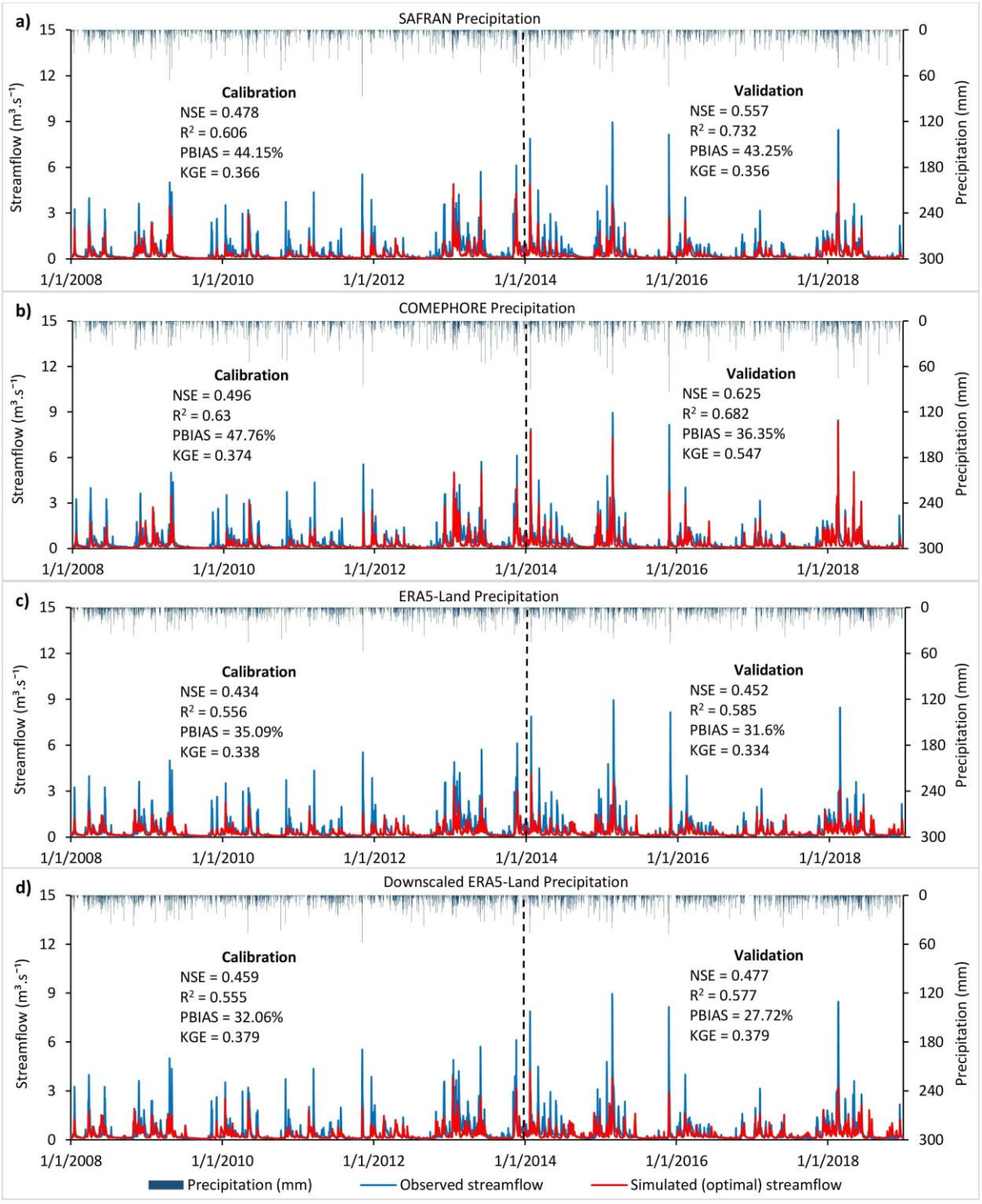

Figure 25. Daily observed and simulated streamflow of the Baget catchment in years 2008–2018, using the ISPEEKH model driven by precipitation of the (a) SAFRAN, (b) COMEPHORE, (c) ERA5-Land, and (d) downscaled ERA5-Land reanalysis products.

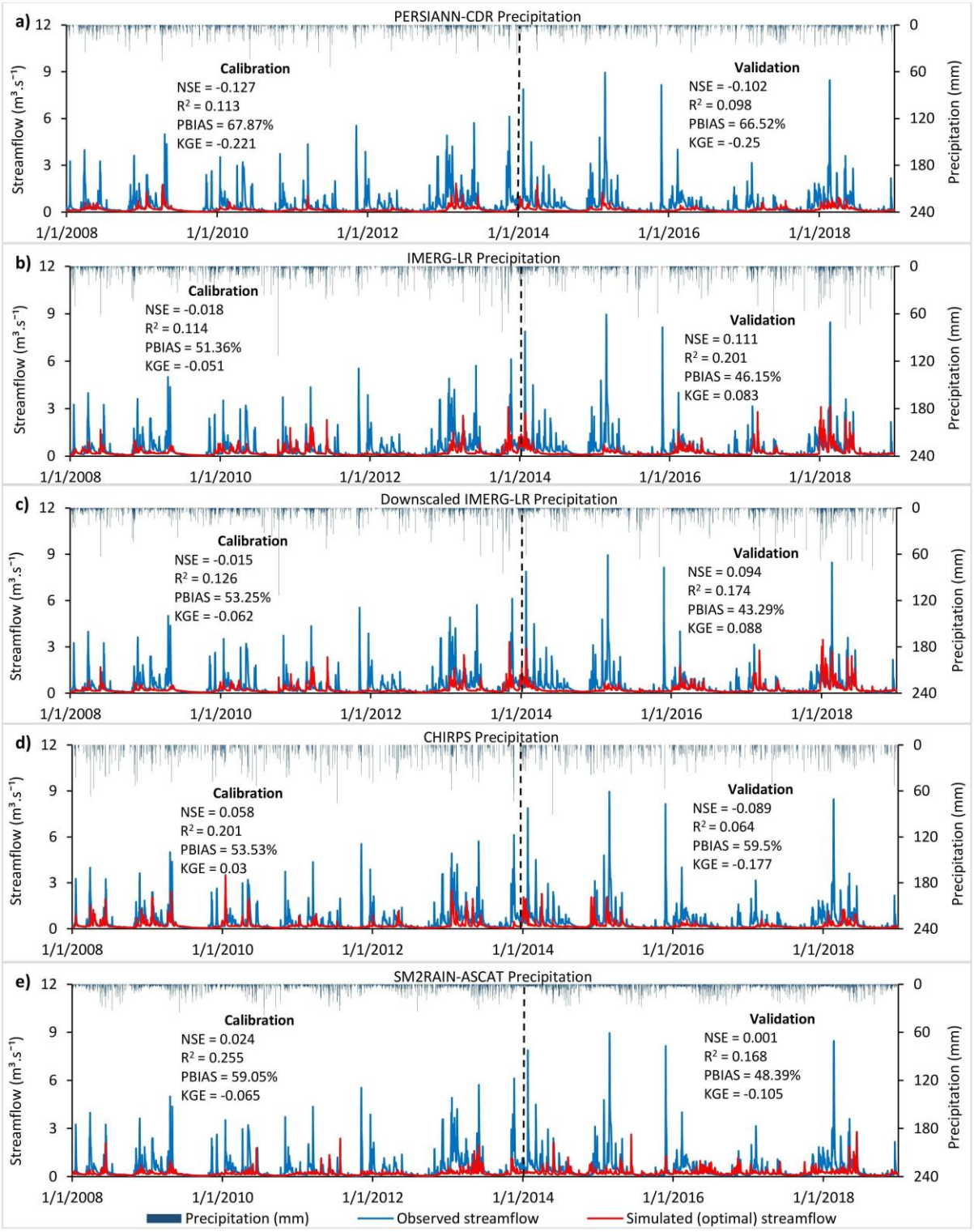

Figure 26. Daily observed and simulated streamflow of the Baget catchment in years 2008–2018, using the ISPEEKH model driven by precipitation of the (a) PERSIANN-CDR, (b) IMERG-LR, (c) Downscaled IMERG-LR, (d) CHIRPS and (e) SM2RAIN-ASCAT satellite-based products.

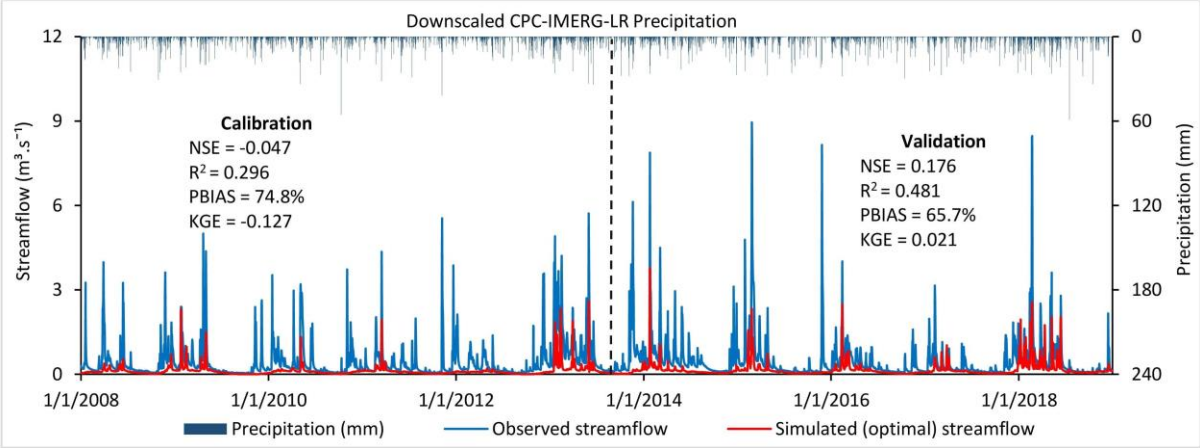

Figure 27. Daily observed and simulated streamflow of the Baget catchment in years 2008–2018, using the ISPEEKH model driven by downscaled precipitation of the merged CPC-IMERG-LR product.

The optimal values of the emptying exponents (alpha) of the epikarst, matrix and conduit fluxes are summarized in **Table 11**. The values of the epikarst-to-conduit flow emptying exponent α_{EC} (1.775–2.5; Mean: 2.309) and conduit-to-spring flow emptying exponent α_{CS} (1.536–2.5; Mean: 2.126) indicate that ISPEEKH simulated the conduit fluxes in the Baget catchment as nonlinear, which is consistent with the karst aquifer discharge dynamics. These results indicate that the model is well adapted to reproduce the hydrodynamic behavior of the study catchment, despite underestimating streamflow under all precipitation products. On the other hand, the emptying exponent of the matrix-to-conduit bidirectional flow rate α_{MC} (0.939–1.3; Mean: 1.081) was mostly close to 1, suggesting that the exchange flow between the conduit and the surrounding matrix is primarily determined by the hydraulic conductivity of the fissured system.

Table 11. Optimal values of the emptying exponents (alpha) of the epikarst, matrix and conduit fluxes simulated by ISPEEKH under different precipitation datasets.

Precipitation dataset	α_{EM}	α_{EC}	α_{MC}	α_{MS}	α_{CS}
Saint Girons	1.000	2.500	1.129	0.519	2.201
CPC	0.863	2.484	1.055	0.512	2.466
CPC-ds	0.738	2.433	1.300	0.543	2.452
E-OBS	0.867	2.468	1.025	0.506	2.467
E-OBS-ds	0.920	2.474	1.085	0.506	2.462
SAFRAN	0.799	2.500	1.176	0.578	1.536
COMEPHORE	0.789	2.430	1.056	0.513	1.885
ERA5-Land	0.721	2.500	1.061	0.575	2.077
ERA5-Land-ds	0.734	2.500	0.939	0.570	1.985
PERSIANN-CDR	0.738	1.929	1.094	0.575	1.737
IMERG-LR	0.757	1.775	1.070	0.593	1.776
IMERG-LR-ds	0.743	1.788	1.032	0.585	1.920
CPC-IMERG-LR-ds	0.923	2.487	1.124	0.519	2.491
CHIRPS	0.764	1.918	1.033	0.584	1.933
SM2RAIN-ASCAT	0.820	2.455	1.033	0.503	2.500
Min	0.721	1.775	0.939	0.503	1.536
Max	1.000	2.500	1.300	0.593	2.500
Mean	0.812	2.309	1.081	0.545	2.126

5.3.3 Performance of volume-corrected downscaled precipitation datasets for catchment water balance and streamflow simulation

Following the correction of the COMEPHORE, CPC-ds, E-OBS-ds, ERA5-Land-ds, IMERG-LR-ds and merged CPC-IMERG-LR-ds precipitation data, the calibrated ISPEEKH models yielded comparable values of the water balance components for the 2008−2018 period, with mean annual PCP of 1781−1824 mm, ET_a of 598−620 mm (equivalent to 33−35% of PCP), Q_{SURF} of 194−237 mm, $RECH$ and Q_{SPRING} of 920−963 mm, and Q_{STREAM} of 1160−1194 mm (equivalent to 65−67% of PCP) (**Table 12**). Q_{SPRING} represented 78−82% of Q_{STREAM} and channel flow amounted to the remaining 18−22%. The PBIAS (absolute values) were reduced considerably to less than 5% in calibration and 10% in validation after precipitation correction.

Table 12. Mean annual water balance fluxes in the Baget catchment (mm.year^{-1}) for years for 2008−2018, simulated using ISPEEKH with the corrected precipitation datasets of the 1-km resolution COMEPHORE and downscaled CPC, E-OBS, ERA5-Land, IMERG-LR, and CPC-IMERG-LR products.

Precipitation dataset	PCP	PET	ET_a	Q_{SURF}	$RECH$	Q_{SPRING}	Q_{STREAM}
CPC-ds	1801.51	684.69	608.15	224.41	919.75	919.47	1164.76
E-OBS-ds	1788.33	685.09	602.63	210.29	963.24	962.91	1193.82
COMEPHORE	1823.76	685.15	598.35	236.71	926.39	926.24	1184.05
ERA5-Land-ds	1780.99	684.39	620.16	207.46	933.96	932.08	1159.57
IMERG-LR-ds	1792.90	688.06	619.85	193.71	951.99	949.33	1162.39
CPC-IMERG-LR-ds	1799.23	685.19	617.59	208.93	944.92	944.48	1173.16

The corrected COMEPHORE precipitation yielded the streamflow simulation with the highest overall NSE, R^2, and KGE values (**Table 13**), indicating satisfactory ($0.50 < NSE \leq 0.70$; $0.60 < R^2 \leq 0.75$) to good performance ($0.70 < NSE \leq 0.80$; $0.75 < KGE \leq 0.85$) based on Moriasi et al. (2015) and Jeannin et al. (2021). The corrected E-OBS-ds precipitation improved the model predictive performance from unacceptable to satisfactory, both in calibration and validation. The CPC-ds and merged CPC-IMERG-LR-ds precipitation correction also enhanced the model performance, particularly in calibration where both NSE and R^2 surpassed 0.6 compared to 0.5 in validation, while KGE exceeded 0.7 in calibration and 0.6 in validation. On the other hand, the NSE and R^2 metrics varied only marginally under the corrected ERA5-Land-ds precipitation, as opposed to KGE increasing from 0.38 to above 0.6 and 0.5 in calibration and validation, respectively. Finally, the corrected IMERG-LR-ds precipitation consistently performed poorly in streamflow simulation, with very low NSE, R^2, and KGE metrics.

Table 13. Daily streamflow statistical performance indices for the ISPEEKH simulations driven by the corrected COMEPHORE and downscaled ERA5-Land, CPC, E-OBS, IMERG-LR, and merged CPC-IMERG-LR precipitation datasets.

	Calibration				Validation			
Precipitation dataset	**NSE**	**R^2**	**PBIAS**	**KGE**	**NSE**	**R^2**	**PBIAS**	**KGE**
CPC-ds(1)	0.638	0.65	2.58%	0.787	0.533	0.54	-6.33%	0.666
CPC-ds(2)	-0.103	0.266	78.2%	-0.179	0.101	0.474	69.7%	-0.057
E-OBS-ds(1)	0.646	0.666	-2.25%	0.81	0.67	0.66	-6.23%	0.786
E-OBS-ds(2)	0.049	0.351	71.36%	-0.034	0.268	0.525	64.62%	0.101
COMEPHORE(1)	0.719	0.736	3.20%	0.854	0.637	0.732	-10.65%	0.772
COMEPHORE(2)	0.496	0.63	47.76%	0.374	0.625	0.682	36.35%	0.547
ERA5-Land-ds(1)	0.56	0.564	1%	0.603	0.523	0.531	-4%	0.547
ERA5-Land-ds(2)	0.459	0.555	32.06%	0.379	0.477	0.577	27.72%	0.379
IMERG-LR-ds(1)	0.016	0.087	3.87%	0.168	0.014	0.108	-7.37%	0.232
IMERG-LR-ds(2)	-0.015	0.126	53.25%	-0.062	0.094	0.174	43.29%	0.088
CPC-IMERG-LR-ds(1)	0.623	0.624	2.1%	0.719	0.499	0.503	-7.3%	0.614
CPC-IMERG-LR-ds (2)	-0.047	0.296	74.8%	-0.127	0.176	0.481	65.7%	0.021

(1) precipitation dataset after correction; (2) precipitation dataset before correction

Although precipitation correction ensured water balance closure by mitigating the streamflow volume underestimation, this approach did not improve streamflow simulation for every precipitation dataset. The model driven by the corrected COMEPHORE precipitation best reproduced the discharge patterns during the high-flow periods by preserving the rising and recession of the observed hydrograph, while accurately estimating most peak flow values (**Figure 28c**). In comparison, the models run with the corrected CPC-ds (**Figure 28a**), E-OBS-ds (**Figure 28b**) and merged CPC-IMERG-LR-ds (**Figure 28f**) precipitation datasets often underestimated peaks greater than 3 $m^3.s^{-1}$. Moreover, the model better estimated flow during recession under the corrected COMEPHORE precipitation rather than the CPC-ds, EOBS-ds and merged CPC-IMERG-LR-ds precipitation. Under the corrected ERA5-Land-ds precipitation, peak flow rates were generally underestimated, while intermediate and low flows were overestimated, resulting in simulated falling limbs that are higher than the falling limbs of the observed hydrograph (**Figure. 28d**). Moreover, the simulated and observed hydrographs under the corrected IMERG-LR-ds precipitation were asynchronous and showed noticeable discrepancies for the high- and low-flow magnitudes (**Figure 28e**). Nonetheless, the NSE, KGE, KGENP, Rp and Rs metrics, calculated for the mean simulated daily streamflow hydrographs and plotted in radar charts for the calibration and validation periods (**Figure 29**), showed a globally higher model predictive performance under

the ensemble of corrected precipitation data. **Figure 30** illustrates the observed and best estimated daily streamflow with prior and posterior prediction uncertainty bands under the corrected COMEPHORE precipitation. The plot in **Figure 30a** represents the prior parameter ensembles with wider uncertainty bands, while the plot in **Figure 30b** shows the posterior ensemble that reduced the uncertainty band, indicating that the ensemble smoother has incorporated the observational data effectively with higher quality precipitation data.

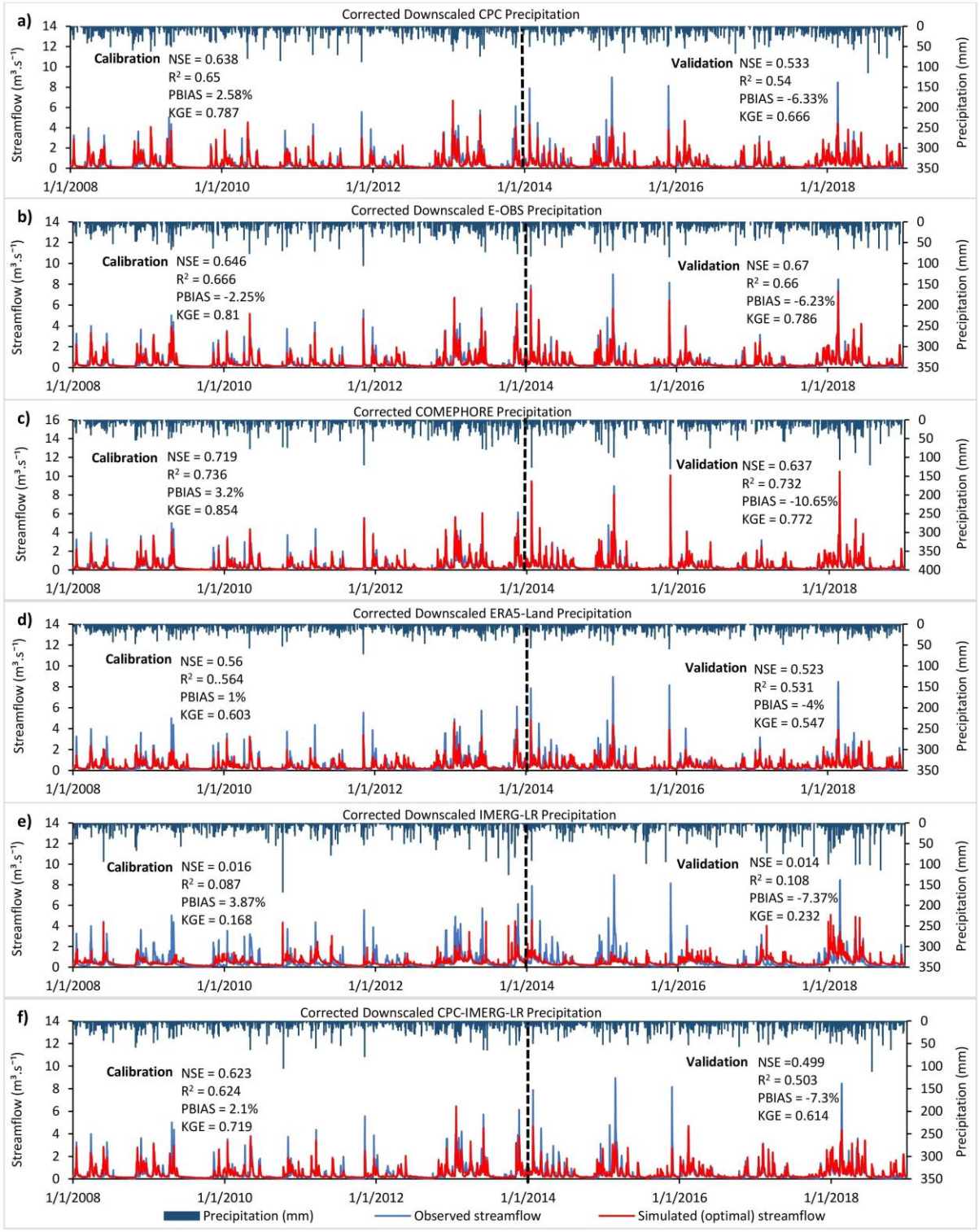

Figure 28. Daily observed and simulated streamflow of the Baget catchment in years 2008–2018, using the ISPEEKH model driven by the corrected (a) downscaled CPC precipitation, (b) downscaled E-OBS precipitation, (c) COMEPHORE precipitation, (d) downscaled ERA5-Land precipitation, (e) downscaled

IMERG-LR precipitation, and (f) downscaled merged CPC-IMERG-LR precipitation. NSE: Nash–Sutcliffe Efficiency; R^2: coefficient of determination; PBIAS: percent bias; KGE: Kling–Gupta Efficiency

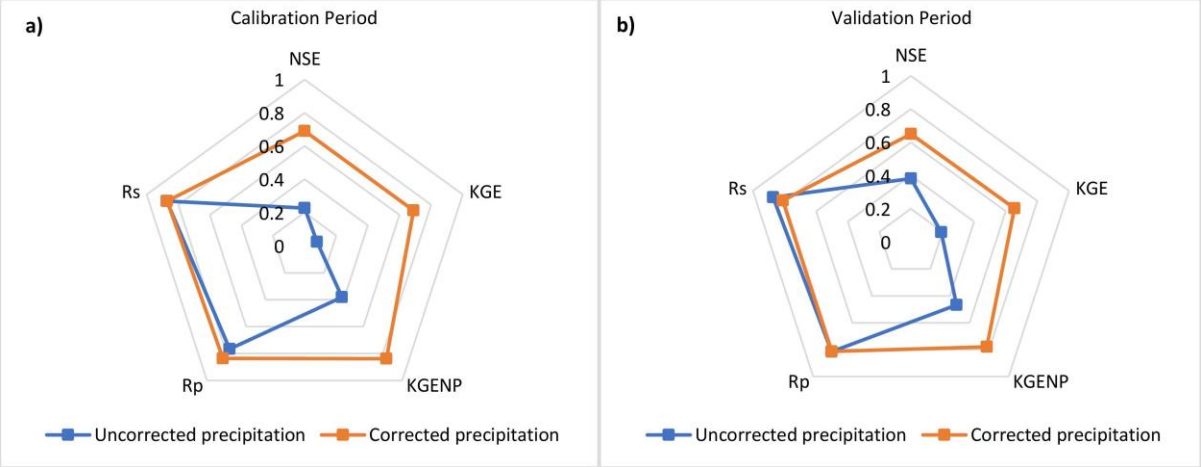

Figure 29. Radar chart of the NSE (Nash-Sutcliffe Efficiency), KGE (Kling Gupta Efficiency), KGENP (Kling Gupta Efficiency Non-Parametric), Rp (Pearson correlation coefficient), and Rs (Spearman correlation coefficient) performance criteria for the (a) calibration and (b) validation periods of the mean daily streamflow ISPEEKH simulations with the uncorrected and corrected precipitation datasets.

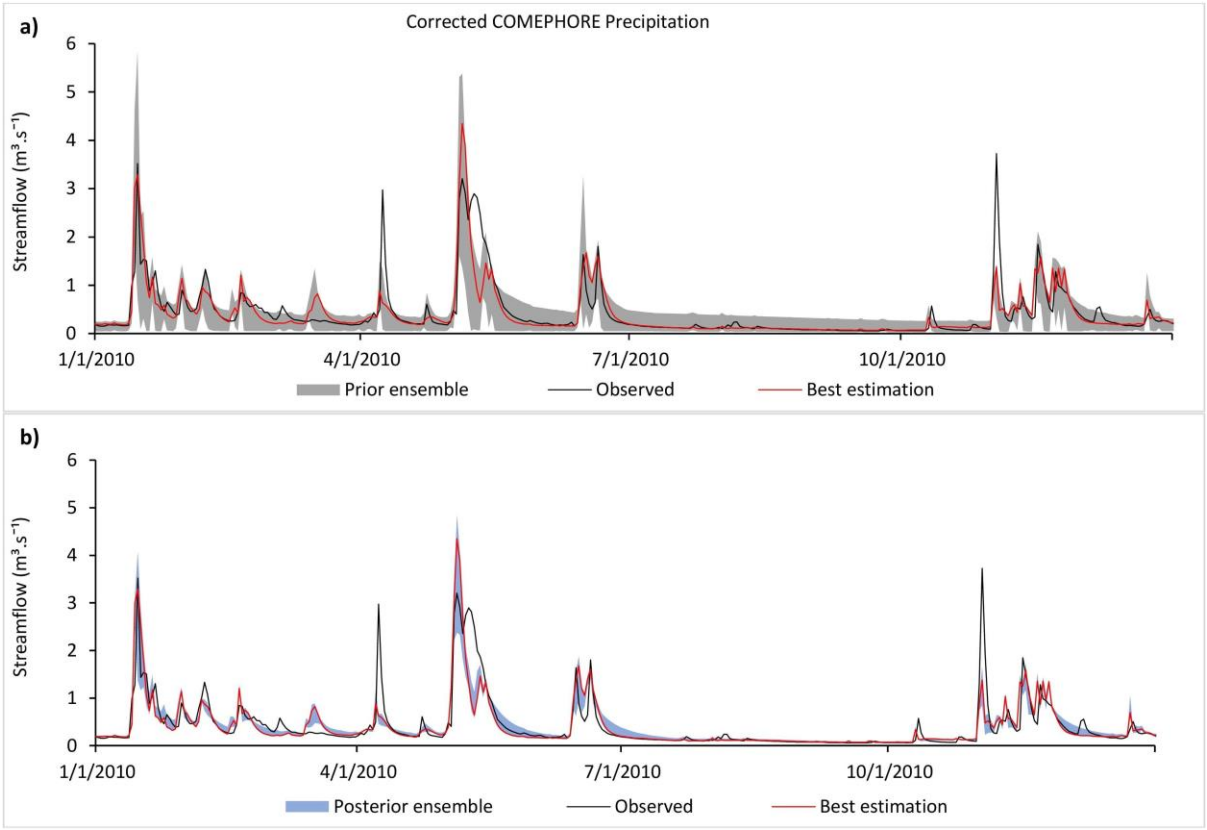

Figure 30. (a) Prior and (b) posterior prediction uncertainty bands for streamflow simulation in the Baget catchment using ISPEEKH driven by corrected COMEPHORE precipitation dataset.

Figure 31 shows the Pearson correlation coefficient (Rp) performance metric as a function of time scale, based on the application of an orthogonal wavelet decomposition on the observed and simulated streamflow under the uncorrected and corrected 1-km resolution precipitation datasets. The uncorrected COMEPHORE and ERA5-Land-ds reanalysis precipitation products had comparable performances and outperformed their counterparts for the various scales. Correlations under COMEPHORE ranged from 0.289 to 0.874 in the calibration period and 0.228 to 0.906 in the validation period for the 2- to 32-day scales, while correlations under ERA5-Land-ds varied from 0.098 (2 days) to 0.819 (32 days) in calibration and 0.156 (2 days) to 0.836 (16 days) in validation. The uncorrected CPC-ds and E-OBS-ds gauge-based precipitation datasets yielded correlations of 0.182−0.564 and 0.245−0.666, respectively, in calibration for the 2- to 32-day scales, and correlations of 0.262−0.767 and 0.198−0.827, respectively, in validation. Moreover, the uncorrected CPC-IMERG-LR-ds precipitation scored correlations in the range of

0.201 (2 days)−0.588 (32 days) during calibration and 0.401 (2 days)−0.804 (32 days) during validation. The model driven by the uncorrected IMERG-LR-ds precipitation showed the poorest performances: correlations were negative for the 2-day scale, and varied from 0.132 (4 days) to 0.252 (32 days) in calibration and 0.160 (4 days) to 0.387 (16 days) in validation.

Model performance improved across the various time scales under the corrected COMEPHORE, E-OBS-ds, and CPC-ds products. The corrected COMEPHORE precipitation exhibited the highest correlations, which ranged from 0.785 to 0.941 in the calibration period and 0.769 to 0.931 in the validation period for the scales from 4 days to 32 days. Under the E-OBS-ds precipitation, correlations increased to 0.686 (4 days)–0.932 (32 days) in calibration and to 0.703 (4 days)–0.919 (32 days) in validation. Correlations also improved considerably under the corrected CPC-ds precipitation, increasing to 0.699–0.862 and 0.656–0.819 for the 4- to 32-day scales. On the other hand, correlations were higher with the CPC-IMERG-LR-ds precipitation mainly during calibration, increasing to 0.322 (2 days)–0.846 (32 days). Under the corrected ERA5-Land-ds precipitation, correlation values increased slightly (0.652−0.833) in the calibration period for the 4- to 32-day scales but decreased (0.031−0.741) in the validation period, showing an overall comparable model performance to the uncorrected ERA5-Land-ds precipitation. Correlations only increased in the calibration period for the 16- to 32-day scales but diminished in the validation period under the corrected IMERG-LR-ds precipitation, indicating a lower model performance for the high compared to the uncorrected IMERG-LR-ds precipitation.

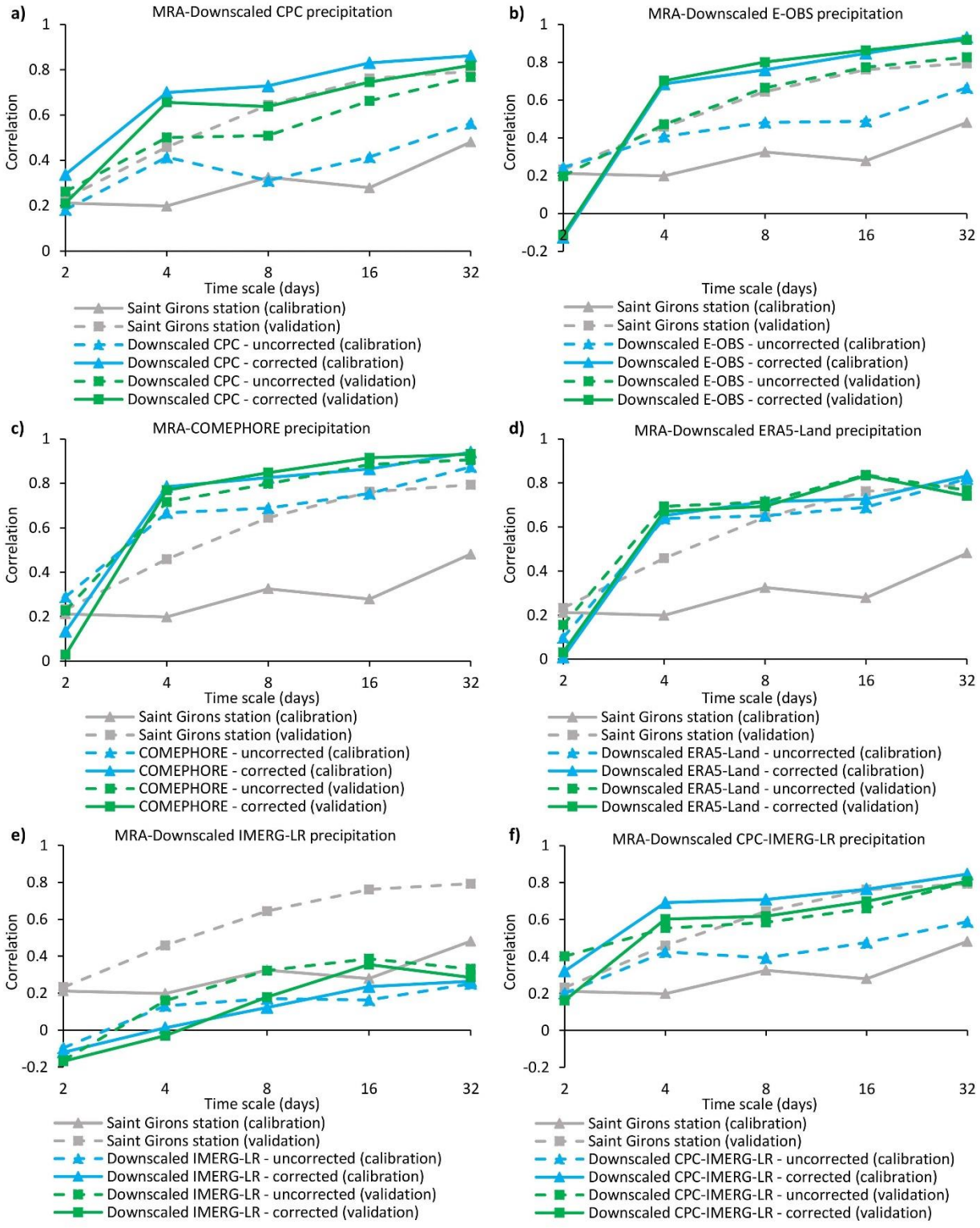

Figure 31. Pearson correlation coefficient (Rp) performance criteria on the calibration and validation periods, based on orthogonal wavelet decomposition on observed and simulated streamflow times series under the uncorrected and corrected 1-km resolution precipitation datasets.

Figure 32 shows the envelopes of monthly average simulated streamflow values under the various uncorrected and corrected 1-km resolution precipitation datasets. The envelope formed with the uncorrected precipitation data reveals significant discrepancies between simulated and observed discharge, at both monthly and annual scales. This suggests limitations in the ISPEEKH model's ability to accurately reproduce the catchment hydrological processes when driven with uncorrected precipitation inputs. In contrast, the envelope with corrected precipitation datasets demonstrates satisfactory predictive performances, with narrower ranges of simulated streamflow values and reduced discrepancies between the simulated and observed discharge patterns, both in the calibration and validation periods. Thus, the incorporation of corrected precipitation data has enhanced the reliability and predictive capability of the hydrological model, leading to more robust simulations of streamflow dynamics.

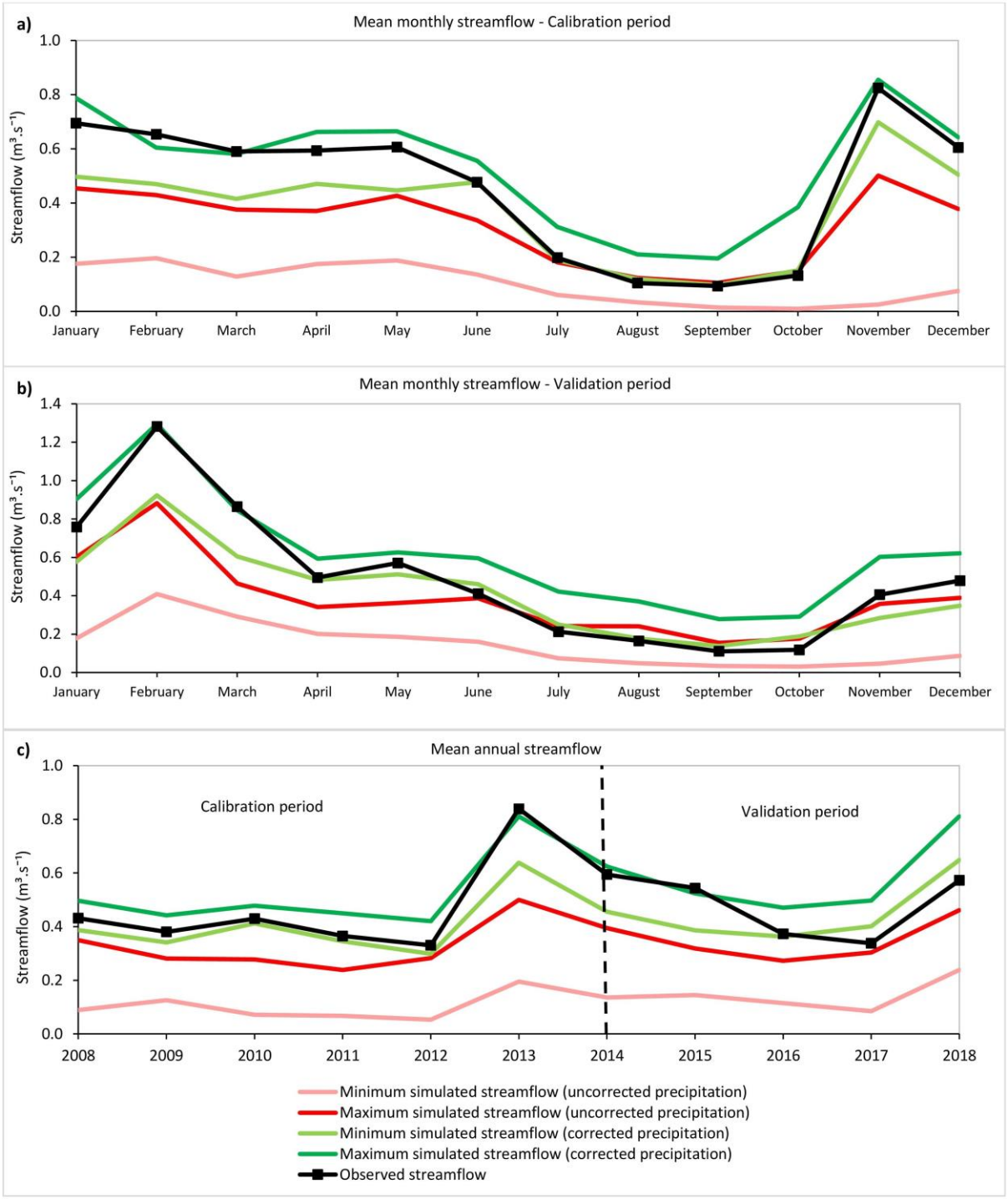

Figure 32. Mean observed streamflow and mean minimum and maximum values of the ensemble of ISPEEKH streamflow simulations under the uncorrected and corrected precipitation datasets considering (a) the calibration period at monthly scale, (b) validation period at monthly scale, and (c) both calibration and validation periods at annual scale.

Overall, these findings underscore the importance of accurate precipitation data quality for the hydrological modeling of small-scale karst watersheds characterized by quick flow processes, and highlight the value of incorporating corrected precipitation datasets to enhance the hydrological model's predictive capability as opposed to relying on globally used gauge-, and satellite-based and reanalysis precipitation products, both at coarse and downscaled spatial resolutions. The COMEPHORE reanalysis of precipitation by merging radar and rain gauge data, covering metropolitan France, was found to be more reliable than the global gauge- and satellite-based precipitation products. Therefore, for future research, daily and subdaily operating rain gauges should be installed at different altitudes in the Baget catchment in order to capture the spatial and temporal distribution characteristics of the catchment precipitation, then evaluate the spatial and temporal scale accuracy of regional and global precipitation products with respect to the station-measured precipitation. Subsequently, different bias correction methods could be applied to these products (Ye et al., 2023), and watershed hydrological modeling can be performed with the raw and corrected precipitation datasets so as to re-evaluate their accuracy at daily and subdaily time scales, and assess the performance of the bias correction methods. Additionally, this study suggests that the development of fine-resolution native reanalysis precipitation products could serve as base data for streamflow simulation in remote meso-scale karst catchments. To improve the model streamflow prediction performance, it is recommended to either apply watershed-scale precipitation volume correction methods (e.g., "Doing Hydrology Backward (DHB)" (Kirchner's methodology) if there are no representative ground stations or use precipitation information from available representative nearby stations to correct the base precipitation.

5.3.4 Study limitations and future perspectives

This study underscored the importance of accurate precipitation data quality for the hydrological modeling of mesoscale ungauged karst catchments characterized by quick flow processes. It highlighted the value of applying corrected precipitation datasets at downscaled spatial resolution to enhance the hydrological model's predictive capability of streamflow in such catchments as opposed to relying on globally used gauge-based, satellite-based and reanalysis precipitation products at coarse spatial resolutions. A catchment-scale precipitation volume correction was performed to close the water budget before model calibration by "Doing Hydrology Backward (DHB)" (Kirchner's methodology), with orographic correction multiplicative factors

calculated for the 1-km resolution precipitation products. This correction method, however, did not improve the simulated hydrographs under all precipitation datasets. The corrected COMEPHORE reanalysis product, specifically developed by merging radar and rain gauge data for metropolitan France, delivered the best simulation results, suggesting that fine-resolution regionally-tailored reanalysis precipitation products could serve as base data for streamflow simulation in remote meso-scale karst catchments.

This finding underscores a critical limitation: the absence of representative precipitation gauges within the study catchment. Raw precipitation products, whether gauged-based, satellite-based or reanalysis, cannot fully substitute for direct, localized observations. Moreover, the bias correction of these products, while necessary, is insufficient to achieve high accuracy without a robust network of precipitation gauges within the catchment. The presence of such gauges is indispensable for capturing the spatial and temporal variability of precipitation, ensuring the reliability of hydrological models in similar ungauged or sparsely gauged regions. Thus, for future research, daily and subdaily operating rain gauges should be installed at different altitudes in the Baget catchment in order to capture the spatial and temporal distribution characteristics of the catchment precipitation, then evaluate the spatial and temporal scale accuracy of regional and global precipitation products with respect to the station-measured precipitation. Subsequently, different correction methods could be applied to these products, and watershed hydrological modeling could then be performed with the raw and corrected precipitation datasets so as to re-evaluate their accuracy at daily and subdaily time scales, and assess the performance of the correction methods.

Several approaches are reported in the literature to correct gridded precipitation products with gauge observations such as ratio bias correction, dual-core smoothing correction, Bayesian correction, cokriging, probability matching, optimal interpolation–probability matching, integrated fusion through inverse error variance weighting (Ye et al., 2023), artificial neural networks (Ait Dhmane et al., 2023), frequency correction (Li et al., 2023), and distribution mapping (Londhe et al., 2023).On the other hand, the elevation bands method has been commonly used in SWAT to consider the orographic effects on precipitation in mountainous regions. The method applies up to ten equally spaced elevation bands in each subbasin to adjust regional precipitation by weighting the elevation difference between the rain gauge and the band, and multiplying the elevation difference by a constant input precipitation lapse rate (Tuo et al., 2016).

Several studies have shown that the elevation bands method in SWAT enhanced the accuracy of the precipitation estimation and runoff simulations in mountainous regions (Chiphang et al., 2020; Wu et al., 2019; Zhang et al., 2015), while others underlined the need to improve it as the increase in precipitation with altitude should not constant but rather dependent on the precipitation amount. In their study, Galván et al. (2014) observed that the elevation band method in SWAT often underestimates intense precipitation and overestimates lower precipitation due to discrepancies between subbasin altitudes and rain gauge elevations. To address this, they proposed a modification to the SWAT source code that calculates a ratio to multiply precipitation at the recording gauge and determine precipitation in the elevation band, rather than adding a constant value. Similarly, Grusson et al. (2015) identified issues with SWAT's overestimation of snow at higher elevations, attributing this to the use of uniform temperature and precipitation lapse rates. They suggested two approaches to mitigate this: (1) increasing the number of elevation bands, or (2) using the existing bands more effectively by setting thinner bands at higher altitudes to cover smaller elevation ranges. In SWAT+, the precipitation and temperature lapse rates should adjust precipitation and temperature based on elevation data from spatial objects and weather files. Although these changes were planned to be reflected in the SWAT+ source code and documentation, the new inputs were not operational in the version of SWAT+ used in this study.

Finally, continuous streamflow data from gauge station B1 was used to calibrate the model. However, since spring flow is a major component of streamflow in the Baget catchment, the absence of continuous spring flow measurements for calibration limits the model's ability to fully capture groundwater dynamics, introducing uncertainty in simulating both spring flow and overall streamflow. Therefore, future work should prioritize the collection of continuous spring flow data at Las Hountas, along with groundwater level measurements and hydrogeochemical data, to enable a more comprehensive model calibration. This would result in a more accurate representation of water fluxes and storage dynamics within the karst aquifer, ultimately improving streamflow predictions.

5.4 Conclusions

This study evaluated the performance of several coarse- and fine-resolution precipitation products in simulating daily streamflow in the small-scale Baget karst catchment (13.25 km^2), located in a sparsely monitored region in the Pyrenees mountains, southwest of France, and characterized by rapid rainwater infiltration. The ensemble of precipitation datasets used in this

study included: the gauged-based products CPC and E-OBS, the reanalysis products SAFRAN, COMEPHORE and ERA5-Land, and the satellite-based products PERSIANN-CDR, IMERG-LR, SM2RAIN-ASCAT, and CHIRPS. The CPC, E-OBS, ERA5-Land, and IMERG-LR precipitation datasets were downscaled to 1-km resolution and applied together with 1-km resolution merged CPC-IMERG-LR precipitation in the hydrological analysis. The Baget catchment's hydrological response to the precipitation products was simulated over years 2006–2018 using the ISPEEKH model, a modified variant of the Soil and Water Assessment Tool (SWAT+) for spring flow-dominated karst watersheds. This model incorporates three nonlinear reservoirs to simulate fluxes of the epikarst, conduit, and matrix water-bearing components in a karst aquifer. In conclusion:

- The discharge coefficients and emptying exponents governing the epikarst outflow to the conduits and the conduit outflow to the spring were the most sensitive model parameters across the precipitation products used in this study. This result aligns with the discharge patterns observed in the Baget catchment, where fast recharge and conduit-dominated flow behavior are prevalent.
- Water balance analysis from 2008 to 2018 revealed a noticeable deficit under the ensemble of the precipitation datasets. The gauge- and satellite-based precipitation products yielded the lowest model prediction performances, with a flow underestimation bias of around 48 to 74%. The reanalysis products outperformed the gauge- and satellite-based precipitation products, scoring higher NSE, R^2, and KGE metrics, and an overall 30–44% flow underestimation bias. The COMEPHORE precipitation performed best, followed by SAFRAN and ERA5-Land precipitation.
- The downscaling of the CPC, IMERG-LR, ERA5-Land and E-OBS precipitation datasets to finer 1-km spatial resolution improved the model predictive performance insubstantially or only marginally compared to the coarse datasets.
- The optimal values of the emptying exponents of the epikarst-to-conduit and conduit-to-spring outflows, simulated under the ensemble of the precipitation products, were mostly greater than 2, suggesting that ISPEEKH was adapted to reproduce the nonlinear conduit flow dynamics in the Baget catchment and that the discrepancy in the model predictive performance is mainly related to precipitation quality.
- Finally, this study underscored the significance of incorporating spatially distributed corrected precipitation from various products in order to enhance the reliability of models

in the hydrological simulation of highly responsive small karst catchments. Based on catchment-scale precipitation correction, the COMEPHORE reanalysis of precipitation covering mainland France generated the best streamflow simulation, highlighting the need to install in-situ gauges stations at various altitudes in the catchment to correct the fine resolution reanalysis precipitation data for further improvement of the discharge simulations.

CHAPTER 6: Conclusions and future perspectives

6.1 Conclusions

The Soil and Water Assessment Tool (SWAT) has experienced significant global growth in conducting environmental studies, with over 5000 peer-reviewed articles published. SWAT review studies covered a variety of applications including SWAT developments in landscape representation, stream routing, soil phosphorus dynamics, ecosystem services quantification, runoff simulation, hydrological impacts assessment under a changing environment, non-point source pollution, and coastal watershed applications. However, numerical simulation of karst watersheds and their processes in SWAT is still ongoing, despite advancements in SWAT models and methods.

A review of 75 peer-reviewed studies published between 2000 and 2022 examined the applications of standard and modified SWAT models in karst-influenced and karst-dominated watersheds. The review emphasized the limited number of studies that used karst numerical modeling with SWAT. Most studies reported direct application of standard SWAT in karst watersheds, while few have modified the source code or integrated it with other karst aquifer-based groundwater models to improve karst watershed hydrology simulation. While SWAT adequately simulated streamflow in several karst areas, it was found to have poor predictive performance in complex karst watersheds, failing to accurately reproduce peak and low flows, generating faster regressions than observed data, and underpredicting runoff volumes due to the lack of explicit representation of karst features hydrodynamics. Additionally, the modified SWAT models did not fully reproduce flow functions of epikarst, matrix, and conduits in karst aquifers using a non-linear storage-discharge relationship.

The study proposes a semi-distributed karst hydrological model called ISPEEKH for simulating surface and subsurface flow processes in karst-dominated catchments. The model was developed by modifying the recharge functions of the SWAT+ source code and implementing a non-linear three-reservoir karst module that reproduces the epikarst-matrix-conduit system. ISPEEKH was applied to model the water balance of the Baget karst catchment in the southwestern French Pyrénées from 2008-2018, characterized by fast response to rainfall, nonlinear flow patterns and dominant karst spring discharge through underground conduits. The model accurately simulated daily discharge at the catchment outlet (NSE = 0.67, R^2 = 0.68, and PBIAS = 0.7% for

the 2008−2013 calibration period, and NSE = 0.65, R^2 = 0.69, and PBIAS = -13.83% for the 2014−2018 validation period), using COMEPHORE reanalysis precipitation adjusted by an orographic correction multiplicative factor of 1.44. It also represented the internal matrix-conduit flow dynamics of catchment adequately. ISPEEKH was used to predict the impacts of land-use change scenarios of afforestation and deforestation on the Baget catchment hydrology. Results showed that afforestation did not significantly influence annual water yield, while deforestation had mixed impacts. The transition from forests to transitional woodland/shrub reduced annual evapotranspiration and increased recharge and discharge, particularly in the low-flow season, whereas the transition from forests to pastures increased evapotranspiration and reduced discharge, primarily in the high-flow season. Following the development of ISPEEKH and its first application in the Baget, a second study was conducted to compare the reliability of reanalysis, gauge-, and satellite-based precipitation products for daily water balance and streamflow simulation in a meso-scale karst catchment with short response time to precipitation and sparse precipitation monitoring network, taking the Baget catchment as a case study. To run the simulations, ISPEEKH was integrated with a Parameter ESTimation Tool (PEST) framework for automated calibration, global sensitivity analysis, and parameter estimation. The study included daily precipitation datasets from Saint Girons weather station, CPC and E-OBS gauge-based products, SAFRAN, COMEPHORE, and ERA5-Land reanalysis products, and IMERG-LR, PERSIANN-CDR, CHIRPS, and SM2RAIN-ASCAT satellite-based products. The CPC, E-OBS, ERA5-Land, and IMERG-LR coarse precipitation datasets were downscaled to 1-km resolution using CHELSA, which is based on a mechanistical statistical downscaling of global reanalysis data or global circulation model output, and a triple collocation technique was subsequently applied to merge the downscaled datasets CPC and IMERG-LR datasets. The resulting kilometric precipitation products were also used in hydrological modeling of the Baget catchment. The study analyzed the sensitivity of selected ISPEEKH parameters under the various precipitation datasets using the Morris screening method. The top four most sensitive parameters were the discharge coefficients and emptying exponents of the conduit-to-spring flow and epikarst-to-conduit flow across all input precipitation datasets. Overall, the parameters governing karst groundwater flow and infiltration were the most sensitive, while surface runoff and evapotranspiration parameters were among the least sensitive. The optimal values of emptying exponents of epikarst-to-conduit and conduit-to-spring outflows

were mostly greater than 2, indicating that ISPEEKH was adapted to reproduce nonlinear conduit flow dynamics in the Baget catchment

The Baget catchment water balance for the 2008-2018 period showed a considerable deficit under all precipitation datasets, resulting in a flow underestimation bias of 69% to 79% under the CPC precipitation for the calibration and validation periods, and 28% to 32% under the 1-km resolution ERA5-Land precipitation. Overall, the reanalysis COMEPHORE, SAFRAN, and ERA5-Land precipitation products outperformed the gauge- and satellite-based precipitation products. The study found that downscaling of the CPC, IMERG-LR, E-OBS and ERA5-Land precipitation datasets to 1-km spatial resolution improved the model predictive performance unsubstantially compared to the coarse datasets. The study also highlighted the importance of incorporating spatially distributed corrected precipitation to enhance model reliability in hydrological simulations of highly responsive small karst catchments. The water balance discrepancy was resolved by correcting the precipitation datasets at 1-km resolution using orographic correction multiplicative factors, calculated using the "Doing Hydrology Backward" methodology. The envelopes of monthly average simulated streamflow values under the various uncorrected and corrected 1-km resolution precipitation datasets were compared. The envelope of the uncorrected datasets showed significant discrepancies between simulated and observed discharge, indicating limitations in the model's ability to accurately reproduce catchment hydrological processes. Meanwhile, the envelope for the corrected datasets show satisfactory predictive performances, with narrower ranges of simulated streamflow values and reduced discrepancies between simulated and observed discharge patterns during calibration and validation periods, highlighting the need for in-situ representative gauge stations for further correction of correct fine resolution precipitation products. The COMEPHORE reanalysis of precipitation covering mainland France generated the best streamflow simulation (NSE = 0.719, R^2 = 0.736, PBIAS = 3.2%, and KGE = 0.854 for the 2008−2013 calibration period, and NSE = 0.637, R^2 = 0.732, PBIAS = -10.65%, and KGE = 0.772 for the 2014−2018 validation period), suggesting that fine-resolution native reanalysis precipitation could serve as the base dataset for the streamflow modeling in remote meso-scale karst catchments.

6.2 Future perspectives

A semi-distributed karst hydrological model with spatially variable recharge can be developed either by increasing model complexity through the addition of flow processes and parameters, or by incorporating spatial information about the meteorological forcing and karst watershed landscape characteristics into the model. Following the development of ISPEEKH, future research should focus on verifying whether or not semi-distributed models that explicitly integrate the spatial variability of the groundwater recharge and other streamflow dominant controls yield better predictive performance in the hydrological simulation of karst (-dominated) watersheds than lumped parameter models. To address this question, an ensemble of karst watersheds, having an increasing order of heterogeneity of the landscape properties, groundwater recharge mechanisms, discharge signatures, and anthropogenic pressure, should be selected. For each watershed, distinct karst mathematical models (e.g., KarstMod, LuKARS and ISPEEKH), exploring different level of functional complexity to reproduce the recharge and streamflow spatial variability should be developed. KarstMod and LuKARS are lumped-parameter models that use spatially aggregated effective precipitation to model recharge from the karst aquifer autogenic recharge area and discharge from one main karst outlet. Both models simulate groundwater withdrawals and allogenic recharge as spatially aggregated time series. While KarstMod uses a single reservoir to simulate lumped recharge from the unsaturated zone, LuKARS considers recharge spatial variability by grouping areas of homogeneous land use and soil properties as distinct recharge reservoirs called hydrotopes. ISPEEKH, on the other hand, integrates the spatial variability of all meteorological inputs and landscape properties of the watershed recharge area at the hydrological response unit (HRU) scale. It models the unsaturated zone flow processes at the HRU scale and groundwater flow in the saturated zone, including discharge to multiple outlets for both karst and non-karst recharge areas. ISPEEKH also allows the simulation of water withdrawals from aquifers underlying the delineated subbasins and allogenic recharge as a function of water losses from the channels connecting subbasins.

Following model calibration, a comparative performance evaluation of the KarstMod, LuKARS and ISPEEKH flow simulations in each watershed can be conducted using statistical and signature metrics commonly applied in karst hydrology. First, the simulated flow time series of the three models should be compared to the observed flow time series at the gauging station(s) in each watershed, using performance metrics for low flow (e.g., mean square error of log discharge

MSEL, Transformed root mean square error TRMSE), high flow (e.g., Nash–Sutcliffe efficiency NSE, Root mean square error RMSE), discharge dynamics (e.g., coefficient of determination R^2), volume of transit (e.g., modified balance error BE, volumetric error VE), in addition to the Kling-Gupta efficiency coefficient KGE and non-parametric Kling-Gupta efficiency KGENP, among other metrics. In addition, the Akaike Informative Coefficient AIC [*AIC = 2 k + Nln(RSS), where k is the number of model parameters, N the number of observations and RSS is the sum of the squared residuals*] can be computed to evaluate how the flow simulation performance evolves with the increasing number of parameters in the three models. The autocorrelation function (ACF) on both observed and simulated discharge, and the cross-correlation function (CCF) between precipitation and both observed and simulated discharge with each watershed model can be calculated, and complemented with cross wavelet spectrum (XWT) and cross wavelet coherence (WTC) analysis to highlight the relationships between simulated recharge and observed discharge signals (Pfannerstill et al., 2014; Sivelle et al., 2022). Finally, the findings from the watershed modeling set can be compiled to validate if the use of a semi-distributed model with a finer representation of the recharge-discharge spatial variability improves the hydrological simulation performance compared to lumped modeling.

The ISPEEKH model configuration applied to the Baget catchment is suitable for unary or conservative karst watersheds where autogenic recharge over the karst surface topographic basin is the primary component of spring flow. However, it cannot be used to simulate flow in binary karst watersheds where both autogenic recharge and allogenic recharge from neighbouring (often non-karst) basins contribute to the karst spring discharge. Therefore, a new configuration of ISPEEKH should be proposed for binary karst watersheds by incorporating the recharge and groundwater flow processes of combined karst and non-karst aquifers, including the contribution of allogenic recharge by interbasin groundwater flow to the karst spring flow. The new ISPEEKH model can be tested in the Touvre binary karst system as a case study. The perennial Touvre karst spring, located in the west of France, is the second largest water resurgence in the country after the Fontaine de Vaucluse, with a mean streamflow that varies between 3 $m^3.s^{-1}$ and 49 $m^3.s^{-1}$ annually. The Touvre basin is fed by autogenic recharge on a karst impluvium of 550 km^2 and by allogenic recharge from sinking streams that drain three external non-karst basins (Tardoire, Bandiat, and Bonnieure), bringing its total groundwater recharge contribution zone to nearly 1600

km^2. In addition, it is exploited for domestic, agricultural, and industrial water demand, requiring further modifications to the original ISPEEKH source code to integrate user-defined input files for domestic/municipal, industrial or irrigation water demand, and water supply from river channels or aquifers.

Future research should also focus on addressing water scarcity issues in karst watersheds, driven by climate change and anthropogenic pressure. Taking the Touvre basin as a case study, synthetic scenarios of climate projections and anthropogenic pressures should be implemented (e.g., at horizon 2100) using the calibrated ISPEEKH model of the Touvre. The first step would be to assess future water resources in the Touvre basin considering climate projections only and no changes in the anthropogenic drivers of water scarcity from the reference period into the future period (i.e., same land use and or groundwater abstraction patterns from the reference period into the future). The climate projections of the DRIAS-2020 dataset (total precipitation, air temperature, wind speed, and relative humidity), available over France through the DRIAS portal (http://www.drias-climat.fr/), downscaled to 8-km resolution and bias-corrected with respect to Safran reanalysis data (Soubeyroux et al., 2020) could be used for the analysis. Next, future water resources in the Touvre watershed can be evaluated under the climate projections combined with changes in the land use and or groundwater abstraction patterns from the reference period into the future. For instance, the land-use change scenarios can be implemented by generating new land use maps that consider 10–100% conversion of cropland to natural vegetation, and or 10–100% conversion of natural vegetation to cropland, resulting in changes in future groundwater abstractions for irrigation. The impact of groundwater abstraction on available water resources can also be studied by considering 10–100% increase/decrease in domestic water withdrawals. The hydrological response of the watershed under all scenarios can be assessed using a comprehensive set of flow measures from the model simulations, with a primary focus on low-flow conditions (e.g., mean annual runoff, mean daily flow, absolute minimum flow, flow duration curve and flows with 70−99% time exceedance) (Smakhtin, 2001).

The impact of multi-site streamflow calibration on the predictive performance of the ISPEEKH−Touvre model could be investigated by applying: (1) single-gauge calibration with respect to the daily karst spring flow measured at the Foulpougne station, and (2) multi-gauge calibration with the daily karst spring flow measured at the Foulpougne station and streamflow measured at the Montbron, Feuillade, Saint-Ciers and Coulgens stations, using a weighted

objective function. Future research could also focus on investigating the impact of using evapotranspiration (e.g., evapotranspiration derived from the remote sensing-driven evapotranspiration model SimpKcET in karst areas, Ollivier et al., 2021) and or measured groundwater levels as additional calibration variables on the model performance.

Semi-distributed models such as ISPEEKH can still carry a large number of parameters, whereby their direct determination with necessary confidence makes them computationally costly. Surrogate models offer a reliable approach to address this issue, commonly known as "the curse of dimensionality" (Verleysen and François, 2005), by fusion of computationally optimized versions of existing modeling pipelines, based on both lumped and semi-distributed karst models, with an effective dimensionality reduction technique that can handle the spatiotemporal hydrological data and provide the means to quantify the uncertainty. In this context, more advanced research could focus on model reduction based on the variable bandwidth Diffusion Maps nonlinear dimensionality reduction approach (Berry, 2016; Coifman, 2006) combined with the kernel ridge regression for learning surrogate model parameters in the reduced space. Unlike other methods (e.g., the active subspace method applied by Teixeira Parente et al. (2019)), this nonlinear dimensionality reduction technique does not require a knowledge of the prior distribution of the input parameters. Instead, its optional bandwidth calibration step requires the knowledge of the data sampling density, which can be effectively interpolated from the geographical locations of observational stations. It is also well suited for exploratory data analysis because of its tolerance to the low amount and/or accuracy of the collected experimental data (Van Der Maaten et al., 2009). Moreover, the deterministic nature of this method allows the computation of the parameter sensitivity (Harlim, 2018). The surrogate model can then be used to perform Bayesian inversion of the model parameters and parametric uncertainty quantification.

The ISPEEKH model proposed in this thesis has not been developed for modeling solute transport. Therefore, future research should aim to couple the karst aquifer flow model with solute transport models that reproduce the dominant solute transport processes (of major ions such as K, Na, Ca, Mg, Cl, and SO_4 or anthropogenic contaminants such as NO_3) in the epikarst, matrix and conduit compartments, considering stationary karst aquifers. Different solute transport modeling approaches with varying orders of complexity can be tested for each subsystem. For instance, perfect mixing of solutes (Amin and Campana, 1996, van der Velde, 2012), Nash cascade with

perfect mixing (Nash, 1957; 1959), and calibrated transfer function are three methods that can be tested for the epikarst transport processes, while the perfect mixing and dual-domain (mobile-immobile) models (Becker and Bellin, 2013) could be applied for the conduit system. As for the matrix, where different transit times of the water flowing through the domain should be considered together with the solute concentration gradient in the flow exchange between matrix and conduits, the applicability of the following modeling approaches can be investigated: (1) a simple bucket model that considers perfect solute mixing in the matrix, that is the solute mixing will be instantaneous on the model time-discretization level, (2) the 1-dimensional advection-dispersion equation commonly implemented in homogeneous porous media transport models, and (3) a transfer function that can simulate different transit times of a solute in the matrix (Jury, 1982).

6.3 Conclusion (French version)

L'outil d'évaluation des sols et de l'eau (SWAT) a connu une croissance mondiale significative pour mener des études environnementales, avec plus de 5 000 articles évalués par des pairs. Les études d'évaluation de SWAT ont couvert une variété d'applications, y compris les développements de SWAT dans la représentation du paysage, le routage des cours d'eau, la dynamique du phosphore dans le sol, la quantification des services écosystémiques, la simulation du ruissellement, l'évaluation des impacts hydrologiques dus à l'évolution de l'environnement, la pollution des sources non ponctuelles et les applications pour les bassins versants côtiers. Cependant, la simulation numérique des bassins versants karstiques et de leurs processus dans SWAT est toujours en cours, malgré les progrès des modèles et des méthodes SWAT.

Une revue de 75 études évaluées par des pairs et publiées entre 2000 et 2022 a examiné les applications des modèles SWAT standard et modifiés dans les bassins versants influencés et dominés par le karst. La revue a souligné le nombre limité d'études qui ont utilisé SWAT pour la modélisation numérique du karst. La plupart des études indiquent une application directe de SWAT standard dans les bassins versants karstiques, alors que peu d'entre elles ont modifié le code source ou l'ont intégré à d'autres modèles d'eaux souterraines basés sur des aquifères karstiques afin d'améliorer la simulation de l'hydrologie des bassins versants karstiques. Bien que SWAT ait simulé de manière adéquate le débit des cours d'eau dans plusieurs zones karstiques, il s'est avéré que sa performance était médiocre dans les bassins versants karstiques complexes, ne parvenant pas à reproduire avec précision les débits de pointe et les faibles débits, générant des régressions

plus rapides que les données observées, et sous-estimant les volumes de ruissellement en raison du manque de représentation explicite de l'hydrodynamique des composantes karstiques. En outre, les modèles SWAT modifiés n'ont pas entièrement reproduit les fonctions d'écoulement de l'épikarst, de la matrice et des conduits dans les aquifères karstiques en utilisant une relation stockage-débit non linéaire.

Cette étude propose un modèle hydrologique karstique semi-distribué appelé ISPEEKH pour simuler les processus d'écoulement de surface et souterrains dans les bassins versants karstiques. Le modèle a été développé en modifiant les fonctions de recharge du code source de SWAT+ et en mettant en œuvre un module karstique non linéaire à trois réservoirs qui reproduit le système épikarst-matrice-conduit. ISPEEKH a été appliqué pour modéliser le bilan hydrique du bassin versant karstique de Baget dans le sud-ouest des Pyrénées françaises de 2008 à 2018, caractérisé par une réponse rapide aux précipitations, un flux non linéaire et une décharge dominante des sources karstiques à travers des conduits souterrains. Le modèle a simulé avec précision le débit journalier à l'exutoire du bassin versant (NSE = 0,67, R^2 = 0,68, et PBIAS = 0,7% pour la période de calibration 2008-2013, et NSE = 0,65, R^2 = 0,69, et PBIAS = -13,83% pour la période de validation 2014-2018), en utilisant les précipitations de la réanalyse COMEPHORE ajustées par un facteur multiplicatif de correction orographique de 1,44. Il a également représenté la dynamique du flux interne matrice-conduit du bassin versant de manière adéquate. ISPEEKH a été utilisé pour évaluer l'impact des scénarios de changement d'occupation du sol (boisement et déboisement) sur l'hydrologie du bassin versant de Baget. Les résultats ont montré que le boisement n'avait pas d'influence significative sur la ressource en eau annuelle, tandis que la déforestation avait des effets mixtes. Le changement du couvert forestier à un couvert arbustif de transition a réduit l'évapotranspiration annuelle et augmenté la recharge et le décharge à l’exutoire, en particulier pendant la saison de faible débit, tandis que le changement du couvert forestier à des pâturages a augmenté l'évapotranspiration et réduit la décharge, principalement pendant la saison de fort débit. Après le développement d'ISPEEKH et sa première application sur le Baget, une deuxième étude a été menée pour évaluer la pertinence d’un ensemble de produits de précipitation basés sur des données pluviométriques, de réanalyse et satellitaires pour la simulation du bilan hydrique quotidien et du débit dans un bassin versant karstique de méso-échelle caractérisé par un temps de réponse court aux précipitations et un réseau de suivi des précipitations peu dense.

Pour effectuer les simulations, ISPEEKH a été intégré à un outil d'estimation des paramètres (Parameter ESTimation Tool - PEST) pour une calibration automatisée, une analyse de sensibilité globale et une estimation des paramètres. L'étude a inclus les précipitations quotidiennes provenant de la station météorologique de Saint-Girons et l'ensemble de précipitations quotidiennes basés sur des données pluviométriques des produits CPC et E-OBS, de réanalyse SAFRAN, COMEPHORE et ERA5-Land, et satellitaires IMERG-LR, PERSIANN-CDR, CHIRPS et SM2RAIN-ASCAT. Les données CPC, E-OBS, ERA5-Land, et IMERG-LR sur les précipitations brutes ont été réduites à une résolution de 1 km en utilisant CHELSA, qui est basé sur une réduction d'échelle statistique mécanique des données de réanalyse globale ou des sorties de modèles de circulation globale, et une technique de triple colocalisation a ensuite été appliquée pour fusionner les données réduites CPC et IMERG-LR. Tous les produits de précipitations à une résolution de 1 km ont également été utilisés dans la modélisation hydrologique du bassin versant de Baget. L'étude a analysé la sensibilité d'une série de paramètres ISPEEKH sous les données de précipitation en utilisant la méthode de sélection de Morris. Les quatre paramètres les plus sensibles étaient les coefficients de décharge et les exposants de vidange de l'écoulement du conduit vers la source et de l'écoulement de l'épikarst vers le conduit pour toutes les données de précipitations d'entrée. Dans l'ensemble, les paramètres régissant l'écoulement et l'infiltration des eaux souterraines karstiques étaient les plus sensibles, tandis que les paramètres du ruissellement de surface et de l'évapotranspiration étaient parmi les moins sensibles. Les valeurs optimales des exposants de vidange des débits de l'épikarst vers le conduit et du conduit vers la source étaient pour la plupart supérieures à 2, ce qui indique que le model ISPEEKH a été adapté pour reproduire la dynamique non linéaire de l'écoulement du conduit dans le bassin versant de Baget.

Le bilan hydrique du bassin versant de Baget pour la période 2008-2018 a montré un déficit considérable sous l'ensemble de données de précipitation, entraînant un biais de sous-estimation du débit de 69% à 79% avec les précipitations CPC pour les périodes de calibration et de validation, et de 28% à 32% avec les précipitations ERA5-Land à 1 km de résolution. Globalement, les produits de précipitations de la réanalyse COMEPHORE, SAFRAN et ERA5-Land ont été plus performants que les produits de précipitations basés sur les données pluviométriques et satellitaires. L'étude a montré que la réduction d'échelle des données de précipitation CPC, IMERG-LR, E-OBS et ERA5-Land à une résolution spatiale de 1 km améliorait la performance

prédictive des modèles de manière non substantielle par rapport aux ensembles de données brutes. L'étude a également mis en évidence l'importance d'incorporer des précipitations corrigées spatialisées pour améliorer la fiabilité du modèle dans les simulations hydrologiques de petits bassins versants karstiques très réactifs. La divergence du bilan hydrique a été résolue en corrigeant les ensembles de données de précipitations à une résolution de 1 km à l'aide de facteurs multiplicatifs de correction orographique, calculés en utilisant la méthodologie "Doing Hydrology Backward". Les enveloppes des valeurs moyennes mensuelles du débit simulé sous les différentes données de précipitation non corrigées et corrigées à une résolution de 1 km ont été comparées. L'enveloppe de l'ensemble de données non corrigés a montré des écarts significatifs entre les débits simulés et observés, ce qui indique des limites dans la capacité du modèle à reproduire avec précision les processus hydrologiques du bassin versant. En revanche, l'enveloppe de l'ensemble de données corrigées montre des performances prédictives satisfaisantes, avec des plages plus étroites de valeurs de débit simulées et des écarts réduits entre les modèles de débit simulés et observés pendant les périodes de calibration et de validation, ce qui souligne la nécessité de disposer de stations de mesure de précipitation représentatives in situ pour corriger davantage les produits de précipitations à résolution fine. La réanalyse COMEPHORE des précipitations couvrant la France continentale a généré la meilleure simulation de débit (NSE = 0,719, R^2 = 0,736, PBIAS = 3,2%, et KGE = 0,854 pour la période de calibration 2008-2013, et NSE = 0,637, R^2 = 0. 732, PBIAS = -10.65%, et KGE = 0.772 pour la période de validation 2014-2018), suggérant que les précipitations de réanalyse native à résolution fine pourraient servir comme un ensemble de données de base pour la modélisation du débit des cours d'eau dans les bassins versants karstiques à méso-échelle.

6.4 Future perspectives (French version)

Un modèle hydrologique karstique semi-distribué avec une recharge spatialement variable peut être développé soit en augmentant la complexité du modèle par l'ajout de processus d'écoulement et de paramètres, soit en incorporant des informations spatiales sur le forçage météorologique et les caractéristiques du bassin versant karstique dans le modèle. Suite au développement d'ISPEEKH, les recherches futures devraient se concentrer sur la vérification du fait que les modèles semi-distribués qui intègrent explicitement la variabilité spatiale de la recharge des eaux souterraines et d'autres facteurs qui influencent l'écoulement aboutissent à une meilleure

performance prédictive dans la simulation hydrologique des bassins versants karstiques (-dominés) que les modèles à paramètres globaux. Pour répondre à cette question, il convient de sélectionner un ensemble de bassins versants karstiques présentant un ordre croissant d'hétérogénéité des propriétés du bassin versant, des mécanismes de recharge des eaux souterraines, des patrons d'écoulement et de la pression anthropique. Pour chaque bassin versant, des modèles mathématiques karstiques distincts (par exemple, KarstMod, LuKARS et ISPEEKH), explorant différents niveaux de complexité fonctionnelle pour reproduire la recharge et la variabilité spatiale des écoulements, devraient être développés. KarstMod et LuKARS sont des modèles à paramètres globaux qui utilisent des précipitations effectives agrégées dans l'espace pour modéliser la recharge à partir de la zone de recharge autogène de l'aquifère karstique et l'écoulement à partir d'un exutoire karstique principal. Les deux modèles simulent les prélèvements d'eau souterraine et la recharge allogène sous forme de séries temporelles agrégées dans l'espace. Alors que KarstMod utilise un seul réservoir pour simuler la recharge ~~forfaitaire~~ de la zone non saturée, LuKARS considère la variabilité spatiale de la recharge en regroupant les zones homogènes d'occupation du sol et des types du sol comme des réservoirs de recharge distincts appelés hydrotopes. ISPEEKH, quant à lui, intègre la variabilité spatiale de tous les apports météorologiques et des propriétés du paysage de la zone de recharge du bassin versant à l'échelle de l'unité de réponse hydrologique (HRU). Il simule les processus d'écoulement de la zone non saturée à l'échelle de l'HRU et l'écoulement des eaux souterraines dans la zone saturée, y compris l'écoulement vers des exutoires multiples pour les zones de recharge karstiques et non karstiques. ISPEEKH permet également de simuler les prélèvements d'eau dans les aquifères sous-jacents aux sous-bassins délimités et la recharge allogène en fonction des pertes d'eau dans les conduits reliant les sous-bassins.

Après la calibration du modèle, une évaluation comparative des performances des simulations de débit de KarstMod, LuKARS et ISPEEKH dans chaque bassin versant peut être réalisée à l'aide de mesures statistiques couramment appliquées en hydrologie karstique. Tout d'abord, les séries temporelles de débit simulées par les trois modèles doivent être comparées aux séries temporelles de débit observées à la (aux) station(s) de jaugeage dans chaque bassin versant, en utilisant des mesures de performance pour les faibles débits (par exemple, l'erreur quadratique moyenne du logarithme du débit MSEL, l'erreur quadratique moyenne transformée TRMSE), les forts débits (par exemple, l'efficacité de Nash-Sutcliffe, erreur quadratique moyenne RMSE), la

dynamique du débit (par exemple, coefficient de détermination R^2), le volume de transit (par exemple, erreur d'équilibre modifiée BE, erreur volumétrique VE), en plus du coefficient d'efficacité de Kling-Gupta KGE et de l'efficacité non paramétrique de Kling-Gupta KGENP, parmi d'autres mesures. En outre, le coefficient informatif d'Akaike AIC [AIC = 2 k + Nln(RSS), où k est le nombre de paramètres du modèle, N le nombre d'observations et RSS la somme des carrés des résidus] peut être calculé pour évaluer l'évolution des performances de la simulation de flux par rapport à l'augmentation du nombre de paramètres dans les trois modèles. La fonction d'autocorrélation (ACF) sur les débits observés et simulés, et la fonction de corrélation croisée (CCF) entre les précipitations et les débits observés et simulés avec chaque modèle de bassin versant peuvent être calculées, et complétées par l'analyse du spectre d'ondelettes croisées (XWT) et de la cohérence d'ondelettes croisées (WTC) pour mettre en évidence les relations entre la recharge simulée et les signaux de débits observés (Pfannerstill et al., 2014 ; Sivelle et al., 2022). Enfin, les résultats de la modélisation du bassin versant peuvent être compilés pour valider si l'utilisation d'un modèle semi-distribué avec une représentation plus fine de la variabilité spatiale de la recharge-décharge améliore la performance de la simulation hydrologique par rapport à la modélisation forfaitaire.

La configuration du modèle ISPEEKH appliquée au bassin versant de Baget convient aux bassins versants karstiques unaires où la recharge autogène sur le bassin topographique de surface du karst est la principale composante de la décharge des sources. Cependant, il ne peut pas être utilisé pour simuler l'écoulement dans les bassins versants karstiques binaires où la recharge autogène et la recharge allogène des bassins voisins (souvent non karstiques) contribuent à l'écoulement de la source karstique. Par conséquent, une nouvelle configuration d'ISPEEKH devrait être proposée pour les bassins versants karstiques binaires en incorporant les processus de recharge et d'écoulement des eaux souterraines des aquifères karstiques et non karstiques combinés, y compris la contribution de la recharge allogène par l'écoulement des eaux souterraines entre les bassins à la décharge des sources karstiques. Le nouveau modèle ISPEEKH peut être testé dans le système karstique binaire de la Touvre comme cas d'étude. La source karstique pérenne de la Touvre, située dans l'ouest de la France, est la deuxième plus grande résurgence d'eau du pays après la Fontaine de Vaucluse, avec un débit moyen qui varie entre 3 $m^3.s^{-1}$ et 49 $m^3.s^{-1}$ par an. Le bassin de la Touvre est alimenté par une recharge autogène sur un impluvium karstique de 550 km^2 et par une recharge allogène à partir de cours d'eau descendants qui drainent trois bassins

extérieurs non karstiques (Tardoire, Bandiat et Bonnieure), ce qui porte à près de 1600 km^2 la zone totale de contribution à l'alimentation de la nappe phréatique.

Les recherches futures devraient également se concentrer sur les problèmes de pénurie d'eau dans les bassins versants karstiques, engendrés par le changement climatique et les pressions anthropogéniques. En prenant le bassin de la Touvre comme exemple, des scénarios synthétiques de projections climatiques et de pressions anthropiques devraient être mis en œuvre (par exemple, à l'horizon 2100) en utilisant le modèle ISPEEKH calibré de la Touvre. La première étape consisterait à évaluer les futures ressources en eau dans le bassin de la Touvre en tenant compte uniquement des projections climatiques et de l'absence de changements dans les facteurs anthropiques de pénurie d'eau entre la période de référence et la période future (c'est-à-dire les mêmes schémas d'occupation des sols et/ou de prélèvement d'eau souterraine entre la période de référence et la période future). Les projections climatiques issues des données DRIAS-2020 (précipitations totales, température de l'air, vitesse du vent et humidité relative), disponibles pour la France sur le portail DRIAS (http://www.drias-climat.fr/), mises à l'échelle à une résolution de 8 km et corrigées des biais par rapport aux données de la réanalyse Safran (Soubeyroux et al., 2020), pourraient être utilisées pour l'étude. Ensuite, les ressources en eau futures dans le bassin versant de la Touvre peuvent être évaluées en fonction des projections climatiques combinées à des changements dans l'occupation des sols et/ou dans les schémas de prélèvement d'eau souterraine depuis la période de référence dans le futur. Par exemple, les scénarios de changement d'occupation du sol peuvent être mis en œuvre en générant de nouvelles cartes d'occupation du sol qui tiennent compte d'une conversion de 10 à 100% des sols cultivés en végétation naturelle, ou d'une conversion de 10 à 100% de la végétation naturelle en sols cultivés, ce qui entraîne des changements dans les futurs prélèvements d'eau souterraine pour l'irrigation. L'impact des prélèvements d'eau souterraine sur les ressources en eau disponibles peut également être étudié en considérant une augmentation/diminution de 10 à 100% des prélèvements d'eau à usage domestique. La réponse hydrologique du bassin versant en fonction de tous les scénarios peut être évaluée à l'aide d'un ensemble de mesures de débit issues des simulations du modèle, en se concentrant principalement sur les conditions d'étiage (par exemple, ruissellement annuel moyen, débit journalier moyen, débit minimum absolu, courbe de durée d'écoulement et débits avec un dépassement de temps de 70 à 99%) (Smakhtin, 2001).

L'impact de la calibration multi-sites des débits sur la performance prédictive du modèle ISPEEKH-Touvre pourrait être étudié en appliquant : (1) une calibration basée sur un seul exutoire par rapport au débit journalier des sources karstiques mesuré à la station de Foulpougne, et (2) une calibration multi-exutoires avec le débit journalier des sources karstiques mesuré à la station de Foulpougne et les débits mesurés aux stations de Montbron, Feuillade, Saint-Ciers et Coulgens, en utilisant une fonction objective pondérée. Les recherches futures pourraient également se concentrer sur l'étude de l'impact de l'utilisation de l'évapotranspiration (par exemple, l'évapotranspiration dérivée du modèle d'évapotranspiration basé sur les données de télédétection SimpKcET dans les zones karstiques, Ollivier et al., 2021) et des niveaux d'eau souterraine mesurés comme variables de calibration supplémentaires sur la performance du modèle.

Les modèles semi-distribués tels que ISPEEKH peuvent encore comprendre un grand nombre de paramètres, dont la détermination directe avec le degré de confiance nécessaire les rend coûteux en termes de calcul. Les modèles de substitution offrent une approche fiable pour résoudre ce problème, communément appelé « the curse of dimensionality» (Verleysen et François, 2005), en fusionnant des versions optimisées sur le plan du calcul des pipelines de modélisation existants, basés sur des modèles karstiques globaux et semi-distribués, avec une technique efficace de réduction de la dimensionnalité qui peut traiter les données hydrologiques spatio-temporelles et fournir les moyens de quantifier l'incertitude. Dans ce contexte, des recherches plus avancées pourraient se concentrer sur la réduction des modèles basée sur l'approche de réduction de la dimensionnalité non linéaire des cartes de diffusion à largeur de bande variable (Berry, 2016; Coifman, 2006) combinée à la régression ridge à noyau pour l'apprentissage des paramètres du modèle de substitution dans l'espace réduit. Contrairement à d'autres méthodes (par exemple, la méthode du sous-espace actif appliquée par Teixeira Parente et al. (2019)), cette technique de réduction de la dimensionnalité non linéaire ne nécessite pas de connaître la distribution préalable des paramètres d'entrée. Par contre, son étape optionnelle de calibration de la bande passante nécessite la connaissance de la densité d'échantillonnage des données, qui peut être efficacement interpolée à partir des emplacements géographiques des stations d'observation. Il est également bien adapté à l'analyse exploratoire des données en raison de sa tolérance à la faible quantité et/ou précision des données expérimentales collectées (Van Der Maaten et al., 2009). De plus, la nature déterministe de cette méthode permet de calculer la sensibilité des paramètres (Harlim, 2018). Le

modèle de substitution peut alors être utilisé pour réaliser l'inversion bayésienne des paramètres du modèle et la quantification de l'incertitude paramétrique.

Le modèle ISPEEKH proposé dans cette thèse n'a pas été développé pour modéliser le transport de solutés. Par conséquent, les recherches futures devraient viser à coupler le modèle des flux des aquifères karstiques avec des modèles de transport de solutés qui reproduisent les processus dominants de transport de solutés (des ions majeurs tels que K, Na, Ca, Mg, Cl, et SO_4 ou des contaminants anthropogéniques tels que NO_3) dans les compartiments de l'épikarst, de la matrice et du conduit, en partant de l'hypothèse d'aquifères karstiques stationnaires. Différentes approches de modélisation du transport des solutés avec différents niveaux de complexité peuvent être testées pour chaque sous-système. Par exemple, le mélange parfait des solutés (Amin and Campana, 1996, van der Velde, 2012), la cascade de Nash avec mélange parfait (Nash, 1957; 1959), et la fonction de transfert calibrée sont trois méthodes qui peuvent être testées pour les processus de transport dans l'épikarst, tandis que le mélange parfait et les modèles à double domaine (mobile-immobile) (Becker and Bellin, 2013) pourraient être appliqués pour le système de conduits. En ce qui concerne la matrice, où différents temps de transit de l'eau s'écoulant à travers le domaine doivent être pris en compte avec le gradient de concentration de soluté dans l'échange de flux entre la matrice et les conduits, l'applicabilité des approches de modélisation suivantes peut être étudiée : (1) un modèle « réservoir » qui considère un mélange parfait de soluté dans la matrice, c'est-à-dire que le mélange de soluté sera instantané au niveau de la discrétisation temporelle du modèle, (2) l'équation unidimensionnelle d'advection-dispersion couramment mise en œuvre dans les modèles de transport en milieu poreux homogène, et (3) une fonction de transfert qui peut simuler différents temps de transit d'un soluté dans la matrice (Jury, 1982).

References

1. Abbas, S.A., Bailey, R.T., White, J.T., Arnold, J.G., White, M.J., Čerkasova, N., Gao, J., 2024. A framework for parameter estimation, sensitivity analysis, and uncertainty analysis for holistic hydrologic modeling using SWAT+. Hydrol. Earth Syst. Sci. 28, 21–48. https://doi.org/10.5194/hess-28-21-2024
2. Abbaspour, K.C., Rouholahnejad, E., Vaghefi, S., Srinivasan, R., Yang, H., Kløve, B., 2015. A continental-scale hydrology and water quality model for Europe: Calibration and uncertainty of a high-resolution large-scale SWAT model. J. Hydrol. 524, 733–752. https://doi.org/10.1016/j.jhydrol.2015.03.027
3. Abbaspour, K.C., Vaghefi, S., Srinivasan, R., 2018. A Guideline for Successful Calibration and Uncertainty Analysis for Soil and Water Assessment: A Review of Papers from the 2016 International SWAT Conference. Water 10, 6. https://doi.org/10.3390/w10010006
4. Abiodun, O.O., Guan, H., Post, V.E.A., Batelaan, O., 2018. Comparison of MODIS and SWAT evapotranspiration over a complex terrain at different spatial scales. Hydrol. Earth Syst. Sci. 22, 2775–2794. https://doi.org/10.5194/hess-22-2775-2018
5. Adinehvand, R., Raeisi, E., Hartmann, A., 2017. A step-wise semi-distributed simulation approach to characterize a karst aquifer and to support dam construction in a data-scarce environment. J. Hydrol. 554, 470–481. https://doi.org/10.1016/j.jhydrol.2017.08.056
6. Afinowicz, J.D., Munster, C.L., Wilcox, B.P., 2005. Modeling effects of brush management on the rangeland water budget: Edwards Plateau, Texas. J. Am. Water Resour. Assoc. 41, 181–193. https://doi.org/10.1111/j.1752-1688.2005.tb03727.x
7. Ait Dhmane, L., Moustadraf, J., Rachdane, M., Saidi, M.E., Benjmel, K., Amraoui, F., Ezzaouini, M.A., Ait Sliman, A., Hadri, A., 2023. Spatiotemporal Assessment and Correction of Gridded Precipitation Products in North Western Morocco. Atmosphere 14(8), 1239. https://doi.org/10.3390/atmos14081239
8. Al Aamery, N., Adams, E., Fox, J., Husic, A., Zhu, J., Gerlitz, M., Agouridis, C., Bettel, L. 2021. Numerical model development for investigating hydrologic pathways in shallow fluviokarst. J. Hydrol., 593, 125844. https://doi.org/10.1016/j.jhydrol.2020.125844
9. Al Khoury, I., Boithias, L., Bailey, R.T., Ollivier, C., Sivelle, V., Labat, D., 2023a. Impact of land-use change on karst spring response by integration of surface processes in karst

hydrology: The ISPEEKH model. J. Hydrol. 626, 130300. https://doi.org/10.1016/j.jhydrol.2023.130300

10. Al Khoury, I., Boithias, L., Labat, D., 2023b. A Review of the Application of the Soil and Water Assessment Tool (SWAT) in Karst Watersheds. Water 15, 954. https://doi.org/10.3390/w15050954
11. Alemayehu, T., van Griensven, A., Woldegiorgis, B.T., Bauwens, W. 2017 An improved SWAT vegetation growth module and its evaluation for four tropical ecosystems. Hydrol. Earth Syst. Sci., 21, 4449–4467. https://doi.org/10.5194/hess-21-4449-2017
12. Alitane, A., Essahlaoui, A., Van Griensven, A., Yimer, E.A., Essahlaoui, N., Mohajane, M., Chawanda, C.J., Van Rompaey, A., 2022. Towards a Decision-Making Approach of Sustainable Water Resources Management Based on Hydrological Modeling: A Case Study in Central Morocco. Sustainability, 14, 10848. https://doi.org/10.3390/su141710848
13. Aloui, S., Mazzoni, A., Elomri, A., Aouissi, J., Boufekane, A., Zghibi, A., 2023. A review of Soil and Water Assessment Tool (SWAT) studies of Mediterranean catchments: Applications, feasibility, and future directions. J. Environ. Manage. 326, 116799. https://doi.org/10.1016/j.jenvman.2022.116799
14. Amatya, D.M., Jha, M., Edwards, A.E., Williams, T.M., Hitchcock, D.R., 2011. SWAT-Based Streamflow and Embayment Modeling of Karst-Affected Chapel Branch Watershed, South Carolina. Trans. ASABE, 4, 1311–1323. https://doi.org/10.13031/2013.39033
15. Amatya, D.M., Jha, M.K., Williams, T.M., Edwards, A.E., Hitchcock, D.R., 2013. SWAT Model Prediction of Phosphorus Loading in a South Carolina Karst Watershed with a Downstream Embayment. J. Environ. Prot., 4, 75–90. https://doi.org/10.4236/jep.2013.47A010
16. Amin, I. E., Campana, M. E., 1996. A general lumped parameter model for the interpretation of tracer data and transit time calculation in hydrologic systems. J. Hydrol., 179(1-4), 1-21. https://doi.org/10.1016/0022-1694(95)02880-3
17. Amin, M.G.M., Karsten, H.D., Veith, T.L., Beegle, D.B., Kleinman, P.J., 2018. Conservation dairy farming impact on water quality in a karst watershed in north-eastern US. Agric. Syst., 165, 187–196. https://doi.org/10.1016/j.agsy.2018.06.010
18. Amin, M.G.M., Veith, T.L., Collick, A.S., Karsten, H.D., Buda, A.R., 2017. Simulating hydrological and nonpoint source pollution processes in a karst watershed: A variable source

area hydrology model evaluation. Agric. Water Manag., 180, 212–223. https://doi.org/10.1016/j.agwat.2016.07.011

19. Amin, M.G.M., Veith, T.L., Shortle, J.S., Karsten, H.D., Kleinman, P.J.A, 2020. Addressing the spatial disconnect between national-scale total maximum daily loads and localized land management decisions. J. Environ. Qual., 49, 613–627. https://doi.org/10.1002/jeq2.20051
20. An, L., Hao, Y., Yeh, T.-C.J., Liu, Y., Liu, W., Zhang, B., 2020. Simulation of karst spring discharge using a combination of time–frequency analysis methods and long short-term memory neural networks. J. Hydrol. 589, 125320. https://doi.org/10.1016/j.jhydrol.2020.125320
21. Aouissi, J., Benabdallah, S., Chabaâne, Z.L., Cudennec, C. 2016. Evaluation of potential evapotranspiration assessment methods for hydrological modelling with SWAT—Application in data-scarce rural Tunisia. Agric. Water Manag., 174, 39–51. https://doi.org/10.1016/j.agwat.2016.03.004.
22. Arnaud, P., Lavabre, J., Fouchier, C., Diss, S., Javelle, P., 2011. Sensitivity of hydrological models to uncertainty in rainfall input. Hydrol. Sci. J. 56, 397–410. https://doi.org/10.1080/02626667.2011.563742
23. Arnold, J.G., Moriasi, D.N., Gassman, P.W., Abbaspour, K.C., White, M.J., Srinivasan, R., Santhi, C., Harmel, R.D., Griensven, A.V., Liew, M.W.V., Kannan, N., Jha, M.K., 2012. SWAT: Model Use, Calibration, and Validation. Trans. ASABE 55, 1491–1508. https://doi.org/10.13031/2013.42256
24. Arnold, J.G., Srinivasan, R., Muttiah, R.S., Williams, J.R., 1998. Large area hydrologic modeling and assessment part I: model development. J. Am. Water Resour. Assoc. 34, 73–89. https://doi.org/10.1111/j.1752-1688.1998.tb05961.x
25. Aryal, A., Tran, T.-N.-D., Kumar, B., Lakshmi, V., 2023. Evaluation of Satellite-Derived Precipitation Products for Streamflow Simulation of a Mountainous Himalayan Watershed: A Study of Myagdi Khola in Kali Gandaki Basin, Nepal. Remote Sens. 15, 4762. https://doi.org/10.3390/rs15194762
26. Ashouri, H., Hsu, K.-L., Sorooshian, S., Braithwaite, D.K., Knapp, K.R., Cecil, L.D., Nelson, B.R., Prat, O.P., 2015. PERSIANN-CDR: Daily Precipitation Climate Data Record from Multisatellite Observations for Hydrological and Climate Studies. Bull. Am. Meteorol. Soc. 96, 69–83. https://doi.org/10.1175/BAMS-D-13-00068.1

27. Auler, A.S., Stevanović, Z., 2021. Preface: Five decades of advances in karst hydrogeology. Hydrogeol. J., 29, 1–6. https://doi.org/10.1007/s10040-020-02292-x
28. Aune-Lundberg, L., Strand, G.-H., 2021. The content and accuracy of the CORINE Land Cover dataset for Norway. Int. J. Appl. Earth Obs. Geoinformation 96, 102266. https://doi.org/10.1016/j.jag.2020.102266
29. Ayivi, F., Jha, M.K., 2018. Estimation of water balance and water yield in the Reedy Fork-Buffalo Creek Watershed in North Carolina using SWAT. Int. Soil Water Conserv. Res. 6, 203–213. https://doi.org/10.1016/j.iswcr.2018.03.007
30. Azari, M., Moradi, H. R., Saghafian, B., Faramarzi, M., 2015. Climate change impacts on streamflow and sediment yield in the North of Iran. Hydrol. Sci. J., 61(1), 123–133. https://doi.org/10.1080/02626667.2014.967695
31. Azimi, S., Massari, C., Formetta, G., Barbetta, S., Tazioli, A., Fronzi, D., Modanesi, S., Tarpanelli, A., Rigon, R., 2023. On understanding mountainous carbonate basins of the Mediterranean using parsimonious modeling solutions. Hydrol. Earth Syst. Sci. 27, 4485–4503. https://doi.org/10.5194/hess-27-4485-2023
32. Bacopoulos, P., Tang, Y., Wang, D., Hagen, S.C. 2017. Integrated Hydrologic-Hydrodynamic Modeling of Estuarine-Riverine Flooding: 2008 Tropical Storm Fay. J. Hydrol. Eng., 22, 04017022. https://doi.org/10.1061/(ASCE)HE.1943-5584.0001539
33. Baffaut, Benson, 2009. Modeling Flow and Pollutant Transport in a Karst Watershed with SWAT. Trans. ASABE 52, 469–479. https://doi.org/10.13031/2013.26840
34. Baffaut, C., Benson, V.W., 2009. Modeling Flow and Pollutant Transport in a Karst Watershed with SWAT. Trans. ASABE 52(2), 469–479. https://doi.org/10.13031/2013.26840
35. Baffaut, C., John Sadler, E., Ghidey, F., Anderson, S.H., 2015. Long-Term Agroecosystem Research in the Central Mississippi River Basin: SWAT Simulation of Flow and Water Quality in the Goodwater Creek Experimental Watershed. J. Environ. Qual., 44, 84–96. https://doi.org/10.2134/jeq2014.02.0068
36. Bai, Y., Ochuodho, T.O., Yang, J., 2019. Impact of land use and climate change on water-related ecosystem services in Kentucky, USA. Ecol. Indic. 102, 51–64. https://doi.org/10.1016/j.ecolind.2019.01.079

37. Bailey, R.T., Bieger, K., Flores, L., Tomer, M., 2022. Evaluating the contribution of subsurface drainage to watershed water yield using SWAT+ with groundwater modeling. Sci. Total Environ. 802, 149962. https://doi.org/10.1016/j.scitotenv.2021.149962
38. Bailly-Comte, V., Jourde, H., Roesch, A., Pistre, S., Batiot-Guilhe, C., 2008. Time series analyses for Karst/River interactions assessment: Case of the Coulazou river (southern France). J. Hydrol. 349, 98–114. https://doi.org/10.1016/j.jhydrol.2007.10.028
39. Bárdossy, A., Kilsby, C., Birkinshaw, S., Wang, N., Anwar, F., 2022. Is Precipitation Responsible for the Most Hydrological Model Uncertainty? Front. Water 4, 836554. https://doi.org/10.3389/frwa.2022.836554
40. Basu, B., Morrissey, P., Gill, L.W., 2022. Application of Nonlinear Time Series and Machine Learning Algorithms for Forecasting Groundwater Flooding in a Lowland Karst Area. Water Resour. Res. 58. https://doi.org/10.1029/2021WR029576
41. Baudement, C., Arfib, B., Mazzilli, N., Jouves, J., Lamarque, T., Guglielmi, Y., 2017. Groundwater management of a highly dynamic karst by assessing baseflow and quickflow with a rainfall-discharge model (Dardennes springs, SE France). Bull. Société Géologique Fr. 188, 40. https://doi.org/10.1051/bsgf/2017203
42. Baudoux, L., Inglada, J., Mallet, C., 2021. Toward a Yearly Country-Scale CORINE Land-Cover Map without Using Images: A Map Translation Approach. Remote Sens. 13, 1060. https://doi.org/10.3390/rs13061060
43. Bauer, S., Liedl, R., Sauter, M., 2005. Modeling the influence of epikarst evolution on karst aquifer genesis: A time-variant recharge boundary condition for joint karst-epikarst development: JOINT KARST-EPIKARST EVOLUTION. Water Resour. Res. 41. https://doi.org/10.1029/2004WR003321
44. Becker, M., Bellin, A., 2013. A reservoir model of tracer transport for karstic flow systems. Hydrog. J., 21(5), 1011-1019. https://doi.org/10.1007/s10040-013-0991-2
45. Benham, B.L., Baffaut, C., Zeckoski, R.W., Mankin, K.R., Pachepsky, Y.A., Sadeghi, A.M., Brannan, K.M., Soupir, M.L., Habersack, M.J., 2006. Modeling bacteria fate and transport in watersheds to support TMDLs. Trans. ASABE, 49, 987–1002. https://doi.org/10.13031/2013.21739
46. Bennour, A., Jia, L., Menenti, M., Zheng, C., Zeng, Y., Asenso Barnieh, B., Jiang, M., 2022. Calibration and Validation of SWAT Model by Using Hydrological Remote Sensing

Observables in the Lake Chad Basin. Remote Sens., 14, 1511. https://doi.org/10.3390/rs14061511

47. Berry, T., Harlim, J., 2016. Variable bandwidth diffusion kernels. Appl. Comput. Harmon. Anal. 40 (1), 68–96. https://doi.org/10.1016/j.acha.2015.01.001
48. Beven, K., Binley, A., 1992. The future of distributed models: Model calibration and uncertainty prediction. Hydrol. Process. 6, 279–298. https://doi.org/10.1002/hyp.3360060305
49. Bieger, K., Arnold, J.G., Rathjens, H., White, M.J., Bosch, D.D., Allen, P.M., 2019. Representing the Connectivity of Upland Areas to Floodplains and Streams in SWAT+. JAWRA J. Am. Water Resour. Assoc. 55, 578–590. https://doi.org/10.1111/1752-1688.12728
50. Bieger, K., Arnold, J.G., Rathjens, H., White, M.J., Bosch, D.D., Allen, P.M., Volk, M., Srinivasan, R., 2017. Introduction to SWAT+, A Completely Restructured Version of the Soil and Water Assessment Tool. JAWRA J. Am. Water Resour. Assoc. 53, 115–130. https://doi.org/10.1111/1752-1688.12482
51. Bieger, K., Georg Hörmann, G., Fohrer, N. Detailed spatial analysis of SWAT-simulated surface runoff and sediment yield in a mountainous watershed in China. Hydrol. Sci. J. 2015, 60, 784–800. https://doi.org/10.1080/02626667.2014.965172
52. Biondić, R., Meaški, H., Biondić, B., Loborec, J. Karst Aquifer Vulnerability Assessment (KAVA) Method—A Novel GIS-Based Method for Deep Karst Aquifers. Sustainability 2021, 13, 3325. https://doi.org/10.3390/su13063325
53. Bitew, M.M., Gebremichael, M., Ghebremichael, L.T., Bayissa, Y.A., 2012. Evaluation of High-Resolution Satellite Rainfall Products through Streamflow Simulation in a Hydrological Modeling of a Small Mountainous Watershed in Ethiopia. J. Hydrometeorol. 13, 338–350. https://doi.org/10.1175/2011JHM1292.1
54. Bittner, D., Narany, T.S., Kohl, B., Disse, M., Chiogna, G., 2018. Modeling the hydrological impact of land use change in a dolomite-dominated karst system. J. Hydrol. 567, 267–279. https://doi.org/10.1016/j.jhydrol.2018.10.017
55. Boufala, M., El Hmaidi, A., Essahlaoui, A., Chadli, K., El Ouali, A., Lahjouj, A. Assessment of the best management practices under a semi arid basin using SWAT model (case of M'dez Watershed, Morocco). Model. Earth Syst. Environ. 2022, 8, 713–731. https://doi.org/10.1007/s40808-021-01123-6

56. Brighenti, T. M., Bonumá, N. B., Srinivasan, R., Chaffe, P. L. B., 2019. Simulating sub-daily hydrological process with SWAT: a review. Hydrol. Sci. J. 64(12), 1415–1423. https://doi.org/10.1080/02626667.2019.1642477
57. Brocca, L., Ciabatta, L., Massari, C., Moramarco, T., Hahn, S., Hasenauer, S., Kidd, R., Dorigo, W., Wagner, W., Levizzani, V., 2014. Soil as a natural rain gauge: Estimating global rainfall from satellite soil moisture data. J. Geophys. Res. Atmospheres 119, 5128–5141. https://doi.org/10.1002/2014JD021489
58. Brocca, L., Filippucci, P., Hahn, S., Ciabatta, L., Massari, C., Camici, S., Schüller, L., Bojkov, B., Wagner, W., 2019. SM2RAIN–ASCAT (2007–2018): global daily satellite rainfall data from ASCAT soil moisture observations. Earth Syst. Sci. Data 11, 1583–1601. https://doi.org/10.5194/essd-11-1583-2019
59. Brown, A.E., Zhang, L., McMahon, T.A., Western, A.W., Vertessy, R.A., 2005. A review of paired catchment studies for determining changes in water yield resulting from alterations in vegetation. J. Hydrol. 310, 28–61. https://doi.org/10.1016/j.jhydrol.2004.12.010
60. Bucak, T., Trolle, D., Andersen, H.E., Thodsen, H., Erdoğan, S., Levi, E.E., Filiz, N., Jeppesen, E., Beklioğlu, M. Future water availability in the largest freshwater Mediterranean lake is at great risk as evidenced from simulations with the SWAT model, Sci. Total Environ. 2017, 581–582, 413–425. https://doi.org/10.1016/j.scitotenv.2016.12.149
61. Busico, G., Ntona, M.M., Carvalho, S.C.P., Patrikaki, O., Voudouris, K., Kazakis, N. Simulating Future Groundwater Recharge in Coastal and Inland Catchments. Water Resour. Manag. 2021, 35, 3617–3632. https://doi.org/10.1007/s11269-021-02907-2
62. Butscher, C., Huggenberger, P., 2008. Intrinsic vulnerability assessment in karst areas: A numerical modeling approach. Water Resour. Res. 44, 2007WR006277. https://doi.org/10.1029/2007WR006277
63. Camici, S., Ciabatta, L., Massari, C., Brocca, L., 2018. How reliable are satellite precipitation estimates for driving hydrological models: A verification study over the Mediterranean area. J. Hydrol. 563, 950–961. https://doi.org/10.1016/j.jhydrol.2018.06.067
64. Campbell, A., Pradhanang, S.M., Anbaran S.K., Sargent, J., Palmer, Z., Audette, M. Assessing the impact of urbanization on flood risk and severity for the Pawtuxet watershed, Rhode Island. Lake Reserv. Manag. 2018, 34, 74–87, https://doi.org/10.1080/10402381.2017.1390016

65. CARD, 2022. SWAT Literature Database for Peer-Reviewed Journal Articles. Center for Agricultural and Rural Development: Iowa State University, Ames, IA, USA. Available online: https://www.card.iastate.edu/swat_articles/ (accessed on 24 November 2022).
66. CARD, 2023. SWAT Literature Database for Peer-Reviewed Journal Articles. https://www.card.iastate.edu/swat_articles/ (accessed 18 March 2023).
67. Cardoso de Salis, H.H., Monteiro da Costa, A., Moreira Vianna, J.H., Azeneth Schuler, M., Künne, A., Sanches Fernandes, L.F., Leal Pacheco, F.A., 2019. Hydrologic Modeling for Sustainable Water Resources Management in Urbanized Karst Areas. Int. J. Environ. Res. Public. Health 16, 2542. https://doi.org/10.3390/ijerph16142542
68. Cecílio, R.A., Pimentel, S.M., Zanetti, S.S., 2019. Modeling the influence of forest cover on streamflows by different approaches. CATENA 178, 49–58. https://doi.org/10.1016/j.catena.2019.03.006
69. Chang, W., Li, W., Ma, H., Wang, D., Bandala, E.R., Yu, Y., Rodrigo-Comino, J. An integrated approach for shaping drought characteristics at the watershed scale. J. Hydro. 2022, 604, 127248. https://doi.org/10.1016/j.jhydrol.2021.127248
70. Chang, W., Wan, J., Tan, J., Wang, Z., Jiang, C., Huang, K., 2021. Responses of Spring Discharge to Different Rainfall Events for Single-Conduit Karst Aquifers in Western Hunan Province, China. Int. J. Environ. Res. Public. Health 18, 5775. https://doi.org/10.3390/ijerph18115775
71. Chang, Y., Qi, Y., Wang, Z., 2024. Comprehensive evaluation of IMERG, ERA5-Land and their fusion products in the hydrological simulation of three karst catchments in Southwest China. J. Hydrol. Reg. Stud. 52, 101671. https://doi.org/10.1016/j.ejrh.2024.101671
72. Chang, Y., Wu, J., Jiang, G., 2015. Modeling the hydrological behavior of a karst spring using a nonlinear reservoir-pipe model. Hydrogeol. J. 23, 901–914. https://doi.org/10.1007/s10040-015-1241-6
73. Chang, Y., Wu, J., Jiang, G., Liu, L., Reimann, T., Sauter, M., 2019. Modelling spring discharge and solute transport in conduits by coupling CFPv2 to an epikarst reservoir for a karst aquifer. J. Hydrol. 569, 587–599. https://doi.org/10.1016/j.jhydrol.2018.11.075
74. Chawanda, C.J., 2022. SWAT+ Toolbox (0.7.6). Zenodo. https://doi.org/10.5281/zenodo.6331716

75. Chen, H., Wang, S., Wang, Y., Zhu, J., 2020. Probabilistic projections of hydrological droughts through convection‐permitting climate simulations and multimodel hydrological predictions. J. Geophys. Res.: Atmos., 125, e2020JD032914. https://doi.org/10.1029/2020JD032914
76. Chen, M., Shi, W., Xie, P., Silva, V.B.S., Kousky, V.E., Wayne Higgins, R., Janowiak, J.E., 2008. Assessing objective techniques for gauge‐based analyses of global daily precipitation. J. Geophys. Res. Atmospheres 113, 2007JD009132. https://doi.org/10.1029/2007JD009132
77. Chen, X., Zhang, Z., Soulsby, C., Cheng, Q., Binley, A., Jiang, R., Tao, M., 2018. Characterizing the heterogeneity of karst critical zone and its hydrological function: an integrated approach. Hydrol. Process., 32, 2932–2946. https://doi.org/10.1002/hyp.13232
78. Chen, Y., Nakatsugawa, M., 2021. Analysis of Changes in Land Use/Land Cover and Hydrological Processes Caused by Earthquakes in the Atsuma River Basin in Japan. Sustainability, 13, 13041. https://doi.org/10.3390/su132313041
79. Chen, Y., Oliver, D.S., 2013. Levenberg–Marquardt forms of the iterative ensemble smoother for efficient history matching and uncertainty quantification. Comput. Geosci. 17, 689–703. https://doi.org/10.1007/s10596-013-9351-5
80. Chen, Z., Auler, A.S., Bakalowicz, M., Drew, D., Griger, F., Hartmann, J., Jiang, G., Moosdorf, N., Richts, A., Stevanovic, Z., Veni, G., Goldscheider, N., 2017. The World Karst Aquifer Mapping project: concept, mapping procedure and map of Europe. Hydrogeol. J. 25, 771–785. https://doi.org/10.1007/s10040-016-1519-3
81. Chiphang, N., Bandyopadhyay, A., Bhadra, A., 2020. Assessing the Effects of Snowmelt Dynamics on Streamflow and Water Balance Components in an Eastern Himalayan River Basin Using SWAT Model. Environ Model Assess 25, 861–883. https://doi.org/10.1007/s10666-020-09716-8
82. Chotpantarat, S., Boonkaewwan, S., 2018. Impacts of land-use changes on watershed discharge and water quality in a large intensive agricultural area in Thailand. Hydrol. Sci. J., 63(9), 1386–1407. https://doi.org/10.1080/02626667.2018.1506128
83. Chow, V.T., Maidment, D.R., Mays, L.W., 1988. Applied Hydrology. McGrawHill: New York, NY, USA.
84. Coffey, M.E., Workman, S.R, Taraba, J.L., Fogle, A.W., 2004 Statistical procedures for evaluating daily and monthly hydrologic model predictions. Trans. ASABE, 47, 59–68. https://doi.org/10.13031/2013.15870

85. Coifman, R.R., Lafon, S., 2006. Diffusion maps. Appl. Comput. Harmon. Anal. 21 (1), 5–30. https://doi.org/10.1016/j.acha.2006.04.006
86. Cornes, R.C., Van Der Schrier, G., Van Den Besselaar, E.J.M., Jones, P.D., 2018. An Ensemble Version of the E‐OBS Temperature and Precipitation Data Sets. J. Geophys. Res. Atmospheres 123, 9391‐9409. https://doi.org/10.1029/2017JD028200
87. Cousquer, Y., Jourde, H., 2022. Reducing uncertainty of karst aquifer modeling with complementary hydrological observations for the sustainable management of groundwater resources. J. Hydrol. 612, 128130. https://doi.org/10.1016/j.jhydrol.2022.128130
88. Cunge, J.A., 1969. On the subject of a flood propagation computation method (Muskingum method). J. Hydraul. Res., 7, 205–230. https://doi.org/10.1080/00221686909500264
89. Dal Soglio, L., Danquigny, C., Mazzilli, N., Emblanch, C., Massonnat, G., 2020a. Modeling the Matrix-Conduit Exchanges in Both the Epikarst and the Transmission Zone of Karst Systems. Water 12(11), 3219. https://doi.org/10.3390/w12113219
90. Dal Soglio, L., Danquigny, C., Mazzilli, N., Emblanch, C., Massonnat, G., 2020b. Taking into Account both Explicit Conduits and the Unsaturated Zone in Karst Reservoir Hybrid Models: Impact on the Outlet Hydrograph. Water 12(11), 3221. https://doi.org/10.3390/w12113221
91. Dash, S.D., Sahoo, B., Raghuwanshi, N.S., 2020. A novel embedded pothole module for Soil and Water Assessment Tool (SWAT) improving streamflow estimation in paddy-dominated catchments. J. Hydrol., 588, 125103. https://doi.org/10.1016/j.jhydrol.2020.125103.
92. De Girolamo, A.M., Bouraoui, F., Buffagni, A., Pappagallo, G., Lo Porto, A., 2017. Hydrology under climate change in a temporary river system: Potential impact on water balance and flow regime. River Res. Appl, 33, 1219–1232. https://doi.org/10.1002/rra.3165
93. de Rooij, R., Graham, W., 2017. Generation of complex karstic conduit networks with a hydrochemical model: GENERATION OF KARSTIC CONDUIT NETWORKS. Water Resour. Res. 53, 6993–7011. https://doi.org/10.1002/2017WR020768
94. Debroas, E.-J., 2009. Géologie du bassin versant du Baget (zone nord-pyrénéenne, Ariège, France): Nouvelles observations et conséquences. STRATA, 2, 46.
95. Delavar, M., Eini, M.R., Kuchak, V.S., Zaghiyan, M.R., Shahbazi, A., Nourmohammadi, F., Motamedi, 2022. A. Model-based water accounting for integrated assessment of water resources systems at the basin scale. Sci. Total Environ., 830, 154810. https://doi.org/10.1016/j.scitotenv.2022.154810

96. Delavar, M., Morid, S., Morid, R., Farokhnia, A., Babaeian, F., Srinivasan, R., Karimi, P., 2020. Basin-wide water accounting based on modified SWAT model and WA+ framework for better policy making. J. Hydrol., 585, 124762. https://doi.org/10.1016/j.jhydrol.2020.124762
97. Demetropoulou, L., Lilli, M.A., Petousi, I., Nikolaou, T., Fountoulakis, M., Kritsotakis, M., Panakoulia, S., Giannakis, G.V., Manios, T. Nikolaidis, N. P., 2019. Innovative methodology for the prioritization of the Program of Measures for integrated water resources management of the Region of Crete, Greece. Sci. Total Environ., 672, 61-70. https://doi.org/10.1016/j.scitotenv.2019.03.397
98. Déqué, M., Dreveton, C., Braun, A., Cariolle, D., 1994. The ARPEGE/IFS atmosphere model: a contribution to the French community climate modelling. Clim. Dyn. 10, 249–266. https://doi.org/10.1007/BF00208992
99. Dile, Y.T., Daggupati, P., George, C., Srinivasan, R., Arnold, J., 2016. Introducing a new open source GIS user interface for the SWAT model. Environ. Model. Softw., 85, 129–138. https://doi.org/10.1016/j.envsoft.2016.08.004
100. Doherty, J., 2018. PEST Model-Independent Parameter Estimation User Manual, 7th edition. ed. Watermark Numerical Computing, Brisbane, Queensland, Australia.
101. Dos Reis, J., Rennó, C., Lopes, E., 2017. Validation of Satellite Rainfall Products over a Mountainous Watershed in a Humid Subtropical Climate Region of Brazil. Remote Sens. 9, 1240. https://doi.org/10.3390/rs9121240
102. Douglas-Mankin, K.R., Srinivasan, R., J. G. Arnold, J.G., 2010. Soil and Water Assessment Tool (SWAT) Model: Current Developments and Applications. Trans. ASABE 2010, 53, 1423–1431. https://doi.org/10.13031/2013.34915
103. Doummar, J., Hassan Kassem, A., Gurdak, J.J., 2018. Impact of historic and future climate on spring recharge and discharge based on an integrated numerical modelling approach: Application on a snow-governed semi-arid karst catchment area. J. Hydrol. 565, 636–649. https://doi.org/10.1016/j.jhydrol.2018.08.062
104. Doummar, J., Sauter, M., Geyer, T., 2012. Simulation of flow processes in a large scale karst system with an integrated catchment model (Mike She) – Identification of relevant parameters influencing spring discharge. J. Hydrol. 426–427, 112–123. https://doi.org/10.1016/j.jhydrol.2012.01.021

105. Duran, L., Massei, N., Lecoq, N., Fournier, M., Labat, D., 2020. Analyzing multi-scale hydrodynamic processes in karst with a coupled conceptual modeling and signal decomposition approach. J. Hydrol. 583, 124625. https://doi.org/10.1016/j.jhydrol.2020.124625

106. Durand, Y., Brun, E., Mérindol, L., Guyomarc'h, G., Lesaffre, B., Martin, E., 1993. A meteorological estimation of relevant parameters for snow models. Ann. Glaciol. 18, 65–71. https://doi.org/10.3189/S0260305500011277

107. Dwarakish, G.S., Ganasri, B.P., 2015. Impact of land-use change on hydrological systems: A review of current modeling approaches. Cogent Geosci., 1, 1115691. https://doi.org/10.1080/23312041.2015.1115691

108. Efthimiou, N., 2018. Hydrological simulation using the SWAT model: the case of Kalamas River catchment. J. Appl. Water Eng. Res. 6, 210–227. https://doi.org/10.1080/23249676.2016.1265471

109. Eini, R.M., Javadi, S., Delavar, M., Gassman, P.W., Jarihani, B., 2020. Development of alternative SWAT-based models for simulating water budget components and streamflow for a karstic-influenced watershed. CATENA 195, 104801. https://doi.org/10.1016/j.catena.2020.104801

110. Emmanuel, I., Payrastre, O., Andrieu, H., Zuber, F., 2017. A method for assessing the influence of rainfall spatial variability on hydrograph modeling. First case study in the Cevennes Region, southern France. J. Hydrol. 555, 314–322. https://doi.org/10.1016/j.jhydrol.2017.10.011

111. Entezari, M., Yamani, M., Jafari Aghdam, M., 2016. Evaluation of intrinsic vulnerability, hazard and risk mapping for karst aquifers, Khorein aquifer, Kermanshah province: a case study. Environ. Earth Sci., 75, 435. https://doi.org/10.1007/s12665-016-5258-5

112. Eris, E., Wittenberg, H., 2015. Estimation of baseflow and water transfer in karst catchments in Mediterranean Turkey by nonlinear recession analysis. J. Hydrol., 530, 500–507. https://doi.org/10.1016/j.jhydrol.2015.10.017

113. Evensen, G., 1994. Sequential data assimilation with a nonlinear quasi‐geostrophic model using Monte Carlo methods to forecast error statistics. J. Geophys. Res. Oceans 99, 10143‐10162. https://doi.org/10.1029/94JC00572

114. Ferreira, A. do N., de Almeida, A., Koide, S., Minoti, R.T., Siqueira, M.B.B. de, 2021. Evaluation of Evapotranspiration in Brazilian Cerrado Biome Simulated with the SWAT Model. Water 13, 2037. https://doi.org/10.3390/w13152037

115. Fidelibus, M.D., Balacco, G., Gioia, A., Iacobellis, V., Spilotro, G., 2017. Mass transport triggered by heavy rainfall: the role of endorheic basins and epikarst in a regional karst aquifer: Epikarst under heavy rainfall causes temporary groundwater pollution. Hydrol. Process. 31, 394–408. https://doi.org/10.1002/hyp.11037

116. Filippucci, P., Ciabatta, L., Mosaffa, H., Brocca, L., 2024. Improving the resolution of satellite precipitation products in Europe. Presented at the EGU General Assembly 2024, Vienna, Austria. https://doi.org/10.5194/egusphere-egu24-16956

117. Filoso, S., Bezerra, M.O., Weiss, K.C.B., Palmer, M.A., 2017. Impacts of forest restoration on water yield: A systematic review. PLOS ONE 12, e0183210. https://doi.org/10.1371/journal.pone.0183210

118. Fiorillo, F., Guadagno, F.M., 2012. Long karst spring discharge time series and droughts occurrence in Southern Italy. Environ. Earth Sci. 65, 2273–2283. https://doi.org/10.1007/s12665-011-1495-9

119. Fischer, P., Jardani, A., Lecoq, N., 2018. Hydraulic tomography of discrete networks of conduits and fractures in a karstic aquifer by using a deterministic inversion algorithm. Adv. Water Resour. 112, 83–94. https://doi.org/10.1016/j.advwatres.2017.11.029

120. Fleury, P., Ladouche, B., Conroux, Y., Jourde, H., Dörfliger, N., 2009. Modelling the hydrologic functions of a karst aquifer under active water management – The Lez spring. J. Hydrol. 365, 235–243. https://doi.org/10.1016/j.jhydrol.2008.11.037

121. Fleury, P., Plagnes, V., Bakalowicz, M., 2007. Modelling of the functioning of karst aquifers with a reservoir model: Application to Fontaine de Vaucluse (South of France). J. Hydrol. 345, 38–49. https://doi.org/10.1016/j.jhydrol.2007.07.014

122. Francesconi, W., Srinivasan, R., Pérez-Miñana, E., Willcock, S.P., Quintero, M., 2016. Using the Soil and Water Assessment Tool (SWAT) to model ecosystem services: A systematic review. J. Hydrol., 535, 625–636. https://doi.org/10.1016/j.jhydrol.2016.01.034

123. Frank, S., Goeppert, N., Goldscheider, N., 2021. Improved understanding of dynamic water and mass budgets of high‐alpine karst systems obtained from studying a well‐defined catchment area. Hydrol. Process. 35. https://doi.org/10.1002/hyp.14033

124. Fu, C., James, A.L., Yao, H., 2014. SWAT-CS: Revision and testing of SWAT for Canadian Shield catchments. J. Hydrol., 511, 16, 719-735. https://doi.org/10.1016/j.jhydrol.2014.02.023

125. Fumière, Q., Déqué, M., Nuissier, O., Somot, S., Alias, A., Caillaud, C., Laurantin, O., Seity, Y., 2020. Extreme rainfall in Mediterranean France during the fall: added value of the CNRM-AROME Convection-Permitting Regional Climate Model. Clim. Dyn. 55, 77–91. https://doi.org/10.1007/s00382-019-04898-8

126. Funk, C., Peterson, P., Landsfeld, M., Pedreros, D., Verdin, J., Shukla, S., Husak, G., Rowland, J., Harrison, L., Hoell, A., Michaelsen, J., 2015. The climate hazards infrared precipitation with stations—a new environmental record for monitoring extremes. Sci. Data 2, 150066. https://doi.org/10.1038/sdata.2015.66

127. Furl, C., Ghebreyesus, D., Sharif, H., 2018. Assessment of the Performance of Satellite-Based Precipitation Products for Flood Events across Diverse Spatial Scales Using GSSHA Modeling System. Geosciences 8, 191. https://doi.org/10.3390/geosciences8060191

128. Gaillardet, J., Braud, I., Hankard, F., Anquetin, S., Bour, O., Dorfliger, N., de Dreuzy, J.R., Galle, S., Galy, C., Gogo, S., Gourcy, L., Habets, F., Laggoun, F., Longuevergne, L., Le Borgne, T., Naaim-Bouvet, F., Nord, G., Simonneaux, V., Six, D., Tallec, T., Valentin, C., Abril, G., Allemand, P., Arènes, A., Arfib, B., Arnaud, L., Arnaud, N., Arnaud, P., Audry, S., Comte, V.B., Batiot, C., Battais, A., Bellot, H., Bernard, E., Bertrand, C., Bessière, H., Binet, S., Bodin, J., Bodin, X., Boithias, L., Bouchez, J., Boudevillain, B., Moussa, I.B., Branger, F., Braun, J.J., Brunet, P., Caceres, B., Calmels, D., Cappelaere, B., Celle-Jeanton, H., Chabaux, F., Chalikakis, K., Champollion, C., Copard, Y., Cotel, C., Davy, P., Deline, P., Delrieu, G., Demarty, J., Dessert, C., Dumont, M., Emblanch, C., Ezzahar, J., Estèves, M., Favier, V., Faucheux, M., Filizola, N., Flammarion, P., Floury, P., Fovet, O., Fournier, M., Francez, A.J., Gandois, L., Gascuel, C., Gayer, E., Genthon, C., Gérard, M.F., Gilbert, D., Gouttevin, I., Grippa, M., Gruau, G., Jardani, A., Jeanneau, L., Join, J.L., Jourde, H., Karbou, F., Labat, D., Lagadeuc, Y., Lajeunesse, E., Lastennet, R., Lavado, W., Lawin, E., Lebel, T., Le Bouteiller, C., Legout, C., Lejeune, Y., Le Meur, E., Le Moigne, N., Lions, J., Lucas, A., Malet, J.P., Marais-Sicre, C., Maréchal, J.C., Marlin, C., Martin, P., Martins, J., Martinez, J.M., Massei, N., Mauclerc, A., Mazzilli, N., Molénat, J., Moreira-Turcq, P., Mougin, E., Morin, S., Ngoupayou, J.N., Panthou, G., Peugeot, C., Picard, G., Pierret, M.C., Porel, G., Probst, A.,

Probst, J.L., Rabatel, A., Raclot, D., Ravanel, L., Rejiba, F., René, P., Ribolzi, O., Riotte, J., Rivière, A., Robain, H., Ruiz, L., Sanchez-Perez, J.M., Santini, W., Sauvage, S., Schoeneich, P., Seidel, J.L., Sekhar, M., Sengtaheuanghoung, O., Silvera, N., Steinmann, M., Soruco, A., Tallec, G., Thibert, E., Lao, D.V., Vincent, C., Viville, D., Wagnon, P., Zitouna, R., 2018. OZCAR: The French Network of Critical Zone Observatories. Vadose Zone J. 17, 1–24. https://doi.org/10.2136/vzj2018.04.0067

129. Galván, L., Olías, M., Izquierdo, T., Cerón, J.C., Fernández de Villarán, R., 2014. Rainfall estimation in SWAT: an alternative method to simulate orographic precipitation. J. Hydrol. 509, 257–265. https://doi.org/10.1016/j.jhydrol.2013.11.044

130. Gamvroudis, C., Nikolaidis, N., Tzoraki, O., Papadoulakis, V., Karalemas, N., 2015. Water and sediment transport modeling of a large temporary river basin in Greece. Sci. Total Environ., 508, 354–365. https://doi.org/10.1016/j.scitotenv.2014.12.005

131. Gan, F., Gao, Y., Xiao, L., 2021. Comprehensive validation of the latest IMERG V06 precipitation estimates over a basin coupled with coastal locations, tropical climate and hill-karst combined landform. Atmospheric Res. 249, 105293. https://doi.org/10.1016/j.atmosres.2020.105293

132. Gan, F., Gao, Y., Xiao, L., Qin, L., Huang, Y., Zhang, H., 2020. An applicability evaluation of version 05 IMERG precipitation products over a coastal basin located in the tropics with hilly and karst combined Landform, China. Int. J. Remote Sens. 41, 4570–4589. https://doi.org/10.1080/01431161.2020.1723174

133. Gan, R., Luo, Y., 2013. Using the nonlinear aquifer storage–discharge relationship to simulate the baseflow of glacier and snowmelt dominated basins in Northwest China. Hydrol. Earth Syst. Sci., 10, 5535–5561. Doi: 10.5194/hessd-10-5535-2013

134. Gao, J., Jiang, Y., Anker, Y., 2021. Contribution analysis on spatial tradeoff/synergy of Karst soil conservation and water retention for various geomorphological types: Geographical detector application. Ecol. Indic., 125, 107470. https://doi.org/10.1016/j.ecolind.2021.107470

135. García-Ruiz, J.M., López-Moreno, J.I., Vicente-Serrano, S.M., Lasanta–Martínez, T., Beguería, S., 2011. Mediterranean water resources in a global change scenario. Earth-Sci. Rev. 105, 121–139. https://doi.org/10.1016/j.earscirev.2011.01.006

136. Gashaw, T., Tulu, T., Argaw, M., Worqlul, A.W., 2018. Modeling the hydrological impacts of land use/land cover changes in the Andassa watershed, Blue Nile Basin, Ethiopia. Sci. Total Environ. 619–620, 1394–1408. https://doi.org/10.1016/j.scitotenv.2017.11.191

137. Gassman, P.W., Reyes, M.R., Green, C.H., Arnold, J.G., 2007. The soil and water assessment tool: historical development, applications, and future research directions. Trans. ASABE, 50, 1211–1250. https://doi.org/10.13031/2013.23637

138. Geng, X., Zhang, C., Zhang, F., Chen, Z., Nie, Z., Liu, M., 2021. Hydrological Modeling of Karst Watershed Containing Subterranean River Using a Modified SWAT Model: A Case Study of the Daotian River Basin, Southwest China. Water 13, 3552. https://doi.org/10.3390/w13243552

139. Geyer, T., Birk, S., Reimann, T., Dörfliger, N., Sauter, M., 2013. Differentiated characterization of karst aquifers: some contributions. Carbonates Evaporites 28, 41–46. https://doi.org/10.1007/s13146-013-0150-9

140. Ghasemizadeh, R., Hellweger, F., Butscher, C., Padilla, I., Vesper, D., Field, M., Alshawabkeh, A., 2012. Review: Groundwater flow and transport modeling of karst aquifers, with particular reference to the North Coast Limestone aquifer system of Puerto Rico. Hydrogeol. J. 20, 1441–1461. https://doi.org/10.1007/s10040-012-0897-4

141. Giese, M., Reimann, T., Bailly‐Comte, V., Maréchal, J.‐C., Sauter, M., Geyer, T., 2018. Turbulent and Laminar Flow in Karst Conduits Under Unsteady Flow Conditions: Interpretation of Pumping Tests by Discrete Conduit‐Continuum Modeling. Water Resour. Res. 54, 1918–1933. https://doi.org/10.1002/2017WR020658

142. Gill, L.W., Schuler, P., Duran, L., Morrissey, P., Johnston, P.M., 2021. An evaluation of semidistributed-pipe-network and distributed-finite-difference models to simulate karst systems. Hydrogeol. J. 29, 259–279. https://doi.org/10.1007/s10040-020-02241-8

143. Goldscheider, N., 2019. A holistic approach to groundwater protection and ecosystem services in karst terrains. Carbonates Evaporites, 34, 1241–1249. https://doi.org/10.1007/s13146-019-00492-5

144. Goldscheider, N., Chen, Z., Auler, A.S., Bakalowicz, M., Broda, S., Drew, D., Hartmann, J., Jiang, G., Moosdorf, N., Stevanovic, Z., Veni, G., 2020. Global distribution of carbonate rocks and karst water resources. Hydrogeol. J. 28, 1661–1677. https://doi.org/10.1007/s10040-020-02139-5

145. Goldscheider, N., Drew, D., 2007. Methods in Karst Hydrogeology: IAH: International Contributions to Hydrogeology, 26. Taylor & Francis, Londoo, UK.

146. Golmohammadi, G., Prasher, S., Madani, A., Rudra, R., 2014. Evaluating Three Hydrological Distributed Watershed Models: MIKE-SHE, APEX, SWAT. Hydrology 1(1), 20–39. https://doi.org/10.3390/hydrology1010020

147. Goyal, M. K., Madramootoo, C. A., & Richards, J. F., 2015. Simulation of the Streamflow for the Rio Nuevo Watershed of Jamaica for use in agriculture water scarcity planning. J. Irrig. Drain. Eng., 141(3), 04014056. https://doi.org/10.1061/(ASCE)IR.1943-4774.0000802

148. Grusson, Y., Sun, X., Gascoin, S., Sauvage, S., Raghavan, S., Anctil, F., et al., 2015. Assessing the capability of the SWAT model to simulate snow, snow melt and streamflow dynamics over an alpine watershed. J. Hydrol. 531 (Part 3), 574. https://doi.org/10.1016/j.jhydrol.2015.10.070

149. Gunn, K.M., Buda, A.R., Preisendanz, H.E., Cibin, R., Kennedy, C.D., Veith, T.L., 2021. Integrating Daily CO2 Concentrations in SWAT-VSA to Examine Climate Change Impacts on Hydrology in a Karst Watershed. Trans. ASABE, 64, 1303–1318. https://doi.org/10.13031/trans.13711

150. Guo, Q., Yu, C., Xu, Z., Yang, Y., Wang, X., 2023. Impacts of climate and land-use changes on water yields: Similarities and differences among typical watersheds distributed throughout China. J. Hydrol. Reg. Stud. 45, 101294. https://doi.org/10.1016/j.ejrh.2022.101294

151. Gupta, H.V., Kling, H., Yilmaz, K.K., Martinez, G., 2009. Decomposition of the mean squared error and NSE performance criteria: implications for improving hydrological modelling. J. Hydrol. 377, 80–91. https://doi.org/10.1016/j. jhydrol.2009.08.003

152. Gupta, H.V., Sorooshian, S., Yapo, P.O., 1999. Status of Automatic Calibration for Hydrologic Models: Comparison with Multilevel Expert Calibration. J. Hydrol. Eng. 4, 135–143. https://doi.org/10.1061/(ASCE)1084-0699(1999)4:2(135)

153. Guse, B., Pfannerstill, M., Gafurov, A., Kiesel, J., Lehr, C., Fohrer, N., 2017. Identifying the connective strength between model parameters and performance criteria, Hydrol. Earth Syst. Sci., 21, 5663–5679. https://doi.org/10.5194/hess-21-5663-2017

154. Gutiérrez, F., Parise, M., De Waele, J., Jourde, H., 2014. A review on natural and human-induced geohazards and impacts in karst. Earth-Sci. Rev., 138, 61–88. https://doi.org/10.1016/j.earscirev.2014.08.002

155. Hao, Y., Ma, J., Chen, J., Wang, D., Wang, Y., Xu, H. 2018. Assessment of Changes in Water Balance Components under 1.5 °C and 2.0 °C Global Warming in Transitional Climate Basin by Multi-RCPs and Multi-GCMs Approach. Water, 10(12):1863. https://doi.org/10.3390/w10121863

156. Hao, Y., Wang, Y., Zhu, Y., Lin, Y., Wen, J.-C., Yeh, T.-C.J., 2009. Response of karst springs to climate change and anthropogenic activities: the Niangziguan Springs, China. Prog. Phys. Geogr. Earth Environ. 33, 634–649. https://doi.org/10.1177/0309133309346651

157. Hargreaves, G.H., Hargreaves, G.L., Riley, J.P., 1985. Agricultural benefits for Senegal River Basin. J. Irrig. Drain. Eng., 111, 113–124. https://doi.org/10.1061/(ASCE)0733-9437(1985)111:2(113)

158. Hargreaves, G.H., Samani, Z.A., 1985. Reference Crop Evapotranspiration from Temperature. Appl. Eng. Agric. 1, 96–99. https://doi.org/10.13031/2013.26773

159. Harlim, J., 2018. Data-driven computational methods: parameter and operator estimations. Cambridge University Press. https://doi.org/10.1017/9781108562461

160. Hartmann, A., Barberá, J.A., Lange, J., Andreo, B., Weiler, M., 2013. Progress in the hydrologic simulation of time variant recharge areas of karst systems – Exemplified at a karst spring in Southern Spain. Adv. Water Resour. 54, 149–160. https://doi.org/10.1016/j.advwatres.2013.01.010

161. Hartmann, A., Goldscheider, N., Wagener, T., Lange, J., Weiler, M., 2014. Karst water resources in a changing world: Review of hydrological modeling approaches: KARST WATER RESOURCES PREDICTION. Rev. Geophys. 52, 218–242. https://doi.org/10.1002/2013RG000443

162. Hartmann, A., Goldscheider, N., Wagener, T., Lange, J., Weiler, M., 2014. Karst water resources in a changing world: Review of hydrological modeling approaches, Rev. Geophys., 52, 218–242. https://doi.org/10.1002/2013RG000443

163. Hartmann, A., Lange, J., Vivó Aguado, À., Mizyed, N., Smiatek, G., Kunstmann, H., 2012. A multi-model approach for improved simulations of future water availability at a large Eastern

Mediterranean karst spring. J. Hydrol. 468–469, 130–138. https://doi.org/10.1016/j.jhydrol.2012.08.024

164. Hartmann, A., Liu, Y., Olarinoye, T., Berthelin, R., Marx, V., 2021. Integrating field work and large-scale modeling to improve assessment of karst water resources. Hydrogeol. J. 29, 315–329. https://doi.org/10.1007/s10040-020-02258-z

165. Haylock, M.R., Hofstra, N., Klein Tank, A.M.G., Klok, E.J., Jones, P.D., New, M., 2008. A European daily high‐resolution gridded data set of surface temperature and precipitation for 1950‐2006. J. Geophys. Res. Atmospheres 113, 2008JD010201. https://doi.org/10.1029/2008JD010201

166. Her, Y., Jeong, J., Arnold, J., Gosselink, L., Glick, R., Jaber, F., 2017a. A new framework for modeling decentralized low impact developments using Soil and Water Assessment Tool. Environ. Model. Softw., 96, 305–322. https://doi.org/10.1016/j.envsoft.2017.06.005

167. Her, Y., Jeong, J., Bieger, K., Rathjens, H., Arnold, J., Srinivasan, R., 2017b. Implications of Conceptual Channel Representation on SWAT Streamflow and Sediment Modeling. JAWRA J. Am. Water Resour. Assoc. 53, 725–747. https://doi.org/10.1111/1752-1688.12533

168. Hersbach, H., Bell, B., Berrisford, P., Hirahara, S., Horányi, A., Muñoz‐Sabater, J., Nicolas, J., Peubey, C., Radu, R., Schepers, D., Simmons, A., Soci, C., Abdalla, S., Abellan, X., Balsamo, G., Bechtold, P., Biavati, G., Bidlot, J., Bonavita, M., De Chiara, G., Dahlgren, P., Dee, D., Diamantakis, M., Dragani, R., Flemming, J., Forbes, R., Fuentes, M., Geer, A., Haimberger, L., Healy, S., Hogan, R.J., Hólm, E., Janisková, M., Keeley, S., Laloyaux, P., Lopez, P., Lupu, C., Radnoti, G., De Rosnay, P., Rozum, I., Vamborg, F., Villaume, S., Thépaut, J., 2020. The ERA5 global reanalysis. Q. J. R. Meteorol. Soc. 146, 1999–2049. https://doi.org/10.1002/qj.3803

169. Holvoet, K., van Griensven, A., Gevaert, V., Seuntjens, P., Vanrolleghem, P.A., 2008. Modifications to the SWAT code for modelling direct pesticide losses. Environ. Model. Softw. 23, 72–81. https://doi.org/10.1016/j.envsoft.2007.05.002

170. Hou, W., Gao, J., 2019. Simulating runoff generation and its spatial correlation with environmental factors in Sancha River Basin: The southern source of the Wujiang River. J. Geogr. Sci., 29, 432–448. https://doi.org/10.1007/s11442-019-1608-z

171. Hou, W., Gao, J., Wu, S., 2020. Quantitative Analysis of the Influencing Factors and Their Interactions in Runoff Generation in a Karst Basin of Southwestern China. Water, 12, 2898. https://doi.org/10.3390/w12102898

172. Hou, Y., Wei, X., Zhang, M., Creed, I.F., McNulty, S.G., Ferraz, S.F.B., 2023. A global synthesis of hydrological sensitivities to deforestation and forestation. For. Ecol. Manag. 529, 120718. https://doi.org/10.1016/j.foreco.2022.120718

173. Houet, T., Grémont, M., Vacquié, L., Forget, Y., Marriotti, A., Puissant, A., Bernardie, S., Thiery, Y., Vandromme, R., Grandjean, G., 2017. Downscaling scenarios of future land use and land cover changes using a participatory approach: an application to mountain risk assessment in the Pyrenees (France). Reg. Environ. Change 17, 2293–2307. https://doi.org/10.1007/s10113-017-1171-z

174. Huang, Y., Bárdossy, A., Zhang, K., 2019. Sensitivity of hydrological models to temporal and spatial resolutions of rainfall data. Hydrol. Earth Syst. Sci. 23, 2647–2663. https://doi.org/10.5194/hess-23-2647-2019

175. Huffman, G.J., Bolvin, D.T., Braithwaite, D., Hsu, K., Joyce, R., Kidd, C., Nelkin, E.J., Sorooshian, S., Tan, J., Xie, P., 2019. NASA Global Precipitation Measurement (GPM) Integrated Multi-satellitE Retrievals for GPM (IMERG). Algorithm theoretical basis document (ATBD) version, 4(26), p.30. https://gpm.nasa.gov/sites/default/files/document_files/IMERG_ATBD_V06.pdf

176. Iván, V., Mádl-Szőnyi, J., 2017. State of the art of karst vulnerability assessment: overview, evaluation and outlook. Environ. Earth. Sci., 76, 112. https://doi.org/10.1007/s12665-017-6422-2

177. Jain, S., Ale, S., Munster, C., Ansley, R., Kiniry, J., 2015. Simulating the Hydrologic Impact of Arundo donax Invasion on the Headwaters of the Nueces River in Texas. Hydrology 2, 134–147. https://doi.org/10.3390/hydrology2030134

178. Jakada, H., Chen, Z., 2020. An approach to runoff modelling in small karst watersheds using the SWAT model. Arab J. Geosci. 13, 318. https://doi.org/10.1007/s12517-020-05291-0

179. Jeannin, P.-Y., Artigue, G., Butscher, C., Chang, Y., Charlier, J.-B., Duran, L., Gill, L., Hartmann, A., Johannet, A., Jourde, H., Kavousi, A., Liesch, T., Liu, Y., Lüthi, M., Malard, A., Mazzilli, N., Pardo-Igúzquiza, E., Thiéry, D., Reimann, T., Schuler, P., Wöhling, T.,

Wunsch, A., 2021. Karst modelling challenge 1: Results of hydrological modelling. J. Hydrol. 600, 126508. https://doi.org/10.1016/j.jhydrol.2021.126508

180. Jia, Z., Zang, H., Zheng, X., Xu, Y., 2017. Climate Change and Its Influence on the Karst Groundwater Recharge in the Jinci Spring Region, Northern China. Water 9, 267. https://doi.org/10.3390/w9040267

181. Jiang, R., Li, Y., Wang, Q., Kuramochi, K., Hayakawa, A., Woli, K.P., Hatano, R., 2011. Modeling the water balance processes for understanding the components of river discharge in a non-conservative watershed. Trans. ASABE 54, 2171–2180. https://doi.org/10.13031/2013.40656

182. Jiang, S., Wei, L., Ren, L., Zhang, L., Wang, M., Cui, H., 2023. Evaluation of IMERG, TMPA, ERA5, and CPC precipitation products over mainland China: Spatiotemporal patterns and extremes. Water Sci. Eng. 16, 45–56. https://doi.org/10.1016/j.wse.2022.05.001

183. Jiang, Y., Gao, J., Yang, L., Wu, S., Dai, E., 2021. The interactive effects of elevation, precipitation and lithology on karst rainfall and runoff erosivity. CATENA, 207, 105588. https://doi.org/10.1016/j.catena.2021.105588

184. Johannet, A., Mangin, A., Vayssade, B., 2008. Modélisation d'un système karstique par réseaux de neurones : simulation des débits du karst du Baget, France. Collect. EDYTEM Cah. Géographie 7, 51–62. https://doi.org/10.3406/edyte.2008.1054

185. Jourde, H., Massei, N., Mazzilli, N., Binet, S., Batiot-Guilhe, C., Labat, D., Steinmann, M., Bailly-Comte, V., Seidel, J.L., Arfib, B., Charlier, J.B., Guinot, V., Jardani, A., Fournier, M., Aliouache, M., Babic, M., Bertrand, C., Brunet, P., Boyer, J.F., Bricquet, J.P., Camboulive, T., Carrière, S.D., Celle-Jeanton, H., Chalikakis, K., Chen, N., Cholet, C., Clauzon, V., Soglio, L.D., Danquigny, C., Défargue, C., Denimal, S., Emblanch, C., Hernandez, F., Gillon, M., Gutierrez, A., Sanchez, L.H., Hery, M., Houillon, N., Johannet, A., Jouves, J., Jozja, N., Ladouche, B., Leonardi, V., Lorette, G., Loup, C., Marchand, P., de Montety, V., Muller, R., Ollivier, C., Sivelle, V., Lastennet, R., Lecoq, N., Maréchal, J.C., Perotin, L., Perrin, J., Petre, M.A., Peyraube, N., Pistre, S., Plagnes, V., Probst, A., Probst, J.L., Simler, R., Stefani, V., Valdes-Lao, D., Viseur, S., Wang, X., 2018. SNO KARST: A French Network of Observatories for the Multidisciplinary Study of Critical Zone Processes in Karst Watersheds and Aquifers. Vadose Zone J. 17, 1–18. https://doi.org/10.2136/vzj2018.04.0094

186. Jukic, D., Denic-Jukic, V., 2006. Nonlinear kernel functions for karst aquifers. J. Hydrol. 328, 360–374. https://doi.org/10.1016/j.jhydrol.2005.12.030

187. Jury, W. A., 1982. Simulation of solute transport using a transfer function model. Water Resour. Res. 18(2), 363-368. https://doi.org/10.1029/WR018i002p00363

188. Kampf, S.K., Burges, S.J., Hammond, J.C., Bhaskar, A., Covino, T.P., Eurich, A., Harrison, H., Lefsky, M., Martin, C., McGrath, D. and Puntenney‐Desmond, K., 2020. The case for an open water balance: Re‐envisioning network design and data analysis for a complex, uncertain world. Water Resour. Res. 56, p.e2019WR026699. https://doi.org/10.1029/2019WR026699

189. Karger, D.N., Conrad, O., Böhner, J., Kawohl, T., Kreft, H., Soria-Auza, R.W., Zimmermann, N.E., Linder, H.P., Kessler, M., 2017. Climatologies at high resolution for the earth's land surface areas. Sci. Data 4, 170122. https://doi.org/10.1038/sdata.2017.122

190. Karki, R., Srivastava, P., Kalin, L., Mitra, S., Singh, S., 2021. Assessment of impact in groundwater levels and stream-aquifer interaction due to increased groundwater withdrawal in the lower Apalachicola-Chattahoochee-Flint (ACF) River Basin using MODFLOW. J. Hydrol.: Reg. Stud., 34, 100802. https://doi.org/10.1016/j.ejrh.2021.100802

191. Karki, R., Srivastava, P., Veith, T. L., 2020. Application of the Soil and Water Assessment Tool (SWAT) at Field Scale: Categorizing Methods and Review of Applications. Trans. ASABE, 63, 513–522. https://doi.org/10.13031/trans.13545

192. Kazakis, N., Chalikakis, K., Mazzilli, N., Ollivier, C., Manakos, A., Voudouris, K., 2018. Management and research strategies of karst aquifers in Greece: Literature overview and exemplification based on hydrodynamic modelling and vulnerability assessment of a strategic karst aquifer. Sci. Total Environ. 643, 592–609. https://doi.org/10.1016/j.scitotenv.2018.06.184

193. Khan, A., Koch, M., 2018. Correction and Informed Regionalization of Precipitation Data in a High Mountainous Region (Upper Indus Basin) and Its Effect on SWAT-Modelled Discharge. Water 10, 1557. https://doi.org/10.3390/w10111557

194. Kibii, J.K., Kipkorir, E.C., Kosgei, J.R., 2021. Application of Soil and Water Assessment Tool (SWAT) to Evaluate the Impact of Land-use and Climate Variability on the Kaptagat Catchment River Discharge. Sustainability, 13, 1802. https://doi.org/10.3390/su13041802

195. Kim, J., Choi, J., Choi, C., Park, S. 2013. Impacts of changes in climate and land-use/land cover under IPCC RCP scenarios on streamflow in the Hoeya River Basin, Korea. Sci. Total Environ. 2013, 452–453, 181–195. https://doi.org/10.1016/j.scitotenv.2013.02.005

196. Klaas, D.K.S.Y., Imteaz, M.A., Sudiayem, I., Klaas, E.M.E., Klaas, E.C.M., 2020. Assessing climate changes impacts on tropical karst catchment: Implications on groundwater resource sustainability and management strategies. J. Hydrol. 582, 124426. https://doi.org/10.1016/j.jhydrol.2019.124426

197. Kourgialas, N.N., Karatzas, G.P., Nikolaidis, N.P., 2010. An integrated framework for the hydrologic simulation of a complex geomorphological river basin. J. Hydrol., 381, 308–321. https://doi.org/10.1016/j.jhydrol.2009.12.003

198. Kovačič, G., Petrič, M., Ravbar, N., 2020. Evaluation and Quantification of the Effects of Climate and Vegetation Cover Change on Karst Water Sources: Case Studies of Two Springs in South-Western Slovenia. Water 12, 3087. https://doi.org/10.3390/w12113087

199. Kurtulus, B., Razack, M., 2007. Evaluation of the ability of an artificial neural network model to simulate the input-output responses of a large karstic aquifer: the La Rochefoucauld aquifer (Charente, France). Hydrogeol. J. 15, 241–254. https://doi.org/10.1007/s10040-006-0077-5

200. Kushwaha, A., Jain, M.K., 2013. Hydrological Simulation in a Forest Dominated Watershed in Himalayan Region using SWAT Model. Water Resour Manage 27, 3005–3023. https://doi.org/10.1007/s11269-013-0329-9

201. Labat, D., Ababou, R., Mangin, A., 1999. Linear and nonlinear input/output models for karstic springflow and flood prediction at different time scales. Stoch. Environ. Res. Risk Assess. 13, 337. https://doi.org/10.1007/s004770050055

202. Labat, D., Ababou, R., Mangin, A., 2000a. Rainfall–runoff relations for karstic springs. Part I: convolution and spectral analyses. J. Hydrol. 238, 123–148. https://doi.org/10.1016/S0022-1694(00)00321-8

203. Labat, D., Ababou, R., Mangin, A., 2000b. Rainfall–runoff relations for karstic springs. Part II: continuous wavelet and discrete orthogonal multiresolution analyses. J. Hydrol. 238, 149–178. https://doi.org/10.1016/S0022-1694(00)00322-X

204. Labat, D., Argouze, R., Mazzilli, N., Ollivier, C., Sivelle, V., 2022. Impact of Withdrawals on Karst Watershed Water Supply. Water 14, 1339. https://doi.org/10.3390/w14091339

205. Le Mesnil, M., Charlier, J.-B., Moussa, R., Caballero, Y., Dörfliger, N., 2020. Interbasin groundwater flow: Characterization, role of karst areas, impact on annual water balance and flood processes. J. Hydrol., 585, 124583. https://doi.org/10.1016/j.jhydrol.2020.124583

206. Le Roy, B., Lemonsu, A., Kounkou‐Arnaud, R., Brion, D., Masson, V., 2020. Long time series spatialized data for urban climatological studies: A case study of Paris, France. Int. J. Climatol. 40, 3567‐3584. https://doi.org/10.1002/joc.6414

207. Li, H., Ma, J., Yang, Y., Niu, L.; Lu, X., 2023. Performance of Frequency-Corrected Precipitation in Ungauged High Mountain Hydrological Simulation. Water 15(8), 1461. https://doi.org/10.3390/w15081461

208. Li, J., Yuan, D., Liu, J., Jiang, Y., Chen, Y., Hsu, K.L., Sorooshian, S., 2019. Predicting floods in a large karst river basin by coupling PERSIANN-CCS QPEs with a physically based distributed hydrological model. Hydrol. Earth Syst. Sci. 23, 1505–1532. https://doi.org/10.5194/hess-23-1505-2019

209. Lilli, M.A., Efstathiou, D., Moraetis, D., Schuite, J., Nerantzaki, S.D., Nikolaidis, N.P., 2020a. A Multi-Disciplinary Approach to Understand Hydrologic and Geochemical Processes at Koiliaris Critical Zone Observatory. Water 12(9), 2474. https://doi.org/10.3390/w12092474

210. Lilli, M.A., Nerantzaki, S.D., Riziotis, C., Kotronakis, M., Efstathiou, D., Kontakos, D., Lymberakis, P., Avramakis, M., Tsakirakis, A., Protopapadakis, K., Nikolaidis, N.P., 2020b Vision-Based Decision-Making Methodology for Riparian Forest Restoration and Flood Protection Using Nature-Based Solutions. Sustainability, 12, 3305. https://doi.org/10.3390/su12083305

211. Lobligeois, F., Andréassian, V., Perrin, C., Tabary, P., Loumagne, C., 2014. When does higher spatial resolution rainfall information improve streamflow simulation? An evaluation using 3620 flood events. Hydrol. Earth Syst. Sci. 18, 575–594. https://doi.org/10.5194/hess-18-575-2014

212. Lončar, G., Šreng, Ž., Bekić, D., Kunštek, D., 2018. Hydraulic-Hydrology Analysis of the Turbulent Seepage Flow within Karst Aquifer of the Golubinka Spring Catchment. Geofluids 2018, 1–12. https://doi.org/10.1155/2018/6424702

213. Londhe, D.S., Katpatal, Y.B., Bokde, N.D., 2023. Performance Assessment of Bias Correction Methods for Precipitation and Temperature from CMIP5 Model Simulation. Appl. Sci. 13(16), 9142. https://doi.org/10.3390/app13169142

214. Lukač Reberski, J., Rubinić, J., Terzić, J., Maja Radišić, 2020. Climate Change Impacts on Groundwater Resources in the Coastal Karstic Adriatic Area: A Case Study from the Dinaric Karst. Nat. Resour. Res., 29, 1975–1988. https://doi.org/10.1007/s11053-019-09558-6

215. Lukač Reberski, J., Terzić, J., Maurice, L.D., Lapworth, D.J., 2022. Emerging organic contaminants in karst groundwater: A global level assessment. J. Hydrol. 604, 127242. https://doi.org/10.1016/j.jhydrol.2021.127242

216. Luo, Y., Arnold, J., Allen, P., Chen, X., 2012. Baseflow simulation using SWAT model in an inland river basin in Tianshan Mountains, Northwest China. Hydrol. Earth Syst. Sci., 16, 1259–1267. https://doi.org/10.5194/hess-16-1259-2012

217. Luo, Y., He, C., Sophocleous, M., Yin, Z., Hongrui, R., Ouyang, Z., 2008. Assessment of crop growth and soil water modules in SWAT 2000 using extensive field experiment data in an irrigation district of the Yellow River Basin. J. Hydrol., 352, 139–156. https://doi.org/10.1016/j.jhydrol.2008.01.003

218. Ma, T., Duan, Z., Runkui Li, R., Song, X., 2019. Enhancing SWAT with remotely sensed LAI for improved modelling of ecohydrological process in subtropics. J. Hydrol., 570, 802–815. https://doi.org/10.1016/j.jhydrol.2019.01.024

219. Maggioni, V., Massari, C., 2018. On the performance of satellite precipitation products in riverine flood modeling: A review. J. Hydrol. 558, 214–224. https://doi.org/10.1016/j.jhydrol.2018.01.039

220. Malagò, A., Efstathiou, D., Bouraoui, F., Nikolaidis, N.P., Franchini, M., Bidoglio, G., Kritsotakis, M., 2016. Regional scale hydrologic modeling of a karst-dominant geomorphology: The case study of the Island of Crete. J. Hydrol. 540, 64–81. https://doi.org/10.1016/j.jhydrol.2016.05.061

221. Malagò, A., Pagliero, L., Bouraoui, F., Franchini, M., 2015. Comparing calibrated parameter sets of the SWAT model for the Scandinavian and Iberian peninsulas. Hydrol. Sci. J., 60, 949–967. https://doi.org/10.1080/02626667.2014.978332

222. Malagò, A., Vigiak, O., Bouraoui, F., Pagliero, L., Franchini, M., 2018. The Hillslope Length Impact on SWAT Streamflow Prediction in Large Basins. J. Environ. Inform., 32, 82–97. https://doi.org/10.3808/jei.201700384

223. Malenica, L., Gotovac, H., Kamber, G., Simunovic, S., Allu, S., Divic, V., 2018. Groundwater Flow Modeling in Karst Aquifers: Coupling 3D Matrix and 1D Conduit Flow

via Control Volume Isogeometric Analysis—Experimental Verification with a 3D Physical Model. Water 10, 1787. https://doi.org/10.3390/w10121787

224. Mangin, A., 1975. Contribution à l'étude hydrodynamique des aquifères karstiques (Thesis). Université de Dijon, France.

225. Mann, H.B., Whitney, D.R., 1947. On a Test of Whether one of Two Random Variables is Stochastically Larger than the Other. Ann. Math. Stat. 18, 50–60. https://doi.org/10.1214/aoms/1177730491

226. Mapes, K.L., Pricope, N.G., 2020. Evaluating SWAT Model Performance for Runoff, Percolation, and Sediment Loss Estimation in Low-Gradient Watersheds of the Atlantic Coastal Plain. Hydrology 7(2), 21. https://doi.org/10.3390/hydrology7020021

227. Marhaento, H., Martijn, J.B., Hoekstra, A.Y., 2018. Hydrological response to future land-use change and climate change in a tropical catchment. Hydrol. Sci. J., 63, 1368–1385. https://doi.org/10.1080/02626667.2018.1511054

228. Martínez-Salvador, A., Conesa-García, C., 2020. Suitability of the SWAT Model for Simulating Water Discharge and Sediment Load in a Karst Watershed of the Semiarid Mediterranean Basin. Water Resour. Manag., 34, 785–802. https://doi.org/10.1007/s11269-019-02477-4

229. Mazzilli, N., Guinot, V., Jourde, H., Lecoq, N., Labat, D., Arfib, B., Baudement, C., Danquigny, C., Dal Soglio, L., Bertin, D., 2019. KarstMod: A modelling platform for rainfall - discharge analysis and modelling dedicated to karst systems. Environ. Model. Softw. 122, 103927. https://doi.org/10.1016/j.envsoft.2017.03.015

230. Mehdi, B., Ludwig, R., Lehner, B., 2015. Evaluating the impacts of climate change and crop land use change on streamflow, nitrates and phosphorus: A modeling study in Bavaria. J. Hydrol. Reg. Stud. 4, 60–90. https://doi.org/10.1016/j.ejrh.2015.04.009

231. Merriman, K.R., Daggupati, P., Srinivasan, R., Hayhurst, B., 2019. Assessment of site-specific agricultural Best Management Practices in the Upper East River watershed, Wisconsin, using a field-scale SWAT model. J. Great Lakes Res., 45, 619–641. https://doi.org/10.1016/j.jglr.2019.02.004

232. Messerschmid, C., Aliewi, A., 2022. Spatial distribution of groundwater recharge, based on regionalised soil moisture models in Wadi Natuf karst aquifers, Palestine. Hydrol. Earth Syst. Sci. 26, 1043–1061. https://doi.org/10.5194/hess-26-1043-2022

233. Messerschmid, C., Sauter, M., Lange, J., 2020. Field-based estimation and modelling of distributed groundwater recharge in a Mediterranean karst catchment, Wadi Natuf, West Bank. Hydrol. Earth Syst. Sci. 24, 887–917. https://doi.org/10.5194/hess-24-887-2020

234. Mittal, N., Bhave, A. G., Mishra, A., Singh, R., 2016. Impact of Human Intervention and Climate Change on Natural Flow Regime. Water Resour Manage 30, 685–699. https://doi.org/10.1007/s11269-015-1185-6

235. Mittal, N., Bhave, A.G., Mishra, A., Singh. R., 2016. Impact of human intervention and climate change on natural flow regime. Water Resour. Manag., 30, 685-699. https://doi.org/10.1007/s11269-015-1185-6

236. Mo, C., Chen, X., Lei, X., Wang, Y., Ruan, Y., Lai, S., Xing, Z., 2022. Evaluation of Hydrological Simulation in a Karst Basin with Different Calibration Methods and Rainfall Inputs. Atmosphere 13, 844. https://doi.org/10.3390/atmos13050844

237. Mo, C., Lai, S., Yang, Q., Huang, K., Lei, X., Yang, L., Yan, Z., Jiang, C., 2023. A comprehensive assessment of runoff dynamics in response to climate change and human activities in a typical karst watershed, southwest China. J. Environ. Manage. 332, 117380. https://doi.org/10.1016/j.jenvman.2023.117380

238. Mo, C., Zhang, M., Ruan, Y., Qin, J., Wang, Y., Sun, G., Xing, Z., 2020. Accuracy Analysis of IMERG Satellite Rainfall Data and Its Application in Long-term Runoff Simulation. Water 12, 2177. https://doi.org/10.3390/w12082177

239. Monteith, J.L., 1965. Evaporation and environment. Symp. Soc. Exp. Biol. 19, 205–234.

240. Monteith, J.L., 1965. Evaporation and environment. Symp. Soc. Exp. Biol. 19, 205–234.

241. Moriasi, D.N., Gitau, M.W., Pai, N., Daggupati, P., 2015. Hydrologic and Water Quality Models: Performance Measures and Evaluation Criteria. Trans. ASABE 58, 1763–1785. https://doi.org/10.13031/trans.58.10715

242. Moriasi, D.N., Gitau, M.W., Pai, N., P. Daggupati, P., 2015. Hydrologic and Water Quality Models: Performance Measures and Evaluation Criteria. Trans. ASABE, 58, 1763–1785. https://doi.org/10.13031/trans.58.10715

243. Morris, M.D., 1991. Factorial Sampling Plans for Preliminary Computational Experiments. Technometrics 33, 161–174. https://doi.org/10.1080/00401706.1991.10484804

244. Moucha, A., Hanich, L., Tramblay, Y., Saaidi, A., Gascoin, S., Martin, E., Le Page, M., Bouras, E., Szczypta, C., Jarlan, L., 2021. Present and Future High-Resolution Climate

Forcings over Semiarid Catchments: Case of the Tensift (Morocco). Atmosphere 12, 370. https://doi.org/10.3390/atmos12030370

245. Mudarra, M., Hartmann, A., Andreo, B., 2019. Combining experimental methods and modeling to quantify the complex recharge behavior of karst aquifers. Water Resour. Res., 55, 1384–1404. https://doi.org/10.1029/2017WR021819

246. Muñoz-Sabater, J., Dutra, E., Agustí-Panareda, A., Albergel, C., Arduini, G., Balsamo, G., Boussetta, S., Choulga, M., Harrigan, S., Hersbach, H., Martens, B., Miralles, D.G., Piles, M., Rodríguez-Fernández, N.J., Zsoter, E., Buontempo, C., Thépaut, J.-N., 2021. ERA5-Land: a state-of-the-art global reanalysis dataset for land applications. Earth Syst. Sci. Data 13, 4349–4383. https://doi.org/10.5194/essd-13-4349-2021

247. Muthee, S. W., Kuria, B. T. O., Mundia, C. N., Sichangi, A. W., Kuria, D. N., Goebel, M., Rienow, A. 2023. Using SWAT to model the response of evapotranspiration and runoff to varying land uses and climatic conditions in the Muringato basin, Kenya. Model. Earth Syst. Environ. 9, 1531–1543. https://doi.org/10.1007/s40808-022-01579-0

248. Nash, J. E., 1957. The form of the instantaneous unit hydrograph. Intern. Assoc. of Scientific Hydrology, Publ, 3, 114-121.

249. Nash, J. E., 1959. Systematic determination of unit hydrograph parameters. J. Geophys. Res., 64(1), 111-115. https://doi.org/10.1029/JZ064i001p00111

250. Nash, J.E., Sutcliffe, J.V., 1970. River flow forecasting through conceptual models part I — A discussion of principles. J. Hydrol. 10, 282–290. https://doi.org/10.1016/0022-1694(70)90255-6

251. Neitsch, S.L., Arnold, J.G., Kiniry, J.R., Williams, J.R., 2011. Soil and Water Assessment Tool Theoretical Documentation. Texas Water Resources Institute, College Station, TX, USA.

252. Nerantzaki, S. D., Hristopulos, D. T., & Nikolaidis, N. P., 2020. Estimation of the uncertainty of hydrologic predictions in a karstic Mediterranean watershed. Sci. Total Environ. 717, 137131. https://doi.org/10.1016/j.scitotenv.2020.137131

253. Nerantzaki, S.D., Efstathiou, D., Giannakis, G.V., Kritsotakis, M., Grillakis, M.G., Koutroulis, A.G., Tsanis, I.K., Nikolaidis, N.P., 2019. Climate change impact on the hydrological budget of a large Mediterranean island. Hydrol. Sci. J., 64, 1190–1203. https://doi.org/10.1080/02626667.2019.1630741

254. Nerantzaki, S.D., Giannakis, G.V., Efstathiou, D., Nikolaidis, N.P., Sibetheros, A., Karatzas, G.P., Zacharias, I., 2015. Modeling suspended sediment transport and assessing the impacts of climate change in a karstic Mediterranean watershed. Sci. Total Environ., 538, 288–297. https://doi.org/10.1016/j.scitotenv.2015.07.092

255. Nerantzaki, S.D., Hristopulos, D.T., Nikolaidis, N.P. 2020. Estimation of the uncertainty of hydrologic predictions in a karstic Mediterranean watershed. Sci. Total Environ. 2020, 717, 137131. https://doi.org/10.1016/j.scitotenv.2020.137131

256. Nerantzaki, S.D., Nikolaidis, N.P., 2020. The response of three Mediterranean karst springs to drought and the impact of climate change. J. Hydrol. 591, 125296. https://doi.org/10.1016/j.jhydrol.2020.125296

257. Neupane, R.P., Kumar, S., 2015. Estimating the effects of potential climate and land-use changes on hydrologic processes of a large agriculture dominated watershed. J. Hydrol., 529, 418–429. https://doi.org/10.1016/j.jhydrol.2015.07.050.

258. Nguyen, P., Ombadi, M., Sorooshian, S., Hsu, K., AghaKouchak, A., Braithwaite, D., Ashouri, H., Thorstensen, A.R., 2018. The PERSIANN family of global satellite precipitation data: a review and evaluation of products. Hydrol. Earth Syst. Sci. 22, 5801–5816. https://doi.org/10.5194/hess-22-5801-2018

259. Nguyen, V.T., Dietrich, J., 2018. Modification of the SWAT model to simulate regional groundwater flow using a multicell aquifer. Hydrol. process., 32, 939–953. https://doi.org/10.1002/hyp.11466

260. Nguyen, V.T., Dietrich, J., Uniyal, B., 2020. Modeling interbasin groundwater flow in karst areas: Model development, application, and calibration strategy. Environ. Model. Softw. 124, 104606. https://doi.org/10.1016/j.envsoft.2019.104606

261. Nguyen, V.T., Dietrich, J., Uniyal, B., Tran, D.A., 2018. Verification and Correction of the Hydrologic Routing in the Soil and Water Assessment Tool. Water, 10, 1419. https://doi.org/10.3390/w10101419

262. Nikolaidis, N.P., Bouraoui, F., Bidoglio, G., 2013. Hydrologic and geochemical modeling of a karstic Mediterranean watershed. J. Hydrol. 477, 129–138. https://doi.org/10.1016/j.jhydrol.2012.11.018

263. Nilawar, A. P., & Waikar, M. L., 2019. Impacts of climate change on streamflow and sediment concentration under RCP 4.5 and 8.5: A case study in Purna river basin, India. Sci. Total Environ., 650, 2685–2696. https://doi.org/10.1016/j.scitotenv.2018.09.334

264. Nkwasa, A., Chawanda, C.J., Msigwa, A., Komakech, H.C., Verbeiren, B., van Griensven, A., 2020. How Can We Represent Seasonal Land Use Dynamics in SWAT and SWAT+ Models for African Cultivated Catchments? Water 12, 1541. https://doi.org/10.3390/w12061541

265. Oliver, C. W., Radcliffe, D. E., Risse, L. M., Habteselassie, M., Mukundan, R., Jeong, J., Hoghooghi, N., 2014. Quantifying the contribution of on‐site wastewater treatment systems to stream discharge using the SWAT model. J. Environ. Qual., 43(2), 539‐548. https://doi.org/10.2134/jeq2013.05.0195

266. Ollivier, C., Chalikakis, K., Mazzilli, N., Kazakis, N., Lecomte, Y., Danquigny, C., Emblanch, C., 2019. Challenges and Limitations of Karst Aquifer Vulnerability Mapping Based on the PaPRIKa Method—Application to a Large European Karst Aquifer (Fontaine de Vaucluse, France). Environments 6, 39. https://doi.org/10.3390/environments6030039

267. Ollivier, C., Mazzilli, N., Olioso, A., Chalikakis, K., Carrière, S.D., Danquigny, C., Emblanch, C., 2020. Karst recharge-discharge semi distributed model to assess spatial variability of flows. Sci. Total Environ. 703, 134368. https://doi.org/10.1016/j.scitotenv.2019.134368

268. Ollivier, C., Olioso, A., Carrière, S.D., Boulet, G., Chalikakis, K., Chanzy, A., Charlier, J.-B., Combemale, D., Davi, H., Emblanch, C., Marloie, O., Martin-StPaul, N., Mazzilli, N., Simioni, G., Weiss, M., 2021. An evapotranspiration model driven by remote sensing data for assessing groundwater resource in karst watershed. Sci. Total Environ. 781, 146706. https://doi.org/10.1016/j.scitotenv.2021.146706

269. Overton, D.E., 1966. Muskingum flood routing of upland streamflow. J. Hydrol. 4, 185–200. https://doi.org/10.1016/0022-1694(66)90079-5

270. Padilla, A., Pulido-Bosch, A., Mangin, A., 1994. Relative importance of basefow and quickfow from hydrographs of karst spring. Groundwater 32, 267–277. https://doi.org/10.1111/j.1745-6584.1994.tb00641.x

271. Paiva, I., Cunha, L., 2020. Characterization of the hydrodynamic functioning of the Degracias-Sicó Karst Aquifer, Portugal. Hydrogeol. J., 28, 2613–2629. https://doi.org/10.1007/s10040-020-02201-2

272. Palacios-Cabrera, T., Valdes-Abellan, J., Jodar-Abellan, A., Rodrigo-Comino, J., 2022. Land-use changes and precipitation cycles to understand hydrodynamic responses in semiarid Mediterranean karstic watersheds. Sci. Total Environ. 819, 153182. https://doi.org/10.1016/j.scitotenv.2022.153182

273. Palanisamy, B., Workman, S.R., 2015. Hydrologic modeling of flow through sinkholes located in streambeds of cane run stream, Kentucky. J. Hydrol. Eng., 20, 04014066. https://doi.org/10.1061/(ASCE)HE.1943-5584.0001060

274. Palazón, L., Navas, A., 2013. Sediment production of an alpine catchment with SWAT. Z. Geomorphol, 57, 69–85. https://doi.org/10.1127/0372-8854/2013/s-00136

275. Palazón, L., Navas, A., 2014. Modeling sediment sources and yields in a Pyrenean catchment draining to a large reservoir (Ésera River, Ebro Basin). J. Soils Sediments, 14, 1612–1625. https://doi.org/10.1007/s11368-014-0911-7

276. Palazón, L., Navas, A., 2016. Case Study: Effect of Climatic Characterization on River Discharge in an Alpine-Prealpine Catchment of the Spanish Pyrenees Using the SWAT Model. Water, 8, 471. https://doi.org/10.3390/w8100471

277. Parajuli, P.B., Risal, A., 2021. Evaluation of Climate Change on Streamflow, Sediment, and Nutrient Load at Watershed Scale. Climate, 9(11):165. https://doi.org/10.3390/cli9110165

278. Peinó, E., Bech, J., Udina, M., Polls, F., 2024. Disentangling Satellite Precipitation Estimate Errors of Heavy Rainfall at the Daily and Sub-Daily Scales in the Western Mediterranean. Remote Sens. 16, 457. https://doi.org/10.3390/rs16030457

279. Pfannerstill, M., Guse, B., Fohrer, N., 2014. A multi-storage groundwater concept for the SWAT model to emphasize nonlinear groundwater dynamics in lowland catchments. Hydrol. Process. 28, 5599–5612. https://doi.org/10.1002/hyp.10062

280. Phiri, W. K., Vanzo, D., Banda, K., Nyirenda, E., Nyambe, I.A., 2021. A pseudo-reservoir concept in SWAT model for the simulation of an alluvial floodplain in a complex tropical river system. J. Hydrol.: Reg. Stud., 33, 100770. https://doi.org/10.1016/j.ejrh.2020.100770

281. Pool, S., Vis, M., Seibert, J., 2018. Evaluating model performance: towards a non-parametric variant of the Kling-Gupta efficiency. Hydrol. Sci. J. 63, 1941–1953. https://doi.org/10.1080/02626667.2018.1552002

282. Poulain, A., Watlet, A., Kaufmann, O., Van Camp, M., Jourde, H., Mazzilli, N., Rochez, G., Deleu, R., Quinif, Y., Hallet, V., 2018. Assessment of groundwater recharge processes through karst vadose zone by cave percolation monitoring. Hydrol. Process. 32, 2069–2083. https://doi.org/10.1002/hyp.13138

283. Priestley, C.H.B., Taylor, R.J., 1972. On the Assessment of Surface Heat Flux and Evaporation Using Large-Scale Parameters. Mon. Weather Rev. 100, 81–92. https://doi.org/10.1175/1520-0493(1972)100<0081:OTAOSH>2.3.CO,2

284. Qi, J., Zhang, X., McCartyc, G.W., Sadeghi, A.M., Cosh, M.H., Zeng, X., Gao, F., Daughtry, C.S.T., Huang, C., Lang, M.W., Arnold, J.G., 2018. Assessing the performance of a physically-based soil moisture module integrated within the Soil and Water Assessment Tool. Environ. Model. Softw., 109, 329–341. https://doi.org/10.1016/j.envsoft.2018.08.024

285. Quintana-Seguí, P., Le Moigne, P., Durand, Y., Martin, E., Habets, F., Baillon, M., Franchisteguy, L., Morel, S. and Noilhan, J., 2008. The SAFRAN atmospheric analysis: Description and validation. J. Applied Meteorol. and Climatology 47, 92–107. https://doi.org/10.1175/2007JAMC1636.1

286. Rahbeh, M., Srinivasan, R., Mohtar, R., 2019. Numerical and conceptual evaluation of preferential flow in Zarqa River Basin, Jordan. Ecohydrol. Hydrobiol. 19, 224–237. https://doi.org/10.1016/j.ecohyd.2019.04.001

287. Rahman, M.M., Thompson, J.R., Flower, R.J. An Enhanced SWAT Wetland Module to Quantify Hydraulic Interactions between Riparian Depressional Wetlands, Rivers and Aquifers. Environ. Model. Softw. 2016, 84, 263–289. https://doi.org/10.1016/j.envsoft.2016.07.003

288. Raihan, F., Beaumont, L. J., Maina, J., Saiful Islam, A., Harrison, S. P., 2019. Simulating streamflow in the Upper Halda Basin of southeastern Bangladesh using SWAT model. Hydrol. Sci. J., 65(1), 138–151. https://doi.org/10.1080/02626667.2019.1682149

289. Rajib, M. A., Ahiablame, L., Paul, M., 2016. Modeling the effects of future land use change on water quality under multiple scenarios: A case study of low-input agriculture with

hay/pasture production. Sustainability of Water Quality and Ecology, 8, 50–66. https://doi.org/10.1016/j.swaqe.2016.09.001

290. Rashid, H., Yang, K., Zeng, A., Ju, S., Rashid, A., Guo, F., Lan, S., 2022. Predicting the Hydrological Impacts of Future Climate Change in a Humid-Subtropical Watershed. Atmosphere, 13, 12. https://doi.org/10.3390/atmos13010012

291. Richieri, B., Bittner, D., Sivelle, V., Hartmann, A., Labat, D., Chiogna, G., 2024. On the value of hydrochemical data for the interpretation of flow and transport processes in the Baget karst system, France. Hydrogeol. J. 32, 1537–1555. https://doi.org/10.1007/s10040-024-02801-2

292. Rigby, A.M.F., Butcher, P.W.S., Ritsos, P.D., Patil, S.D., 2022. LUCST: A novel toolkit for Land Use Land Cover change assessment in SWAT+ to support flood management decisions. Environ. Model. Softw. 156, 105469. https://doi.org/10.1016/j.envsoft.2022.105469

293. Ritter, B., Geleyn, J.-F., 1992. A Comprehensive Radiation Scheme for Numerical Weather Prediction Models with Potential Applications in Climate Simulations. Mon. Weather Rev. 120, 303–325. https://doi.org/10.1175/1520-0493(1992)120<0303:ACRSFN>2.0.CO,2

294. Romagnoli, M., Portapila, M., Rigalli, A., Maydana, G., Burgués, M., García, C.M., 2017. Assessment of the SWAT model to simulate a watershed with limited available data in the Pampas region, Argentina. Sci. Total Environ. 596–597, 437–450. https://doi.org/10.1016/j.scitotenv.2017.01.041

295. Ruggieri, G., Allocca, V., Borfecchia, F., Cusano, D., Marsiglia, P., De Vita, P., 2021. Testing Evapotranspiration Estimates Based on MODIS Satellite Data in the Assessment of the Groundwater Recharge of Karst Aquifers in Southern Italy. Water , 13, 118. https://doi.org/10.3390/w13020118

296. Ruiz, M.C., Valdés-Abellán, J., Pla, C., Fernández-Mejuto, M., Benavente, D., 2022. Land Cover Changes and Their Influence on Recharge in a Mediterranean Karstic Aquifer (Alicante, Spain). Land 12, 128. https://doi.org/10.3390/land12010128

297. Saha, P.P., Zeleke, K., Hafeez, M., 2014. Streamflow modeling in a fluctuant climate using SWAT: Yass River catchment in south eastern Australia. Environ Earth Sci 71, 5241–5254. https://doi.org/10.1007/s12665-013-2926-6

298. Salerno, F., Tartari, G., 2009. A coupled approach of surface hydrological modelling and Wavelet Analysis for understanding the baseflow components of river discharge in karst environments. J. Hydrol., 376, 295–306. https://doi.org/10.1016/j.jhydrol.2009.07.042

299. Salmani-Dehaghi, N., Samani, N., 2021. Development of bias-correction PERSIANN-CDR models for the simulation and completion of precipitation time series. Atmos. Environ. 246, 117981. https://doi.org/10.1016/j.atmosenv.2020.117981

300. Sánchez-Gómez, A., Martínez-Pérez, S., Pérez-Chavero, F.M., Molina-Navarro, E., 2022. Optimization of a SWAT model by incorporating geological information through calibration strategies. Optim. Eng., 23, 2203–2233. https://doi.org/10.1007/s11081-022-09744-1

301. Sarkar, S., Yonce, H.N., Keeley, A., Canfield, T.J., Butcher, J.B., Paul, M.J., 2019. Integration of SWAT and HSPF for Simulation of Sediment Sources in Legacy Sediment-Impacted Agricultural Watersheds. J. Am. Water Resour. Assoc., 55, 497–510. https://doi.org/10.1111/1752-1688.12731

302. Sarrazin, F., Hartmann, A., Pianosi, F., Rosolem, R., Wagener, T., 2018. V2Karst V1.1: a parsimonious large-scale integrated vegetation–recharge model to simulate the impact of climate and land cover change in karst regions. Geosci. Model Dev. 11, 4933–4964. https://doi.org/10.5194/gmd-11-4933-2018

303. Satgé, F., Ruelland, D., Bonnet, M.-P., Molina, J., Pillco, R., 2019. Consistency of satellite-based precipitation products in space and over time compared with gauge observations and snow- hydrological modelling in the Lake Titicaca region. Hydrol. Earth Syst. Sci. 23, 595–619. https://doi.org/10.5194/hess-23-595-2019

304. Schilling, K.E., Mount, J., Suttles, K.M., McLellan, E.L., Gassman, P.W., White, M.J., Arnold, J.G., 2023. An Approach for Prioritizing Natural Infrastructure Practices to Mitigate Flood and Nitrate Risks in the Mississippi-Atchafalaya River Basin. Land , 12, 276. https://doi.org/10.3390/land12020276

305. Schürz, C., 2019. SWATplusR: Running SWAT2012 and SWAT+ Projects in R. https://doi.org/10.5281/zenodo.3373859

306. Sellami, H., Benabdallah, S., La Jeunesse, I., Vanclooster, M., 2016. Quantifying hydrological responses of small Mediterranean catchments under climate change projections. Sci. Total Environ. 543, 924–936. https://doi.org/10.1016/j.scitotenv.2015.07.006

307. Sellami, H., La Jeunesse, I., Benabdallah, S., Baghdadi, N., Vanclooster, M., 2014. Uncertainty analysis in model parameters regionalization: a case study involving the SWAT model in Mediterranean catchments (Southern France). Hydrol. Earth Syst. Sci., 18, 2393–241. https://doi.org/10.5194/hess-18-2393-2014

308. Senent-Aparicio, J., Alcalá, F.J., Liu, S., Jimeno-Sáez, P., 2020. Coupling SWAT Model and CMB Method for Modeling of High-Permeability Bedrock Basins Receiving Interbasin Groundwater Flow. Water, 12, 657. https://doi.org/10.3390/w12030657

309. Setegn, S.G., Darfahi, B., Srinivasan, R., Melesse, A.M. Modeling of Sediment Yield From Anjeni-Gauged Watershed, Ethiopia using SWAT Model. J. Am. Water Resour. Assoc. 2010, 46, 514–526. https://doi.org/10.1111/j.1752-1688.2010.00431.x

310. Shao, G., Zhang, D., Guan, Y., Xie, Y., Huang, F., 2019. Application of SWAT Model with a Modified Groundwater Module to the Semi-Arid Hailiutu River Catchment, Northwest China. Sustainability, 11, 2031. https://doi.org/10.3390/su11072031

311. Shirafkan, M., Mohammadi, Z., Kavousi, A., Sivelle, V., Labat, D., Reimann, T., 2023. Toward the estimation of the transfer coefficient in karst systems: Using baseflow recession coefficient under matrix-restrained flow regime. J. Hydrol. 620, 129441. https://doi.org/10.1016/j.jhydrol.2023.129441

312. Shrestha, A., Sharma, S., McLean, C. E., Kelly, B. A., Martin, S. C., 2017. Scenario analysis for assessing the impact of hydraulic fracturing on stream low flows using the SWAT model. Hydrol. Sci. J., 62(5), 849–861. https://doi.org/10.1080/02626667.2016.1235276

313. Shrestha, S., Shrestha, M., Babel, M.S., 2016. Modelling the potential impacts of climate change on hydrology and water resources in the Indrawati River Basin, Nepal. Environ Earth Sci 75, 280. https://doi.org/10.1007/s12665-015-5150-8

314. Sinnathamby, S., Douglas-Mankin, K.R., Craige, C., 2017. Field-scale calibration of crop-yield parameters in the Soil and Water Assessment Tool (SWAT). Agric. Water Manag. 180, 61–69. https://doi.org/10.1016/j.agwat.2016.10.024

315. Sivelle, V., Cinkus, G., Mazzilli, N., Labat, D., Arfib, B., Massei, N., Cousquer, Y., Bertin, D., Jourde, H., 2023. Improvement of the KarstMod modeling platform for a better assessment of karst groundwater resources (preprint). Groundwater hydrology/Modelling approaches. https://doi.org/10.5194/hess-2023-17

316. Sivelle, V., Jourde, H., Bittner, D., Mazzilli, N., Tramblay, Y., 2021. Assessment of the relative impacts of climate changes and anthropogenic forcing on spring discharge of a Mediterranean karst system. J. Hydrol. 598, 126396. https://doi.org/10.1016/j.jhydrol.2021.126396

317. Sivelle, V., Jourde, H., Bittner, D., Richieri, B., Labat, D., Hartmann, A., Chiogna, G., 2022. Considering land cover and land use (LCLU) in lumped parameter modeling in forest dominated karst catchments. J. Hydrol. 612, 128264. https://doi.org/10.1016/j.jhydrol.2022.128264

318. Sivelle, V., Labat, D., 2019. Short-term variations in tracer-test responses in a highly karstified watershed. Hydrogeol. J. 27, 2061–2075. https://doi.org/10.1007/s10040-019-01968-3

319. Sivelle, V., Labat, D., Mazzilli, N., Massei, N., Jourde, H., 2019. Dynamics of the Flow Exchanges between Matrix and Conduits in Karstified Watersheds at Multiple Temporal Scales. Water 11, 569. https://doi.org/10.3390/w11030569

320. Sivelle, V., Renard, P., Labat, D., 2020. Coupling SKS and SWMM to Solve the Inverse Problem Based on Artificial Tracer Tests in Karstic Aquifers. Water 12, 1139. https://doi.org/10.3390/w12041139

321. Sloan, P.G., Moore, I.D., 1984. Modeling subsurface stormflow on steeply sloping forested watersheds. Water Resour. Res. 20, 1815–1822. https://doi.org/10.1029/WR020i012p01815

322. Sloan, P.G., Moore, I.D., 1984. Modeling subsurface stormflow on steeply sloping forested watersheds. Water Resour. Res. 20, 1815–1822. https://doi.org/10.1029/WR020i012p01815

323. Smakhtin, V.U., 2001. Low Flow Hydrology: A Review. J. Hydrol., 240 (3–4), 147–186. https://doi.org/10.1016/S0022-1694(00)00340-1

324. Smiatek, G., Kaspar, S., Kunstmann, H., 2013. Hydrological Climate Change Impact Analysis for the Figeh Spring near Damascus, Syria. J. Hydrometeorol. 14, 577–593. https://doi.org/10.1175/JHM-D-12-065.1

325. Soubeyroux, J.-M., Bernus, S., Corre, L., Drouin, A., Dubuisson, B., Etchevers, P., Gouget, V., Josse, P., Kerdoncuff, M., Samacoits, R., Tocque, F., 2020. Les nouvelles projections climatiques de référence DRAIS 2020 pour la Métropole,Tech. rep., Météo France. http://www.drias-climat.fr/document/rapport-DRIAS-2020-red3-2.pdf

326. Spruill, C., Workman, S., Taraba, J. Simulation of daily and monthly stream discharge from small watersheds using the SWAT model. Trans. ASABE 2000, 43, 1431. https://doi.org/10.13031/2013.3041

327. Stefanidis, K., Panagopoulos, Y., Psomas, A., Mimikou, M., 2016. Assessment of the natural flow regime in a Mediterranean river impacted from irrigated agriculture. Sci. Total Environ., 573, 1492–1502. https://doi.org/10.1016/j.scitotenv.2016.08.046

328. Stevanović, Z., 2019. Karst waters in potable water supply: a global scale overview. Environ. Earth Sci. 78, 662. https://doi.org/10.1007/s12665-019-8670-9

329. Strauch, M., Volk, M., 2013. SWAT plant growth modification for improved modeling of perennial vegetation in the tropics. Ecol. Model., 269, 98–112. https://doi.org/10.1016/j.ecolmodel.2013.08.013

330. Stroj, A., Briški, M., Oštrić, M., 2020. Study of Groundwater Flow Properties in a Karst System by Coupled Analysis of Diverse Environmental Tracers and Discharge Dynamics. Water , 12, 2442. https://doi.org/10.3390/w12092442

331. Sullivan, T.P., Gao, Y., Reimann, T., 2019. Nitrate transport in a karst aquifer: Numerical model development and source evaluation. J. Hydrol., 573, 432–448. https://doi.org/10.1016/j.jhydrol.2019.03.078

332. Sunde, M., He, H.S., Hubbart, J.A., Scroggins, G., 2016. Forecasting streamflow response to increased imperviousness in an urbanizing Midwestern watershed using a coupled modeling approach. Appl. Geogr., 72, 14–25. https://doi.org/10.1016/j.apgeog.2016.05.002

333. Sunde, M.G., He, H.S., Hubbart, J.A., Urban, M.A., 2017. Integrating downscaled CMIP5 data with a physically based hydrologic model to estimate potential climate change impacts on streamflow processes in a mixed-use watershed. Hydrol. Process., 31, 1790–1803. https://doi.org/10.1002/hyp.11150

334. Sunde, M.G., He, H.S., Hubbart, J.A., Urban, M.A., 2018. An integrated modeling approach for estimating hydrologic responses to future urbanization and climate changes in a mixed-use midwestern watershed. J. Environ. Manage. 220, 149–162. https://doi.org/10.1016/j.jenvman.2018.05.025

335. Tabary, P., 2007. The New French Operational Radar Rainfall Product. Part I: Methodology. Weather Forecast. 22, 393–408. https://doi.org/10.1175/WAF1004.1

336. Tabary, P., Dupuy, P., L'Henaff, G., Gueguen, C., Moulin, L., Laurantin, O., Merlier, C., Soubeyroux, J.-M., 2012. A 10-year (1997—2006) reanalysis of Quantitative Precipitation Estimation over France: methodology and first results. Presented at the Weather radar and hydrology, IAHS-AISH publication, pp. 255–260.

337. Taheri, K., Taheri, M., Parise, M., 2016. Impact of intensive groundwater exploitation on an unprotected covered karst aquifer: a case study in Kermanshah Province, western Iran. Environ. Earth Sci. 75, 1221. https://doi.org/10.1007/s12665-016-5995-5

338. Tan, M. L., Ibrahim, A. L., Yusop, Z., Duan, Z., Ling, L., 2015. Impacts of land-use and climate variability on hydrological components in the Johor River Basin, Malaysia. Hydrol. Sci. J. 60(5), 873–889. https://doi.org/10.1080/02626667.2014.967246

339. Tan, M.L., Gassman, P.W., Yang, X., Haywood, J., 2020. A review of SWAT applications, performance and future needs for simulation of hydro-climatic extremes. Adv. Water Resour., 143, 103662. https://doi.org/10.1016/j.advwatres.2020.103662

340. Tapoglou, E., Vozinaki, A.E., Tsanis, I., 2019. Climate Change Impact on the Frequency of Hydrometeorological Extremes in the Island of Crete. Water, 11, 587. https://doi.org/10.3390/w11030587

341. Teixeira Parente, M., Bittner, D., Mattis, S. A., Chiogna, G., Wohlmuth, B., 2019. Bayesian Calibration and Sensitivity Analysis for a Karst Aquifer Model Using Active Subspaces. Water Resour. Res. 55, 7086–7107. https://doi.org/10.1029/2019WR024739

342. Thomas, T., Ghosh, N.C., Sudheer, K.P., 2021. Optimal reservoir operation – A climate change adaptation strategy for Narmada basin in central India. J. Hydrol. 598, 126238. https://doi.org/10.1016/j.jhydrol.2021.126238

343. Tian, Y., Wang, S., Bai, X., Luo, G., Xu, Y., 2016. Trade-offs among ecosystem services in a typical Karst watershed, SW China. Sci. Total Environ., 566, 1297–1308. https://doi.org/10.1016/j.scitotenv.2016.05.190

344. Tritz, S., Guinot, V., Jourde, H., 2011. Modelling the behaviour of a karst system catchment using non-linear hysteretic conceptual model. J. Hydrol. 397, 250–262. https://doi.org/10.1016/j.jhydrol.2010.12.001

345. Tuo, Y., Duan, Z., Disse, M., Chiogna, G., 2016. Evaluation of precipitation input for SWAT modeling in Alpine catchment: A case study in the Adige river basin (Italy). Sci. Total Environ. 573, 66-82. https://doi.org/10.1016/j.scitotenv.2016.08.034

346. Tuppad, P., Douglas-Mankin, K.R., Lee, T., Srinivasan, R., Arnold, J.G., 2011. Soil and Water Assessment Tool (SWAT) Hydrologic/Water Quality Model: Extended Capability and Wider Adoption. Trans. ASABE, 5, 1677–1684. https://doi.org/10.13031/2013.39856

347. Tzoraki, O., Cooper, D., Kjeldsen, T., Nikolaidis, N.P., Gamvroudis, C., Froebrich, J., Querner, E., Gallart, F., Karalemas, N., 2013. Flood generation and classification of a semi-arid intermittent flow watershed: Evrotas river. Int. J. River Basin Manag., 11, 77–92, https://doi.org/10.1080/15715124.2013.768623

348. Uhlenbrook, S., Roser, S., Tilch, N., 2004. Hydrological process representation at the meso-scale: the potential of a distributed, conceptual catchment model. J. Hydrol. 291, 278–296. https://doi.org/10.1016/j.jhydrol.2003.12.038

349. Ulloa-Cedamanos, F., Probst, A., Dos-Santos, V., Camboulive, T., Granouillac, F., Probst, J.-L., 2021. Stream Hydrochemical Response to Flood Events in a Multi-Lithological Karstic Catchment from the Pyrenees Mountains (SW France). Water 13, 1818. https://doi.org/10.3390/w13131818

350. Ulloa-Cedamanos, F., Probst, J.-L., Binet, S., Camboulive, T., Payre-Suc, V., Pautot, C., Bakalowicz, M., Beranger, S., Probst, A., 2020. A Forty-Year Karstic Critical Zone Survey (Baget Catchment, Pyrenees-France): Lithologic and Hydroclimatic Controls on Seasonal and Inter-Annual Variations of Stream Water Chemical Composition, pCO2, and Carbonate Equilibrium. Water 12, 1227. https://doi.org/10.3390/w12051227

351. Ulloa-Cedamanos, F., Probst, J.L., Marais-Sicre, C., Vrech, E., Maire, E., Probst, A., 2022. Potential influence of landscape transition on stream water chemistry trends during the last decades in a karst catchment (Pyrenees, SW France) in a context of global environmental changes. Ecol. Indic. 140, 109023. https://doi.org/10.1016/j.ecolind.2022.109023

352. Uniyal, B., Dietrich, J., 2019. Modifying automatic irrigation in swat for plant water stress scheduling. Agric. Water Manag., 223, 105714. https://doi.org/10.1016/j.agwat.2019.105714

353. Uniyal, B., Dietrich, J., Vu, N.Q., Jha, M.K., Arumí, J.L., 2019. Simulation of regional irrigation requirement with SWAT in different agro-climatic zones driven by observed climate and two reanalysis datasets. Sci. Total Environ., 649, 846–865. https://doi.org/10.1016/j.scitotenv.2018.08.248

354. USDA-SCS, 1972. National Engineering Handbook, Section 4: Hydrology. Washington, D.C.: USDA.

355. USDA-SCS, 1972. National Engineering Handbook, Section 4: Hydrology. Washington, D.C.: USDA.

356. Vale, M., Holman, I.P., 2009. Understanding the hydrological functioning of a shallow lake system within a coastal karstic aquifer in Wales, UK. J. Hydrol., 376, 285–294. https://doi.org/10.1016/j.jhydrol.2009.07.041

357. Van Der Maaten, L., Postma, E., Van den Herik, J., 2009. Dimensionality reduction: a comparative review. J. Mach. Learn. Res. 10 (66–71).

358. van der Velde, Y., Torfs, P. J. J. F., Van der Zee, S. E. A. T. M., Uijlenhoet, R., 2012. Quantifying catchment‐scale mixing and its effect on time‐varying travel time distributions. Water Resour. Res., 48(6). https://doi.org/10.1029/2011WR011310

359. Van Griensven, A., Meixner, T., 2006. Methods to quantify and identify the sources of uncertainty for river basin water quality models. Water Sci. Technol. 53, 51–59. https://doi.org/10.2166/wst.2006.007

360. Van Leeuwen, P.J., Evensen, G., 1996. Data Assimilation and Inverse Methods in Terms of a Probabilistic Formulation. Mon. Weather Rev. 124, 2898–2913. https://doi.org/10.1175/1520-0493(1996)124<2898:DAAIMI>2.0.CO,2

361. Verleysen, M., François, D., 2005. The Curse of Dimensionality in Data Mining and Time Series Prediction. In: Cabestany, J., Prieto, A., Sandoval, F. (eds) Computational Intelligence and Bioinspired Systems. IWANN 2005. Lecture Notes in Computer Science, vol 3512. Springer, Berlin, Heidelberg. https://doi.org/10.1007/11494669_93

362. Vidal, J.-P., Martin, E., Franchistéguy, L., Baillon, M., Soubeyroux, J.-M., 2010. A 50-year high-resolution atmospheric reanalysis over France with the Safran system: A 50-YEAR HIGH-RESOLUTION ATMOSPHERIC REANALYSIS OVER FRANCE. Int. J. Climatol. 30, 1627–1644. https://doi.org/10.1002/joc.2003

363. Vigiak, O., Malagó, A., Bouraoui, F., Vanmaercke, M., Obreja, F., Poesen, P., Habersack, H., Fehér, J., Grošelj., S., 2017. Modelling sediment fluxes in the Danube River Basin with SWAT. Sci. Total Environ., 599–600, 992–1012. https://doi.org/10.1016/j.scitotenv.2017.04.236

364. Wagner, W., Hahn, S., Kidd, R., Melzer, T., Bartalis, Z., Hasenauer, S., Figa-Saldaña, J., De Rosnay, P., Jann, A., Schneider, S., Komma, J., Kubu, G., Brugger, K., Aubrecht, C., Züger, J., Gangkofner, U., Kienberger, S., Brocca, L., Wang, Y., Blöschl, G., Eitzinger, J.,

Steinnocher, K., 2013. The ASCAT Soil Moisture Product: A Review of its Specifications, Validation Results, and Emerging Applications. Meteorol. Z. 22, 5–33. https://doi.org/10.1127/0941-2948/2013/0399

365. Wang, R., Kalin, L., Kuang, W., Hanqin, T., 2014. Individual and combined effects of land-use/cover and climate change on Wolf Bay watershed streamflow in southern Alabama. Hydrol. Process., 28, 5530–5546. https://doi.org/10.1002/hyp.10057

366. Wang, Y., Brubaker, K., 2014. Implementing a nonlinear groundwater module in the soil and water assessment tool (SWAT): NONLINEAR GROUNDWATER MODULE IN SWAT. Hydrol. Process. 28, 3388–3403. https://doi.org/10.1002/hyp.9893

367. Wang, Y., Jiang, R., Xie, J., Zhao, Y., Yan, D., and Yang, S., 2019a. Soil and water assessment tool (SWAT) model: A systemic review. J. Coast. Res., 93, 22–30. https://doi.org/10.2112/SI93-004.1

368. Wang, Y., Shao, J., Su, C., Cui, Y., Zhang, Q., 2019b. The Application of Improved SWAT Model to Hydrological Cycle Study in Karst Area of South China. Sustainability, 11, 5024. https://doi.org/10.3390/su11185024

369. Wang, Z., Yin, J.-J., Pu, J., Wang, P., Liang, X., Yang, P., He, Q., Gou, P., Yuan, D., 2020. Integrated understanding of the Critical Zone processes in a subtropical karst watershed (Qingmuguan, Southwestern China): Hydrochemical and isotopic constraints Sci. Total Environ., 749, 141257. https://doi.org/10.1016/j.scitotenv.2020.141257

370. Wang, Z., Zhong, R., Lai, C., 2017. Evaluation and hydrologic validation of TMPA satellite precipitation product downstream of the Pearl River Basin, China. Hydrol. Process. 31, 4169–4182. https://doi.org/10.1002/hyp.11350

371. Welde, K., Gebremariam, B., 2017. Effect of land use land cover dynamics on hydrological response of watershed: Case study of Tekeze Dam watershed, northern Ethiopia. Int. Soil Water Conserv. Res., 5(1), 1–16. https://doi.org/10.1016/j.swaqe.2016.09.001

372. Welter, D.E., White, J.T., Hunt, R.J., Doherty, J.E., 2015. Approaches in highly parameterized inversion—PEST++ Version 3, a Parameter ESTimation and uncertainty analysis software suite optimized for large environmental models: U.S. Geological Survey Techniques and Methods (Techniques and Methods No. book 7, chap. C12). U.S. Geological Survey Techniques and Methods.

373. White, J.T., 2018. A model-independent iterative ensemble smoother for efficient history-matching and uncertainty quantification in very high dimensions. Environ. Model. Softw. 109, 191–201. https://doi.org/10.1016/j.envsoft.2018.06.009

374. White, J.T., Hunt, R.J., Fienen, M.N., Doherty, J.E., 2020. Approaches to Highly Parameterized Inversion: PEST++ Version 5, a Software Suite for Parameter Estimation, Uncertainty Analysis, Management Optimization and Sensitivity Analysis, U.S. Geological Survey Techniques and Methods 7C26.

375. Williams, J.R., 1969. Flood Routing with Variable Travel Time or Variable Storage Coefficients. Trans. ASAE 12, 0100–0103. https://doi.org/10.13031/2013.38772

376. Williams, J.R., Jones, C.A., Kiniry, J.R., Spanel, D.A., 1989. The EPIC Crop Growth Model. Trans. ASAE 32, 0497–0511. https://doi.org/10.13031/2013.31032

377. Williams, T. M., Amatya, D.M., Hitchcock, D.R., Edwards, A.E., 2014. Streamflow and Nutrients from a Karst Watershed with a Downstream Embayment: Chapel Branch Creek. J. Hydrol. Eng., 19, 428–438. https://doi.org/10.1061/(asce)he.1943-5584.0000794

378. Wilson, G.L., Dalzell, B.J., Mulla, D.J., Dogwiler, T., Porter, P.M., 2014. Estimating water quality effects of conservation practices and grazing land use scenarios. J. Soil Water Conserv., 69, 330–342. https://doi.org/10.2489/jswc.69.4.330

379. Wittenberg, H., 1994. Nonlinear analysis of flow recession curves. IAHS Publ., 221, 61–67.

380. Woldesenbet, T.A., Elagib, N.A., Ribbe, L., Heinrich, J., 2017. Hydrological responses to land use/cover changes in the source region of the Upper Blue Nile Basin, Ethiopia. Sci. Total Environ. 575, 724–741. https://doi.org/10.1016/j.scitotenv.2016.09.124

381. Wu, J., Yen, H., Arnold, J.G., Yang, Y.C.E., Cai, X., White, M.J., Santhi, C., Miao, C., Srinivasan, R., 2020. Development of reservoir operation functions in SWAT+ for national environmental assessments. J. Hydrol. 583, 124556. https://doi.org/10.1016/j.jhydrol.2020.124556

382. Wu, J., Zheng, H., Xi, Y., 2019. SWAT-based runoff simulation and runoff responses to climate change in the headwaters of the Yellow River, China. Atmosphere 10(9), 509. https://doi.org/10.3390/atmos10090509

383. Wu, X., Su, J., Ren, W., Lü, H., Yuan, F., 2023. Statistical comparison and hydrological utility evaluation of ERA5-Land and IMERG precipitation products on the Tibetan Plateau. J. Hydrol. 620, 129384. https://doi.org/10.1016/j.jhydrol.2023.129384

384. Xie, H., Longuevergne, L., Ringler, C., Scanlon, B.R., 2020. Integrating groundwater irrigation into hydrological simulation of India: Case of improving model representation of anthropogenic water use impact using GRACE. J. Hydrol.: Reg. Stud., 29, 100681. https://doi.org/10.1016/j.ejrh.2020.100681

385. Xie, P., Chen, M., Yang, S., Yatagai, A., Hayasaka, T., Fukushima, Y., Liu, C., 2007. A Gauge-Based Analysis of Daily Precipitation over East Asia. J. Hydrometeorol. 8, 607–626. https://doi.org/10.1175/JHM583.1

386. Xin, J., Chansheng, H., Lanhui, Z, Baoqing, Z., 2018. A Modified Groundwater Module in SWAT for Improved Streamflow Simulation in a Large, Arid Endorheic River Watershed in Northwest China. Chin. Geogr. Sci., 28, 47–60. https://doi.org/10.1007/s11769-018-0931-0

387. Yactayo, G.A., 2009. Modification of the SWAT Model to Simulate Hydrologic Processes in a Karst-Influenced Watershed. Master's Thesis, Virginia Tech, Blacksburg, VA, USA.

388. Yan, Y., Dai, Q., Yang, Y., Yan, L., Yi, X., 2022. Epikarst shallow fissure soil systems are key to eliminating karst drought limitations in the karst rocky desertification area of SW China. Ecohydrology 15. https://doi.org/10.1002/eco.2372

389. Yang, W., Chen, L., Chen, X., Chen, H., 2022. Sub-daily precipitation-streamflow modelling of the karst-dominated basin using an improved grid-based distributed Xinanjiang hydrological model. J. Hydrol. Reg. Stud. 42, 101125. https://doi.org/10.1016/j.ejrh.2022.101125

390. Ye, J., Lu, Y., Yang, X., He, Z., Huang, P., Zheng, X., 2023. Bias Correction of Hourly Satellite Precipitation Products and Their Application in Hydrological Modeling in a Hilly Watershed, China. Water 16, 49. https://doi.org/10.3390/w16010049

391. Yesuf, H.M., Assen, M., Alamirew, T., Melesse, A.M., 2015. Modeling of sediment yield in Maybar gauged watershed using SWAT, northeast Ethiopia. CATENA, 127, 191–205. https://doi.org/10.1016/j.catena.2014.12.032

392. Yuan, J., Li, R., Huang, K., 2022. Driving factors of the variation of ecosystem service and the trade-off and synergistic relationships in typical karst basin. Ecol. Indic., 142, 109253. https://doi.org/10.1016/j.ecolind.2022.109253

393. Zabaleta, A., Meaurio, M., Ruiz, E., Antigüedad, I., 2014. Simulation climate change impact on runoff and sediment yield in a small watershed in the Basque Country, northern Spain. J. Environ. Qual., 43(1), 235–245. https://doi.org/10.2134/jeq2012.0209

394. Zaibak, I., Meddi, M., 2022. Simulating streamflow in the Cheliff basin of west northern Algeria using the SWAT model. J. Earth Syst. Sci., 131, 25. https://doi.org/10.1007/s12040-021-01777-x

395. Zango, B.-S., Seidou, O., Sartaj, M., Nakhael, N., Stiles, K., 2022. Impacts of urbanization and climate change on water quantity and quality in the Carp River Watershed. J. Water Clim. Change, 13, 786–816. https://doi.org/10.2166/wcc.2021.158

396. Zeiger, S.J., Owen, M.R., Pavlowsky, R.T., 2021. Simulating nonpoint source pollutant loading in a karst basin: A SWAT modeling application. Sci. Total Environ. 785, 147295. https://doi.org/10.1016/j.scitotenv.2021.147295

397. Zettam, A., Taleb, A., Sauvage, S., Boithias, L., Belaidi, N., Sánchez-Pérez, J.M., 2017. Modelling Hydrology and Sediment Transport in a Semi-Arid and Anthropized Catchment Using the SWAT Model: The Case of the Tafna River (Northwest Algeria). Water, 9, 216. https://doi.org/10.3390/w9030216

398. Zhang, J., Zhang, P., Song, Y., 2022. Comparative Water Environment Simulation Study of Two Typical Models with BMPs in a Karst Basin. Agriculture, 12, 69. https://doi.org/10.3390/agriculture12010069

399. Zhang, M., Liu, N., Harper, R., Li, Q., Liu, K., Wei, X., Ning, D., Hou, Y., Liu, S., 2017. A global review on hydrological responses to forest change across multiple spatial scales: Importance of scale, climate, forest type and hydrological regime. J. Hydrol. 546, 44–59. https://doi.org/10.1016/j.jhydrol.2016.12.040

400. Zhang, Y., Hanati, G., Danierhan, S., Liu, Q., Xu, Z., 2020. Evaluation and Comparison of Daily GPM/TRMM Precipitation Products over the Tianshan Mountains in China. Water 12, 3088. https://doi.org/10.3390/w12113088

401. Zhang, Y., Su, F., Hao, Z., Xu, C., Yu, Z., Wang, L., Tong, K., 2015. Impact of projected climate change on the hydrology in the headwaters of the Yellow River basin. Hydrol. Process. 29(20), 4379-4397. https://doi.org/10.1002/hyp.8171

402. Zhao, F., Wu, Y., Qiu, L., Sun, Y., Sun, L., Li, Q., Niu, J., Wang, G., 2018. Parameter Uncertainty Analysis of the SWAT Model in a Mountain-Loess Transitional Watershed on the Chinese Loess Plateau. Water 10, 690. https://doi.org/10.3390/w10060690

403. Zhao, L., Yang, Y., Cao, J., Wang, Z., Luan, S., Xia, R., 2021. Applying a modified conduit flow process to understand conduit-matrix exchange of a karst aquifer. China Geol. 4, 1–8. https://doi.org/10.31035/cg2021046

404. Zhao, L.-j., Yang, Y., Cao, J.-w., Wang, Z., Luan, S., Xia, R.-y., 2022. Applying a modified conduit flow process to understand conduit-matrix exchange of a karst aquifer, China Geol., 5, 26–33. https://doi.org/10.1016/S2096-5192(22)00083-0

405. Zhou, F., Xu, Y., Chen, Y., Xu, C.-Y., Gao, Y., Du, J., 2013. Hydrological response to urbanization at different spatio-temporal scales simulated by coupling of CLUE-S and the SWAT model in the Yangtze River Delta region. J. Hydrol. 485, 113–125. https://doi.org/10.1016/j.jhydrol.2012.12.040

406. Zhou, Y., Zhao, L., Cao, J., Wang, Y., 2022. Using an Improved SWAT Model to Simulate Karst Sinkholes: A Case Study in Southwest China. Front. Environ. Sci. 10, 950098. https://doi.org/10.3389/fenvs.2022.950098

RÉPUBLIQUE FRANÇAISE
Liberté
Égalité
Fraternité

Université de Toulouse

Titre : Modélisation spatialisée semi-conceptuelle des flux d'eaux surface - souterrain en milieu karstique

Mots clés : modélisation semi-distributée, Bassins versants karstiques, SWAT, KarstMod, ISPEEKH, Hydrologie karstique

Résumé : Les aquifères karstiques, fournissant de l'eau potable à environ 25% de la population mondiale, sont confrontés à des surexploitations en sus du changement climatique. Des modèles hydrologiques ont été préconisés pour une gestion efficace des ressources en eau karstique. Cette thèse développe le modèle numérique semi-conceptuel spatialisé ISPEEKH en couplant SWAT+, la version restructurée du modèle éco-hydrologique semi-distribué SWAT, avec le module de réservoirs non linéaires épikarst-matrice-conduit du modèle de ruissellement pluvial KarstMod pour simuler les flux d'eau de surface-souterraine dans les bassins versants karstiques. ISPEEKH a été appliqué pour simuler le bilan hydrique quotidien du bassin versant du Baget (13.25 km2), situé dans les Pyrénées françaises et caractérisé par un écoulement non linéaire dominé par des conduits. Le modèle a simulé le débit du bassin versant de manière satisfaisante (NSE = 0,67, R2 = 0,68, et PBIAS = 0,7% pour la période de calibration 2008–2013, et NSE = 0,65, R2 = 0,69, et PBIAS = -13. 83% pour la période de validation 2014–2018), permettant l'estimation des flux des compartiments de l'épikarst, de la matrice et des conduits, y compris le débit d'échange entre la matrice et les conduits, et la contribution de la matrice et des flux de sortie du conduit principal au débit de la source karstique. La réponse hydrologique du bassin versant du Baget à des scénarios synthétiques de changement d'occupation du sol (reforestation et déforestation) a ensuite été évaluée à l'aide du modèle ISPEEKH. Les résultats ont montré que la reforestation sur l'ensemble du bassin versant n'a pas eu d'impact significatif sur son bilan hydrique, Le changement du couvert forestier à un couvert arbustif de transition a augmenté le débit annuel moyen de 6 à 9%, notamment pendant les périodes de faible débit, tandis que le changement du couvert forestier à des pâturages a réduit le débit annuel moyen de 5 à 7%, principalement en périodes de fort débit. En outre, un ensemble de données de précipitation a été évalué pour la simulation du débit journalier dans le bassin versant de 2006 à 2018, y compris les produits basés sur des données pluviométriques (CPC et E-OBS), de réanalyse (SAFRAN, COMEPHORE et ERA5-Land) et satellitaires (PERSIANN-CDR, IMERG-LR, SM2RAIN-ASCAT et CHIRPS). ISPEEKH a été intégré avec PEST pour la calibration automatisée, l'analyse de la sensibilité et la quantification de l'incertitude. Les résultats ont montré que le débit des cours d'eau était significativement sous-estimé sous l'ensemble des produits de précipitations. Les produits basés sur des données pluviométriques et satellitaires sont les moins performantes, avec un biais de sous-estimation du débit allant de 48 à 74%, tandis que les données de réanalyse ont fourni de meilleurs résultats de simulation du débit, avec un biais de sous-estimation du débit allant de 30 à 44%. Les données CPC, E-OBS, ERA5-Land, et IMERG-LR, ainsi que les données fusionnés CPC-IMERG-LR à une résolution de 1 km n'ont pas amélioré la capacité de prédiction du modèle par rapport aux données brutes. Les données à échelle réduite ainsi que COMEPHORE ont été corrigés pour réduire le biais de l'écart du bilan hydrique et ont été réappliqués pour la modélisation hydrologique. La simulation du débit a été améliorée significativement avec les données de précipitations COMEPHORE, E-OBS, CPC, et CPC-IMERG-LR corrigées. COMEPHORE a fourni la meilleure performance prédictive du modèle, suggérant que les précipitations de réanalyse locale à résolution fine pourraient être utilisées comme ensemble de données de base pour la modélisation hydrologique des bassins versants karstiques de méso-échelle.

Title: Semi-conceptual spatialized modeling of surface - underground water flows in a karst environment

Key words: semi-distributed numerical modeling, karst watersheds, SWAT, KarstMod, ISPEEKH, Karst hydrology

Abstract: Karst aquifers, which supply freshwater to nearly 25% of the global population, are facing depletion due to climate change and anthropogenic pressure. Hydrological models have been advocated for effective karst water resources planning and management, but studies integrating the recharge-discharge characteristics of karst watersheds and evaluating their response to changes in the flow dominant controls remain limited due to their inherent heterogeneity, anisotropy, flow duality, and non-linearity. This thesis developed the semi-conceptual spatialized numerical model ISPEEKH (Integration of Surface ProcEssEs in Karst Hydrology) by coupling SWAT+, the restructured version of the semi-distributed eco-hydrological model SWAT (Soil and Water Assessment Tool), with the non-linear epikarst-matrix-conduit reservoir module of the rainfall-runoff model KarstMod to simulate the surface-underground water flows in karst watersheds. ISPEEKH was applied to simulate the daily water balance of the Baget catchment (13.25 km2), located in a poorly gauged region of the French Pyrénées and characterized by conduit-dominated non-linear flow. The model simulated the catchment streamflow satisfactorily (NSE = 0.67, R2 = 0.68, and PBIAS = 0.7% for the 2008–2013 calibration period, and NSE = 0.65, R2 = 0.69, and PBIAS = -13.83% for the 2014–2018 validation period), allowing the estimation of the epikarst, matrix, and conduit fluxes, including the bidirectional matrix-conduit exchange flow rate, the contribution of the matrix and conduit outflows to spring flow, and their seasonal variability. The Baget catchment's hydrological response to synthetic land-use change scenarios of afforestation and deforestation was then assessed using ISPEEKH. Results showed that afforestation over the entire catchment did not significantly affect its water balance, while deforestation for wood production increased the mean annual discharge by 6–9%, notably in the low-flow periods, and deforestation for pastureland development reduced the mean annual discharge by 5–7%, mainly in the high-flow period. Various precipitation datasets were then evaluated for the simulation of daily streamflow in the catchment from 2006–2018, including the gauge-based (CPC and E-OBS), reanalysis (SAFRAN, COMEPHORE and ERA5-Land), and satellite-based (PERSIANN-CDR, IMERG-LR, SM2RAIN-ASCAT and CHIRPS) products. ISPEEKH was integrated with a PEST framework for automated calibration, sensitivity analysis, and uncertainty quantification. Results showed that streamflow was significantly underestimated under the ensemble of the precipitation products. The gauge- and satellite-based precipitation products had the worst performance, with a flow underestimation bias ranging from 48 to 74%, while the reanalysis products yielded better streamflow simulation results with a flow underestimation bias of 30–44%. The CPC, E-OBS, ERA5-Land, IMERG-LR, and merged CPC-IMERG-LR datasets downscaled to 1-km spatial resolution did not improve the model predictive performance compared to the coarse datasets. The downscaled datasets along with COMEPHORE were bias corrected to reduce the water balance discrepancy and re-applied for hydrological modeling. Significant improvement in the streamflow simulation were observed under the corrected COMEPHORE and downscaled E-OBS, CPC, and merged CPC-IMERG-LR precipitation datasets, with COMEPHORE yielding the best model predictive performance (NSE = 0.719, R2 = 0.736, and PBIAS = 3.2% for the calibration period, and NSE = 0.637, R2 = 0.732, and PBIAS = -10.65% for the validation period), suggesting that fine-resolution native reanalysis precipitation could be used as a base dataset for the hydrological modeling of remote meso-scale karst catchments.